Effect of background turbulence on the scalar field of a turbulent jet

by

Alejandro Perez-Alvarado

Department of Mechanical Engineering
McGill University
Montreal, Canada
August 2016

A thesis submitted to McGill University
in partial fulfillment of the requirements of the degree of
Doctor of Philosophy

Dedications

In memory of my grandmother Isidra

The old Antonio taught me that one is as big as the enemy chosen to fight and one is inversely proportional to the fear that one feels. "Choose a huge enemy and this will force you to grow and become better. Make your fear small because if it grows, then you would become smaller", the old Antonio told me during a rainy evening of May.
Write it in a story. Write that the old Antonio taught you. We all have had, sometime, an old Antonio. But if you have not, then I lend you mine for this time. Tell that the indigenous people of the south of Mexico make their fear small to become bigger and chose huge enemies to grow and become better.

Insurgent Sub-Commander Marcos in a letter to Eduardo Galeano

Abstract

The effect of background turbulence on the scalar field of an axisymmetric turbulent jet is investigated experimentally. The present investigation builds on the work of Gaskin *et al.* (2004), who studied the concentration and velocity fields of a plane jet in a shallow coflow with different turbulence levels and Khorsandi *et al.* (2013), who studied the velocity field of an axisymmetric turbulent jet emitted into a turbulent background. The primary objective of the present work was to systematically study the effect of a nearly homogeneous isotropic turbulent background with negligible mean flow on the mixing of a high-Schmidt-number scalar within a turbulent jet. The secondary objective, which was accomplished prior to the primary one, was to study the effect of the driving algorithm of a random jet array (RJA) in generating nearly homogeneous isotropic zero-mean-flow turbulence in a large water tank.

Different driving algorithms for a large RJA were tested and the statistics of the turbulence generated downstream of the RJA were compared to characterize the algorithms' performance. Variations in the spatial configuration of jets operating at any given instant, as well as in the statistics of their on/off times were studied. It was found that all the algorithms generated flows with non-zero skewness of the velocity fluctuation normal to the plane of the RJA and slightly super-Gaussian kurtoses of the velocity fluctuations in all directions. (The former was identified as a limitation of mono-planar RJAs resulting from the imposed forcing from only one side of the tank). The results showed that the algorithms imposing a regular spatial configuration of operating jets generated flows that were more isotropic, however, they suffered from large mean flows

and low turbulent kinetic energies. The algorithm identified as RANDOM generated the closest approximation of zero-mean-flow homogeneous isotropic turbulence. The flow generated by the RANDOM algorithm had a relatively high turbulent Reynolds number ($Re_T = u_T\ell/\nu = 2360$, where u_T is a characteristic RMS velocity, ℓ is the integral length scale of the flow, ν is the kinematic viscosity of the water) and the integral length scale ($\ell = 11.6$ cm) is the largest reported to date. Thus, RANDOM algorithm was used to generate the background turbulence for the investigation of scalar mixing within a turbulent jet.

The effect of background turbulence on the mixing of a passive scalar within a turbulent jet at different Reynolds numbers was investigated. To this end, planar laser-induced fluorescence was employed to obtain concentration measurements of dye (disodium fluorescein, Schmidt number = 2000) within the jet at different downstream distances. Two jet Reynolds numbers ($Re=U_jD/\nu$, where U_j is the jet exit velocity, D is the nozzle diameter and ν is the kinematic viscosity of the jet fluid, water) were studied: 10600 and 5800. The experiments were conducted with the jet discharging into either a quiescent background or a nearly homogeneous isotropic turbulent background with negligible mean flow. The resulting statistics of the scalar fields showed that the mean concentrations of jets emitted into turbulent backgrounds were lower than those of jets emitted into a quiescent background near the centerline. However, near the edges of the jet ($r/x>0.15$), the concentrations were higher for the jets issued into turbulent surroundings. The RMS concentrations of the jet emitted into a turbulent background significantly increased. Examination of the probability density functions of concentration revealed a higher degree of intermittency of the scalar field. The probability of low concentrations increased in the presence of background turbulence although the maximum concentrations were comparable to those of the jet emitted into a quiescent background. Flow visualizations revealed meandering of the jet issued into background turbulence, which is associated with the increased probability of lower concentrations and higher intermittency. Additionally, the widths of the jets emitted into a turbulent background were increased. For the lower jet Reynolds number, the described effects were more evident and the jet structure was destroyed by the background turbulence within the measurement region, resulting in flat radial profiles of both the mean and RMS concentrations. Comparison of the results of the scalar field with those of the hydrodynamic jet of Khorsandi *et al.* (2013) revealed a similar behavior of the two fields. However, the most significant difference was the larger radial extent of the profiles of mean and RMS concentrations, which resulted from the meandering of the jet and increased transport of scalar by turbulent diffusion. The flow visualizations suggest that the entrainment and mixing in the jet in a turbulent background changes with the destruction of jet structure, from jet driven entrainment to become potentially dominated by i) increased lateral advection of the jet by large scales of the background turbulence during the meandering of the jet, which is subsequently mixed by its smaller scales, and ii) turbulent diffusion that is significantly enhanced by the turbulent background.

Résumé

L'effet de la turbulence ambiante sur le champ scalaire d'un jet turbulent axisymétrique est étudié expérimentalement. La présente enquête se fonde sur les travaux de i) Gaskin et al. (2004), qui ont étudié les champs de vitesse et scalaire d'un jet plan au sein d’un écoulement peu profond avec différents niveaux de turbulence, et ii) Khorsandi et al. (2013), qui ont étudié le champ d'un jet turbulent axisymétrique émis en milieu turbulent. L'objectif principal de ce travail est d'étudier systématiquement l'effet d'un milieu turbulent quasi-homogène et isotrope à débit moyen négligeable sur le mélange d'un scalaire à grand nombre de Schmidt dans un jet turbulent. L'objectif secondaire, accompli avant l’objectif primaire, était d'étudier l'effet de l'algorithme de fonctionnement d'un « Random Jet Array » (RJA) sur la génération d’un milieu turbulent, homogène et isotrope, avec écoulement moyen nul dans un grand réservoir d'eau.

De différents algorithmes de fonctionnement d’un RJA ont été testés et les statistiques de la turbulence générée en aval du RJA ont été comparées pour caractériser la performance des algorithmes. Les variations de la configuration spatiale et temporelle du fonctionnement des jets ont été étudiées. Il a été constaté que tous les algorithmes génèrent des écoulements avec asymétrie de la fluctuation de la vitesse normale au plan du RJA, et des coefficients d'aplatissement des fluctuations de vitesse (en toutes les directions) légèrement super-gaussiens. (Le premier est une limitation de RJAs mono-planaires, résultant du forçage unilatéral.) Les résultats montrent que les algorithmes imposant une configuration spatiale régulière des jets régulière génèrent des

écoulements plus isotropes, mais avec de grandes vitesses moyennes et de faibles énergies cinétiques turbulentes. L'algorithme nommé « RANDOM » génère l'écoulement qui s'approche le plus de l'écoulement idéal : un écoulement turbulent homogène et isotrope avec vitesses moyennes nulles. L'écoulement généré par l'algorithme RANDOM avait un nombre de Reynolds turbulent ($Re_T = u_T\ell/\nu = 2360$, où u_T est une vitesse RMS caractéristique, ℓ est l'échelle intégrale de l'écoulement, ν est la viscosité cinématique de l'eau) relativement élevé, et une échelle intégrale de longueur (ℓ = 11,6 cm) étant la plus grande créée dans un RJA, à ce jour. Ainsi, l'algorithme RANDOM a été utilisé pour générer le milieu turbulent dans l'étude du mélange de scalaire au sein d'un jet turbulent.

Par la suite, cette recherche a visé l'effet du milieu turbulent sur le mélange d'un scalaire passif dans un jet turbulent à différents nombres de Reynolds. A cette fin, la fluorescence induite par laser a été utilisé pour obtenir des mesures de concentration d'une teinture fluorescente (*disodium fluorescein*, ayant un nombre de Schmidt = 2000) d'un jet à des distances en aval différentes. Deux nombres de Reynolds ($Re=U_jD/\nu$, où U_j est la vitesse du fluide à la sortie du jet, D est le diamètre de la buse, et ν est la viscosité cinématique du jet) ont été étudiés: 10600 et 5800. Les expériences ont été réalisées en émettant le jet en milieu i) tranquille, et ii) homogène et isotrope à petites vitesses moyennes. Les statistiques des champs scalaires montrent que les concentrations moyennes induites par un jet émis en milieu turbulent sont inférieures à celles d'un jet émis en milieu tranquille aux alentours de l'axe du jet. Cependant, aux bords du jet ($r/x > 0,15$), les concentrations s'avèrent plus élevées pour un jet émis en milieu turbulent. Les concentrations RMS du jet émis en milieu turbulent se révèlent considérablement

augmentées. Les fonctions de densité de probabilité de concentration révèlent un degré élevé de l'intermittence du champ scalaire. La probabilité de faible concentration augmente en milieu turbulent, bien que les concentrations maximales soient comparables à celles du jet émis en milieu tranquille. La visualisation du jet révèle le trajet sinueux d’un jet émis en milieu turbulent, qui est associé à la probabilité accrue des concentrations faibles et l’intermittence élevée du jet. En outre, les largeurs des jets émis en milieu turbulent augmentent. Pour le jet de nombre de Reynolds inférieur, l’intensité de ces effets accroit, et la structure du jet est, éventuellement, détruite par le milieu turbulent, ayant pour résultat des profils radiaux de concentrations (moyennes et RMS) plats. La comparaison des résultats du champ scalaire avec celles du champ hydrodynamique de Khorsandi et al. (2013) montre un comportement similaire des deux champs. Cependant, la différence la plus significative est l'étendue radiale plus grande des profils des concentrations (moyennes et RMS), qui résulte du méandre du jet et l'augmentation du transport du scalaire par la diffusion turbulente. Les visualisations suggèrent que l'entraînement et le mélange dans le jet émis en milieu turbulent peuvent potentiellement être reliés à i) l’accroissement de l’advection latérale du jet par les grandes échelles du milieu turbulent pendant les méandres du jet, qui est ensuite mélangé par ses échelles plus petites, et ii) la diffusion turbulente, qui est considérablement renforcée par le milieu turbulent.

Acknowledgements

The completion of this thesis would not have been possible without the help of many people. First, I would like to express my gratitude to my supervisors, Professor Laurent Mydlarski and Professor Susan Gaskin. I will be always grateful for their support, guidance and patience during my time at McGill University.

I also would like to thank Professor Baltasar Mena for his guidance during my undergraduate studies at UNAM. He became a role model, a mentor and encouraged me to start my Ph.D. studies.

I am grateful to CONACyT for their support during the first two years of the program. I am also grateful to the Faculty of Engineering for their support by way of a McGill Engineering Doctoral award.

I would like to thank the members of the technical staff for their assistance in the laboratory. I am thankful to John Bartczak for his help during the assembly of the experimental setup. I really appreciate the help of Marek Przykorski with the electronics. Moreover, Jorge Sayat and Dr. William Cook were very helpful with the computer problems in the laboratory.

Thanks also to my fellow graduate students Yulia, Dan, Stephen, Hossein, Sisi, Hauke and Claire. They were good classmates, lab mates and even better friends. I am

thankful to Saskatchewan FC for letting me be part of the amazing team. I also would like to thank the Mexican community at McGill for helping me to avoid homesickness.

Finally, I would like to express my deepest gratitude to all the members of my family for their confidence in me and for making me feel happy during my trips back home. Especially, I would like to thank my parents and my brother for their unconditional love and support during my whole life.

Preface

The experimental work outlined in this manuscript thesis was carried out in the Environmental Hydraulics laboratory in the Department of Civil Engineering and Applied Mechanics at McGill University. It is submitted to McGill University in partial fulfillment of the requirements of the degree of Doctor of Philosophy.

This manuscript-based thesis is comprised of two articles. Although the work presented in this thesis is the result of the collaboration with my co-supervisors, Professor Susan Gaskin and Professor Laurent Mydlarski, my contribution has been the predominant one. The details of the contributions for each article are summarized below:

Manuscript 1 (Chapter 4): *Effect of the driving algorithm on the turbulence generated by a random jet array*. This article has been published in *Experiments in Fluids*. Under the supervision of my two co-authors, Susan Gaskin and Laurent Mydlarski, I:

i) designed the driving algorithms to be tested,

ii) performed the experiments and data collection,

iii) analyzed the results, and

iv) wrote the manuscript, which was subsequently edited for publication by Susan Gaskin and Laurent Mydlarski.

Manuscript 2 (Chapter 5): *Effect of background turbulence on the scalar field of a turbulent jet*. This manuscript will be submitted for publication to the *Journal of Fluid Mechanics*. Under the supervision of my two co-authors, Susan Gaskin and Laurent Mydlarski, I:

i) modified and extended the existing experimental setup,

ii) performed the experiments and data collection,

iii) analyzed the results, and

iv) wrote the manuscript, which was subsequently edited for publication by Susan Gaskin and Laurent Mydlarski.

Statement of originality

The objective of the present work is to study the effect of a nearly homogeneous isotropic turbulent background with negligible mean flow on the scalar field of a turbulent jet. To this end, I tested different driving algorithms for a planar random jet array (RJA) to further characterize their performance and find an optimal algorithm that approximates zero-mean-flow homogeneous isotropic turbulence. Specific advantages and limitations of RJA systems were identified during the testing of the algorithms. The different driving algorithms investigated may be used by future researchers who require certain specific characteristics in a flow. The algorithm identified as RANDOM generated the most closely

approximated zero-mean-flow homogeneous isotropic turbulence. Subsequently, the effect of a background turbulence (generated by RANDOM) on the mixing of a high-Schmidt-number scalar within a turbulent jet was investigated. The statistics of the scalar field (including radial profiles of mean and RMS concentrations, half-widths and probability density functions of concentrations as well as their downstream evolution) and fluid visualizations helped to identify the characteristics of the scalar mixing within a turbulent jet emitted into a turbulent background. To the best of my knowledge, this is the first investigation of the effect of zero-mean-flow homogeneous isotropic turbulence on the scalar field of a turbulent jet and the results may be used in future work to benchmark numerical simulations to study more complex phenomena.

Table of contents

List of figures

List of tables

Chapter 1

Introduction

1.1 Background

The study of scalar mixing in turbulent flows has been an active area of research given its direct applications to both natural and industrial phenomena, such as the release of dangerous materials into the environment, chemical mixing, and combustion. Moreover, a common engineering flow used to mix scalars is the turbulent jet. For example, smokestacks emit pollutants into the atmosphere and outfalls release sewage into oceans by way of a turbulent jet. The reduction of the adverse effects to the environment and human health relies on the dilution of the pollutants with the ambient fluid by entrainment and mixing. Similarly, fuel is commonly injected into a combustor in the same manner. Thus, the understanding of the mixing within a turbulent jet is critical to both natural and industrial flows/phenomena.

Furthermore, most natural and industrial jet-like flows occur in the presence of external turbulence. Yet, the vast majority of previous studies of turbulent jets considered the emission of jets into quiescent or laminar surroundings. This seriously hinders the complete understanding and prediction of the behavior of turbulent jets in realistic situations, such as those described above. Moreover, “real” flows are further complicated by the addition of effects such as: i) mean flow advection, ii) ambient density stratification, or iii) boundary effects. Although it is extremely difficult to account for all the mentioned variables, it is clearly beneficial to study their individual contributions to the mixing process. The present work will therefore focus on the effect of background turbulence on the scalar mixing that occurs within a turbulent jet.

To date, two principal hypotheses on the effect of background turbulence on the evolution of turbulent jets have been proposed. The standard assumption, which was assumed to be a conservative estimate for practical applications, was superposition of the dilution effects of the jet and of the turbulent surroundings. Wright (1994) proposed a model in which the entrainment coefficient was increased to account for this superposition of effects leading to increased jet dilution. Although certain experimental studies of plumes (Ching *et al.* 1995) and jets (Guo *et al.* 1999, 2005; Law *et al.* 2001; Cuthbertson *et al.* 2006) emitted in grid-generated turbulence support this prediction, the results have been questioned (Gaskin *et al.* 2004) because, in these studies, the jet/plume was released perpendicularly to the grid, resulting in the intensity of the background turbulence increasing in the downstream direction of the jet/plume. In contrast, Hunt (1994) argued that the effect of the external turbulence may be to disrupt the jet structure, resulting in decreased entrainment, and thus a reduced spreading rate of the jet, leading to decreased dilution of the jet. Gaskin *et al.* (2004) presented velocity and concentration measurements in support of this hypothesis for plane jets in a turbulent co-flow. Khorsandi *et al.* (2013) measured lower mass flow rates in axisymmetric turbulent jets emitted into a turbulent background with zero mean flow which were associated with lower entrainment into the jet. The latter may imply lower levels of scalar mixing. Consequently, the effect of background turbulence on turbulent jets requires additional research necessary to aid in resolving these contradictions and understand the processes in more detail.

1.2 Objectives

The present work is an experimental investigation of the effect of background turbulence on the mixing of a passive scalar within a momentum-driven, axisymmetric turbulent jet. The background turbulence is generated by a random jet array (RJA). The

RJA generated a nearly homogenous, isotropic turbulent background with negligible mean flow, which therefore permits the isolation of the effect of the velocity fluctuations on the jet from advection effects.

The main objective of the present thesis is to study the effect of the background turbulence on a scalar field within a turbulent jet. To this end, planar laser-induced fluorescence is employed to obtain concentration measurements of dye (disodium fluorescein, Schmidt number = 2000) within the turbulent jet at different distances from the nozzle exit ($10 \le x/D \le 70$). Concentration measurements of the scalar within a jet emitted into a *quiescent* background are first obtained to benchmark the experimental technique used herein. The results of these experiments are compared to previous studies to validate the experimental method. Subsequently, the effect of the background turbulence on the mixing of the scalar within the jet is investigated. To this end, concentration measurements of dye within the jet emitted into a turbulent background are obtained. The statistics of the scalar field are compared with those of the jet emitted into a quiescent background to quantify the effect of the background turbulence. Flow visualizations of the jet are used to describe the characteristics of the mixing process in the presence of background turbulence, as well as to understand the resulting statistics of the scalar field. Additionally, the measured statistics of the scalar field are compared to those of the hydrodynamic jet of Khorsandi *et al.* (2013) (obtained in the same experimental facility) to observe any differences in the evolution of the two fields. Two jet Reynolds numbers are investigated: 5800 and 10600. The larger Reynolds number is selected to be above the mixing transition ($\sim 10^4$, Dimotakis 2000) and the low Reynolds number is chosen so as to observe the complete destruction of the jet structure (by the background turbulence) within the measurement region.

A secondary objective of the present study (achieved prior to the main one) is to investigate the effect of the driving algorithms on the turbulence generated by a random jet array (RJA). Different algorithms are tested and their performance characterized by comparing the statistics of the turbulence generated downstream of the RJA. Velocity measurements employing acoustic Doppler velocimetry are obtained and their statistics compared to determine the "optimal" driving algorithm, which produces the closest approximation to zero-mean-flow, homogeneous, isotropic turbulence.

1.3 Organization of the Thesis

The remainder of the thesis is organized as follows. Chapter 2 presents a literature review of i) the evolution of passive scalars within turbulent jets emitted into quiescent backgrounds, ii) entrainment in turbulent jets emitted into quiescent backgrounds, iii) homogeneous, isotropic turbulence, iv) the effect of background turbulence on boundary layers, wakes, jets and plumes, and v) laser-induced fluorescence (LIF).

The experimental apparatus is presented in Chapter 3. This includes a description of the experimental setup used to obtain velocity measurements of the turbulence generated by the different driving algorithms for the RJA. The experimental apparatus for the concentration measurements is described in detail and the calibration procedure is presented.

The results and discussions of the experiments are presented in Chapters 4 and 5. Those presented in Chapter 4 pertain to the study of the effect of the different driving algorithms tested to generate the closest approximation of zero-mean-flow, homogeneous, isotropic turbulence. In Chapter 5, statistics of the scalar field within turbulent jets emitted into both quiescent and turbulent backgrounds are presented and discussed. In addition, the results of the scalar field of jets emitted into a turbulent background is compared to those of the hydrodynamic jet of Khorsandi *et al.* (2013), and a discussion of the mixing process in jets emitted into a turbulent background is presented.

Finally, the conclusions, novel contributions and recommendations for future work are presented in Chapter 6.

Chapter 2

Literature review

A review of the following topics, closely related to this research, is presented: i) the evolution of passive scalars within turbulent jets emitted into quiescent backgrounds, ii) entrainment in turbulent jets emitted into quiescent background, iii) homogeneous isotropic turbulence, iv) the effect of background turbulence on boundary layers, wakes, jets and plumes, and v) laser-induced fluorescence (LIF).

2.1 Passive scalar in turbulent jets

Turbulent jets are one of the most frequently studied free shear flows. They are relatively simple flows that commonly occur in practical applications (e.g. the release of harmful materials into the atmosphere and oceans) and are used in laboratories to study and understand more complex phenomena. The flow under consideration in the present study is a steady-state, momentum-driven, axisymmetric, turbulent jet. The axisymmetric jet is a free shear flow with dominant mean motion in the axial direction, spreading of the jet in the radial direction, and zero mean velocity in the azimuthal direction (i.e. no swirl). For a jet emitted into a quiescent background the axial gradients are small compared to the radial gradients, and the boundary layer approximations can be applied to the equations of motion (Pope 2000). The boundary layer approximations for this flow reduce the continuity and axial momentum equations to:

$$\frac{\partial\langle U\rangle}{\partial x}+\frac{1}{r}\,\frac{\partial(r\langle V\rangle)}{\partial r}=0 \tag{2.1}$$

$$\langle U\rangle\frac{\partial\langle U\rangle}{\partial x}+\langle V\rangle\,\frac{\partial\langle U\rangle}{\partial r}=\frac{\nu}{r}\frac{\partial}{\partial r}\left(r\,\frac{\partial\langle U\rangle}{\partial r}\right)-\frac{1}{r}\frac{\partial}{\partial r}(r\langle uv\rangle) \tag{2.2}$$

where U is the axial velocity, x is the axial coordinate, V is the radial velocity, r is radial coordinate, u is the fluctuating axial velocity, v is the fluctuating radial velocity, ν is the kinematic viscosity, and $\langle\cdot\rangle$ denotes averaging. The mean pressure distribution has been obtained from the radial momentum equation and subsequently substituted in equation 2.2. The velocity field of an axisymmetric jet discharging into a quiescent background has been investigated extensively and its behaviour is well documented (Wygnanski and Fiedler 1969; Panchapakesan and Lumley 1993a; Hussain *et al.* 1994; Xu and Antonia 2002; Lipari and Stansby 2011; Darisse et al. 2015; and the references therein). At some distance downstream (after the so-called developing region), the jet becomes self-similar and the axial mean velocity profile is approximately Gaussian. Under self-similar conditions, the centerline mean velocity of an axisymmetric turbulent jet decays as x^{-1} and the half-width (defined as the radial distance at which the mean axial velocity decays to half of its centerline value) increases as x^1. The root mean square (RMS) of the velocity fluctuations also becomes self-preserving farther downstream.

Turbulent flows (such as a turbulent jet) are characterized by the existence of a continuum of length scales (some with specific physical interpretations) bounded by the largest scales (with dimensions characteristic of the geometry of the flow) and the smallest ones (at which the diffusive action of molecular diffusivity and viscosity smear the concentration and velocity fluctuations, respectively (Tennekes and Lumley 1972)). Such an extent of scales is the motivation for the use of spectral analysis, which provides information on the range of scales in the turbulent motion. Kolmogorov theory (Kolmogorov 1941a,b) postulates that the smallest (Kolmogorov) scales of the velocity field (at which the turbulent kinetic energy is converted into internal energy by viscous dissipation) depend only on the kinematic viscosity (ν) and the dissipation rate of turbulent kinetic energy per unit mass (ε). Consequently, the Kolmogorov length scale is defined as $\eta \equiv (\nu^3/\varepsilon)^{1/4}$. Kolmogorov theory furthermore predicts a -5/3 power law region of the energy spectrum in the so-called inertial subrange, occurring at scales between the largest and the Kolmogorov scales, where viscosity and large-scale effects are small/negligible.

When studying scalars fields, the Schmidt number ($Sc=\nu/\mathcal{D}$, where $\mathcal{D}$ is the molecular diffusivity of the scalar in the given fluid) is an important parameter. It dictates the size of the smallest (dissipative) scales of the scalar field. Using similar arguments to those underlying Kolmogorov theory, Corrsin (1951) defined the smallest scales of a scalar field in which Sc<<1 as $\eta_\theta \equiv (\mathcal{D}^3/\varepsilon)^{1/4} = \eta Sc^{-3/4}$. When the Schmidt number is equal to or smaller than one (as it is for gases), the “Corrsin scale” (η_θ) is equal to or larger than the Kolmogorov scale, and the spectra of the scalar fluctuations is predicted to exhibit a -5/3 power law region (similar to the velocity field) in the so-called inertial-convective subrange, which occurs at scales between the largest and the smallest (η_θ) scales (Oboukhov 1949, Corrsin 1951). In a later investigation, Batchelor (1959) defined the smallest scales of the scalar field for Sc>>1 as $\eta_B \equiv (\nu\mathcal{D}^2/\varepsilon)= \eta Sc^{-1/2}$, called the “Batchelor scale,” in his honour. If Sc is much larger than one (which is often the case for scalars in liquids), the Batchelor scale is smaller than the Kolmogorov scale, and the prediction establishes two power law regions for the spectra of the scalar fluctuations. The first one is a -5/3 power law decay occurring between the largest and the Kolmogorov scales (known as the inertial-convective subrange) and the second one is a -1 power law decay between the Kolmogorov and the Batchelor scales (in the viscous-convective subrange).

A passive scalar is a non-reactive "contaminant" whose presence does not affect the velocity field in which it is transported. The transport of a passive scalar (C) in a non-reacting flow is governed by the advection-diffusion equation:

$$\frac{\partial C}{\partial t} + u_i \frac{\partial C}{\partial x_i} = \mathcal{D} \frac{\partial^2 C}{\partial x_i \partial x_i} \tag{2.3}$$

where C is the concentration of the passive scalar, t is time, u_i is the velocity in the i-direction and $\mathcal{D}$ is the molecular diffusivity of the passive scalar. A non dimensionalized equation for the normalized concentration can be obtained by defining the non-dimensional variables $C^*=C/C_o$, $t^*=U_j t/D$, $u_i^*=u_i/U_j$, and $x_i^*=x_i/D$, where C_o is the jet nozzle concentration, U_j the jet exit velocity and D the jet nozzle diameter in the present flow. Substitution of the non-dimensional variables into the advection-diffusion equation results in:

$$\frac{\partial C^*}{\partial t^*} + u_i^* \frac{\partial C^*}{\partial x_i^*} = \frac{1}{ReSc} \frac{\partial^2 C^*}{\partial x_i^* \partial x_i^*} \tag{2.4}$$

where $Re=U_j D/\nu$ and $Sc=\nu/\mathcal{D}$, which are the definitions of the Reynolds and Schmidt numbers, respectively. The product ReSc can be interpreted as the Péclet number (Pe=ReSc). From the normalized concentration equation, it is clear that the evolution of the scalar concentration depends on the product of the Reynolds and Schmidt numbers.

A considerable number of experimental investigations of the scalar field in turbulent jets discharging into a quiescent background have been conducted. Different techniques have been employed over the years and different experimental conditions have been imposed. Although most of the experimental setups were unable to resolve the smallest scales (Batchelor scale), most statistics of the scalar fields were similar to and followed the same trends observed in studies fully resolving all scales. A review of the most important studies of the scalar field advected by a turbulent jet, and discharging into a quiescent environment is presented in the following paragraphs. In this section, gas-phase (Sc~1) studies will be discussed first, followed by a review of liquid-phase experiments (generally with Sc~2000).

When the passive scalar is temperature, the thermal diffusivity (α) replaces the molecular diffusivity in the definition of Sc and the resulting dimensionless parameter is called the Prandtl number ($Pr=\nu/\alpha$). Wilson and Danckwerts (1964) performed temperature measurements ($Pr \sim 1$) in a hot air jet at different temperature excesses. Measurements were recorded using a resistance-thermometer in jets with Reynolds numbers in the range $2x10^4 < Re < 4x10^4$. The axial mean temperature excess was found to follow an x^{-1} decay, and the half-width of the scalar profile was found to increase as x^1. The mean radial profile of temperature excess was well described by a Gaussian function, which was self-similar after 20 jet diameters downstream of the jet exit, whereas the RMS profile of the temperature fluctuations was found to become self-similar after 40 jet diameters. Also, the normalized RMS temperature fluctuations ($\theta_{RMS}/\Delta T$) along the centerline were found to asymptote to 0.18. These characteristics form the basis of the generally accepted behaviour of the passive scalar concentration field in turbulent jets, however, other, more recent results are presented below.

Becker *et al.* (1967) presented a novel light-scattering technique to study the concentration field of a free air jet (Re=54000) using smoke as the marker (Sc~38000). The normalized RMS centerline concentration fluctuation attained a constant value of approximately 0.22. The concentration power spectra at the centerline exhibited a -5/3 power region. However, a k^{-1} region was not identified due to the inadequate spatial resolution of the technique, which was unable to resolve the smallest scales.

Birch *et al.* (1978) performed concentration measurements in a methane jet (Re=1600 and Sc~1) using Raman scattering of laser light. When comparing the results with those of hot air jets, the RMS concentration fluctuations along the centerline, as well as the peak of the radial RMS concentration, were higher for the methane jet. The probability density function (pdf) of the concentration became self-preserving 20 diameters downstream of the jet exit. At the centerline, the pdf was approximately Gaussian with a slight negative skewness, and became bimodal with high probabilities of zero concentration near the edges of the jet (a consequence of the intermittency of the flow at that location).

Lockwood *et al.* (1980) reported measurements of temperature in a heated inert round free jet (Pr~1) using a thermocouple. The Reynolds number was approximately 5×10^4. The centreline intensity of the temperature fluctuations attained a constant value about 0.21 at 40 diameters downstream. The radial profile of the temperature intensities showed that the maximum values corresponded with those of the steepest gradient of the mean temperature profile. The length of the -5/3 power law region in the power spectra was also found to increase with radial distance.

An extensive investigation of the transport of a scalar in a turbulent gas phase jet was conducted by Dowling and Dimotakis (1990). Rayleigh scattering was used to measure the scalar field of different jet/reservoir combinations (Sc~1) at Re = 5000, 16000 and 40000. The apparatus employed could resolve the smallest scales for Re =5000 and 16000 but not for the Re=40000. The radial profiles of the RMS concentration fluctuations broadened with increasing Re. A similar effect was observed when the Schmidt number was increased by comparing with the experiments of Dahm and Dimotakis (1990) in which a water jet was seeded with disodium fluorescein (Sc~2000). The pdfs of concentration fluctuations in the work of Dowling and Dimotakis (1990) showed no unmixed fluid on the jet axis, in contrast with the findings at higher Schmidt number (Dahm and Dimotakis, 1990).

Panchapakesan and Lumley (1993a,b) performed simultaneous measurements of the scalar concentration and two velocity components in both jets of air and helium (Sc~0.7) discharging into air using a composite hot-wire/concentration probe. The measurements spanned the transition region between the non-buoyant jet and the plume region (50 < x/D <120 in their flow). It was observed that the i) mean concentration profile was wider for the helium jet than that of a pure air jet, and ii) axial RMS of the velocity fluctuations was higher in the helium jet than in the air jet, which was explained by the additional buoyancy effects.

An investigation into the fine-scale scalar mixing in a gaseous jet was carried out by Su and Clemens (2003). Simultaneous planar Rayleigh scattering and planar laser induced fluorescence (PLIF) measurements were performed in parallel planes, obtaining instantaneous three-dimensional scalar measurements. The Reynolds number ranged from 3290 to 8330. It was observed that the scalar dissipation rate field is organized into layer-like structures consistent with previous observations of Buch and Dahm (1996) for a water jet (Sc~2000).

Darisse *et al.* (2015) performed simultaneous measurements of velocity and concentration in a free round turbulent air jet. They performed punctual (i.e. at a point) measurements employing laser Doppler velocimetry and cold-wire thermometry in a turbulent jet at Re = 1.4×10^5. The jet air was slightly heated to use temperature as a passive scalar and the measurements were performed at x/D = 30. The results were in agreement with the well accepted profiles of (mean and RMS) concentration and velocity. Additionally, the simultaneous measurements of concentration and velocity allowed the direct calculation of the terms of the budgets of turbulent kinetic energy and scalar variance (except the dissipation terms) as well as the terms of the budget of turbulent heat fluxes.

Liquid-phase turbulent jets have also been studied to determine the scalar field at high Schmidt numbers. Dahm and Dimotakis (1990) employed LIF to obtain point measurements as well as visualizations of the concentration field (disodium fluorescein dye in water; Sc~2000). The measurements spanned a Reynolds number range of 1500 to 20000. Although the resolution of their experiment was unable to resolve the smallest scales of the scalar field at the highest Reynolds number, their apparatus was capable of resolving the smallest hydrodynamic (Kolmogorov) scales of the flow in all cases. Images of the jet showed that the instantaneous scalar concentration field in the jet consisted of large regions of high concentration fluid separated by unmixed fluid, confirming the apparent presence of a large-scale organization in the jet far-field (Dahm and Dimotakis, 1987). Time traces of concentration at the centerline revealed that less ambient fluid reached the axis as the Re increased. Pdfs of the concentration at Re=5000 and 20000 differed only at lower concentrations (with the high concentration parts being in agreement).

Miller and Dimotakis (1991) examined the centerline scalar concentration fluctuations in a high-Schmidt-number turbulent jet by means of punctual LIF. The Reynolds number ranged from 3000 to 24000 and the dye used was sodium fluorescein ($Sc \sim 10^3$). The results showed that the normalized RMS scalar fluctuations decreased with increasing Re, apparently asymptoting to a value of 0.2 at high Reynolds numbers, a value similar to that found in gas phase jets. It was observed that the pdf of the concentration and the shape of the normalized scalar power spectra changed as the Reynolds number was varied, contrasting with the low Schmidt number behavior, for which a much weaker Reynolds number dependence is observed (presumably a manifestation of the larger Schmidt number). The scalar power spectra did not exhibit a k^{-1} region although the measurements were fully spatially resolved for all the Reynolds numbers investigated.

Yoda *et al.* (1994) studied the concentration field in a water jet using a novel system capable of measuring three-dimensional concentration fields. The Reynolds numbers spanned the range of 1000 to 4000. The system employed planar laser induced fluorescence (PLIF), where a pulsed laser sheet was scanned through the measurement volume. The dye used was disodium fluorescein (Sc~2000). Due to the limitations in the acquisition, storage and data processing, the experiments only resolved the Kolmogorov microscales. The analysis of iso-concentration surfaces at different views revealed the presence of high concentration structures.

An extensive study of scalar power spectra in a turbulent jet of water was presented by Miller and Dimotakis (1996). In this work, the Reynolds number varied from 1.25×10^4 to 7.2×10^4. The measurements were made along the jet centerline using punctual laser induced fluorescence (LIF) and the dye used was disodium fluorescein (Sc~2000). The spatial resolution therein represented an improvement with respect to previous experimental investigations, but remained an order of magnitude larger than the Batchelor scale. The spectra at different downstream locations were found to collapse for the same Reynolds number but a k^{-1} region in the spectra was not observed. Furthermore, the spectra departed from the high-frequency/wavenumber prediction of Batchelor (1959) with increasing Re.

Buch and Dahm (1996) investigated the fine-scale structure of scalar mixing in a turbulent water jet. The Reynolds number ranged from 2000 to 10000 and the Schmidt number was approximately 2000. Planar laser induced fluorescence was used to measure the concentration of a small planar segment centered on the jet axis. The authors claimed to resolve the smallest scales of the flow although a larger proportionality constant (of 11.2) was used in the estimate of the Batchelor scales (i.e. $\eta_B=11.2\eta Sc^{-1/2}$). The scalar dissipation rate field was found to be organized into sheet-like structures in which the vast majority of the dissipation was concentrated, irrespective of the Reynolds number.

Catrakis and Dimotakis (1996) studied the scalar concentration and geometry of isoconcentration surfaces in a turbulent water jet. The surfaces analyzed were perpendicular to the jet axis and the Reynolds number covered the range 4.5×10^3 - 1.8×10^4. The concentration measurements were obtained using planar laser induced fluorescence and the dye was disodium fluorescein ($Sc\sim2000$). At the low Reynolds numbers investigated, the two-dimensional concentration profile, radial scalar power spectra, and the pdfs of the concentration fluctuations were found to be Reynolds number dependent. Thus, it was concluded that a mixing transition occurs somewhere in the range of Reynolds numbers studied.

The mixing transition was later described by Dimotakis (2000) for different flows, including turbulent jets. It was observed that the statistics of the flow had little Reynolds number dependence above a certain value. Flow visualizations and statistics of the scalar field confirmed a transition to a better mixed state above a minimum Reynolds number. A universal Reynolds number of approximately 10^4 was proposed as a requirement to attain fully-developed turbulence. It was hypothesized that a minimum Reynolds number was needed for the flow to decouple the largest and smallest scales of the turbulence.

Law and Wang (2000) introduced a novel system able to perform simultaneous velocity and concentration measurements. The system coupled digital particle image velocimetry (DPIV) and planar laser induced fluorescence, and was used to perform measurements in a turbulent water jet (Re=12700 and Sc~3000) as validation. The limitations in the cameras and data acquisition prevented the system from having both adequate spatial and temporal resolutions. However, the agreement of the mean concentration and velocity profiles with previous studies was satisfactory, although differences in the turbulent intensities were found.

Antoine *et al.* (2001) presented a new system capable of performing simultaneous measurements of velocity and concentration. The system coupled 2D laser Doppler velocimetry and laser induced fluorescence. It was used to perform measurements in a turbulent jet (Re=10000) discharging into a low velocity co-flowing stream, with the fluorescent dye being Rhodamine B (Sc~3000). The experiment was unable to resolve the Kolmogorov nor the Batchelor scales. Nevertheless, the mean and RMS profiles of velocities and concentration followed the accepted shapes although some differences were observed with respect to previous studies.

2.2 Entrainment in turbulent jets

In jets of incompressible fluid, the increase of the width with axial distance is accomplished by the inclusion of ambient fluid to the mean flow of the jet. In the case of turbulent jets, the ambient fluid becomes turbulent. The process of drawing surrounding fluid into the jet is termed entrainment. The entrainment hypothesis, first presented by Morton *et al.* (1956), relates the increase in mass flow to a constant entrainment velocity (V_e) normal to the surface of the jet boundary that is proportional to a characteristic velocity (u_m) at each location of the jet ($V_e = \alpha u_m$). The local characteristic velocity is the centerline velocity (at a given downstream position) and α is a constant of proportionality known as the entrainment coefficient. From experiments, the well accepted value of the entrainment coefficient (α) for jets is 0.0535 (Fischer, 1979). Although the entrainment hypothesis proposes that the entrainment velocity around the jet boundary is proportional to the mean axial velocity, it does not give information about the *mechanism* of entrainment.

Despite the importance of the entrainment process for practical purposes, the mechanism of entrainment is still not well described. The two principal hypotheses pertaining to the mechanisms of entrainment attribute the important role of entrainment to different scales. On one hand, the *equilibrium hypothesis* (Townsend 1966) explains entrainment as being a cyclical process in which large eddies engulf big volumes of fluid. Thus the large-scale eddies are considered responsible for the entrainment process. On the other hand, the *superlayer hypothesis* proposes that the transformation of ambient fluid to turbulent flow occurs across a thin surface (separating the ambient and turbulent flow) by the action of the small scales. Different experiments have been designed to obtain insight on the importance of the different scales associated with the entrainment process, some supporting the importance of large-scale processes, while others supported that of small-scale processes.

The *equilibrium hypothesis*, described by Townsend (1966), proposes that entrainment consists of a cyclical process characterized by periods of quiescence and abrupt growth and decay of large eddies responsible of the conversion of ambient fluid into turbulent flow. In such a scenario, the large-scale eddies play the most important role in entrainment, engulfing large quantities of ambient fluid that is incorporated to the mean flow of the jet. There are some investigations supporting the presence of large-scale processes (Yule, 1978; Long and Chu, 1981; Dahm and Dimotakis, 1987; Shlien, 1987). These studies identified engulfment by large-scale structures by means of flow visualization. Additionally, instantaneous measurements of concentration and velocity were related to the presence of large-scale structures. Unmixed ambient fluid deep within the jet and peaks in the instantaneous velocities were presented as evidence of large-scale entrainment.

The *superlayer hypothesis* (Corrsin and Kistler, 1955) proposes that the small scales are responsible for transforming ambient fluid into turbulent flow. The distinction between turbulent and non-turbulent flow is the presence or absence, respectively, of vorticity. Based on the fact that the diffusion of vorticity is only possible by means of viscous effects, Corrsin and Kistler (1955) proposed the existence of a “laminar superlayer” (of the order of the Kolmogorov length scale) separating the turbulent and ambient flow. The function of the superlayer is the transport of mean and fluctuating vorticity into the ambient (irrotational) fluid. In recent years, the bounding surface between the turbulent and nonturbulent flow has been referred as the turbulent/nonturbulent interface (TNTI) and the (small-scale) viscous diffusion of vorticity has been termed nibbling. The results of some investigations suggest that entrainment in turbulent jets is dominated by the nibbling mechanism (Mathew and Basu, 2002; Westerweel *et al.*, 2005, 2009; Wolf *et al.*, 2012). In those studies, the detection of the TNTI involves applying a low-vorticity (or concentration) magnitude threshold to the instantaneous fields. Subsequently, the volume of the flow that acquires vorticity through the interface is quantified (the fluid entrained by engulfment is detected through low-vorticity or concentration values). The results showed that the entrainment process was dominated by small scales at the TNTI, with large-scale engulfment making a small contribution. Hence, although early works (based mainly on flow visualizations) support a large-scale mechanism of entrainment, the recent investigations taking advantage of the advances (both experimental and computational) to detect a TNTI have shown nibbling to be the dominant entrainment process.

It should be noted that the TNTI approach has become an active research topic in the recent years due to: i) the possibility of understanding transport phenomena across such interfaces in different types of flows, ii) a possible new standard for calculating conditional statistics relative to the TNTI position, and iii) the advances in computational and measurement techniques (velocity and concentration) allowing such an approach. The TNTI approach has been applied to different types of flows including turbulent jets, wakes, mixing layers and boundary layers although the characteristics of these interfaces are not universal and depend on the type of the turbulent flow (Bisset *et al.* 2002; Taveira *et al.* 2013; Chauhan *et al.* 2014; da Silva *et al.* 2014; Iovieno *et al.* 2014; Philip *et al.* 2014; Watanabe *et al.* 2015; and the references therein).

2.3 Homogeneous isotropic turbulence

Although turbulent flows are, in general, neither homogeneous nor isotropic, the study of homogeneous isotropic turbulence plays a fundamental role in furthering our understanding of the physics of turbulent flows, as it is the simplest realization of the latter. An important advantage of studying homogenous isotropic turbulence is that it isolates the self-interaction of turbulent fluctuations (Orszag, 1977), and avoids complications arising from additional processes encountered in natural and man-made flows, such as density stratification, mean shear and the effects of fluid-solid boundaries (Tsinober, 2004). Consequently, homogeneous isotropic turbulent flows are often used to study the fundamental properties and mechanisms of turbulence (e.g. internal intermittency, spectral energy transfer). Despite the fact that homogeneous isotropic turbulence is a (relatively) simple flow, it can be difficult to create in the laboratory, since mean velocity gradients are generally necessary for the initial production of turbulent kinetic energy.

To date, the most commonly studied homogeneous isotropic turbulent flow has been grid-generated wind tunnel turbulence, which can achieve relatively high Reynolds numbers, given recent advances such as the development of active grids (Makita, 1991; Mydlarski and Warhaft, 1996) and low-viscosity-fluid wind tunnels (Bodenschatz *et al.* 2014). However, the existence of a mean flow in such arrangements can present a problem in certain situations. For example, Lagrangian measurements in such experimental setups require moving the apparatus with the mean flow — an impractical condition for a variety of reasons (e.g. the need to translate camera systems, the requirement of long flow facilities to follow a stream for a relatively long time interval). These impracticalities can be overcome by utilizing zero-mean-flow turbulence. Moreover, homogeneous isotropic turbulence with zero mean flow permits the study of the fluctuating components of the velocity (and their ensuing effects in phenomena such as turbulent scalar transport, mixing and particle dispersion) in isolation. The generation of three-dimensional homogeneous isotropic turbulence with zero-mean flow has been attempted using diverse novel systems, the first of which involved one, or two, parallel grids (separated by certain distance) oscillating in the direction normal to the plane of the grids (Thomson and Turner, 1975; McDougall, 1979; Brumley and Jirka, 1987; De Silva and Fernando, 1994; Villermaux *et al.* 1995; Srdic *et al.* 1996; Shy *et al.* 1997; Ott and Mann, 2000; McKenna, 2004; Blum *et al.* 2010; and Blum *et al.* 2011). Although, optimal mesh sizes, strokes and frequencies of the grid's oscillation have been proposed, the flows generated by this type of system suffer from large mean flows (with the minimum values of mean flows being approximately 25% of the root-mean-square (RMS) velocities, and maximum values of 60% and 30% for single and double-oscillating grids, respectively). Additionally, the oscillation of the grid is accomplished by coupling the grid to a mechanical system driven by a motor, thus making it more difficult to build large experimental setups for experiments at high Reynolds numbers.

Another approach to generating nearly zero-mean-flow homogeneous isotropic turbulence has been to place loudspeakers pointing towards the center of a chamber (Hwang and Eaton, 2004; Webster *et al.* 2004; Warnaars *et al.* 2006; Lu *et al.* 2008; Goepfert *et al.* 2010; and Chang *et al.* 2012), with the locations of the speakers obeying symmetry with respect to the chamber's center. Typically the loudspeakers push fluid through circular orifices to generate pulsed (synthetic) jets and induce vortex rings. Although the quality of the turbulent flow is better than that generated by oscillating grids (very low mean flows that are approximately isotropic), the desired flow is confined to a small region in the center of the chamber. For example, Chang *et al.* (2012), with the use of 32 loudspeakers, were able to generate an almost zero-mean-flow homogeneous isotropic turbulence at the center of a chamber with a Taylor-microscale Reynolds number (Re_λ) of approximately 480. However, the central (isotropic) volume of this flow covered a radius of only 5 cm. A similar method to create such flows uses symmetrically placed propellers pointing towards the center of a chamber containing a fluid (Fallon and Rogers, 2002; Birouk *et al.* 2003; De Jong *et al.* 2009; and Zimmermann *et al.* 2010). Again, the homogeneity and isotropy of the flow ends up being limited to a small central region.

Symmetrically arranged rotating elements have also been employed to achieve zero-mean-flow turbulence. Rotating grids (Liu *et al.* 1999) and propellers (Berg *et al.*

2006) have been used to create homogeneous isotropic turbulent flow in the center of a rectangular tank. However the levels of turbulence were modest ($Re_λ$ ~ 290 and 172, respectively) and the isotropic flow was limited to a central volume of approximately 4×4×4 cm^3. Two counter-rotating disks in cylindrical containers have been widely used (introduced by Douady *et al.* 1991 and further used by Fauve *et al.* 1993; Maurer *et al.* 1994; Cadot *et al.* 1995; Belin *et al.* 1996; Aumaitre *et al.* 2000; Mordant *et al.* 2001; and Voth *et al.* 2002). Due to the physical characteristics of this type of system, it generates a cylindrical region of turbulence, with axial extension depending on the size of the tank (e.g. Machicoane *et al.* (2014), and references therein), negligible mean flow and relatively high $Re_λ$. (Voth *et al.* (2002) reached $Re_λ$=970.) However, the flow suffers from anisotropy and the radial extent of the optimal flow covers only a few centimeters. In a modification of this technique Liberzon *et al.* (2005) used eight counter-rotating disks to generate the turbulence. However, the flow generated at the center of their tank had a low Reynolds number ($Re_λ$ ~ 40).

Random jet arrays (RJAs) are relatively new systems that have been developed and used to generate approximately homogeneous isotropic turbulence with zero mean flow (Variano *et al.* 2004; Lavertu, 2006; Variano and Cowen, 2008; Delbos *et al.* 2009; Khorsandi *et al.* 2013; and Bellani and Variano, 2014). A (single) RJA is a planar configuration of jets that, randomly and independently, turn on and off to produce turbulence downstream of the array. The RJA is able to create a nearly homogenous flow (albeit with an unavoidable decay in the direction normal to the plane of the jets) with a negligible mean flow (less than 10% of the RMS velocities in all directions) over a large spatial region (Variano and Cowen, 2008). Additionally, the isotropy of the flow is of the same order as that of grid-generated, wind tunnel turbulence and relatively high Reynolds numbers can be reached (Re_λ = 314 in Variano and Cowen, 2008). The isotropy, quantified as the ratio of RMS velocities (i.e. $u_{\alpha\text{-RMS}}/u_{\beta\text{-RMS}}$), measured in mono-planar RJAs (Variano *et al.* 2004 (0.81); Lavertu, 2006 (0.66); Variano and Cowen, 2008 (0.79); Delbos *et al.* 2009 (0.76); Khorsandi *et al.* 2013 (0.71)) can be as low as two-thirds, presumably resulting from the forcing from only one plane. Most recently, Bellani and Variano (2014) placed two RJAs separated by a distance and facing each other. The resulting profile of the turbulent kinetic energy had zero slope at the tank center due to the underlying symmetry of their arrangement. This configuration generated a nearly homogeneous isotropic turbulent flow with a negligible mean flow at the center of the tank. Using this arrangement, the isotropy was significantly improved (compared to single RJAs) and found to be in the range 0.95-0.99 in the center of the tank. The Taylor-microscale Reynolds number was 334 and the region of homogeneity and isotropy was roughly 0.4×0.4×0.2 m^3 (the largest reported to date).

2.4 The effect of background turbulence on turbulent flows

The effect of background turbulence on turbulent flows such as boundary layers, wakes and jets has received comparatively little attention to the enormous number of studies considering such flows with uniform free streams (i.e. wakes, co-flowing jets and boundary layers) and jets emitted into quiescent surroundings, even with the knowledge that most natural and engineering phenomena occur on the presence of external turbulence. Part of the reason is that i) the effect of external turbulence on turbulent flows further complicates phenomena that are already complex, and ii) more elaborate experimental facilities must be employed to study these aforementioned flows. Nevertheless, some studies have tried to improve the knowledge in this matter. In this section the investigation of free-stream turbulence on a boundary layer will be discussed first. This will be followed by a review of the effect of free-stream turbulence on wakes. Finally, jets discharging into turbulent surroundings will be reviewed.

2.4.1 Boundary layers with turbulent free streams

The studies undertaken to understand the effect of the external turbulence on turbulent boundary layers imposed high intensity turbulence in the external flow. The intensity of the external flow is defined as u'/U_∞, where u' is the RMS velocity fluctuation and U_∞ is the mean external velocity in the downstream direction. Although there are many studies of boundary layers with large U_∞ (and most likely turbulent), the intensity of the turbulence of the free stream was not always reported and the experimental setups were unable to vary this parameter. Hence, only the works in which the external turbulence intensity was varied and the results were compared to identify the effects of the increased free-stream turbulence will be reviewed herein.

Hancock and Bradshaw (1983) studied the effect of the free-stream turbulence in a boundary layer using a wind tunnel with the turbulence generated by a grid. The intensities of the free-stream turbulence roughly ranged from 2% to 6% with the momentum thickness Reynolds number ranging from 1600 to 6000 which used the mean free-stream velocity as the characteristic speed. At the highest intensities studied, the effect of the external turbulence was found to reduce the rate at which the mean velocity asymptotes to the mean external velocity. Additionally, the skin friction was calculated and found to increase with increasing intensity of the external turbulence.

In a later experiment, Hancock and Bradshaw (1989) included flow visualizations using smoke and observed that the free-stream turbulence increased the irregularity of the interface between the boundary layer and the external fluid stream. To quantify the mixing, the plate was heated and the hot and cold (ambient) fluid was measured. Enhanced mixing in the outer part of the boundary layer was observed with an increase in the intensity of the free-stream turbulence. Similarly, more cold (ambient) fluid penetrated deep into the boundary layer with increasing free-stream turbulence. At low intensities ($u'/U_\infty \sim 2.5\%$) the normal Reynolds stresses $\langle u^2 \rangle$ and $\langle v^2 \rangle$ increased within the boundary layer. However, they exhibited different behaviors at the highest intensity ($u'/U_\infty \sim 6\%$): $\langle u^2 \rangle$ increased in the boundary layer with respect to the value of this quantity in the free-stream, while $\langle v^2 \rangle$ decreased inside the boundary layer, as compared to the external turbulence as a result of the no-penetration ($v=0$) constraint at the surface.

To increase the external turbulence intensity to the range 10-20% Thole and Bogard (1996) used an array of jets discharging perpendicularly to the free-stream in a section located upstream of the measurements region of a boundary layer. Within the boundary layer, the log-law region still persisted near the wall for all the external intensities studied. In contrast, the outer part of the boundary layer became much flatter due to the enhanced mixing (resulting in the velocity defect being drastically decreased). Energy spectra were analyzed at a position deep inside the boundary layer for the different free-stream turbulence intensities and the results showed that for the high intensity cases, the power spectra resembled those of the external turbulence, indicating a strong penetration of the external turbulence into the boundary layer for the high-turbulence-intensity cases.

A study of the effect of the free-stream turbulence on a boundary layer using an active grid was presented by Sharp *et al.* (2009). In the experimental set up, the active grid was placed at the beginning of the test section and able to vary the turbulence intensity of the free stream from 0.25% to 10.5%. The momentum thickness Reynolds number of the boundary layer was in the range 550 to 3000, with hot-wire anemometry being employed for the measurements. Apart from the good agreement with other investigations of the mean and variances of the longitudinal velocities, spectral analysis and higher-order moments of the statistics provided additional evidence of the effect of the free-stream turbulence. Namely, the skewness and kurtosis profiles showed nearly constant values when increasing external turbulence intensities (attributed an enhanced mixing). Moreover, the analysis of the premultiplied energy spectra ($k_1E_{11}(k_1)$) revealed significant changes resulting from the imposed external turbulence. In the absence of free-stream turbulence, two peaks in the premultiplied energy spectrum were observed with the lower-wavelength peak being dominant. However, in the presence of external turbulence, the so-called outer (at higher-wavelength) peak reached comparable and even higher values than the inner peak, thus implying that the outer peak was associated with the external turbulence. The analysis of the premultiplied energy spectra at different distances from the wall revealed that the free-stream energy reached deep into the boundary layer, thus proving that the external turbulence can affect the inner scales of the boundary layer.

2.4.2 Wakes with turbulent free streams

As in the case of the boundary layer, external turbulence in a turbulent wake has been imposed through the free-stream flow and the intensity of the external flow quantified as u'/U_∞, where u' remains the RMS of the velocity fluctuations and U_∞ is the mean external velocity. Direct numerical simulations (DNS) of the wake of a sphere at low Re (50-600) and external turbulent intensities (in the range 5-20%) were performed by Bagchi and Balachandar (2004). The general effects of the external turbulence were a reduction of the length of the wake (determined from the velocity deficit), higher streamwise velocities, and a wider wake than in a uniform external flow case. At low Reynolds numbers, the background turbulence favored the early onset of vortex shedding, but at high Re, the vortex shedding and oscillation of the wake was suppressed by the strong external turbulence. The kinetic energy within a wake (in a turbulent or laminar free stream) is reduced as a result of the velocity deficit. The distribution of the total kinetic energy in the wake was analyzed and the results showed that the recovery of energy is more rapid for the turbulent ambient flow than for the uniform free stream. The RMS of the streamwise velocity fluctuations increased within the wake (compared to the free-stream value) for all the external turbulence intensities studied. However, the cross-stream RMS velocity increased only for low external turbulence intensities, and was found to decrease for high intensities.

The wake of a sphere at low Re (200-500) and low turbulent intensity (4%) was studied by Legendre *et al.* (2006) using large-eddy simulation (LES). The half-width of the wake was considerably increased in the presence of external turbulence when compared with the wake in quiescent ambient. The centerline velocity defect showed two power-law decay regions, the first one in the near wake region resembled the laminar case (an x^{-1} decay), while the following region exhibited an x^{-2} decay, which is faster than that of a turbulent wake developing in a quiescence environment ($x^{-2/3}$). The start of the x^{-2} decay region occurs where the velocity defect attains a value of the order of the RMS velocity of the free-stream flow.

Bagchi and Kottam (2008) used direct numerical simulation (DNS) to investigate the heat transfer on the surface of a sphere in a turbulent free stream. The Reynolds numbers of the simulations covered the range 63-400. Isotropic velocity and temperature fields were superimposed on uniform velocity and temperature fields. The intensity of the hydrodynamic turbulence was in the range of 5-26% and that of the temperature, defined as $I_T = T_{RMS}/(1-T_\infty)$, ranged roughly from 4 to 56%. The analysis of the thermal wake revealed that it was shortened by the presence of the turbulent fields and the half-width of the wake was increased, presumably a result of the enhanced mixing produced by the external turbulence.

The effect of external turbulence on a wake was studied experimentally by Amoura *et al.* (2010). The experimental setup consisted of a sphere in the middle of a recirculating square channel, where the turbulence was generated by an array of pumps discharging into a reservoir at the top of the channel and then the turbulent flow was driven by gravity inside the channel. The intensity of the free-stream flow was varied from 15 to 26%. The velocity defect along the centerline was found to decay as x^{-2}, consistent with the findings of previous investigations, but this region started earlier due to the higher external turbulence intensity. The transverse profiles of the RMS velocities were found to attain an almost constant value as a result of the strong mixing induced by the outer turbulence. It was also pointed out that the wake length was shortened and vortex shedding is damped in the presence of external turbulence.

Eames *et al.* (2011) presented a theoretical model for the effect of external turbulence on a wake. The model applies to wakes of Reynolds number less than 1000 because the turbulence generated by the wake was not considered. The model predicts that when the velocity defect becomes comparable to the RMS of the free-stream velocity i) the velocity defect follows an x^{-2} decay, and ii) the width of the wake grows linearly. The model captures the scaling of the velocity defect and wake width (as well as their order of magnitude), although a collapse of the data and the model's predictions was not observed when compared with experiments.

2.4.3 Jets and plumes emitted into turbulent surroundings

Relatively few studies of jets issuing into a turbulent ambient have been carried out. In the few cases of such studies, the turbulent ambient is imposed by a turbulent co-flowing stream or by a turbulent background with zero mean flow. To date, two principal hypotheses on the effect of background turbulence on turbulent jets have been put forth. The standard assumption was that of superposition of the dilution effects of the jet and of the background turbulence. Wright (1994) proposed a model in which a term accounting for the external turbulence was added to the classic entrainment function ($E=2\pi\alpha b u_m$ (Morton *et al.* 1956), where b is the half-width of the velocity profile and u_m is the jet's centreline mean velocity), akin to superposition of the effects of the jet and the turbulent surroundings. However, Hunt (1994) argued that if the external turbulence was large, defined as the RMS velocity of the external turbulence being on the order of the RMS of the jet velocity, the jet structure would be disrupted resulting in a negative forcing and a reduction in the entrainment. Nevertheless, if the jet entrainment velocity was larger than the RMS velocity of the turbulent background, the external turbulence would be entrained and would not disrupt the jet structure. The latter hypothesis predicts a possible reduction in entrainment, contrary to the standard assumption. There exist experimental work in support of both predictions and they are reviewed in the next paragraphs.

Wright (1994) studied the mixing of jets in a turbulent co-flow. The turbulence of the ambient flow was generated by changing the bottom roughness of the channel although only low levels of external turbulence could be produced. The results showed an increase in the dilution as the bottom roughness was increased. This effect was observed to start near the jet outlet indicating that the external turbulence could influence the jet mixing even when the jet velocity is dominant.

Ching *et al.* (1995) experimentally studied the evolution of linear plumes in a turbulent environment by releasing the former into a turbulent ambient with zero-mean-flow created by an oscillating grid. The plume discharged perpendicularly to the oscillating grid (i.e. as it evolved it approached the oscillating grid). The results showed that the plume experienced an abrupt increase in the dispersion at a critical distance from the source in the presence of the external turbulence. Detailed analysis of the results revealed that the break-up of the plume coincided with the position where the ratio of the convective velocity of the plume to the RMS velocity of the turbulent environment (w^*/u_o) was equal to 1.60.

The effect of ambient turbulence on jets was studied by Guo *et al.* (1999, 2005). In this investigation a jet discharged into a zero mean turbulent environment created by an oscillating grid. The jet Reynolds number ranged from 960 to 12000. LIF was used for visualization and velocity measurements were carried out using PIV. The effect of the ambient turbulence on the jet was to significantly increase the spreading angle of the jet at the breakdown location (z_c) where the external turbulence was strong enough to disrupt the jet, similar to the effect observed in linear plumes (Ching *et al.* 1995). The breakdown location, where the mixing and dilution of the jet was significantly enhanced, occurred when the ratio of the RMS turbulent ambient velocity (w_t) to the RMS of the jet velocity (w_j) was roughly 0.44 for the range of Reynolds numbers studied.

Although the use of oscillating grids oriented perpendicular to the direction of release of plumes/jets was shown to considerably increase the dilution, the support of a hypothesis of superposition of the effects of the jet/plume and background turbulence can be challenged by the fact that the background turbulence is increasing in the direction of decreasing plume/jet turbulence and that the grid itself results in a blocking effect on the flow (Gaskin *et al.* 2004).

In a study of differential scalar diffusion within turbulent jets Lavertu (2006) included measurements of the effect of background turbulence on the differential diffusion. The external turbulence was generated by a random jet array (RJA) which created nearly isotropic turbulence with negligible mean flow. The jet axis was parallel to the plane of the jet array to ensure a constant level of external turbulence along the axis of the jet (in contrast with the experiments of Ching *et al.* (1995) and Guo *et al.* (1999, 2005), where the turbulent intensity increased in the downstream direction). The jet Reynolds number ranged from 900 to 10600 and the RMS of the velocity fluctuations of the external turbulence was roughly 1.5 cm/s. The differential diffusion in the turbulent jet was found to increase in the presence of the background turbulence. Although velocity measurements were not performed and scalar measurements were performed at a fixed downstream position, it was suggested that the increase in differential diffusion could be attributed to an increase in entrainment due to the turbulent background.

The first evidence in support of Hunt's prediction of a reduction in entrainment due to the presence of background turbulence is that of Gaskin *et al.* (2004), who studied the effect of background turbulence on plane jets in a shallow co-flow. Their experimental set up consisted of a plane jet released into a shallow flume with a series of ridges at the bottom of the flume to increase the turbulent intensity of the co-flow. The jet Reynolds number was 1200 and the intensity of the external turbulence u'/U_∞ (where u' is the RMS of the velocity fluctuations and U_∞ is the mean co-flow velocity) ranged roughly from 5 to 15%. Flow visualization and concentration measurements were performed using a CCD camera and dye as passive scalar, whereas velocity measurements were obtained by means of hot-film anemometry. The results showed that the external turbulence increased the rate of decay of the mean velocity, reduced the entrainment rate and reduced the dilution, with the effects being more marked and starting closer to the jet outlet with increasing ambient turbulent intensity. The effects described indicate that the jet structure is disrupted by the external turbulence. Specifically, it was pointed out that, once the external turbulence is large enough to disrupt the jet structure, the entrainment becomes dominated by turbulent diffusion by small scales of the external turbulence in contrast with the large scale engulfment due to the jet structure as found in the free jet.

The effect of background turbulence in turbulent jets was studied by Khorsandi (2011) and Khorsandi *et al.* (2013). The experimental setup to produce the background turbulence was the same as that used by Lavertu (2006) however two different turbulent intensities were imposed on the jet and velocity measurements were obtained at different downstream positions. The jet Reynolds numbers were 5300, 5800 and 10600. The turbulent kinetic energy of the turbulent background at the jet location was $\frac{1}{2} \langle u_i u_i \rangle = 4.44$ and $9.33\ m^2/s^2$. Velocity measurements were obtained employing both acoustic Doppler velocimetry (ADV) and flying hot-film anemometry. The results showed increases in the i) decay rate of the mean velocity, and ii) half-widths of the velocity profile. The most interesting result was the decrease of the mass flow rate implying lower entrainment rates confirming the prediction of Hunt (1994) and results of Gaskin *et al.* (2004). Furthermore, these effects increased with higher background turbulence intensities.

2.5 Laser induced fluorescence (LIF)

Laser induced fluorescence (LIF) is a technique that takes advantage of the characteristic of certain substances that emit photons at a different wavelength when excited with energy in the form of light at a certain wavelength. The aforementioned characteristic is called fluorescence and it results from the capability of specific compounds to absorb energy in form of light at the so-called excitation wavelengths and re-emit of light at the emission wavelengths, a process occurring on the order of nanoseconds. The excitation and emission wavelengths differ, with the latter being longer. This shift in wavelength, known as the Stokes shift, is the feature that allows experimentalists to detect and quantify the light emitted by the excited molecules. LIF is exploited to obtain instantaneous species concentration measurements by seeding the flow with a fluorescent dye and relating the intensity of the light emitted to the concentration of the fluorescent substance. Since optical access is essentially the only requirement to perform the measurements, LIF is classified as a non-intrusive technique. The ability to perform measurements at high temporal and spatial resolution makes LIF a powerful tool for the study of turbulent flows. The LIF technique became an intensively employed technique after the publications of Dewey (1976) describing the potential uses of the technique and the work of Owen (1976) obtaining qualitative concentration measurements. Publications contributing to the development of the LIF technique include Breidenthal (1981), Dyer and Crosley (1982), Kyochakoff *et al.* (1982), Koochesfahani and Dimotakis (1985), and Walker (1987).

The fluorescence process starts with the absorption of energy in form of light by a molecule. This absorption can only occur if the excitation light is within the wavelengths bounding the exciting spectrum (different for each fluorescent material). The most common light source used in LIF experiments is a laser operating at wavelengths suitably-chosen for the compound employed. Continuous wave argon ion lasers are the most commonly employed, but the use of pulsed Nd:YAG lasers is recently increasing (Shan *et al.* 2004, Crimaldi 2008; Vanderweel and Tavoularis, 2014). Excitation by laser light causes the molecule to jump from the ground state to a higher energy level (known as the singlet state). Once in the excited energy state, the molecule will lose some energy due to collision with other molecules and return to the ground state, emitting photons of a wavelength within the emission spectrum. Due to the loss of energy arising from intermolecular collisions, the energy liberated in form of light when returning to the ground state is smaller than that which was absorbed and thus the light is emitted at a longer wavelength (lower energy level — the Stokes shift). This shift in wavelengths, however, permits the excitation light and the emitted light to be distinguished by the use of appropriate optical filters.

The expression relating the intensity of the light emitted to the concentration is (Guilbault, 1973):

$$F = \Phi_f I_0 \left(1 - e^{-\beta b C}\right), \tag{2.5}$$

where F is the fluorescence intensity, Φ_f is the quantum efficiency, I_0 is the incident radiant power, β is the molar absorptivity, b is the path length of the cell, and C is the species concentration. For very dilute concentrations, the term $\beta bC<<1$ and the exponential can be expressed as a Taylor series expansion retaining only the first two terms. Thus equation (2.5) simplifies to:

$$F = \Phi_f I_0 \beta b C. \tag{2.6}$$

Therefore, for small concentrations and constant laser power, the fluorescence intensity is conveniently a linear function of the species concentration. At higher concentrations, the fluorescence intensity usually increases with concentration, but at a lower rate than the linear behavior. In some circumstances further increases in concentration will cause a decrease in the intensity. But, as would be expected, the use of LIF is generally in the linear range, which simplifies calibration, data analysis, etc.

The intensity of the fluorescence is independent of the direction and the emitted light can be captured by the use of a photodetector, such as a i) photomultiplier tube (PMT) (e.g. Walker, 1987; Miller and Dimotakis, 1996; Saylor and Sreenivasan, 1998; Wang and Fiedler, 2000a; Lavertu, 2006), ii) photodiode (e.g. Dowling *et al.,* 1989; Shan *et al.,* 2004), or iii) camera (e.g. Prasat and Sreenivasan, 1990; Ferrier *et al.,* 1993; Cetegen and Mohamad, 1993; Coppeta and Rogers, 1998; Law and Wang, 2000; Crimaldi and Koseff, 2001; Deusch and Dracos, 2001; Tian and Roberts, 2003; Westerweel *et al.* 2009).

LIF can be used to obtain concentration measurements i) at a point in space by focusing a laser beam on a small spot (e.g. Walker, 1987; Sreenivasan and Prasad, 1989; Miller and Dimotakis, 1991,1996; Crimaldi, 1997; Saylor and Sreenivasan, 1998; Lavertu 2006), ii) along a line on a section of a laser beam (e.g. Koochesfahani and Dimotakis, 1985; Hannoun and List, 1988; Papantoniou and List, 1989; Dahm and Dimotakis, 1990), iii) on two dimensional planes by creating a laser sheet using a cylindrical lens (e.g. Kychakoff *et al.,* 1982; Dahm and Dimotakis, 1987; Ferrier *et al.* 1993; Cetegen and Mohamad, 1993; Coppeta and Rogers, 1998; Guillard *et al.* 1998, Westerweel *et al.*, 2009) or a rotating mirror to scan the beam across the measurement area (e.g. Barrett and Van Atta, 1991; Stapountzis *et al.* 1992; Catrakis and Dimotakis, 1996; Crimaldi and Koseff, 2001), or iv) in three dimensional volumes by rapidly sweeping a laser sheet (e.g. Yoda *et al.*, 1994; Buch and Dahm, 1996; Deusch and Dracos, 2001; Tian and Roberts, 2003; Su and Clemens, 2003; Van Vliet *et al.,* 2004). Furthermore, simultaneous concentration and velocity fields can be obtained by coupling the capabilities of LIF with velocity measurements techniques such as particle image velocimetry PIV (e.g. Law and Wang, 2000; Westerweel *et al.,* 2009), particle tracking velocimetry PTV (e.g. Webster *et al.* 2001) or laser Doppler velocimetry LDV (e.g. Antoine *et al.* 2001), although the spatial and temporal resolutions can be compromised by the limitation in the number of pixels and rate of acquisition of images of even state-of-the-art cameras.

Whenever employing LIF, appropriate care should be undertaken to avoid undesirable effects such as photobleaching, thermal blooming, attenuation and PMT drift. A few studies have concentrated on describing the details of the potential adverse effects when using LIF (Lavertu 2006). Attenuation occurs when the laser beam has to cross non-negligible amounts of dyed fluid before reaching the measurement section and thus energy is absorbed by the fluorescent tracer. Walker (1987) presented an extensive investigation of the fluorescence characteristics of sodium fluorescein. The tests examined the variation of fluorescence with varying concentration, pH, temperature and laser intensity. The results showed that attenuation was negligible and the fluorescence linear only if the concentration was kept low, typically 10^{-7} [mol/l]. The results also showed that slight variations in pH create great differences on the fluorescence intensity, therefore, considerable changes in pH should be avoided when using sodium fluorescein in experiments.

Photobleaching is the reduction of the fluorescence intensity with time due to constant irradiation. Koochesfahani (1984) took into account the effect of photobleaching in his experiments in mixing layers by the calculation of a photobleaching time constant. Saylor (1995) studied the photobleaching of disodium fluorescein at rest and proposed the use of a half-life ($\tau_{1/2}$), defined as the time for the fluorescent signal to decay to half of its peak value as an appropriate measure of photobleaching. His results also showed that the half-life can be significantly increased with the use of pulsed irradiation ($\tau_{1/2}$=12.3 ms) instead of continuous irradiation ($\tau_{1/2}$=2.9 ms). Nevertheless, the half-life is not a universal constant and it depends on experimental conditions, for example dye concentration and laser power (Sahar and Treves, 1977 and Benson *et al.*, 1985). The investigation of Crimaldi (1997) showed that photobleaching depends on the type of fluorescent dye and the velocity of the flow. He therefore proposed to calibrate the experimental setups using the velocities of the actual experiments. The study of photobleaching by Wang and Fiedler (2000a) presented results confirming the dependence on dye concentration, flow velocity and laser power. The conclusions of the work stated that photobleaching can be reduced by decreasing laser power, dye concentration or increasing the velocity of the flow.

The fluid temperature should also be kept constant when performing LIF experiments since it is known that fluorescence decreases as temperature increases (Guilbault, 1973; Walker, 1987). Furthermore, changes in temperature could result in unwanted density differences creating buoyancy and inertial effects (Miller and Dimotakis, 1991; Lavertu 2006).

Another phenomenon related to temperature is thermal blooming, occurring when the laser beam heats the dyed medium, changing the fluid density and causing the beam to diverge. Beam divergence was first described by Koochesfahani (1984) as a possible source of error in LIF studies (and resulting in weaker fluorescent signals). In a later investigation, Wang and Fiedler (2000a) investigated the combined effects of thermal blooming and photobleaching pointing out that they are related since both depend on the velocity of the fluid. Their results showed that thermal blooming can be reduced by decreasing the laser power (less energy heating the dye) and increasing the velocity of the fluid (reducing the time of continuous irradiation).

The instability of the output signal of PMTs operating for long periods (i.e.drift) in LIF experiments was described by Lavertu (2006). In his preliminary experiments he found that the output voltage of the PMT decreased with time for the same concentration of dye. The solution for the PMT drift was to warm the PMT in the presence of a light source prior to the start of data acquisition. PMT drift is not an issue when performing experiments that only last for few seconds.

Satisfactory spatial resolution and signal-to-noise ratios (SNR) are always desirable when performing LIF experiments. Koochesfahani and Dimotakis (1985) considered the variation in laser uniformity to improve the resolution of the signal detected by their linear photodiode array in a liquid mixing layer. They also mentioned the effect of inadequate spatial resolution resulting in apparent higher mixing. Digital techniques for the correction of signals in planar LIF were presented by Ferrier (1993), and in a later investigation by Guillart *et al.* (1998), who presented a pixel-by-pixel procedure for the calibration of CCD cameras to improve the detected scalar concentration in their experiment in an impingement jet. Vanderweel and Tavoularis (2014) identified and corrected errors in concentration measurements in planar LIF when the laser sheet thickness was comparable or larger than the thickness of a plume. A study of the SNR in high spatial resolution punctual LIF measurements was conducted by Wang and Fiedler (2000b). The experiments were carried out in a mixing layer and the laser beam was focused in a volume of approximately 4 μm^3. Owing to the extremely fine volume, the fluorescent signal from the PMT employed was low and the shot noise from the PMT was dominant, resulting in a low signal-to-noise ratio. To improve the SNR, the laser power and the dye concentration were increased, and although higher concentration signals were obtained in either case, photobleaching and thermal blooming effects became important. Moreover, increased concentrations can lead to operation beyond the linear range of the fluorescence intensity.

Chapter 3

Experimental methods

3.1 Experimental facility

The experiments were carried out in a 1.5 m by 2.4 m by 0.9 m section of a glass tank (1.5 m by 6 m by 0.9 m) in the Environmental Hydraulics laboratory in the Department of Civil Engineering and Applied Mechanics at McGill University. The tank was filled with water and its top was open to the ambient air. The side walls of the tank consisted of single panes of 1.905 cm thick tempered glass. The bottom consisted of two 1.905 cm thick tempered glass panes superposed, giving a total thickness of 3.81 cm. A steel frame was used to support the assembly of glass panes (Figure 3.1).

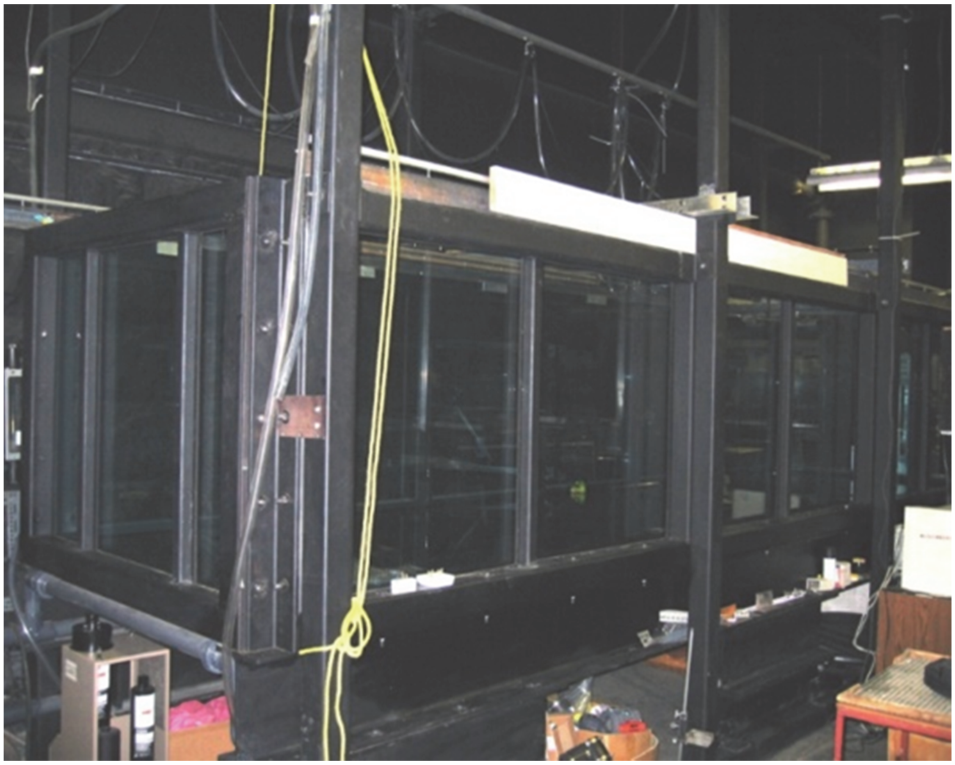

Figure 3.1 Glass tank in which the experiments were carried out.

The experimental apparatus was located in a darkroom, which ensured negligible background light and thus reduced any possible interference of external light with the measurements. Similarly, reflections of the emitted light from the fluorescent dye was minimized since the walls, floor and ceiling were painted black.

3.2 Background conditions

The experiments investigated the effect of background turbulence on the scalar field of a turbulent jet by comparing the results of a jet issued into a quiescent background with those of a jet emitted into turbulent background. When experiments in quiescent conditions were performed, the tank was slowly filled with water and sufficient time (approx. 1.5 hours) was given for the water to come to rest.

When experiments in a turbulent background were performed, a random jet array (RJA) was used to produce an approximately homogeneous, isotropic, zero-mean turbulent flow in the 1.5 m by 2.4 m by 0.9 m section of the tank. The jet array is based on that of Variano and Cowen (2008), but built to a larger scale. The RJA consists of 10 columns of 6 bilge pumps (Rule 25D, 500 GPH) attached to a 1 m by 1.5 m vertical sheet of high density polyethylene (Figure 3.2). A polyvinyl chloride (PVC) elbow joint (Spears 1407-010) was attached to the outlet of each pump to change the direction of the flow upon its exit from the pumps. Moreover, a male adapter (Spears 436-132) and a 15 cm long PVC extension (3.18 cm in diameter) were connected to each pump to expand the outlet diameter and straighten the flow (Figure 3.3). Thus, the pumps draw water in from their base (adjacent to the polyethylene sheet) and discharge it from the PVC extension at a distance of 24 cm from the plane of the polyethylene sheet. Since the suction and discharge occur simultaneously into the same fluid volume, there is a zero net mass flow rate in a control volume containing the pump and extension, which is essential to generating the zero mean flow in the tank. The jets are equally spaced in the horizontal and vertical directions, with a center-to-center distance (M) of 15 cm. Additionally, the distance of the center of the jets at the edges of the array with the glass walls and free surface was chosen to be 0.5M to obey symmetric boundary conditions to minimize possible secondary flows, in analogy with oscillating grid turbulence (Fernando and De Silva 1993). Although two RJAs facing each other has been used to generate background turbulence (Bellani and Variano, 2014), the improvement in the flow with respect to a single RJA does not justify the high cost of a new RJA given that a mono-planar RJA generates the necessary flow for the present investigation in terms of homogeneity and isotropy (Chapter 5).

The power necessary for the functioning of the pumps was provided by a Rapid power supply (Model SPSA2012200). The power supply was operated with a constant 12 V output and variable current, depending on the demand of the pumps. The maximum current provided by the power supply was 200 A. This current was sufficient to provide power to all the pumps in the RJA. The points of connection of the wires of the power supply and the pumps were carefully sealed to avoid short circuits in the water tank. The cables were first connected by a sealed crimp and solder butt splice connector (NSPA Multilink ML5-16). Then, several layers of liquid electrical tape were added on top of the connector. When the liquid electrical tape was dry, an adhesive-lined flexible polyolefin heat shrink tubing was applied as another layer of insulation. And finally, more liquid electrical tape was added on top to ensure optimal insulation from the water.

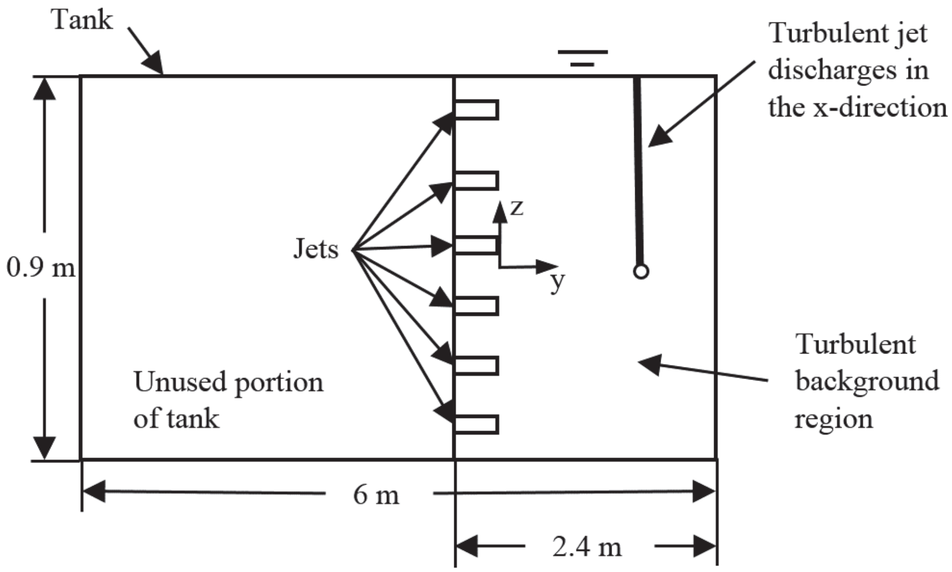

a) Side view

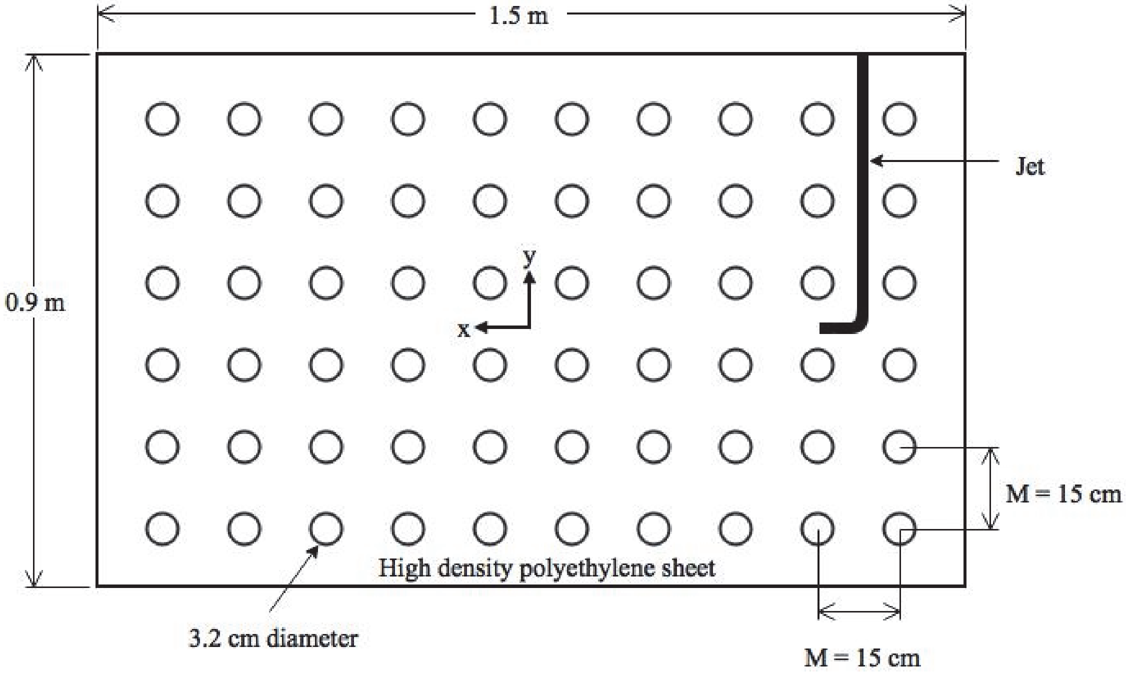

b) Front view

Figure 3.2 Schematic of the RJA and jet setup. a) side view. b) front view.

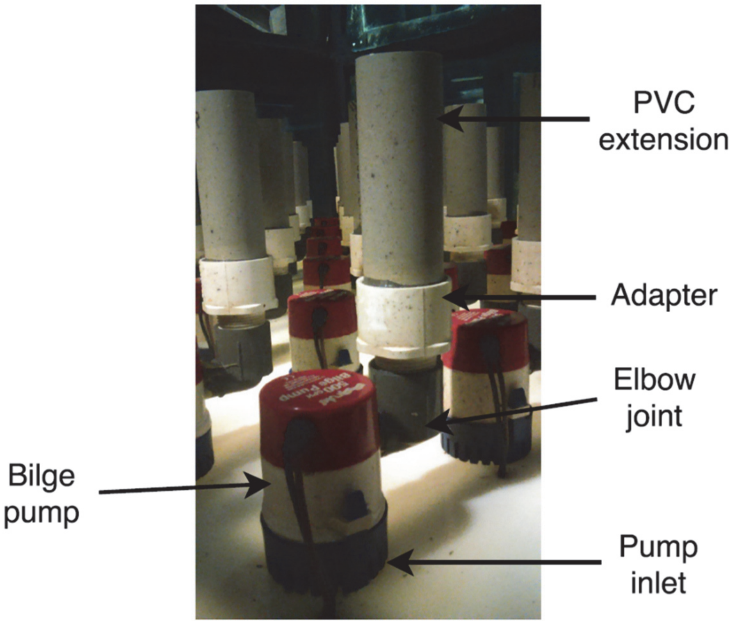

a) Bilge pump and components

b) Array of jets

Figure 3.3 Details of the pump and jet array. a) Bilge pump and components. b) Array of jets.

The random jet array was controlled using a custom algorithm programmed in LabVIEW, which independently turned the pumps on and off. Downstream of the jet array, the jets merge, generating a region of turbulence that decays in the direction normal to the plane of the jet array. The ability to independently operate and control each pump allowed the exploration of different driving algorithms to generate the closest approximation of a homogeneous isotropic zero-mean flow turbulent background. Of particular interest was the spatial configuration of the jets operating at any given instant (an aspect that has not been documented in previous RJAs studies), as well as the statistics of their respective on/off times. The "optimal" algorithm was defined as one that generates turbulence with the lowest possible mean flow, high degrees of isotropy and high RMS velocity. The performance of all the driving algorithms was characterized by comparing the statistics of the turbulence generated downstream of the RJA. It was concluded that the algorithm identified as RANDOM generated the flow with the highest quality (Chapter 5). Therefore the RANDOM algorithm was used to generate the background turbulence during the experiments.

The operation of the RANDOM algorithm is similar to the driving algorithm proposed by Variano and Cowen (2008) for their RJA. When the RANDOM algorithm is used, each pump is independently and randomly turned on and then off. The on and off times are random values determined from normal distributions with adjustable mean (μ) and standard deviation (σ). In this situation, each pump is individually turned on for a randomly selected interval and then forced to turn off during a new randomly chosen amount of time, with the process being repeated indefinitely. Several variations of mean on times, mean off times and standard deviations were investigated in the present study, by Lavertu (2006) and, by Khorsandi (2011) in the same experimental facility. The optimal values for the present RJA were found to be (μ_{on}, σ_{on}) = (12 ,4) seconds and (μ_{off} , σ_{off}) = (108, 36) seconds. These parameters maintain, on average, 10% of the pumps working.

3.3 Turbulent jet apparatus

The jet was placed in the tank to discharge horizontally (in the x-direction) in a plane parallel to the RJA. The jet apparatus consisted of a supply reservoir, a pump, a constant head reservoir, traversing mechanism, and several jet components (Figure 3.4). The design of this setup allowed one to i) maintain a constant flowrate through the jet during the experiments, ii) easily vary the Reynolds number of the jet, and iii) place and align the turbulent jet in the tank.

The supply reservoir was a 35 liter glass cylindrical container placed on the side of the tank. The supply reservoir was used to prepare the mixture of fluorescent dye and water before commencing the experiments. It also served as an overflow reservoir for the dyed water pumped to the constant head tank. A 1/3 hp pump was used to continuously pump dyed fluid during the experiments from the supply reservoir to the constant head tank through plastic tubing (1.27 cm diameter). A ball valve connected at the outlet of the pump controlled the flowrate towards the constant head tank. The ball valve was used to set the flowrate slightly higher than the flow thorough turbulent jet to ensure an overflow back to the supply reservoir and thus maintain a constant level of the head tank.

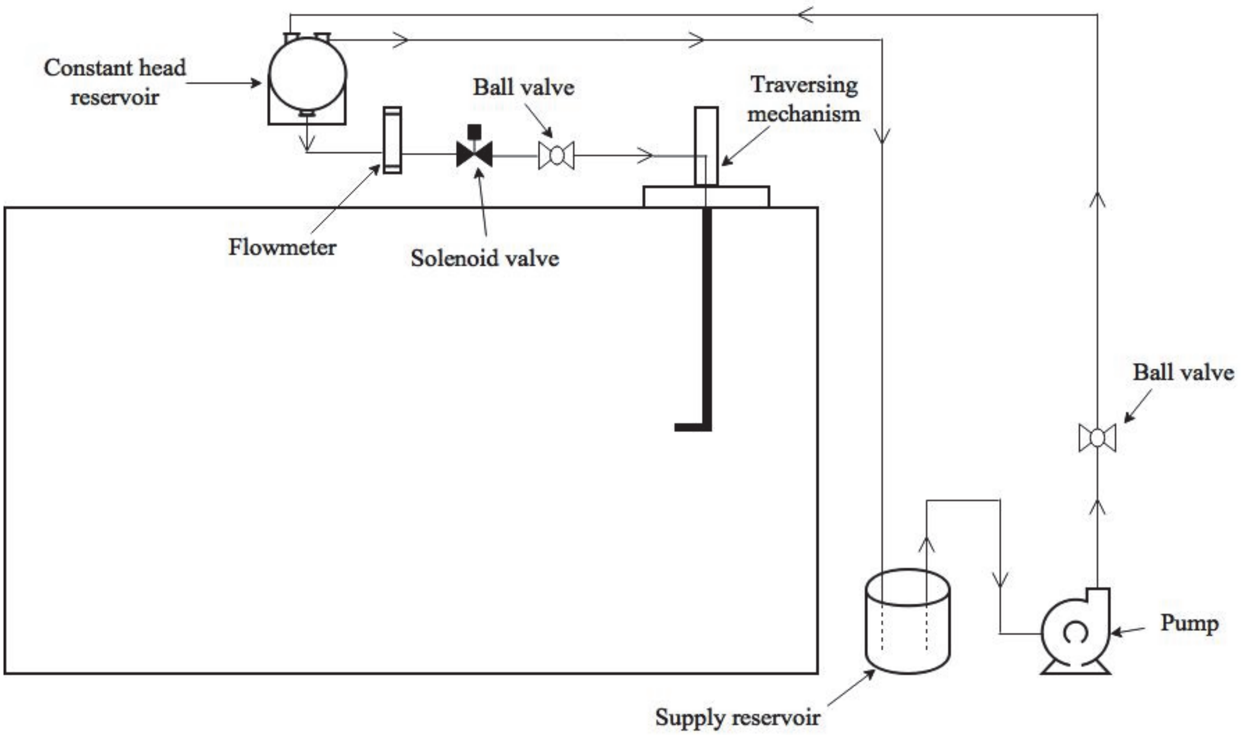

Figure 3.4 Schematic of the jet apparatus.

The constant head reservoir consisted of a 12 liter spherical glass container positioned approximated 2 m above the tank. It was used to maintain a constant pressure difference to drive the jet flow and hence maintain a constant jet Reynolds number during each experiment. The dyed fluid (pumped from the supply reservoir) entered the constant head tank through an inlet at its top. An outlet located just below the inlet served to direct the excess pumped fluid back to the supply reservoir through plastic tubing, ensuring a steady level in the head reservoir. The water from the constant head reservoir was conducted to the jet through plastic tubing (1.9 cm diameter) connected to an outlet at the bottom of the constant head tank. Prior to reaching the jet, the dyed water passed through a flowmeter, a solenoid valve, and a ball valve.

A flowmeter (Omega FL50002A) was used to read the actual flowrate through the jet. The accuracy of the flowmeter is 5% of full scale. A solenoid valve (placed immediately after the flowmeter) was used to turn the jet on or off during the experiments. The state of the solenoid valve was open if a voltage was supplied allowing flow of water towards the jet, otherwise it remained closed. The solenoid valve controller was placed near the supply reservoir to allow remote control of the jet flow. Finally, a ball valve was used to adjust the flowrate towards the jet to achieve the desired Reynolds number. This ball valve along with the flowmeter were employed to set the flowrate for the experiments. The flowrates during the experiments were either 2.2 L/min or 4 L/min, corresponding to jet Reynolds numbers of 5,800 and 10,600 respectively (with $\nu = 1\text{x}10^{-6}$ m^2/s and D = 8 mm).

The jet consisted of a copper pipe of 8 mm inner diameter. The copper pipe extended vertically for 1.6 m and followed by a 90° bend that allowed the jet to discharge horizontally in the tank. After the 90° bend, the 8 mm diameter pipe extended for 0.12 m, resulting in fully developed flow in the pipe at the jet exit. The jet was placed to discharge at 45 cm below the free surface (half-depth of water level). Since the turbulence generated by the RJA decays in the direction normal to the plane of the RJA, the turbulent jet issued horizontally (in the x-direction) in a plane parallel to the RJA to ensure a constant level of background turbulence along the axis of the jet. During the experiments the jet was located at a distance of 110 cm (y/M = 7.3) from the tip of the PVC extensions of the RJA. At this plane, the velocity measurements showed that the turbulence generated by the RJA was nearly homogeneous isotropic with zero-mean flow (Chapter 4).

The accurate positioning of the jet was accomplished by mounting the jet on a traversing mechanism. A Velmex traversing mechanism allowed the jet to be precisely translated in the three directions (x, y, and z). The Velmex traversing mechanism consisted of an array of three BiSlide assemblies (Figure 3.5). Each BiSlide assembly comprised a base, a carriage, and the lead screw driven by a motor. Limit switchers were placed at the bases of each BiSlide assembly to avoid collisions between i) the carriage and the end plates of the base, and ii) the jet and the glass panes of the tank. The motors of the mechanisms were controlled using a Velmex VXM-2 stepper motor controller. The resolution of the mechanism was 0.05 mm in all directions. The total displacement in the x-direction using the mechanism was 130 cm (almost covering the width of the tank). The range of displacement in the y-direction was 24 cm while the maximum displacement attained in the z direction was 55 cm. The movement of the traversing mechanism was controlled using a LabVIEW program. The traversing mechanism was fixed to a C-channel that spanned the tank width in the x-direction. The assembly could be moved in the direction normal to the plane of the RJA along guide rails on the long side of the tank by mounting it on top of short C-channels with wheels. Thus, the jet could be manually positioned at a desired distance from the RJA and then accurately located using the traversing mechanism.

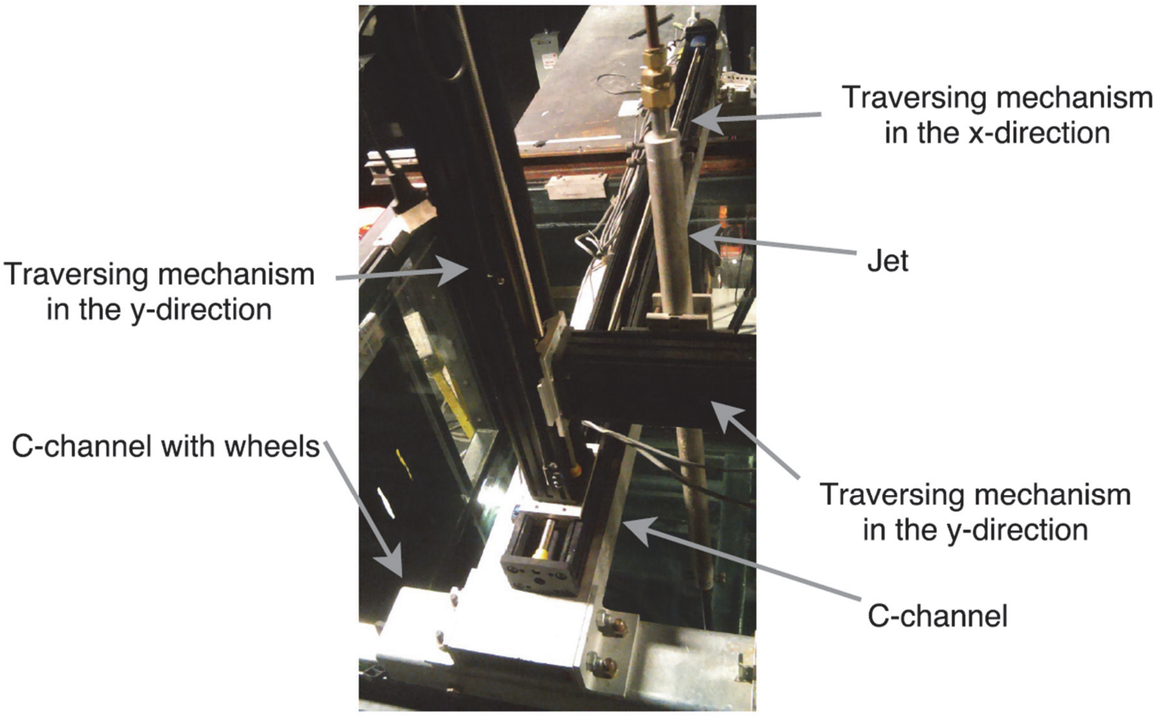

Figure 3.5 Velmex traversing mechanism.

3.4 Accoustic Doppler Velocimeter (ADV) setup

The acoustic velocimeter setup was employed to obtain velocity measurements of the turbulence generated by the RJA using different driving algorithms. Measurements at different downstream positions (y/M) from the RJA were performed (for each algorithm) to calculate the statistics of the flow and quantify the decay of the generated turbulence.

Velocity measurements were obtained using a Nortek Vectrino 10-MHz acoustic Doppler velocimeter (ADV). The ADV consists of a probe, a housing that contains the electronics module, and a power and communication cable to connect with the controlling computer and power supply. The ADV probe was connected to the housing through a 1 m cable. The ADV probe consists of a central transmitter (which emits short ultrasonic pulses) and four receivers that collect the acoustic signals reflected from particles in the measurement volume. The housing holds the power transmitter, analogue and digital signal processing, power conditioner and the standard data recorder. The power and communication cable served to i) supply the external DC power (12-48 V), and ii) connect to the controlling computer for 2-way serial communication.

Given that the ultrasonic pulses do not reflect in clean water, neutrally buoyant 9-13 μm diameter hollow glass spheres (Potters Industries Sphericel) were added to the water to increase the ADV's signal-to-noise ratio (SNR). The minimum acceptable values of SNR and correlation recommended by the ADV manufacturer were 17 dB and 70%, respectively. Sufficient particles were mixed with the water to maintain the values above 20 dB and 97% at all times, ensuring optimal quality of the measurements. Prior to the beginning of the velocity measurements, 30 g of particles were mixed with water in a 4 litre container and then added to the tank. This amount of particles was sufficient to maintain a high SNR for approximately 4 hours. The sampling volume of the ADV is located 5 cm below the probe, thus minimizing flow disturbances, and was set to its maximum volume of 0.42 cm^3. The power level of the ADV was also set to the maximum value, resulting in the highest SNR for the system. The ADV was connected to a computer that controlled the parameter settings and data acquisition through the Vectrino software. 2.25×10^5 data points were recorded in each experiment (at the ADV's maximum sampling rate of 25 Hz for a duration of 2.5 hours). A record of this length ensured that statistics up to fourth order (i.e. kurtosis) were converged. Velocity measurements were taken over a range of distances from the jet array (5.5M - 9.3M) with the probe measurement volume located in the center of planes parallel to the RJA (Figure 3.6). The ADV probe was fixed to a 1.5 m long aluminum pipe. The aluminum pipe and the ADV housing were mounted on a traversing mechanism.

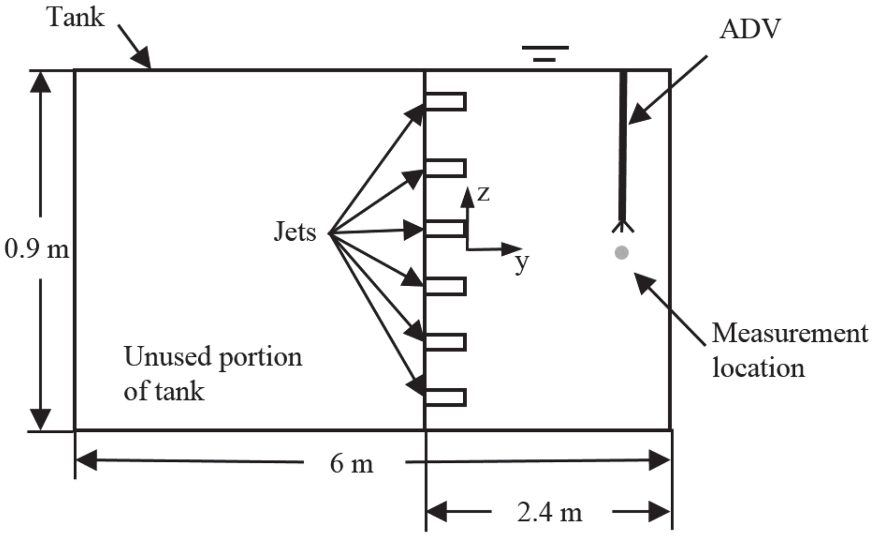

Figure 3.6 Schematic of the location of the ADV in the tank.

The spatial autocorrelation function of the x-component of the velocity was necessary to calculate the integral length scale (ℓ) of the flow. To be able to compute ℓ, the ADV probe was translated at a constant speed in the x-direction on a traversing mechanism. The spatial autocorrelation was subsequently calculated assuming Taylor's hypothesis, which was valid given that the translation velocity was an order of magnitude larger than the characteristic RMS velocity of the background turbulence. The ADV holder and the housing were fixed to an Aerotech traversing mechanism (Figure 3.7). The traversing mechanism was located above the tank and parallel to the plane of the RJA such that the ADV probe could be moved at a constant speed of 0.2 m/s in the x-direction. The Aerotech traversing mechanism consisted of a carriage running on a monorail and driven by a linear motor guided by a magnetic track. The traversing mechanism was controlled using an Aerotech SOLOIST CP10 controller via the Soloist Configuration Manager software. The pipe holding the ADV probe and the housing were attached to the carriage using a small C-chanel. To increase the rigidity of the aluminum pipe holder, three long threaded rods were fixed from the aluminum C-channel to a nut around the pipe.

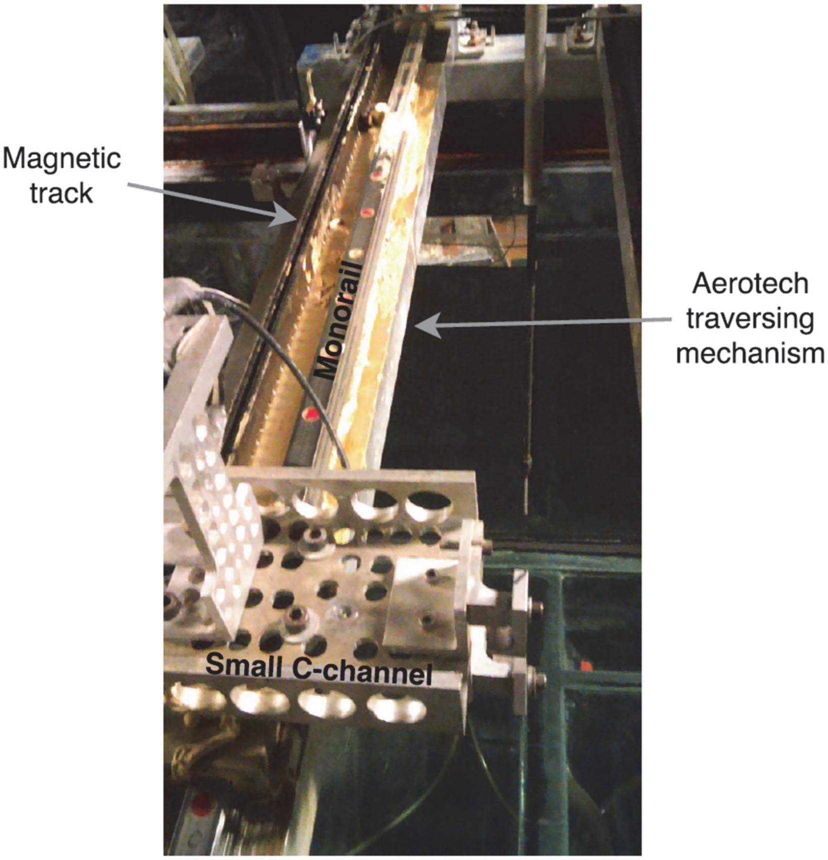

Figure 3.7 Aerotech traversing mechanism.

The Aerotech traversing mechanism was fixed to a C-channel crossing the tank in the x-direction. The assembly could be moved in the direction normal to the plane of the RJA along guide rails on the long sides of the tank by mounting it on top of short C-channels with wheels. Thus, the ADV probe could be manually positioned at the desired distance from the RJA. A measuring tape along the guide rails on the sides of the tank permitted to determine the distance from the RJA. The correct orientation of the ADV probe was verified by translating the probe and holder at a constant speed and observing the velocity measured by the ADV system which should only have one non-zero component. If this was not the case, then the appropriate adjustments were made and the velocity was measured again until the probe was properly oriented.

3.5 Laser induced fluorescence (LIF) apparatus

Planar LIF was employed to obtain concentration measurements within radial cross-sections of the turbulent jet emitted into both quiescent and turbulent backgrounds. The LIF apparatus consisted of the laser sheet generation system and the signal detection system, which were aligned perpendicularly (facing different sides of the tank). The schematic of the LIF system used in this investigation is shown in Figure 3.8. The laser sheet generation system comprised a laser, some mirrors and the laser scanning device. The signal detection system consisted of an (optical) filter, an image intensifier and a camera. A description of the components of both systems is given in the following paragraphs.

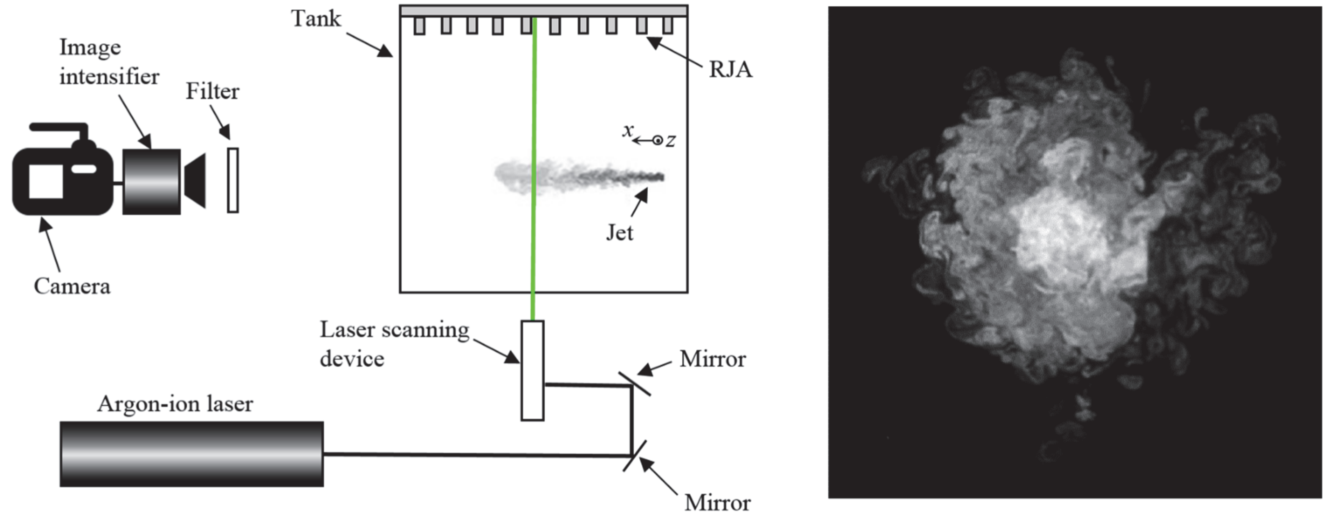

(a) *(b)*

Figure 3.8 (a) Schematic of the planar LIF system (top view). (b) Example of an LIF image

A laser beam originating from an argon-ion laser (Coherent Innova 90) was used to excite the fluorescent dye at the measurement location, making it fluoresce. The laser was operated in the light regulated mode since this mode provided a stable output power. The stability of the output power of the laser was ± 0.5% as estimated by the manufacturer. To ensure stability of its power in the long-term, the laser was warmed up for 60 minutes before commencing the experiments. The power of the emitted beam was determined using a power meter (Coherent Lasermate). The accuracy of its readings was ± 5%. To verify that the laser power was constant during the experiments, it was measured at the beginning and end of each test. The variation in the output power was less than 2% for all the experiments. The laser was operated in single-line mode at a wavelength of 514.5 nm and an output power of 1 W. The aperture of the laser was set to 3.97 mm and the emanating beam was Gaussian in its cross-section. Upon exiting the laser, the beam was directed to the laser scanning device using two mirrors (Melles Griot 02MLQ003/009). The mirrors were mounted on optical holders that allowed fine orientation via their adjustment screws.

A laser scanning device was used to focus the laser beam at the measurement location and produce the laser sheet for the planar measurements of concentration. The laser scanning device consisted of a mirror, a focusing lens and a rotating mirror (Figure 3.9). These three components were aligned and enclosed in an aluminum box. After entering the laser scanning device, the beam was reflected from a 12.7 mm dielectric mirror (Newport 5151) to reach the focusing lens. The dielectric mirror was placed in a black mirror, mount which allowed the orientation of the mirror to be adjusted by rotating two screws. The mount was fixed to the aluminum box.

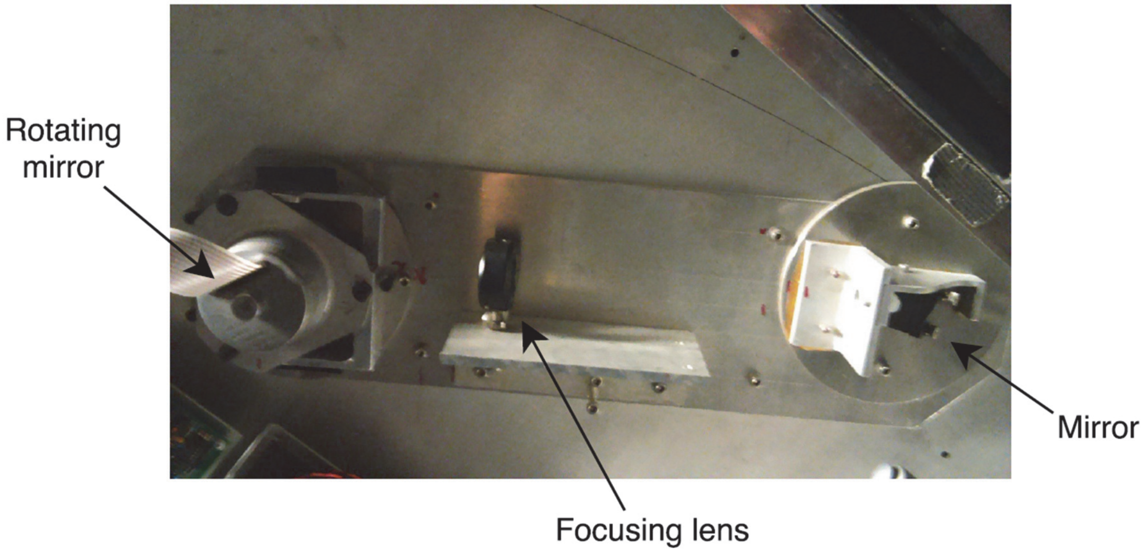

Figure 3.9 Components of the laser scanning device.

The focusing lens was a 1.5 m focal length plano-convex lens (PLCX-25.4-772.6-C). This lens focused the beam down to a waist diameter of 470 μm at the focal point. The optics were located such that the focal point coincided with the axis of the jet. The waist diameter was calculated using the following equation (Ready 1978):

$$d_0 = \frac{2.44\, f_1\, \lambda_1}{D_b} \tag{3.1}$$

where d_0 is the focused diameter, f_1 is the lens focal length, λ_1 is the wavelength of the laser beam, and D_b is the diameter of the laser beam. Also, the Rayleigh range (defined as the distance at which the focused beam increases to $\sqrt{2}$ times the waist diameter) was 22.7 cm. The Rayleigh range was estimated using the following equation (Ready 1978):

$$Z_R = \frac{\pi\, (f_1)^2\, \lambda_1}{D_b} \tag{3.2}$$

where Z_R is the Rayleigh range, f_1 is the lens focal length, λ_1 is the wavelength of the laser beam, and D_b is the diameter of the laser beam. The lens was mounted on an optical holder attached to the laser scanning device.

After crossing the focusing lens, the beam reached the rotating mirror (Lincoln Laser Company DT-08-236-019). It consisted of an 8-sided polygonal mirror coupled to a motor. The motor was set to rotate at its maximum rate of 12000 rpm. The spinning of the mirror rapidly scanned the laser beam through the measurement area, effectively producing a laser sheet. The rotation of the octagonal mirror produced 1600 scans of the laser beam over the measurement area per second. A rotating mirror was selected over cylindrical lenses to generate the laser sheet because the scanning of the laser beam creates a sheet of uniform laser intensity and the rapid movement of the laser beam minimizes the effects of photobleaching and thermal blooming (described in §2.5). The use of cylindrical lenses generates a laser sheet with an inhomogeneous (Gaussian) profile of laser intensity and the laser beam needs to be pulsed to avoid the adverse effects of constant irradiation of the fluid.

The rotating mirror was fixed to the aluminum box ensuring alignment with the focusing lens and the mirror. The proper alignment of all the elements enables the generation of a laser sheet perpendicular to the axis of the turbulent jet. The perpendicular alignment of the laser sheet and the axis of the jet was accomplished in two steps: i) first a vertical alignment with the aid of a plumb bob, and ii) then a fine alignment (in the vertical and horizontal direction) using the traversing mechanism. The vertical alignment of the laser sheet was first adjusted using a plumb bob in the tank filled with water. The laser scanning box was aligned perpendicularly to the glass pane and pointing towards the axis of the jet at the desired measurement section. The string of the plumb bob was then positioned at measurement location and the lights of the laboratory were turned off. The laser and the rotating mirror were turned on to determine the position of the laser sheet. For security, the laser was operated at the minimum output power during the whole process of alignment. The position of the laser sheet was then adjusted such that it coincided with the string of the plumb bob (assuring vertical alignment) through the adjustment screws of the dielectric mirror on the laser scanning device. If changes in the orientation or position of the laser scanning box were necessary, the beam was blocked upon exiting the laser by the laser meter and the scanning device was moved in small increments. When the vertical alignment of the laser sheet was accomplished, the plumb bob was removed from the tank. Then the jet and the Velmex traversing mechanism were used to align the sheet in the horizontal direction. The jet exit was positioned such that it slightly touched the laser sheet. Then, the jet was translated horizontally (in the y-direction) with the traversing mechanism to check the alignment, observing whether or not the jet exit moved out of or crossed the plane of the laser sheet. The necessary adjustments were made using the screws of the mirror on the laser scanning device and one of the mirrors (outside the scanning device) directing the beam to it. The vertical alignment was also verified, moving the jet with the traversing mechanism in the z-direction. The position of the laser sheet was adjusted until the translation of the jet in both the vertical and horizontal direction did not cause the jet exit to move out of the laser plane or cross it, ensuring perpendicular alignment of the laser sheet with respect to the jet axis.

The signal collection system was aligned perpendicularly to the generated laser sheet. The signal collection system comprised an optical filter, an image intensifier and a camera (Figure 3.10). To ensure a correct alignment of the elements of the system, they were secured along a 69 cm long optical rail. The optical rail was supported by two tripods (QuickSet 5-95534-9 and 5-95534-9A), which allowed adjustments of the orientation and height of the system.

The fluorescence signal first reached a 25 mm diameter 550 nm longpass color filter (ThorLabs FGL550) attached to the camera lens (F-Micro-Nikkor 55mm f/2.8). The filter was attached to the front of the camera lens to block any scattered laser light, thus transmitting only fluorescence signal through the lens. The cut off filter rapidly decreased the percentage of transmission at 550 nm such that the transmission at 525 nm was less than 0.0004% (provided by the manufacturer). The wavelengths of the light emitted by disodium fluorescence range from 480 to 650 nm. Thus, any scattered laser light (as well as a small part of the fluorescence signal) was blocked by this filter to ensure that only the emitted fluorescence (with wavelengths above 525 nm) reached the signal detecting equipment (through the camera lens) during the experiments. The specific camera lens was selected because of its focal length and angle of view (43°), which allowed the camera to capture the whole measurement section. The aperture of the lens was set to the maximum to allow the greatest amount of light onto the sensors and hence have the greatest sensitivity to the fluorescence signal.

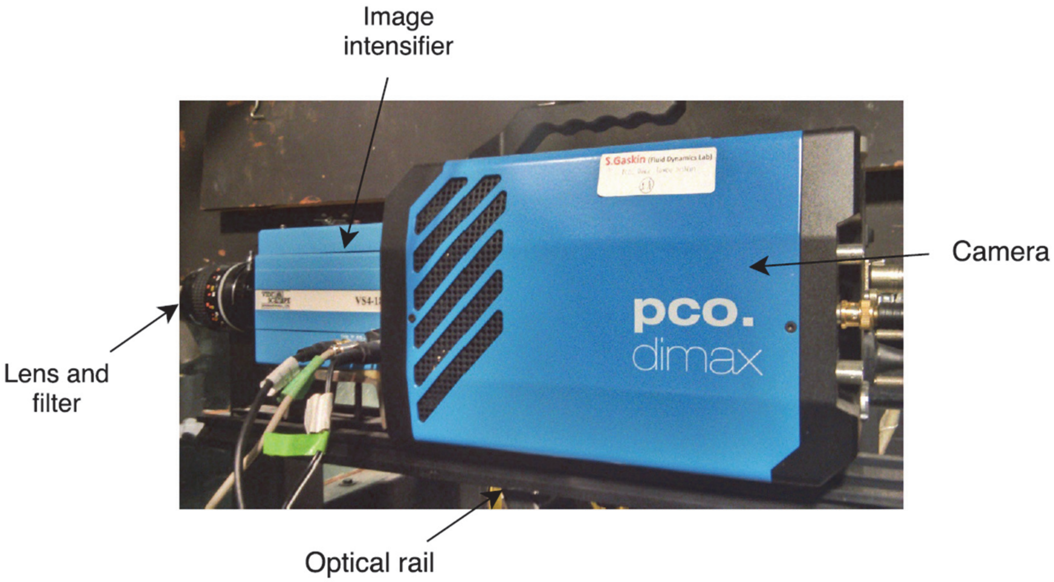

Figure 3.10 Signal collection system.

Due to the characteristically low signal emitted by the fluorescent dye at these concentrations, an image intensifier (Video Scope VS4-1845) was employed to increase the sensitivity of the system. The principle of operation of the image intensifier is to induce two subsequent emissions of electrons (by the incident low level light) between plates with a high DC voltage difference and such that the cascade of electrons impacting on a phosphor screen ultimately causes the emission of light at a higher level than the incident light. The intensification process is accomplished by using three plates at high DC voltage difference to accelerate the flow of electrons: a photocathode, a micro-channel plate and a phosphor screen (Figure 3.11). The low level intensity light enters at the front of the intensifier and reaches a gallium arsenide (GaAs) photocathode. The incident photons cause the photocathode to emit electrons towards the micro-channel plate. The electrons striking the micro-channel plate cause a secondary cascade of electrons towards the phosphor screen. This secondary cascade comprises many more electrons than in the previous stage. The large number of electrons impacting the phosphor screen cause it to emit photons. The emission of light from the phosphor screen is much larger than the light incident on the photocathode due to the increased number of electrons of the secondary cascade, and the signal is thus amplified.

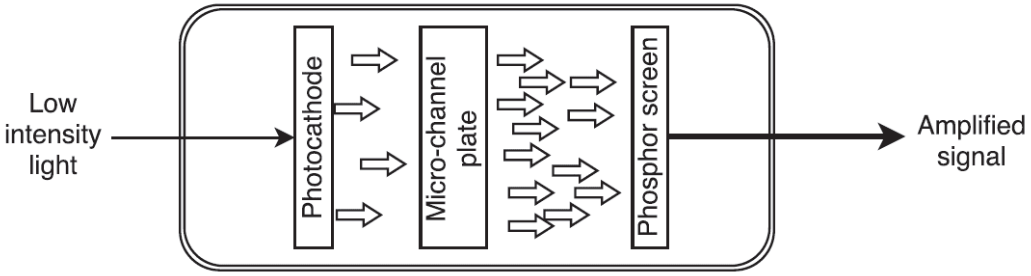

Figure 3.11 Schematic of the intensification process.

The photocathode of the image intensifier is very delicate and even normal light can cause irreparable damage (e.g. loss of sensitivity) or total destruction. Hence, the lights of the laboratory were turned off at the beginning of the experiments and kept off during the entire experiment. The usable range of the intensifier is 450-900 nm which is suitable for the filtered fluorescence signal (525-650 nm). The intensifier was controlled using a computer via the VSI image intensifier controller software provided by the manufacturer. The software can be used to set the following parameters: intensifier gate, intensifier gain and gate delay. The intensifier was operated in the continuous (DC) gate mode which allowed an uninterrupted flow of electrons from the photocathode to the Micro-channel plate, and thus continuous amplification of the signal during the experiments. The gate delay was set to zero and the gain was set to 75000. Using these parameters, the fluorescence signal was continuously amplified during the experiments to levels detected by the camera.

The image intensifier was coupled to the camera using a C-mount adapter allowing the intensified signal to reach the camera for recording. A 12-bit monochrome camera (pco.dimax) was used to record instantaneous images of a cross-section of the dye-containing jet. The camera has a 2016×2016 pixel resolution. Each data image obtained was a matrix whose elements contained the intensity of the light collected by each pixel and subsequently converted to concentrations. The camera was controlled through the Camware application software using an external computer. The coupling of the intensifier and camera reduced the size of the signal detection area to a central circular region of 800 pixels of radius. Additionally, the coupling caused the effective circular area to be more sensitive at the center, and therefore the central region reached saturation levels (4096 counts) faster than the edges. However, a pixel by pixel calibration revealed that it did not affect the measurements of concentration and the sole effect of the coupling was that only a portion of the whole dynamic range (0-4096 counts) was covered by those pixels in the experiments.

Once the elements of the signal detection system were mounted on the optical rail, it was attached to the two tripods. Then, the system was aligned parallel to the jet axis with aid of the traversing mechanism which translated the jet in the x-direction. The lights of the laboratory were turned off and the light of a flashlight was directed to the tank filled with water to create low levels of light to avoid damage to the intensifier. At this point, the image intensifier and camera were turned on. The tip of the jet was positioned at the measurement location and the optical rail was aligned such that the tip of the jet coincided with the center of the image captured by the camera (a red cross displayed using the Camware software marked the center of the image). Then, the jet was translated 400 mm backwards observing the displacement of the tip in the image of the camera. When the translation finished, the position of the tip with respect to the center of the image recorded by the camera was used to correct the alignment of the optical rail. Small increments in the orientation and height of the optical rail were accomplished with assistance of the tripods. After the adjustments were performed, the process was repeated until the translation of the jet maintained the tip at the center of the image. This ensured that the plane of the field of view of the camera was parallel to the plane of the generated laser sheet. Subsequently, the focal length of the image was adjusted. The laser and the rotating mirror were turned on. The laser was operated at its minimum output power. The jet was moved using the traversing mechanism such that its tip slightly touched the generated laser sheet. Then, the focal length of the lens was adjusted to focus the tip of the jet, and thus containing the laser sheet in the field of view. Finally, the jet was moved in the horizontal and vertical directions (y and z-directions) to verify a clear image of the tip of the jet at all positions. This guaranteed a correct alignment of the volume focused by the camera, both containing the laser sheet and being perpendicular to the jet axis.

Three tables were used to support the elements of the laser sheet generation system and the signal collection system. The laser was sitting on top of one table, the laser scanning device on another, and the signal collection system was sitting on a third table. To avoid the misalignment of the LIF system due to possible vibrations in the laboratory, a system to damp the vibrations was used to support the tables. The vibration insolation system consisted of 25.4 mm thick sheets of Sorbothane at the base of the tables. The Sorbothane sheets effectively damped the possible vibrations and thus maintained the relative orientation of the LIF elements.

The dye used in the experiments was disodium fluorescein, having a Schmidt number of 2000. The fluorescent dye is sensitive to external sources of light (and even the normal room lighting could affect its emitted fluorescence), thus the lights of the laboratory were turned off before handling the dye and mixed with water in the supply reservoir prior to the beginning of the experiments, minimizing degradation of the dye. Dilute dye concentrations were used to feed the jet, 0.2 to 0.7 mg of disodium fluorescein were mixed in 30 liters of water in the supply reservoir. Dilute dye concentrations were beneficial for the experiments in several ways. It ensured that the emitted fluorescence was within the linear range. Dilute concentrations also prevented significant density differences between the dyed fluid and the surroundings fluid which could ultimately cause inertial effects. Additionally, using dilute concentrations reduced the possibility of trapping (absorption of emitted fluorescence at another location) and attenuation (decrease of the laser beam intensity along its path due to absorption of energy by the dyed fluid). Using dilute concentrations helped to overcome all these effects which could result in errors in the measurements of concentrations.

3.6 Data acquisition and post-processing

In this section the data acquisition process and the programs used for post-processing will be described. Two experimental setups were used for obtaining measurements of velocity and concentration respectively. Acoustic Doppler velocimetry was employed to obtain velocity measurements in the turbulent background generated by the different driving algorithms for the RJA. LIF was used to obtain measurements of concentrations of a passive scalar within a turbulent jet as described above.

The ADV was connected to an external computer that controlled the data acquisition through the Vectrino software. 2.25×10^5 data points were recorded (at the ADV's maximum sampling rate of 25 Hz for a duration of 2.5 hours) in each experiment.

A record of this length ensured that statistics up to fourth order (i.e. kurtosis) were converged. Each data file contained the 3 components of the velocity along with their respective SNR and correlation. The data were first recorded to the internal memory of the acquisition computer and then transferred to an external hard drive for post-processing. The calculations of the statistics of the flows were performed on the so-called post-processing computer, using custom codes programmed in MATLAB.

In the LIF setup, instantaneous images of cross sections of the dye-containing jet were recorded with a 12-bit monochromatic camera (pco.dimax). The camera was controlled by an external computer using a software package (Camware) provided by the camera supplier. The Camware software allowed the setting of the acquisition rate (frames per second), exposure time and delay. During the actual experiments and calibrations, data was acquired at 30 frames per second with an exposure time of 30 ms and the delay of the exposure was set to zero. Each beam scan lasts 625 μs, therefore a 30 ms exposure captured 48 beam scans per image, minimizing the possibility of large variations in the intensity detected from image to image (e.g. uncompleted beam scans over the measurement interval). The 30 ms exposure (with additional 3.33 ms to allow the internal conversions of light detected to intensity counts in the camera resulting in a temporal resolution of 30 Hz) integrates the fluorescence intensity of 48 beam scans precluding the direct measurement of true instantaneous concentrations. Nevertheless, the results of the statistics of the concentration field of a turbulent jet were in agreement with those studies with higher temporal resolutions (see section 5.3), indicating that the short averaging periods did not adversely affect the measurements. Each data image obtained was a 2016×2016 matrix whose elements contained the intensity of the light collected by each pixel. The acquired images were first stored in the internal memory of the camera, then transferred to the hard disk of the external computer via the Camera Link cable, which offered the highest transfer rates (up to 255 MB/s).

The length of each experiment was limited by re-entrainment of dyed fluid into the jet (which would result in overestimates of the measured concentrations) and the number of images that could be stored in the internal memory of the camera. Preliminary tests showed that 3 minutes of data could be acquired before re-entrainment occurred. This time was also short enough to avoid filling the internal memory of the camera. Thus, the experiments lasted a maximum of 170 seconds, allowing for 5000 images to be recorded in each test. The results showed that for a jet emitted into a quiescent background, data from one experiment was enough for the convergence of the mean and RMS concentrations at each axial location. On the other hand, 25000 to 35000 images were necessary for the jet emitted into a turbulent background, hence 5 to 7 experiments were performed at each axial position. Images of cross sections of the jet were obtained at the following axial distances from the jet exit: x/D = 10, 20, 30, 40, 50, 60 and 70 (where D is the diameter of the jet nozzle).

The size of each data file containing all the images of one experiments was approximately 44 GB. Due to the large size of each data file, the latter were saved in external hard drives for post-processing. The post-processing was performed in an external computer using custom codes programmed in MATLAB to obtain the different results. First, the intensity value of each pixel was converted to concentration value using the calibration curve-fits in a custom MATLAB code. The result was a file (approximately 80 GB in size) containing the concentration values for all the images of one experiment, which was stored in an external hard drive. Custom MATLAB codes were employed to compute results such as mean concentrations, RMS concentrations and probability density functions of the concentrations.

3.7 Calibration and elimination of potential sources of error

As previously noted in §2.5, the expression relating the intensity of the light emitted to the concentration of the fluorescent material (for dilute concentrations of the fluorescent dye) can be written as (Guilbault 1973):

$$F = \Phi_f I_0 \beta b C. \tag{3.3}$$

Therefore, for small concentrations and constant laser power (which was the case of the present experiments), the fluorescence intensity is a linear function of the species concentration.

As explained in §3.5, the coupling of the camera and image intensifier resulted in the central part of the image being more sensitive to the incident light. Hence, the 2^{12} discrete values could be discerned by the pixels near the central region while only around

2^{10} values were used at the edges of the image. Due to this inhomogeneity in the sensitivity of the pixels, a pixel by pixel calibration was necessary to determine the specific (linear) calibration curves for each pixel of the array.

A calibration box was designed and constructed specifically to perform the calibrations. It was a 100 cm by 51 cm by 51 cm rectangular container. The sides of the box consisted of 6.35 mm thick panes of tempered glass. The bottom and top of the calibration box consisted of sheets of 2.54 cm thick plexiglass. The top plexiglass sheet had an opening (70 cm by 30 cm) to allow access. This container was placed inside the big tank for the calibrations (Figure 3.12) and on top of four PVC supports to raise its height such that the camera captured images of the fluid inside the tank. Both tanks were filled with water to the same level prior to commencing the calibration process. The small volume of the calibration box compared with the tank dimensions was beneficial for the calibrations because it: i) reduced the amount of fluorescent dye necessary to complete the calibrations, and ii) minimized the possibility of trapping or attenuation effects since the laser beam travelled across clean water before reaching the calibration tank. The jet was placed inside the calibration box and the dyed fluid for the calibrations was cycled through the jet to closely reproduce the actual experiments. The inlet of the 1/3 HP pump was connected to the calibration box by a plastic hose to pump dyed fluid up to the constant head reservoir to feed the jet. Also, the overflow from the reservoir was directed to the calibration box using plastic tubing. In this way, the dyed fluid for the calibrations was mixed and cycled through the jet by the pump during the calibrations.

The side of the tank from which the laser beam entered the tank was covered with a piece of black cardboard and a slit in the cardboard allowed the passage of only the laser beam (blocking any other scattered light source) during the calibrations and in the actual experiments. Similarly, black plastic plates were attached to the sides of the calibration box to allow the laser beam to enter and leave through slits. The back panes of the tank and calibration box were covered with black material to provide a black background and minimize light reflections. Also, the outer surfaces of the jet and the tubing were painted black which minimized the light reflecting from their surfaces.

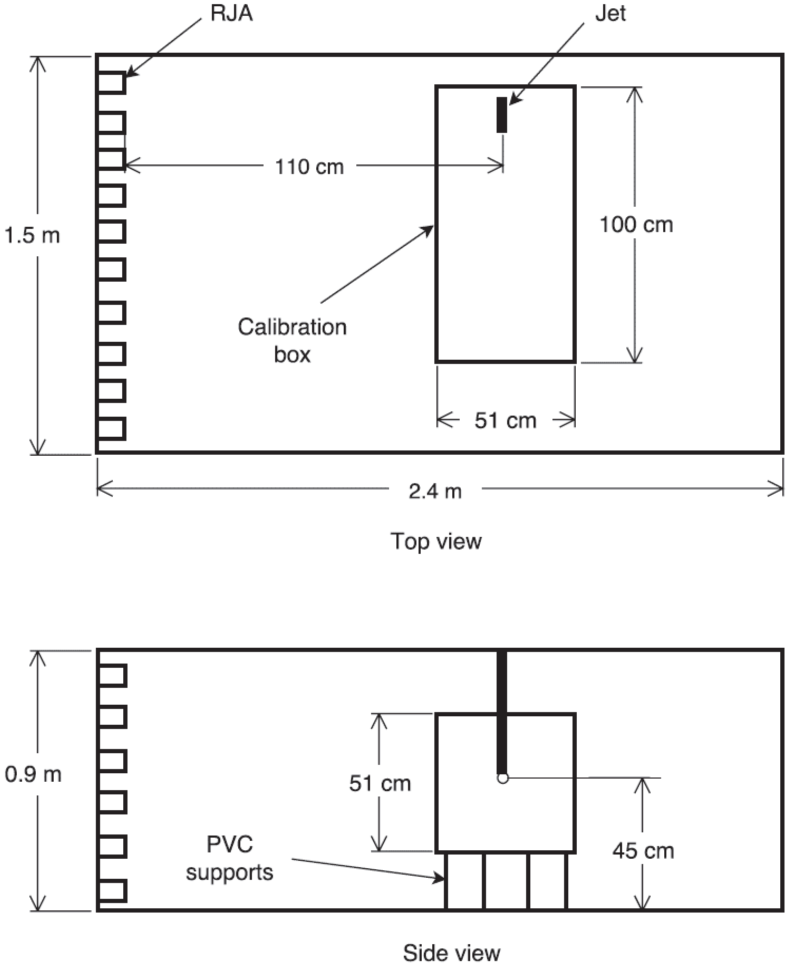

Figure 3.12 Location of the calibration box in the tank.

Each calibration consisted of recording images of the fluorescence signal at the measurement section at progressively higher and known concentrations of disodium fluorescein previously mixed in the calibration box. The image covered a circular area with a radius of approximately 20 cm. Figure 3.13 shows the linear relationship between the intensity counts and the concentration for two pixels. One pixel is located at the center of the image while the other is located near the edge of the field of view. As mentioned previously, the pixels near the edges of the image only used a portion of the total intensity counts. These calibrations verified that the concentration range calibrated lay within the linear range of the relationship between the concentration and fluorescence intensity. During the experiments, jet concentrations were selected such that measured concentrations lay within the calibrated, and hence linear, range.

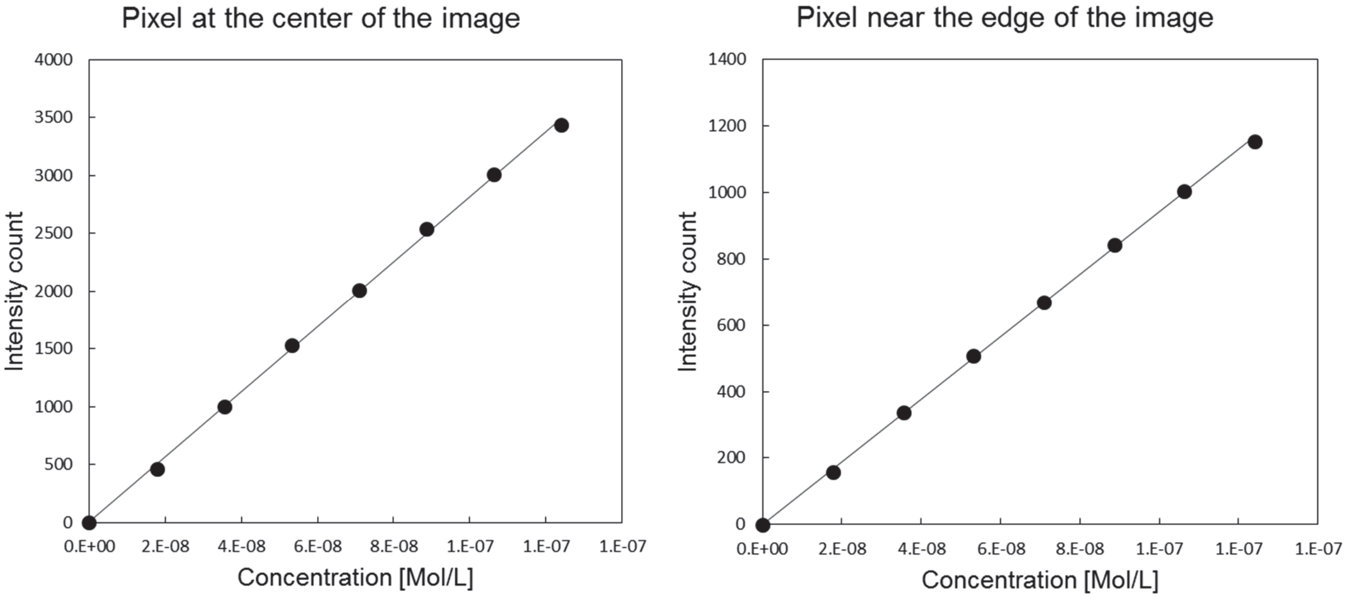

Figure 3.13 Examples of linear calibration curves

The images of the progressively higher fluorescence intensities were stored in an external hard drive and a pixel by pixel analysis was subsequently performed. A linear curve fit was applied to the calibration data for each pixel using a custom code programed in MATLAB. The code separately read the data of each pixel and fitted a linear curve in the form:

$$C_{df} = AI_{cm} + B \tag{3.4}$$

where C_{df} is the concentration of disodium fluorescein, I_{cm} is the intensity value of the pixel, and A and B are constants of the curve fit. The constants of the linear fit for each pixel were stored and later used to convert the data of the actual experiments to concentrations.

Several actions were taken to minimize the potential sources of error and ensure accurate measurement of concentrations. The potential sources of error included photobleaching, thermal blooming, attenuation and inertial effects. The following paragraphs describe the actions taken and tests performed to rule out the effects that could negatively impact the final results.

Thermal blooming refers to the heating of the dyed fluid by the incident beam and photobleaching is the reduction in fluorescence intensity of a dye due to constant irradiation. Thermal blooming and photobleaching were minimized during the experiments and calibrations by rapidly scanning the laser beam across the measurement area, hence avoiding extensive periods of irradiation by the laser. The rotating mirror was set to its highest speed to reduce to the minimum the residence time of the laser beam at the measurement section. In the same experimental facility, Lavertu (2006) performed a test to determine the time for combined photobleaching and thermal blooming effects to become significant. In his test, dyed fluid was continuously irradiated to observe the degradation of the fluorescence signal. He found that the fluorescence signal decreased by 2%, from its peak value, in 200 μs. The residence time of the laser beam in the volume focused by each pixel was calculated to be 2 μs, thus photobleaching and thermal blooming effects were negligible in the present experiments and calibration.

Attenuation of the laser beam occurs when the laser light crosses large volumes of dyed fluid prior to reaching the measurement section (due to absorption of energy by the fluorescent dye). The end effect is a non-linear relationship between the fluorescence intensity and the concentration, since less laser light reaches the measurement location. Due to the low concentrations of disodium fluorescence in the experiments, attenuation was negligible. It was confirmed by the linear relations of the calibrations curves along a line across the field of view. Preliminary calibrations without the image intensifier (and then higher dye concentrations to attain detectable signals by the camera) showed that the calibration curves of pixels at the farthest positions along a line crossing the measurement section, departed from the linear range at high concentrations. This effect was not observed when the image intensifier was employed. Additionally, a test comparing the signals of a known concentration with the tank shifted 10 cm (such that the laser crossed more dyed fluid) with the signal of an actual calibration revealed a negligible difference (less that 1%).

Trapping may occur if the fluorescence emitted at the measurement section is absorbed by dye at another location. This could be possible in the experiments if the dye between the laser sheet and the camera absorbed part of the light emitted by the fluorescent dye at the measurement location. To determine whether or not trapping effects were negligible, a test similar to Saylor (1993) and Lavertu (2006) was performed. In the trapping test, a small glass tank was placed between the calibration box and the camera. First, the signal from a known concentration in the calibration box and clean water in the small tank was recorded. This signal was used as reference for no trapping effects. Then, a known concentration of disodium fluorescein was added to the small tank and the signal from the calibration box was recorded. Comparison of the signals would reveal any trapping effects. The results showed that the difference in the signal was less than 1%, ruling out the trapping effects in the present investigation.

Buoyancy and inertial effects would affect the results if the jet dyed-fluid had a different density than the ambient fluid or the jet fluid was heated by the laser beam. Dilute concentrations of disodium fluorescence were added to the jet fluid. The maximum concentration of disodium fluorescence at the jet exit was 6.2×10^{-8} mol/L. The molecular weight of disodium fluorescein is 376.3 g/mol. Therefore, the difference of the densities of the jet fluid and the water of the surroundings (ρ_w = 1000 kg/m^3) was calculated to be negligible (7×10^{-5} %). A density difference could also result from the jet fluid and background water being at different temperatures. This possibility was eliminated by taking the water for the jet from the big tank prior to the beginning of each experiment.

Heating of the jet fluid by the laser beam was also negligible due to the short residence time of beam at the measurement section, resulting from the rapid rotation of the polygonal mirror.

Chapter 4

Effect of the driving algorithm on the turbulence generated by a random jet array

Different driving algorithms for a large random jet array (RJA) were tested and their performance characterized by comparing the statistics of the turbulence generated downstream of the RJA. Of particular interest was the spatial configuration of the jets operating at any given instant (an aspect that has not been documented in previous RJAs studies), as well as the statistics of their respective on/off times. All algorithms generated flows with non-zero skewnesses of the velocity fluctuation normal to the plane of the RJA (identified as an inherent limitation of the system resulting from the unidirectional forcing imposed from only one side of the RJA), and slightly super-Gaussian kurtoses of the velocity fluctuations in all directions. It was observed that algorithms imposing spatial configurations generated the most isotropic flows, however they suffered from high mean flows and low turbulent kinetic energies. The algorithm identified as RANDOM generated the flow that, on an overall basis, most closely approximated zero-mean-flow homogeneous isotropic turbulence, with variations in horizontal and vertical homogeneities of RMS velocities of no more than ±6%, deviations from isotropy (w_{RMS}/u_{RMS}) in the range of 0.62-0.77, and mean flows on the order of 7% of the RMS velocities (determined by averaging their absolute values over the three velocity components and three downstream distances). A relatively high turbulent Reynolds number ($Re_T = u_T \ell/\nu = 2360$, where ℓ is the integral length scale of the flow and u_T is a characteristic RMS velocity) was achieved using the RANDOM algorithm and the integral length scale ($\ell = 11.5$ cm) is the largest reported to date. The quality of the turbulence in our large facility demonstrates the ability of RJAs to be scaled-up and to be the laboratory system most capable of generating the largest quasi-homogeneous isotropic turbulent regions with zero mean flow. The RANDOM algorithm was subsequently used to generate a turbulent background and study the effect of the latter on the scalar mixing of a turbulent jet (Chapter 5).

4.1 Introduction

Although turbulent flows are, in general, neither homogeneous nor isotropic, the study of homogeneous isotropic turbulence plays a fundamental role in furthering our understanding of the physics of turbulent flows, as it is the simplest realization of the latter. An important advantage of studying homogenous isotropic turbulence is that it isolates the self-interaction of turbulent fluctuations (Orszag, 1977), and avoids complications arising from additional processes encountered in natural and man-made flows, such as density stratification, mean shear and the effects of fluid-solid boundaries (Tsinober, 2004). Consequently, homogeneous isotropic turbulent flows are often used to study the fundamental properties and mechanisms of turbulence (e.g. internal intermittency, spectral energy transfer). Despite the fact that homogeneous isotropic turbulence is a (relatively) simple flow, it can be difficult to create in the laboratory, since mean velocity gradients are generally necessary for the initial production of turbulent kinetic energy.

To date, the most commonly studied homogeneous isotropic turbulent flow has been grid-generated wind tunnel turbulence, which can achieve relatively high Reynolds numbers, given recent advances such as the development of active grids (Makita, 1991; Mydlarski and Warhaft, 1996) and low-viscosity-fluid wind tunnels (Bodenschatz *et al.* 2014). However, the existence of a mean flow in such arrangements can present a problem in certain situations. For example, Lagrangian measurements in such experimental setups require moving the apparatus with the mean flow, an impractical condition for a variety of reasons (e.g. the need to translate camera systems, the requirement of long flow facilities to follow a stream for a relatively long time interval). These impracticalities can be overcome by utilizing zero-mean-flow turbulence. Moreover, homogeneous isotropic turbulence with zero mean flow permits the study of the fluctuating components of the velocity (and their ensuing effects in phenomena such as turbulent scalar transport, mixing and particle dispersion) in isolation. The generation of three-dimensional homogeneous isotropic turbulence with zero-mean flow has been attempted using diverse novel systems, the first of which involved one, or two, parallel grids (separated by certain distance) oscillating in the direction normal to the plane of the grids (Thomson and Turner, 1975; McDougall, 1979; Brumley and Jirka, 1987; De Silva and Fernando, 1994; Villermaux *et al.* 1995; Srdic *et al.* 1996; Shy *et al.* 1997; Ott and Mann, 2000; McKenna, 2004; Blum *et al.* 2010; and Blum *et al.* 2011). Although, the optimal mesh sizes, strokes and frequencies of the grid's oscillation have been proposed, the flows generated by this type of system suffer from large mean flows (with the minimum values of mean flows being approximately 25% of the root-mean-square (RMS) velocities, and maximum values of 60% and 30% for single and double oscillating grids, respectively). Additionally, the oscillation of the grid is accomplished by coupling the grid to a mechanical system driven by a motor, thus making it more difficult to build large experimental setups for experiments at high Reynolds numbers.

Another approach to generating nearly zero-mean-flow homogeneous isotropic turbulence has been to place loudspeakers pointing towards the center of a chamber (Hwang and Eaton, 2004; Webster *et al.* 2004; Warnaars *et al.* 2006; Lu *et al.* 2008; Goepfert *et al.* 2010; and Chang *et al.* 2012), with the locations of the speakers obeying symmetry with respect to the chamber's center. Typically the loudspeakers push fluid through circular orifices to generate pulsed (synthetic) jets and induce vortex rings. Although the quality of the turbulent flow is better than that generated by oscillating grids (very low mean flows that are approximately isotropic), the desired flow is confined to a small region in the center of the chamber. For example, Chang *et al.* (2012), with the use of 32 loudspeakers, were able to generate an almost zero-mean-flow homogeneous isotropic turbulence at the center of a chamber with a Taylor-microscale Reynolds number

(Re_λ) of approximately 480. However, the central (isotropic) volume of this flow covered a radius of only 5 cm. A similar method to create such flows uses symmetrically placed propellers pointing towards the center of a chamber containing a fluid (Fallon and Rogers, 2002; Birouk *et al.* 2003; De Jong *et al.* 2009; and Zimmermann *et al.* 2010). Again, the homogeneity and isotropy of the flow ends up being limited to a small central region.

Symmetrically arranged rotating elements have also been employed to achieve zero-mean-flow turbulence. Rotating grids (Liu *et al.* 1999) and propellers (Berg *et al.* 2006) have been used to create homogeneous isotropic turbulent flow in the center of a rectangular tank. However the levels of turbulence were modest ($Re_\lambda \sim 290$ and 172, respectively) and the isotropic flow was limited to a central volume of approximately $4\times4\times4$ cm^3. Two counter-rotating disks in cylindrical containers have been widely used (introduced by Douady *et al.* 1991 and further used by Fauve *et al.* 1993; Maurer *et al.* 1994; Cadot *et al.* 1995; Belin *et al.* 1996; Aumaitre *et al.* 2000; Mordant *et al.* 2001; and Voth *et al.* 2002). Due to the physical characteristics of this type of system, it generates a cylindrical region of turbulence, with axial extension depending on the size of the tank (e.g. Machicoane *et al*. (2014), and references therein), negligible mean flow and relatively high Re_λ (Voth *et al.* (2002) reached Re_λ=970.) However, the flow suffers from anisotropy and the radial extent of the optimal flow covers only a few centimeters. In a modification of this technique Liberzon *et al.* (2005) used eight counter-rotating disks to generate the turbulence. However, the flow generated at the center of their tank had a low Reynolds number ($Re_\lambda \sim 40$).

Random jet arrays (RJAs) are relatively new systems that have been developed and used to generate approximately homogeneous isotropic turbulence with zero mean flow (Variano *et al.* 2004; Lavertu, 2006; Variano and Cowen, 2008; Delbos *et al.* 2009; Khorsandi *et al.* 2013; and Bellani and Variano, 2014). A (single) RJA is a planar configuration of jets that, randomly and independently, turn on and off to produce turbulence downstream of the array. The RJA is able to create a nearly homogenous flow (albeit with an unavoidable decay in the direction normal to the plane of the jets) with a negligible mean flow (less than 10% of the RMS velocities in all directions) over a large spatial region (Variano and Cowen, 2008). Additionally, the isotropy of the flow is of the same order as that of grid-generated, wind tunnel turbulence and relatively high Reynolds numbers can be reached (Re_λ = 314 in Variano and Cowen, 2008). The isotropy, quantified as the ratio of RMS velocities (i.e. $u_{\alpha\text{-RMS}}/u_{\beta\text{-RMS}}$), measured in mono-planar RJAs (Variano *et al.* 2004 (0.81); Lavertu, 2006 (0.66); Variano and Cowen, 2008 (0.79); Delbos *et al.* 2009 (0.76); Khorsandi *et al.* 2013 (0.71)) can be as low as two-thirds, presumably resulting from the forcing from only one plane. Most recently, Bellani and Variano (2014) placed two RJAs separated by a distance and facing each other. The resulting profile of the turbulent kinetic energy had zero slope at the tank center due to the underlying symmetry of their arrangement. This configuration generated a nearly homogeneous isotropic turbulent flow with a negligible mean flow at the center of the tank. Using this arrangement, the isotropy was significantly improved (compared to single RJAs) and found to be in the range 0.95-0.99 in the center of the tank. The Taylor-microscale Reynolds number was 334 and the region of homogeneity and isotropy was roughly 0.4×0.4×0.2 m^3 (the largest reported to date).

The present investigation is motivated by the growing interest in random jet arrays as laboratory systems that are the most capable of accurately approximating zero-mean-flow homogeneous isotropic turbulence. The objective of this work is to study different RJA driving algorithms to investigate the statistics of the resulting flow in an attempt to both describe and optimize the characteristics of the generated turbulence, while concurrently identifying the limitations of such systems.

4.2 Experimental setup

The experiments were carried out in a 1.5×2.4×0.9 m^3 section of a large glass tank (1.5×6.0×0.9 m^3) in the Environmental Hydraulics Laboratory in the Department of Civil Engineering and Applied Mechanics at McGill University. The tank was filled with water and its top was open to the ambient air.

A planar random jet array was used to produce a turbulent flow in the tank (Figure 4.1). The three other vertical sides of the measurement region were the side walls, which consisted of panes of tempered glass, as did its bottom. The top of the tank was open to the ambient air, with a free surface of water. The RJA consists of 10 columns of 6 bilge pumps (Rule 25D, 500 GPH) attached to a vertical sheet of high density polyethylene (1 x 1.5 m^2). The jet array is based on that of Variano and Cowen (2008), but built to a larger scale. The jets are equally spaced in the horizontal and vertical directions (with center to center distance, M, of 15 cm) having symmetric boundary conditions, which were chosen to minimize possible secondary flows, in analogy with oscillating grid turbulence (Fernando and De Silva, 1993). The pumps draw water in from their base and discharge it from an outlet oriented perpendicularly to the plane of the jet array – see Figure 4.1(c). Since the suction and discharge occur simultaneously into the same fluid volume, there is a zero net mass flow rate in a control volume containing the pump, which is essential to generate the zero mean flow in the tank. A 15 cm extension (3.18 cm in diameter) is attached to the outlet of each pump to straighten the flow upon its exit from the pumps. The random jet array is controlled using a custom algorithm programmed in LabVIEW, which independently turns the pumps on and off. Downstream of the jet array, the jets merge, generating a region of turbulence that decays in the direction normal to the plane of the jet array. The independent functioning of each pump allowed us to explore different driving algorithms (section 4.4) and compare the statistics of the resulting turbulent flows (section 4.5).

4.3 Measurement technique and post-processing

Velocity measurements were obtained using a Nortek Vectrino acoustic Doppler velocimeter (ADV). The ADV probe consists of a central transmitter (which emits short ultrasonic pulses) and four receivers that collect the acoustic signals reflected from particles in the measurement volume. Details of the principles of operation of ADVs can be found in Voulgaris and Trowbridge (1998), McLelland and Nicholas (2000), and the Vectrino Velocimeter User Guide (Nortek, 2004). Given that the ultrasonic pulses do not reflect from clean water, hollow glass microspheres (Potters Industries Sphericel #110P8) with a density (ρ_p) of 1.1 ± 0.05 kg/m^3 were added to the water to increase the ADV's signal-to-noise ratio (SNR). The size distribution of the particles was such that 10% of the

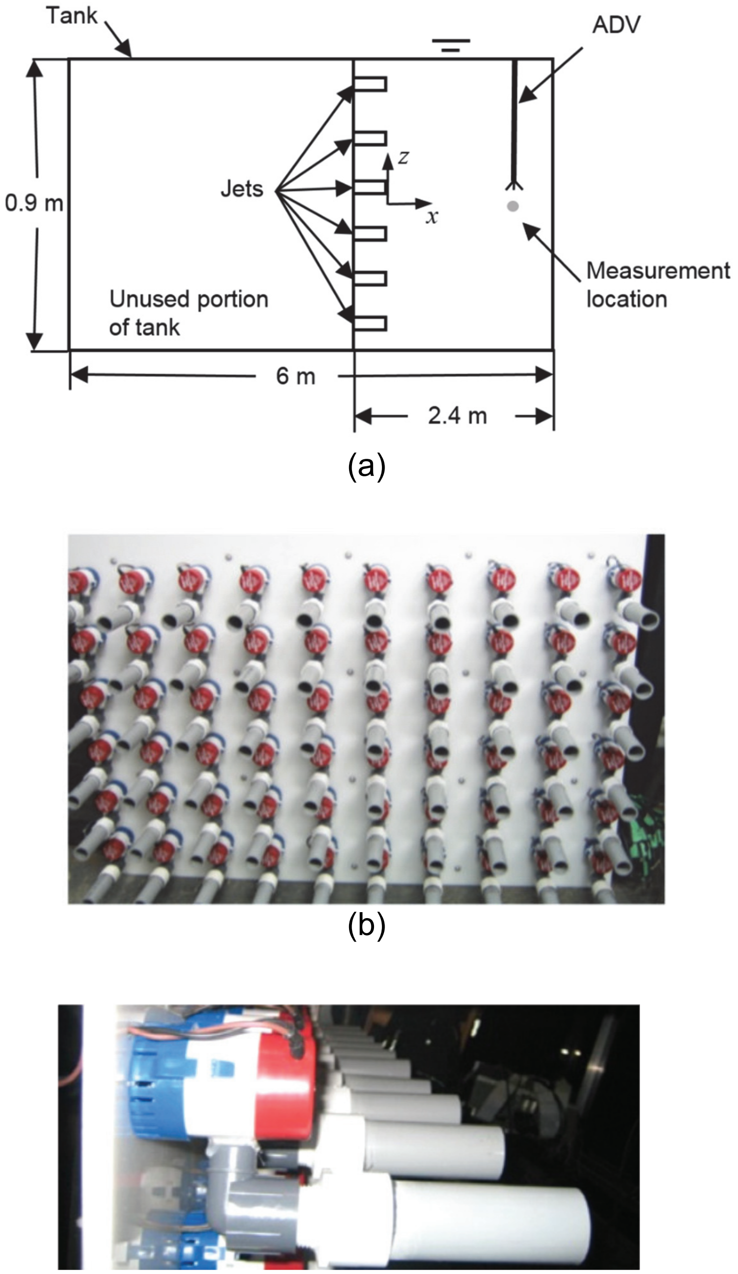

(a)

(b)

(c)

Figure 4.1 Experimental facility: (a) schematic of the apparatus: side view (not to scale); (b) a photograph of the random jet array; (c) a close-up, side view of the bilge pumps in which one can observe their inlets (on their blue bottoms) and the gray PVC extensions to their outlets.

particles' diameters (D_p) were smaller than 5 μm, 50% smaller than 10 μm, 90% smaller than 21 μm, and 97% smaller than 25 μm. The minimum acceptable values of the SNR and correlation recommended by the manufacturer are 17 dB and 70%, respectively. Their values are calculated by the Vectrino software for each velocity measurement. The SNR has its usual definition of SNR= $20\log_{10}(\text{Amplitude}_{\text{signal}}/\text{Amplitude}_{\text{noise}})$ and the correlation is a measure of the similarity of two pulse echoes being measured by the instrument (hence in the range 0-100%). Details of the calculations can be found in the Vectrino Velocimeter User Guide (Nortek, 2004). Sufficient particles were mixed with the water to maintain the values above 20 dB and 97% at all times, ensuring an optimal quality of our measurements. Furthermore, the particles passively followed the flow given their low Stokes number: St = τ_0/τ_η, where τ_η = $(\nu/\varepsilon)^{1/2}$ is the Kolmogorov time scale of the flow (with the dissipation rate of turbulent kinetic energy per unit mass being estimated as $\varepsilon = u^3/\ell$, where ℓ is the integral length scale of the flow) and τ_0 = $\rho_p D_p^2/(18\mu)$ is the particle response time (where μ=0.001 N·s/m^2 is the dynamic viscosity of water). The Stokes number in the present experiments was within the range 9.4×10^{-9} - 2.3×10^{-7}, well below 1, ensuring that the particles passively followed the flow.

The sampling volume of the ADV is located 5 cm below the probe, thus minimizing flow disturbances, and was set to its maximum volume of 0.42 cm^3. The power level of the ADV was also set to the maximum value. Selecting the maximum values of power and volume results in the highest SNR and correlation for the system. The ADV was connected to a computer that controlled the parameter settings and data acquisition through the Vectrino software. 2.25×10^5 data points were recorded for each experiment at the ADV's maximum sampling rate of 25 Hz, for a total duration of 2.5 hours. The latter represents 1000 to 3000 integral time scales, depending on the downstream distance from the RJA. A record of this length ensured that statistics up to fourth order (i.e. kurtosis) were converged.

Velocity measurements were taken over a range of distances from the jet array (5.5M - 9.3M) with the probe measurement volume located in the center of the plane parallel to the RJA. The flow in planes parallel to the RJA was measured in Khorsandi (2011) and was shown to be statistically homogeneous at sufficient distances (> 5M) from the individual jets of the RJA due to the symmetry of the apparatus. Figure 4.2 reproduces two figures from Khorsandi (2011) for one representative driving algorithm ("RANDOM" – see the next section for the details of its operation). Figure 4.2a) indicates that a horizontal transect of $\langle W \rangle$ is constant to within -0.08 to +0.13 cm/s and that w_{RMS} is constant to within ±6% of its mean value at that location. (Quoting percentages for the mean velocities is not sensible, as their nominal value is zero.) Figure 4.4b) indicates that $\langle U \rangle$ and $\langle W \rangle$ fall within the ranges -0.19 to +0.11 cm/s and -0.22 to +0.04 cm/s, respectively, and that u_{RMS} and w_{RMS} are constant to within ±5% and ±4% of their respective mean values. Thus the flow generated by the RJA can be classified as homogeneous, to a reasonable approximation. It goes without saying that the homogeneity may be algorithm dependent, although it is also reasonable to expect that this dependence should decay with increasing distance from the RJA, as the flow continues to mix and differences in velocity are eliminated.

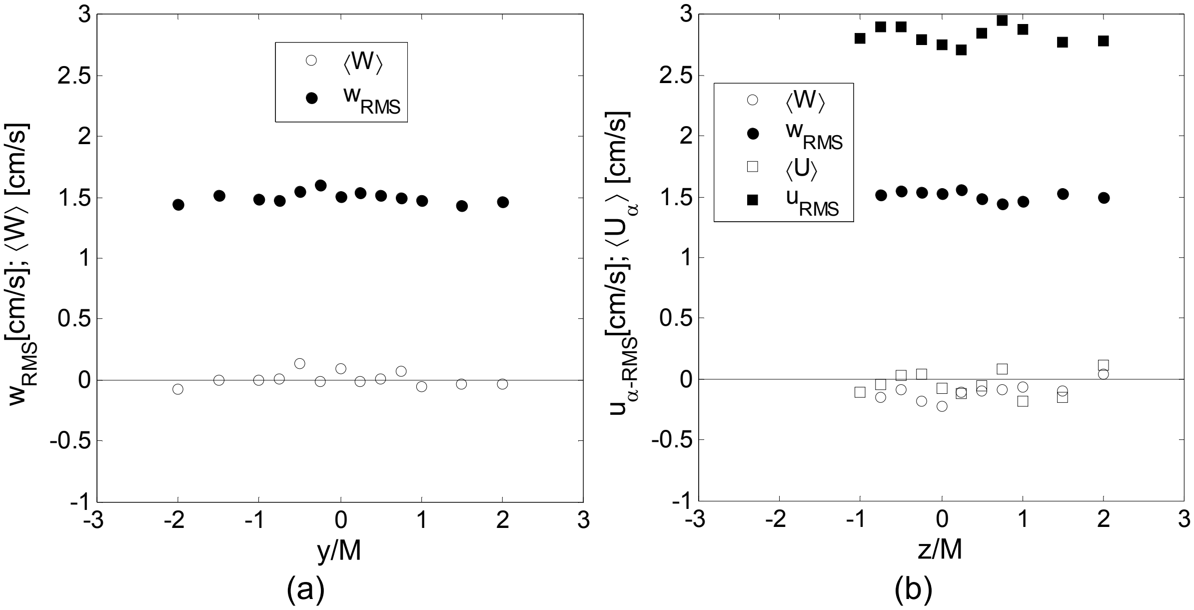

Figure 4.2 Horizontal and vertical homogeneity for RANDOM algorithm. (a) ⟨W⟩ and w_{RMS} velocities along a horizontal line passing through z/M = 1.5 measured at x/M = 7.3. (b) ⟨U⟩, ⟨W⟩, u_{RMS} and w_{RMS} velocities along a vertical line passing through y/M = 0. (⟨U⟩ and u_{RMS} measured at x/M = 5.5. ⟨W⟩ and w_{RMS} measured at x/M = 7.3.) Adapted from Khorsandi (2011).

It is known that the *u* and *v* components of the RMS velocity are overestimated by the ADV systems (Voulgaris and Trowbridge, 1998; Khorsandi *et al.* 2012). Due to the geometry of the ADV, the velocities measured by its four receivers are at a very small angle from the transmitter beam, resulting in a higher precision in the *w* component of the velocity (Nortek, 2004). Therefore the probe was oriented such that its measured *v* and *w* components of velocity were located in a plane parallel to the RJA (Figure 4.1a). This configuration allows the noise correction method for axisymmetric flows of Khorsandi *et al.* (2012) to be applied, correcting the known overestimation in the *u* and *v* components of the RMS velocity. To use the correction method of Khorsandi *et al.* (2012), the ADV probe is oriented so that measured (average) statistics of the *v* and *w* velocities can be assumed to be identical, given the RJA's underlying symmetries. (This assumption was validated by making 3 separate measurements of the 3 components of velocity, each using the ADV oriented in a way that the measurements were made using its highest-precision (*z*) direction. Axisymmetry was confirmed, with the variations in v_{RMS} and w_{RMS} being less than 2% for each of the 3 downstream distances studied herein, using the RANDOM algorithm, to be discussed shortly.) The excess noise variance in the *y*-direction can then be inferred by subtracting the variance of *w* from that of the overestimated variance of *v* (i.e. $\sigma^2_{v\text{-noise}} = \langle v^2 \rangle - \langle v^2 \rangle_{true}$, where $\langle v^2 \rangle_{true} = \langle w^2 \rangle$, and where $\sigma^2_{v\text{-noise}}$ is defined as the noise variance in *v*, assuming that the true signal and the noise are statistically uncorrelated). The noise variance in *v* is converted to that of *u* using the ADV's transformation matrix. The true variance of *u* is then obtained by subtracting the calculated noise variance in *u* from the calculated variance in *u*. The interested reader is referred to Khorsandi (2011) and Khorsandi *et al.* (2012) for more details on this noise correction procedure. (Note the different coordinate system in those references.)

4.4 Jet driving patterns

The ability to independently operate and control each jet in the array allowed us to investigate different RJA driving algorithms generating the turbulence. Of particular interest was the spatial configuration of the pumps turned on at any given instant, as well as the statistics of their respective on/off times. Given the results of Variano and Cowen (2008), who found a superior performance of random algorithms over deterministic ones, we focus mainly on driving algorithms that are spatial variations with a random element whose on/off times are randomly selected from normal distributions with their respective mean (μ) and standard deviation (σ). Table 4.1 summarizes the relevant parameters for each algorithm tested in the present experiments, which are grouped into 4 different classes of algorithms.

Group	Algorithm	μ_{on} [s]	σ_{on} [s]	μ_{off} [s]	σ_{off} [s]
1	RANDOM	12	4	108	36
2	4SECTRANDOM1	12	4	108	36
	4SECTRANDOM2	6	1.5	48	12
	4SECTRANDOM3	4	1	32	8
	4SECTRANDOM4	2	0.5	16	4
3	CHESSBOARD	∞	∞	∞	∞
	EQUALCHESS	12	0	12	0
	RANDOMCHESS	12	4	12	4
4	RANDOMNUMBER	Threshold = 0.98; t = 0.4 s			
		20	19.8	20	19.8

Table 4.1 Summary of algorithm parameters

The RANDOM algorithm is that used by Khorsandi (2011) and Khorsandi *et al.* (2013). It was proposed in Variano and Cowen (2008) as the “sunbathing” algorithm and its parameters were optimized by both groups. We do not, therefore, investigate any further optimization of this class of algorithm. However, neither group documented the results of other classes of algorithms. When the RANDOM algorithm is used, each pump is independently and randomly turned on and off. The on and off times are random values determined from normal distributions with adjustable mean (μ) and standard deviation (σ). For the RJA used herein, Khorsandi (2011) investigated variations of mean on times (ranging from 3-12 s) and mean off times (ranging from 15 to 108 s) with the standard deviations fixed at 1/3 of the respective mean times (e.g. $\sigma_{on}/\mu_{on} = \sigma_{off}/\mu_{off} = 1/3$). The 1/3 ratio was chosen following the analysis of Variano and Cowen (2008), who found very little sensitivity of the mean flow and RMS velocities to the values of σ_{on} and σ_{off}. In the examination of different mean on and off times, Khorsandi (2011) identified that larger times improved the statistics of the flow. The larger on/off times are presumably required given: i) the size of the facility, and ii) the time required for the turbulence generated by the RJA jets to propagate downstream. Short on/off times fail to sustain an optimal turbulent flow in a large tank since the effects of the turbulence generated by the small injections of momentum rapidly vanish within a short distance from the RJA, and the flows generated by adjacent jets do not spread apart far enough to interact and therefore homogenize the flow. Khorsandi *et al.* (2013) found that the optimal values for their larger RJA were $(\mu_{on}, \sigma_{on}) = (12, 4)$ seconds and $(\mu_{off}, \sigma_{off}) = (108, 36)$ seconds, such that, on average, 10% of the pumps are on (or working). We use the same parameters in our investigations of the RANDOM algorithm.

Given the large positive values of the skewness of the *u* velocity measured in the works of Lavertu (2006), Variano and Cowen (2008), and Khorsandi *et al.* (2013), we hypothesized that the RANDOM algorithm may be susceptible to the operation of a single jet (or few adjacent jets), which might cause local, short-term large flows (and hence the large values of skewness). To test this hypothesis a new algorithm named 4SECTRANDOM was proposed and tested. In this algorithm, the RJA is divided into four sections of 3 by 5 pumps (group 2 in Table 4.1). The jets in a given quadrant (e.g. upper left) were then individually turned on and off over random intervals (in the same fashion as in RANDOM) and the rest of the quadrants turned their pumps on and off to obey (odd) symmetry (in both the *y* and *z* directions) with respect to the center of the RJA to ensure a statistically homogeneous distribution of working pumps. In other words, the "master" quadrant independently and randomly turned on the jets while the other three "slave" quadrants operated their jets in a manner that would enforce symmetry. Figure 4.3 shows an instantaneous state of the jet array using an algorithm of the class 4SECTRANDOM. Different on and off times were tested under this conditions (see Table 4.1).

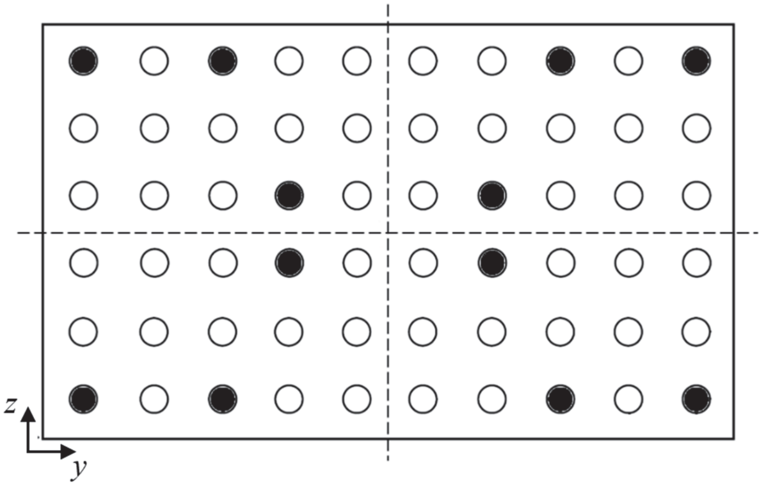

Figure 4.3 Example of a given instantaneous state of the planar array using the 4SECTRANDOM algorithms (front view). Filled circles represent jets turned on. At this instant, three jets are on in the "master" (upper left) quadrant and the other three "slave" quadrants turn their jets on to enforce symmetry with respect to the center.

To further investigate the effect of the spatial distributions of operating jets, less intermittent patterns were also explored. In the CHESSBOARD algorithm (group 3 in Table 4.1), 50% of the pumps were on at all times following the pattern depicted in Figure 4.4. The EQUALCHESS algorithm changed the state of all jets (from on to off and vice versa) in a chessboard distribution every 12 seconds. And the RANDOMCHESS algorithm changed the state of the chessboard at intervals determined from a normal distribution with mean (μ) of 12 seconds and standard deviation (σ) of 4 seconds. The latter algorithm decouples the random nature of the forcing in space and time, by having a deterministic forcing in space, but a random one in time. The mean on times and standard deviation in the chess-like algorithms were selected as 12 and 4 seconds, respectively – the same values as used in the RANDOM algorithm. This served to isolate the effect of the spatial distribution of the operating jets on the generated turbulence.

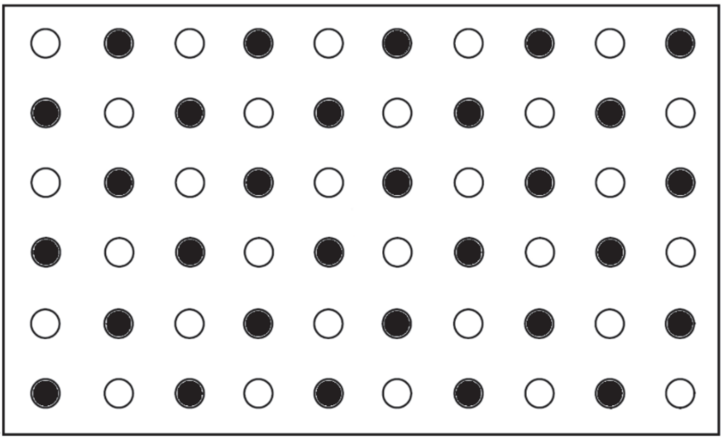

Figure 4.4 Chessboard spatial distribution of jets (front view).

Finally, inspired by the functioning of an active grid, the RANDOMNUMBER algorithm turned the jets on and off independently if a random number (between 0 and 1) generated for each pump was greater than a certain threshold (0.98). A new random number was generated every 0.4 seconds. The threshold and the period for the random number generation are taken in analogy with the active grid operation of Mydlarski and

Warhaft (1998), which has similar characteristics to a RJA (i.e. varying open and closed portions, resulting in discrete jets), as well as similar dimensions (a mesh of 8 x 8 winglets in a wind tunnel of 0.9 x 0.9 m^2 cross section).

4.5 Results

In this section the statistics of the turbulent flows generated by the different algorithms are compared to i) characterize the differences that result from the variation of driving patterns, and ii) identify the optimal algorithm for the production of high-Reynolds-number, homogeneous, isotropic zero-mean-flow turbulence. An "optimal" algorithm is defined as one that generates turbulence with the lowest possible mean flow ($\langle U\rangle/u_{RMS}$, $\langle V\rangle/v_{RMS}$, $\langle W\rangle/w_{RMS} << 1$), high degrees of isotropy ($u_{RMS} \approx v_{RMS} \approx w_{RMS}$; $S_u = S_v = S_w = 0$; and $K_u = K_v = K_w$) and (ideally) high RMS velocity. Measurements at different downstream positions (x/M) from the RJA were performed (for each algorithm) to quantify the decay of the generated turbulence. Table 4.2 presents the results at different measurement positions for all the algorithms tested. It is important to mention that measurements at x/M=9.3 were not performed for some algorithms due to the low levels of turbulence generated at that farthest downstream location.

Algorithm	x/M	$\langle U \rangle$ [cm/s]	$\langle V \rangle$ [cm/s]	$\langle W \rangle$ [cm/s]	u_{RMS} [cm/s]	$v_{RMS}=w_{RMS}$[1] [cm/s]	$\langle U \rangle / u_{RMS}$	$\langle V \rangle / v_{RMS}$	$\langle W \rangle / w_{RMS}$	w_{RMS} / u_{RMS}	S_u	S_v	S_w	K_u	K_v	K_w	TKE [cm^2/s^2]
Group 1 RANDOM	5.5	-0.02	-0.11	-0.15	3.06	1.90	-0.01	-0.06	-0.08	0.62	1.09	0.2	0.13	4.60	4.61	4.15	8.28
	6.7	-0.01	0.04	-0.08	2.65	1.67	0	0.03	-0.05	0.63	1.26	0.04	0.08	5.05	4.62	4.02	6.31
	9.3	-0.31	0.04	-0.23	1.55	1.20	-0.2	0.03	-0.19	0.77	1.42	0.15	0.33	6.72	5.02	4.38	2.64
Group 2 4SECTRANDOM1	5.5	0.24	0.18	-0.30	4.18	1.67	0.06	0.11	-0.18	0.40	1.5	0.28	0.18	5.65	5.60	4.35	11.54
	6.7	0.39	0.15	-0.13	3.47	1.62	0.11	0.09	-0.08	0.47	1.49	0.17	0.33	5.71	5.58	4.73	8.62
	9.3	0.34	0.01	-0.15	2.22	1.21	0.15	0.01	-0.12	0.55	1.84	-0.13	0.45	7.81	6.08	5.22	3.92
4SECTRANDOM2	5.5	-0.13	-0.17	-0.05	2.18	1.38	-0.06	-0.13	-0.04	0.64	1.42	0.29	0.28	6.33	5.40	4.84	4.28
	6.7	0.13	0.11	0.06	1.95	1.23	0.07	0.09	0.05	0.63	1.59	0.09	0.43	6.70	6.60	4.87	3.41
	9.3	-0.09	-0.07	0.06	1.02	0.72	-0.09	-0.1	0.09	0.71	1.86	-0.28	0.52	9.08	5.93	5.00	1.03
4SECTRANDOM3	5.5	-0.85	-0.55	0.09	1.49	0.99	-0.57	-0.55	0.09	0.67	1.7	0.45	0.30	8.60	7.15	5.89	2.10
	6.7	-0.06	0.07	-0.03	1.44	0.92	-0.04	0.08	-0.04	0.64	1.72	0.15	0.41	7.58	7.85	5.16	1.89
	9.3	-0.38	0.05	0.04	0.59	0.53	-0.65	0.09	0.07	0.89	1.41	-0.2	0.49	7.78	6.03	5.70	0.45
4SECTRANDOM4	5.5	0.17	0.09	-0.15	1.50	0.87	0.12	0.1	-0.18	0.58	1.69	0.16	0.37	8.51	9.99	7.31	1.88
	6.7	-0.22	-0.04	-0.15	1.02	0.65	-0.21	-0.06	-0.24	0.64	1.91	-0.07	0.59	9.45	8.26	7.16	0.94
Group 3 CHESSBOARD	5.5	0.52	1	0.42	1.51	1.28	0.34	0.78	0.33	0.85	0.85	0.26	-0.23	4.42	4.69	3.90	2.77
	6.7	0.23	0.64	0.10	1.17	0.87	0.19	0.73	0.12	0.75	1.07	0.33	0.02	4.91	4.83	3.49	1.45
EQUALCHESS	5.5	-0.46	0.71	0.47	1.44	1.02	-0.32	0.7	0.46	0.71	1.65	-0.03	0.27	7.50	6.02	4.91	2.08
	6.7	-0.99	0.67	0.33	0.57	0.70	-1.75	0.95	0.46	1.24	0.68	-0.19	0.12	6.29	3.35	3.14	0.66
RANDOMCHESS	5.5	-0.48	0.57	0.29	1.40	1.01	-0.34	0.57	0.29	0.72	1.58	0.17	0.35	7.27	5.64	4.66	1.99
	6.7	-0.89	0.79	0.45	0.75	0.76	-1.19	1.04	0.59	1.01	1.16	-0.28	0.08	8.53	3.83	3.41	0.86
Group 4 RANDOMNUMBER	5.5	-0.5	0.32	-0.23	2.70	1.81	-0.18	0.18	-0.13	0.67	1.29	0.02	0.13	5.11	4.69	3.98	6.91
	6.7	-0.77	0.18	-0.18	1.91	1.40	-0.4	0.13	-0.13	0.73	1.49	-0.21	0.28	6.43	4.85	4.18	3.79
	9.3	-0.66	0.09	-0.10	1.06	1.08	-0.63	0.09	-0.09	1.02	0.82	-0.12	0.18	5.54	4.43	3.68	1.72

Table 4.2 Measurement position, mean flow, RMS velocity components, isotropy, skewness, kurtosis and turbulent kinetic energy (TKE) for the different algorithms tested.

---

[1] Note that $v_{RMS} = w_{RMS}$ due to our noise elimination procedure described in Section 4.3 which assumes the flow is statistically isotropic in the y-z plane.

Mean and RMS velocity

Although all the algorithms generate turbulence with a low mean flow (less than 1 cm/s in any given direction), it is preferable to normalize the mean velocities with their respective RMS velocities to compare the strength of the mean flow on a relative basis. Considering this parameter, the RANDOM and the different 4SECTRANDOM algorithms produce turbulence with the smallest mean flow in all directions. RANDOM (at x/M = 5.5 and 6.7) and 4SECTRANDOM2 (at the three downstream positions) generated the weakest mean flows (essentially 10% or less of the value of their respective RMS velocities in all directions). On the other hand, the chessboard-like and RANDOMNUMBER algorithms exhibited large relative mean flows (reaching values as high as 1.75 in the worst case). It was also observed that the RANDOMNUMBER algorithm resulted in values of $\langle U \rangle / u_{RMS}$ (velocity component normal to the plane of the RJA) being always higher than that of the other two components of the velocity (a trend not observed in any of the other algorithms tested). Although it is difficult to conclusively explain this observation using single-point Eulerian measurements as is the case herein, this may be due to a large number of jets operating during excessively long periods resulting in large $\langle U \rangle$ overall, which is consistent with the fact that the RANDOMNUMBER algorithm was characterized by the longest value of μ_{on} of all random algorithms, as well as large standard deviations. Alternately expressed, such a scenario is possible given that the jets only change their state if the generated number is higher than the threshold, increasing the chances of jets maintaining their on state for a long time, as opposed to the other algorithms, which alternate the state of the jet in a “cyclical mode” at times defined by the on and off parameters (whose normal distributions reduce the possibility of excessively long intervals of jets operating).

As mentioned in section 4.3, the noise correction of Khorsandi *et al.* (2012) for the RMS velocities was applied to improve the accuracy of the turbulence measurements. Due to the symmetry of the flow and the assumptions involved in the correction, w_{RMS} and v_{RMS} are thus identical. We note that u_{RMS} (normal to the jet array plane) is larger than w_{RMS} for 21 of the 23 cases examined herein. The higher values of u_{RMS} can possibly be attributed to it being the velocity component in the jet exit direction. We note that the measurements of Lavertu (2006) and Khorsandi *et al.* (2013) are consistent with the present results undertaken in the same experimental facility. Moreover Variano and Cowen (2008) also observed the RMS of the velocity component in the direction normal to the plane of the RJA to be the largest. Regarding the 4SECTRANDOM class of algorithms, we observe that the RMS values increase with μ_{on} (4SECTRANDOM4 having the smallest μ_{on} and 4SECTRANDOM1 the largest). The same effect was observed during the exploration of variations of the RANDOM algorithms of Khorsandi (2011). The increase in the calculated RMS with μ_{on} may be attributed to the longer periods of injection of momentum, facilitating its propagation in the downstream direction, and favoring the development of longer "instantaneous gradients of velocity," allowing time for increased turbulent production. (See Variano and Cowen (2008), §5.3 for an extensive discussion of the effects of μ_{on}.) The 3 chessboard-based and the RANDOMNUMBER algorithms produce low RMS velocities, presumably caused by the large number of jets on at a given time, a drawback previously observed in RJAs. Variano and Cowen (2008) studied the effect of the average number of operating jets on the RMS velocities and found an optimal value over which additional (working) jets only serve to reduce the RMS velocities. In their

RJA, the RMS velocities were maximized with 12.5% of pumps working, on average. Consistent with this finding, in our experimental facility the RANDOM and 4SECTRANDOM4 algorithms generate flows with the largest RMS velocities with (on average) 10% of the pumps on.

Isotropy, skewness and kurtosis

The isotropy of the flows is first quantified comparing the ratio $w_{\mathrm{RMS}}/u_{\mathrm{RMS}}$ (Table 4.2). As already noted, we find that u_{RMS} is generally larger than w_{RMS} for almost all combinations of driving algorithm and downstream position. The flows generated by the chessboard patterns and the RANDOMNUMBER algorithms have better isotropy (close to one in some cases). The isotropy of the flows generated by the 4SECTRANDOM algorithms seems to be somewhat altered by changing the values of μ_{on}. The anisotropy observed using the RANDOM and 4SECTRANDOM algorithms is not entirely surprising. It presumably arises from the asymmetric forcing (from only one side of the tank), and has previously been observed in turbulent flows produced by random jet arrays (Variano and Cowen, 2008; Khorsandi *et al.* 2013) as well as in active grid generated turbulence (Makita, 1991; Mydlarski and Warhaft, 1996). Lastly, the isotropy is observed to increase slightly with increasing distance from the jet array for most of the algorithms investigated, similar to that observed by Khorsandi *et al.* (2013). Essentially, the anisotropy resulting from the generation of the turbulence by the jets is gradually “forgotten” as the flow returns to isotropy away from the RJA. Bellani and Variano (2014), who used two RJAs facing each other, also observed that the isotropy improved in the central region of their tank.

Hence, the additional symmetry of their bi-planar RJA system reduces the effect of the decay away from a single RJA and thus improves the isotropy of the flow.

The skewness ($S_\alpha = \langle \alpha^3 \rangle / \langle \alpha^2 \rangle^{3/2}$) quantifies the asymmetry of the distribution of velocity fluctuations. A negative skewness implies that negative fluctuations are more probable than positive ones, and conversely for positive skewness. The calculated values of S_v and S_w are close to zero (indicating essentially equal contributions from positive and negative fluctuations) and is effectively unaltered by the algorithm considered. Given the symmetry of the RJA, such results i) are expected, and ii) validate the statistically homogeneous nature of the flow in planes parallel to the RJA. S_u is found to be positive and order 1 for all the algorithms tested. Similarly, Variano and Cowen (2008) obtained a skewness of the velocity component normal to the plane of the RJA of 1.04. The non-zero skewness of a velocity component is apparently an unavoidable feature of the jet array that presumably results from the unidirectional forcing in the tank and subsequent decay of the turbulence in one direction. The injection of momentum occurs from the jet array and propagates in the downstream direction. Related to this argument, Maxey (1987) and Variano and Cowen (2008) claimed that in nearly homogeneous turbulence, in which the turbulent kinetic energy (TKE) decays in a given direction (e.g. downstream of a grid or RJA), there is a turbulent flux of TKE from the regions of higher TKE to lower TKE leading to a non-zero velocity skewness.

The kurtosis ($K_\alpha = \langle \alpha^4 \rangle / \langle \alpha^2 \rangle^2$) quantifies the importance of the tails of the distribution of velocity fluctuations, such that a high kurtosis is associated with frequently occurring large fluctuations. (A Gaussian distribution exhibits K=3.) Although, large fluctuations may not be desirable in certain situations (e.g. inertial effects becoming important in particle dispersion due to strong and large displacements, or excessive flapping of a scalar source released into a flow), they do not result in anisotropies unless the kurtoses of the different velocity components are unequal. The RANDOM algorithm produces a flow with smaller and approximately similar kurtoses (in the three directions), which are nevertheless super-Gaussian. Other algorithms have higher kurtoses that are considerably different in the 3 directions and are thus, in that sense, less isotropic. Moreover, although effectively Gaussian statistics (S = 0, K = 3) are often defined in the study of homogeneous flows, probability distribution functions of velocity fields with super-Gaussian characteristics are relevant to other areas of fluid mechanics, such as the complex intermittent wind fields in which wind turbines operate (e.g. Good and Warhaft, 2011).

Turbulent kinetic energy (TKE)

The turbulent kinetic energy per unit mass (tabulated in Table 4.2 and plotted in Figure 4.5) is defined as $\frac{1}{2}(\langle u^2\rangle + \langle v^2\rangle + \langle w^2\rangle)$ and used to quantify the intensity of the turbulence at various downstream distances, for the algorithms investigated herein. One observes that all the algorithms with a chessboard configuration produce low levels of TKE. The lower values associated with these algorithms presumably result from the large number of jets operating at a given time (50% of jets on), which reduces the RMS velocities. Variano and Cowen (2008) found that for their RJA, the RMS velocities were maximized with 12.5% of working jets on average. Hence, having 50% of the jets on at a given time (as is the case for this class of chessboard algorithms) may result in insufficient velocity differences/fluctuations, and be the cause of the low TKE. An intermediate level of turbulence was created using the RANDOMNUMBER algorithm. The RANDOM and 4SECTRANDOM series of algorithms produce the highest values of TKE, again resulting from the lower (but not too low) number of working jets (10% on average).

The TKE was also found to increase with increasing mean on times of the jets for the 4SECTRANDOM series of algorithms. RANDOM and 4SECTRANDOM1 produce the turbulence with the highest TKE for a given downstream distance (~10 cm^2/s^2 at *x*/M = 5.5). The TKE resulting from 4SECTRANDOM1 is about 30% higher than that in RANDOM, but exhibits a larger mean flow and anisotropy (Table 4.2). The higher mean flow may be a consequence of the imposition of the same number of jets operating in all quadrants (in the 4SECTRANDOM series of algorithms), which reduces the randomness and therefore possibly generate larger mean flows. Furthermore, an increased mean flow can advect the effects of individual jets (originating from the RJA) farther downstream, resulting in the measured increased anisotropy.

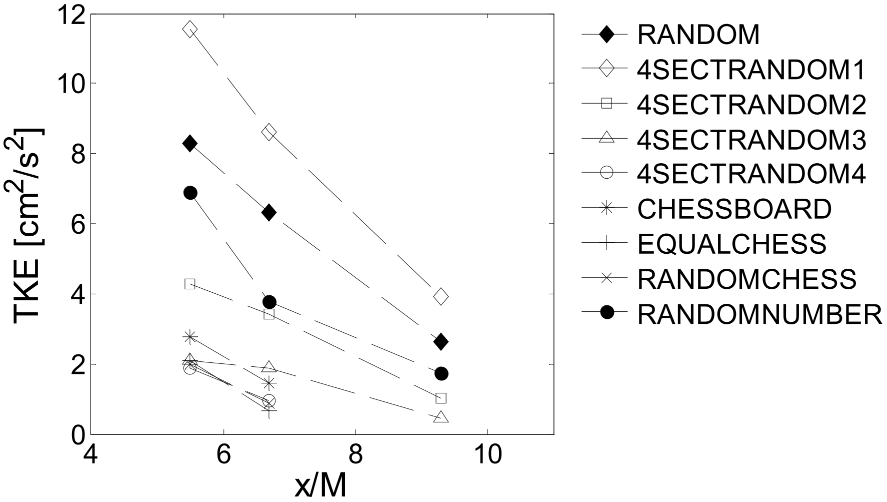

Figure 4.5 Evolution of the TKE with downstream distance.

Evaluation of the algorithms

As previously noted, the optimal algorithm should generate approximately homogeneous isotropic turbulence in our tank with a zero mean flow. Additionally, high levels of turbulence are desirable (as quantified by a large value of turbulent kinetic energy) to achieve Reynolds numbers that are more representative of “real” flows. The requirement of a negligible mean flow eliminates the algorithms of the chessboard type, as they create mean flows as large as 175% of the value of the RMS velocity. However, it should be noted that these algorithms are the least anisotropic. Consequently, these algorithms would be suitable for investigations in which the mean flow and high levels of turbulence are not significant limitations, but isotropy is an important requirement. Furthermore, if we restrict the strength of the mean flow to be less than 10% of the RMS value in all the directions, only 4SECTRANDOM2 and RANDOM (at x/M = 5.5 and 6.7) can be considered as possible optimal algorithms, with the latter exhibiting a marginally smaller average mean flow (averaged over the *absolute value of the mean flow* for the nine cases corresponding to the three flow directions and three downstream positions) of 7% as compared to 8% for 4SECTRANDOM2. For these two cases, the isotopy ($w_{\mathrm{RMS}}/u_{\mathrm{RMS}}$) fell in the range of 0.62-0.77 for the RANDOM driving algorithm and in the range of 0.63-0.71 for the 4SECTRANDOM2 algorithm.

The TKE generated using the RANDOM algorithm is higher than that of 4SECTRANDOM2. Additionally, the turbulence generated using the RANDOM algorithm apparently decays at a slower rate than that created by 4SECTRANDOM2 (see Figure 4.6) when considering the decay in physical space, which is indeed the relevant case in the present context (as opposed to characterizing the decay as a function of eddy turnover time, for example). Furthermore, the TKE at *x*/M=9.3 using the RANDOM algorithm has decreased to 32% of its value at *x*/M=5.5 while for 4SECTRANDOM2 the TKE has decreased to 24% of its respective value at *x*/M=5.5. As previously noted, none of the algorithms studied herein eliminated the non-zero skewness in the *x*-component of the velocity (1.09-1.42 for RANDOM and 1.42-1.86 for 4SECTRANDOM2), suggesting that it is characteristic of all mono-planar RJA systems (as compared with the bi-planar system presented by Bellani and Variano, 2014). Also, the kurtoses are higher than that of a Gaussian distribution (K=3) for all the algorithms tested, however, it is the closest to the Gaussian value in all directions when using the RANDOM driving algorithm (average over the nine cases of 4.80, as compared to 6.08 for 4SECTRANDSOM2). Hence, we conclude that our optimal driving algorithm is RANDOM, as it generates turbulence with negligible mean flow (less than 10% the RMS value in all directions at *x*/M=5.5 and 6.7), high turbulent kinetic energy, and an acceptable degree of isotropy (especially when compared with the other algorithms tested).

The turbulent Reynolds number ($Re_T = u_T \ell / \nu$) was also calculated (see table 4.3), where ℓ is the integral length scale of the flow and u_T is a characteristic RMS velocity. ℓ is calculated from the spatial autocorrelation function ($\rho(r)$) of the *y*-component of the velocity. To be able to measure ℓ, the ADV probe was translated at a constant speed (0.2 m/s) in the *y*-direction. The spatial autocorrelation was subsequently calculated assuming Taylor's hypothesis, which was valid given that the translation velocity was an order of magnitude larger than the characteristic RMS velocity. The spatial autocorrelation functions ($\rho(r)$) used for the calculation of ℓ at the three downstream positions are plotted in Figure 4.7. To account for the slight anisotropy in the velocity components, we calculated a characteristic velocity $u_T = (1/3(u^2_{RMS} + v^2_{RMS} + w^2_{RMS}))^{1/2}$ following the definition used by Variano and Cowen (2008) for their RJA.

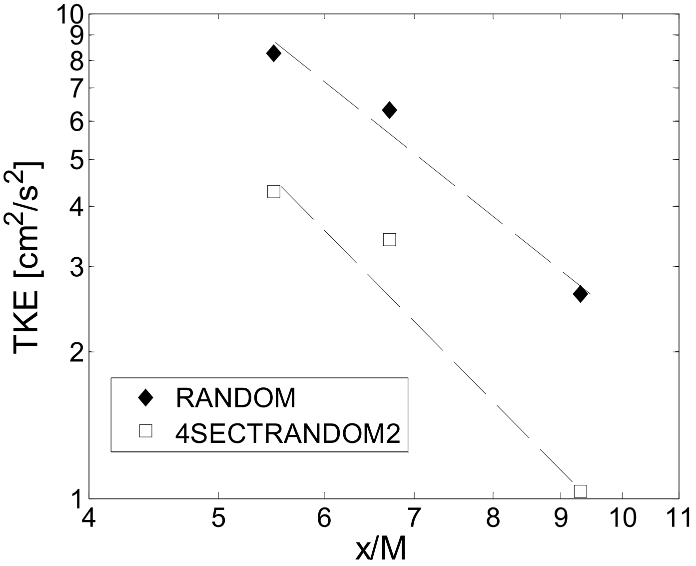

Figure 4.6 Downstream evolution of TKE for the RANDOM and 4SECTRANDOM2 algorithms.

Algorithm	*x*/M	u_T [cm/s]	ℓ [cm]	$Re_T \equiv u_T \ell/\nu$
RANDOM	5.5	2.35	7.5	1760
	6.7	2.05	11.5	2360
	9.3	1.33	11.6	1540

Table 4.3 Characteristic velocity (u_T)*, integral length scale* (ℓ) *and* Re_T *for the flow generated using the RANDOM algorithm.* $\nu = 1\times10^{-6}$ *m*^{2}*/s.*

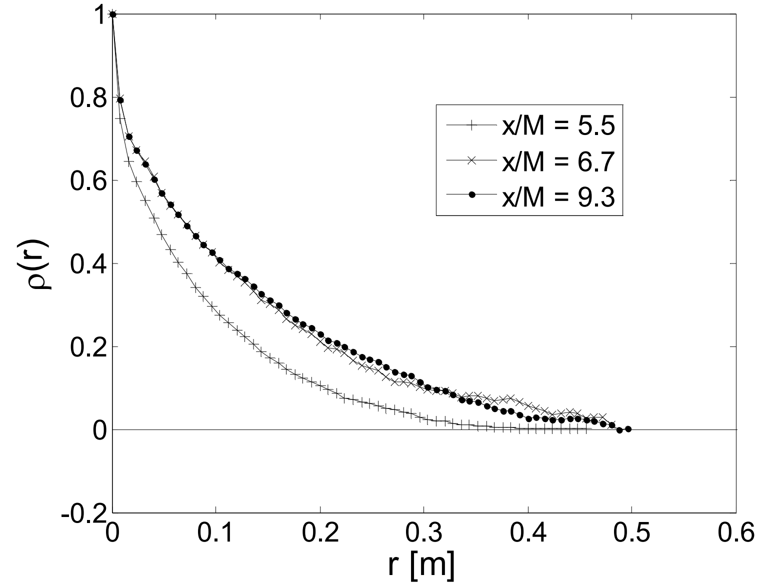

Figure 4.7 Spatial autocorrelations at different distances from the RJA.

The fact that Re_T reaches its highest value at *x*/M = 6.7 may imply that the flow is still under development at *x*/M = 5.5. This result is consistent with the description of a jet-merging region extending up to *x*/M = 6, as suggested by Variano and Cowen (2008). Furthermore, the little change in *ℓ* between *x*/M=6.7 and *x*/M = 9.3 supports the idea that the flow is still developing at *x*/M = 5.5. Thus, we recommend that the measurements in investigations using the turbulent flow generated by RANDOM should be performed at positions farther downstream than *x*/M=5.5, although more measurements would be necessary to fully quantify the evolution of the flow downstream of the RJA.

We compare the results of the flow generated by the RANDOM algorithm with previous investigations in Table 4.4. The results show that our system performs quite well when compared with other ones. Although the mean flow in our system is not zero, it was lower than that in most previous similar systems. The integral length scale (*ℓ*) in our flow is the largest reported. Our ratio ℓ/M = 0.77 at x/M = 6.7 is almost the same as the value of ℓ/M = 0.76 of Variano and Cowen (2008) at x/M = 6.0, which may be interpreted as a sign of the similarity in the development of the two flows despite the larger scale of our facility. A large integral length scale can be useful for the study of the effects of large scales in turbulence. Moreover, along with the Re, large values of ℓ allow the existence of an inertial subrange covering a broad range of (readily measurable) scales. The anisotropy in Table 4.4 corresponds to the lowest ratio of RMS velocities measured at the center of the experimental facilities (in our study it is $w_{\mathrm{RMS}}/u_{\mathrm{RMS}}$). Although some studies reported the variation of the ratio of the RMS velocities in a central plane, others reported the values at the center of their tank, thus for a fair comparison the values used in Table 4.4 are those measured at the center of the apparatuses. The moderate anisotropy in our system is its largest drawback. However, it could be eliminated by converting our system into a double RJA, by the addition of a second RJA facing our existing one. The Reynolds number in our system is one of the highest reported to date and comparable to that of other RJAs (Variano and Cowen, 2008, and Bellani and Variano, 2014). The homogeneity of the flow in planes parallel to the RJA covers a large area of approximately 0.75×0.75 m^2 (see Khorsandi (2011)). Such a large homogeneous region cannot be achieved in most other types of systems, and it is thus encouraging that a relatively high quality turbulent flow was generated in a facility of this size. The approximately zero-mean-flow homogeneous isotropic turbulence generated by our large random jet array proves the flexibility of RJAs to be scaled to study turbulent flows at larger scales.

System	Max ($\langle U_\alpha \rangle / u_{\alpha_{RMS}}$)	ℓ [cm]	Anisotropy ($u_{\alpha_{RMS}} / u_{\beta_{RMS}}$)	Re_T	Reference
Single RJA	0.08	7.5	0.62	1760	Present work, RANDOM at *x*/M=5.5
Single RJA	0.05	11.5	0.63	2360	Present work, RANDOM at *x*/M=6.7
Single RJA	0.2	11.6	0.77	1540	Present work, RANDOM at *x*/M=9.3
Single RJA	0.07	7.6	0.79	3220	Variano and Cowen (2008) at *x*/M=6
Facing dual RJA	0.1	9.5	0.95	2000	Bellani and Variano (2014)
Two oscillating grids	0.3	2.2	0.9	75	Srdic *et al.* (1996)
Two oscillating grids	0.28	0.3	0.9	55	Shy *et al.* (1997)
Rotating grids	0.7	4.7	0.85	2540	Liu *et al.* (1999)
Propellers	0.1	6	0.9	504	Zimmermann *et al.* (2010)
Loudspeakers	0.1	2.8	0.97	1590	Hwang and Eaton (2004)
Loudspeakers	0.04	3.6	0.95	2040	Goepfert *et al.* (2010)
Loudspeakers	0.04	9.9	0.94	4230	Chang *et al.* (2012)

Table 4.4 Comparison with other studies of zero-mean-flow, homogeneous isotropic turbulence.

4.6 Conclusions

Different driving algorithms for a planar random jet array were tested to compare the statistics of the generated turbulence downstream of the RJA in an attempt to both further characterize their performance and find an optimal algorithm that approximates zero-mean-flow homogeneous isotropic turbulence. The algorithm identified as RANDOM generated a flow with relatively high turbulent kinetic energy and the most closely approximated zero-mean-flow homogeneous isotropic turbulence (on an overall basis), exhibiting variations in horizontal and vertical homogeneity of no more than ±6%, and mean flows of 7% of the RMS velocities averaged over (the absolute value of the) three velocity components and three downstream distances measured herein. The measured anisotropy (w_{RMS}/u_{RMS} in the range of 0.62-0.77) was not negligible, but could be reduced at the expense of other desirable characteristics of the flow (e.g. Reynolds number/downstream position; zero mean flow). Also, it should be noted that all of the tested algorithms produced non-zero skewness of the fluctuating velocity normal to the plane of the RJA, as well as super-Gaussian kurtoses of all the three components of velocity. This is identified as an inherent limitation of the system resulting from the unidirectional forcing imposed from only one side of the RJA. This non-zero skewness could be overcome (at least at the center of the tank) by placing two RJAs facing each other such as the apparatus built by Bellani and Variano (2014). The results of Bellani and Variano (2014) showed that the isotropy is improved in a relatively large central section of the tank, however, the evolution of the skewness and kurtosis of the velocity components was not discussed. Our RANDOM algorithm (also called the “sunbathing” algorithm) generates turbulent flow with a relatively high Reynolds number ($Re_T = 2360$) and the largest reported integral length scale ($\ell = 11.5$ cm) for a random jet array. These results validate the versatility of random jet arrays and their ability to be scaled up and continue to generate approximately homogeneous isotropic flow with negligible mean flow. Lastly, the present tabulation and review of the 9 driving algorithms studied herein, including those not deemed optimal, may be used by future researchers who require certain specific characteristics in a flow (e.g. large kurtosis/high levels of intermittency) and who may be less concerned with those that were the focus of the present research (e.g. zero-mean flow).

4.7 Appendix. Sources of error and uncertainty analysis

The purpose of this section is to describe the potential sources of error and quantify their effect on the results. It is important to note that the total uncertainty arises from the i) ADV uncertainty, and ii) propagation of the ADV uncertainties due to the corrections performed.

The analysis that follows considers each potential source of error in the velocity measurements conducted by acoustic Doppler velocimetry. The uncertainty analysis models of Voulgaris and Trowbridge (1998) and Taylor (1997) are used to estimate the uncertainty. The sources of error are then combined to calculate the uncertainty in each component of the velocity. Finally, the total relative uncertainty resulting from the propagation of the ADV uncertainty is calculated.

4.7.1 Acoustic Doppler velocimetry uncertainties

Voulgaris and Trowbridge (1998) identified three sources of error for the total velocity along each receiver beam (σ_t): i) sampling error (σ_m), caused by the inability of the system to resolve the phase shift of the return pulse, ii) Dopler noise (σ_D), due to random scatter motions within the sample volume, and iii) error resulting from the mean velocity shear within the sampling volume (σ_u). σ_u becomes important in the presence of sharp velocity gradients (e.g. in boundary or mixing layers). However, in homogeneous flows like those produced by our algorithms, the mean velocity gradients are negligible far enough from the RJA. Thus, the mean velocity shear error was neglected in our calculations. In the following sections the sampling and Doppler errors are calculated individually. The calculations are made for the RANDOM algorithm at the three downstream positions investigated (similar results are obtained for the other algorithms, but not presented herein).

Sampling error

Sampling error results from the inaccuracy of the A/D converter (in the ADV system) in resolving the changes in phase of the return pulse and the noise induced by the electronics. This error is independent of the flow and depends on the velocity range employed when operating the ADV. During our experiments the ADV's ±0.3 m/s velocity range was used for the velocity measurements at *x*/M= 5.5 and 6.7, while the ±0.1 m/s velocity range was used for the measurements at *x*/M=9.3. The sampling error can be calculated as (Voulgaris and Trowbridge, 1998):

$$\sigma_m^2 = \frac{c^2}{4}\frac{1}{f^2}\frac{1}{4\pi^2}K^2\sigma_s^2\frac{1}{\tau}\frac{1}{(T-t_0)} \ , \tag{4.1}$$

where c is the speed of sound in water (1481 m/s at 20 ˚C), f is the operating frequency of the ADV (10 MHz), K is an empirical constant (1.4, Zedel *et al.* 1996), σ_s^2 is the system's uncertainty to resolve the phase (1.08 and 0.63 for the ±0.3 and ±0.1 m/s velocity range, respectively), τ is the time between transmissions (4.35 and 5.55 ms for the ±0.3 and ±0.1 m/s velocity range, respectively), T is the inverse of the sampling frequency (0.04 s at a sampling frequency of 25 Hz), and t_0 is the time required by the system to carry out the necessary conversions (2 ms). The calculated sampling error is shown in the following table.

Algorithm	*x*/M	ADV's velocity range (m/s)	σ_m^2 (m^2/s^2)
RANDOM	5.5	± 0.3	1.78E-06
	6.7	± 0.3	1.78E-06
	9.3	± 0.1	8.13E-07

Table 4.5 Calculation of sampling error (σ_m^2).

Doppler noise

Doppler noise (an intrinsic feature in Doppler acoustic systems) is caused by: i) the finite residence time of the particles in the sampling volume, ii) turbulence within the sampling volume, and iii) beam divergence. Voulgaris and Trowbridge (1998) presented the following equations for the calculation of the Doppler noise (σ_D^2):

$$\sigma_D^2 = \frac{\pi^{-1/2}}{16}\frac{c^2 B_D}{f^2\, M_{ADV}\, \tau}\ , \tag{4.2}$$

where M_{ADV} (=11) is the number of acoustic pulses averaged for the calculation of the radial velocity, and B_D is the total Doppler bandwidth broadening. B_D is the RMS of the three individual contributions of the bandwidth broadening due to the (as mentioned above) finite residence time (B_r), turbulence within the sample volume (B_t), and the beam divergence (B_d):

$$B_D^2 = B_r^2 + B_t^2 + B_d^2\ . \tag{4.3}$$

B_r, B_t, and B_d can be calculated using the following expressions:

$$B_r = 0.2\frac{U_h}{d}\ , \tag{4.4}$$

where U_h is the mean horizontal speed (i.e. $U_h = (\langle U\rangle^2 + \langle V\rangle^2)^{1/2}$) and d is the transverse size of the sampling volume.

$$B_t = 2.4\frac{f(\varepsilon d)^{1/3}}{c} , \tag{4.5}$$

where ε is the turbulence dissipation rate (estimated from u^3/ℓ , where u is the characteristic velocity and ℓ is the integral length scale, both calculated in section 4.5).

$$B_d = 0.84\sin(\Delta\theta)\frac{fU_c}{c} , \tag{4.6}$$

where Δθ is the angle bisector between the transmitter and receiver (15˚ for our system), and U_c is the cross-beam or transverse velocity component (⟨V⟩). The following table summarizes the quantities used to ultimately calculate σ_D^2:

Algorithm	*x*/M	B_r (1/s)	B_t (1/s)	B_d (1/s)	σ_D^2 (m^2/s^2)
RANDOM	5.5	3.5E-02	168.77	0.22	2.73E-06
	6.7	1.4E-02	127.64	0.11	2.06E-06
	9.3	9.6E-02	82.49	4.58	1.05E-06

Table 4.6 Calculation of the Doppler noise (σ_D^2)

Uncertainty for the acoustic Doppler velocimetry measurements.

The total uncertainty of the ADV measurements is calculated assuming random independent errors. It can be calculated using the following equation (Taylor, 1997):

$$Total\ Uncertainty\ = \sqrt{(Uncertainty_1)^2 + (Uncertainty_2)^2 + (Uncertainty_3)^2 + \cdots} \tag{4.7}$$

The total velocity uncertainty ($\sigma_{t\text{-}RMS}^2$) for the RMS velocity along each receiver beam of the ADV can then be calculated as the sum of the sampling error (σ_m^2) and the Doppler noise (σ_D^2). Recall that the error due to the mean velocity shear is negligible, thus $\sigma_{t\text{-RMS}}^2 = \sigma_m^2 + \sigma_D^2$, which is tabulated below:

Algorithm	x/M	$\sigma_{t\text{-RMS}}^2$ (m^2/s^2)
RANDOM	5.5	4.51E-06
	6.7	3.84E-06
	9.3	1.86E-06

Table 4.7 Calculation of the total velocity uncertainty for the RMS along each receiver ($\sigma_{t\text{-RMS}}^2$)

We can assume that σ_t^2 is the same along each receiver beam if the receiver transducers are identical and ideal. Under this assumption, the uncertainty of the RMS velocity for each velocity component ($\sigma_{i\text{-RMS}}^2$) can be calculated using the ADV's transformation matrix. The following table presents the uncertainties for the three RMS velocity components.

Algorithm	x/M	$\sigma_{x\text{-RMS}}^2$ (m^2/s^2)	$\sigma_{y\text{-RMS}}^2$ (m^2/s^2)	$\sigma_{z\text{-RMS}}^2$ (m^2/s^2)
RANDOM	5.5	3.71E-05	3.66E-05	2.40E-06
	6.7	3.16E-05	3.12E-05	2.05E-06
	9.3	1.53E-05	1.51E-05	9.90E-07

Table 4.8 Calculation of the total uncertainty for each velocity component ($\sigma_{i\text{-RMS}}^2$)

We note the smaller uncertainty for the *z*-component of velocity (*w*), as previously discussed, as well as in Khorsandi *et al.* (2012).

4.7.2 Propagation of uncertainties

As mentioned in section 4.3, some corrections were applied to the calculated RMS velocities. The corrections included in some cases the combination of the three calculated

RMS velocities resulting in a propagation of the uncertainties. The RMS velocity in the *z*-direction was not modified and thus the corresponding uncertainty remains the same (i.e. $w_{\text{RMS}} = [\langle w^2 \rangle + \sigma_{z\text{-RMS}}{}^2]^{1/2}$). The RMS velocity in the *y*-direction was assumed to be the same as that of the *z*-direction due to the axisymmetric nature of the flow, then the uncertainty in *v* is the same as that of *w* (*z*-direction). On the other hand, the corrected RMS velocity in the *x*-direction was calculated using the three calculated RMS velocity components u_{RMS}, v_{RMS}, and w_{RMS} (each one with a corresponding uncertainty). The expression used in the correction of u_{RMS} (process described in section 4.3) is the following:

$$u_{c-RMS} = \left[u_{RMS}^2 - \frac{(a_{11}^2+a_{12}^2+a_{13}^2 + a_{14}^2)}{(a_{21}^2+a_{22}^2+a_{23}^2 + a_{24}^2)}(v_{RMS}^2 - w_{RMS}^2)\right]^{1/2}, \qquad (4.8)$$

where $u_{\text{c-RMS}}$ is the corrected RMS velocity, and a_{ij} are elements of the transformation matrix. The total relative uncertainties for the RMS velocities were calculated performing a step-by-step analysis of uncertainty propagation (Taylor, 1997). The final results are presented in the following table:

Algorithm	*x*/M	% u_{RMS} error	% v_{RMS} error	% w_{RMS} error
RANDOM	5.5	2.81	0.33	0.33
	6.7	3.18	0.37	0.37
	9.3	4.49	0.35	0.35

Table 4.9 Calculation of the total relative uncertainties for the RMS velocity components.

The table above shows that the total relative uncertainty for the RMS velocity is less than 5% in any given direction, being the largest for the *u*-component of the velocity.

Chapter 5

Effect of background turbulence on the scalar field of a turbulent jet

The effect of background turbulence on the mixing of a high-Schmidt-number scalar within a turbulent jet was investigated. The present study builds on the work of Gaskin *et al.* (2004), who studied the concentration and velocity fields of a plane jet in a shallow coflow with different turbulence levels and Khorsandi *et al.* (2013), who studied the velocity field of an axisymmetric turbulent jet emitted into a turbulent background with zero mean flow. Nearly homogeneous isotropic background turbulence with negligible mean flow was generated by a random jet array using the optimal driving algorithm RANDOM (described in Chapter 4). Concentrations measurements of a passive scalar within the jet were obtained employing laser induced fluorescence for two jet Reynolds numbers. The results showed increased i) rates of decay of mean concentration, ii) widths and iii) root-mean-square concentrations for the jets emitted into a turbulent background. In the presence of background turbulence, the maximum concentrations were on the same order of those of the jet issued into quiescent surroundings. Visualizations of the jet emitted into a turbulent background revealed a complicated mechanism of entrainment and mixing which, with the destruction of the jet structure, changes from jet driven entrainment to become potentially dominated by i) increased lateral advection of the jet by large scales of the turbulent background during the meandering of the jet, which is subsequently mixed by its smaller scales, and ii) turbulent diffusion significantly enhanced by the turbulent background. The evolution of the velocity (Khorsandi *et al.* 2013) and scalar fields was similar although the radial extents of the profiles of the concentration were larger than those of the velocity.

5.1 Introduction

The study of the transport of passive scalars by turbulent flows has been an active area of research given its ultimate applications to natural and industrial phenomena such as environmental pollutant dispersion, chemical mixing, and combustion. The disposal of man-made waste often occurs by means of a turbulent jet emitted into the atmosphere or hydrosphere. The reduction of the damage to both the environment and human health relies on the dilution of the pollutants (by entrainment and mixing) with the ambient fluid. Hence, accurate predictions of the concentrations of pollutants downstream of the point of release are beneficial for the conservation of the ecosystem and improvement of human life. Nevertheless, the vast majority of previous studies of turbulent jets considered jets issuing into quiescent or laminar surroundings, such that their results may not be appropriate for applications to more realistic flows such as a plume emitted from a smokestack into the (turbulent) atmosphere. Although the standard assumption has been that turbulence in the background will increase dilution, recent experimental results (Gaskin *et al.* 2004 and Khorsandi *et al.* 2013) support the hypothesis that external forcing of the jet/plume (e.g. ambient turbulence) will reduce entrainment (Hunt,1994). The present investigation is aimed at further understanding scalar mixing in complex flows (both natural and man-made) and complementing previous studies. We discuss herein the results of the scalar field of a jet emitted into a turbulent background. However, before discussing the results, we briefly review turbulent jets issued into quiescent backgrounds and the few relevant works involving jets emitted into turbulent backgrounds.

The axisymmetric jet is a free shear flow with dominant mean motion in the axial direction, spreading of the jet in the radial direction, and zero mean velocity in the azimuthal direction. The velocity field of an axisymmetric jet discharging into a quiescent background has been investigated extensively and its behaviour is well documented (Wygnanski and Fiedler 1969; Panchapakesan and Lumley 1993a; Hussein *et al.* 1994; Xu and Antonia 2002; Lipari and Stansby 2011; Darisse *et al.* 2015; and the references therein). At some distance downstream (after the so-called developing region), the jet becomes self-similar and the axial mean velocity profile is approximately Gaussian. Under self-similar conditions, the centerline mean velocity of an axisymmetric turbulent jet decays as x^{-1} and the half-width of the velocity field (defined as the radial distance at which the mean axial velocity decays to half of its centerline value) increases as x^1. The profiles of the root mean square (RMS) of the axial velocity fluctuation also become self-similar farther downstream and the RMS velocity at centerline, normalized by the mean centerline velocity, asymptotes to a constant (~0.25). Moreover, a theoretical analysis (assuming self-similarity) supports the observed scaling of the mean axial velocity and half-width (see Tennekes and Lumley 1972, and Pope 2000).

Extensive experimental investigations of the passive scalar field in turbulent jets issuing into a quiescent background have also been carried out (Wilson and Danckerts 1964; Becker *et al.* 1967; Birch *et al.* 1978; Lockwood and Moneib 1980; Dahm and Dimotakis 1987, 1990; Dowling and Dimotakis 1990; Miller and Dimotakis 1991a, 1991b, 1996; Panchapakesan and Lumley 1993b; Yoda *et al.* 1994; Buch and Dahm 1996; Catrakis and Dimotakis 1996; Law and Wang 2000; Antoine *et al.* 2001; Su and Clemens 2003; Darisse *et al.* 2015). The results showed that regardless of the Schmidt number of the scalar ($Sc = \nu/\mathcal{D}$, where ν is the fluid's kinematic viscosity and $\mathcal{D}$ is the molecular diffusivity of the scalar), the scaling of the concentration field quantities are similar to those of the velocity field. The profiles of mean and RMS concentration become self-similar, the mean centerline concentration follows an x^{-1} decay, and the half-width of the scalar field increases as x, although some differences with the velocity field are observed. The most notable variations are: i) the mean and RMS radial profiles of the concentration field are wider than those of the velocity field, ii) the rate of increase of the half-width of the mean concentration is larger than that of the velocity field, and iii) the value of the centerline RMS concentration, normalized by the mean centerline concentration, reaches a slightly lower value (~0.22) than that for the velocity field (Law and Wang 2000; Antoine *et al.* 2001).

In jets of an incompressible fluid emitted into quiescent backgrounds, the increase in the jet's width in the axial direction is accomplished by the inclusion of ambient fluid to the mean flow of the jet (entrainment). In the case of turbulent jets emitted into quiescent backgrounds, ambient fluid is transformed into turbulent flow. Assuming self-similarity, the entrainment hypothesis first presented by Morton *et al.* (1956) models the entrainment flow as proportional to a characteristic velocity at each location of the jet ($Ve=\alpha u_m$) and being due to a constant entrainment velocity (V_e) normal to the surface of the jet boundary. The local characteristic velocity is the centerline velocity (u_m) and α is a constant of proportionality, known as the entrainment coefficient. The entrainment hypothesis proposes an inflow into the jet to explain the increase in volume flux with axial distance, but it does not give any information about the entrainment mechanism.

The two most common hypotheses pertaining to the mechanisms of entrainment involve different scales. On one hand, the equilibrium hypothesis describes entrainment as a cyclical large-scale process in which large eddies engulf big volumes of fluid (Townsend 1966). On the other hand, the superlayer hypothesis proposes that the transformation of ambient fluid to turbulent flow is accomplished by viscous effects through a narrow surface of thickness on the order of the Kolmogorov length scale (Corrsin and Kistler 1955), separating the turbulent flow and ambient fluid. Across this thin interface, called the "laminar superlayer," the transport of vorticity (which distinguishes turbulent flows from laminar ones) occurs by the action of viscous forces. (In recent years, the bounding surface between the turbulent flow and ambient fluid has been referred as the turbulent/nonturbulent interface (TNTI) and the small-scale process has been termed nibbling.) Early works based on flow visualizations and detection of periodic events of low values of velocity or concentration supported the notion of a large-scale dominated entrainment (Yule 1978; Long and Chu 1981; Dahm and Dimotakis 1987; Shlien 1987). However, recent investigations which take advantage of advances in computational and measurement techniques to detect the TNTI have shown nibbling to be the dominant entrainment mechanism (Mathew and Basu 2002; Westerweel *et al*. 2005, 2009; Wolf *et al*. 2012). In those studies, the detection of the TNTI involves applying a low-vorticity (or concentration) magnitude threshold to the instantaneous fields. The volume of the flow that acquires vorticity through the interface is subsequently quantified (*i.e.,* the fluid entrained by engulfment is detected by low vorticity or concentration values). The results showed that the entrainment process was dominated by small scales at the TNTI, with large-scale engulfment making a small contribution (for axisymmetric turbulent jets). Although the entrainment mechanism has been investigated for jets emitted into quiescent surroundings and the dominant mechanism has been identified, the presence of background turbulence disrupts the flow and may significantly change the entrainment mechanism given the loss of self-similarity and the fact that the quantities (e.g. vorticity, RMS velocity) do not rapidly drop to zero outside of the jet (Mathew and Basu 2002; Gaskin *et al.* 2004; Khorsandi *et al.* 2013).

The interaction of a turbulent flow (e.g. jet, wake, boundary layer) with a turbulent background further increases the complexity of the phenomena since the parameters of the external turbulence need to be considered. Relevant parameters pertaining to the turbulent background can include: i) mean flow advection, ii) density stratification, iii) turbulence intensity, and iv) length scales of the background turbulence. Due to the difficulty in accounting for all the mentioned parameters, researchers have focused on the study of their individual effects on fundamental flows. Certain experimental works have studied the effect of the levels of turbulence of the surroundings on the evolution of boundary layers, wakes, plumes and jets. The emphasis on the study of the intensity of the background turbulence was chosen to isolate the effect of the turbulent fluctuations on the flows' structure.

External turbulence in turbulent boundary layers and wakes is imposed through the free-stream flow and its intensity quantified as u'/U_∞, where u' is the RMS of the velocity fluctuations and U_∞ is the mean external velocity. In boundary layers, velocity measurements and flow visualizations have shown that turbulent free streams resulted in a flatter boundary layer and larger RMS velocities than those of a turbulent boundary layer with laminar free streams (Hancock and Bradshaw 1983, 1989; Thole and Bogard 1996). These results were associated with increased mixing due to the presence of the external turbulence and were confirmed by Hancock and Bradshaw (1989), who heated the plate (used to generate the boundary layer) and detected cold fluid deep within the boundary layer. Comparing the velocity spectra at different distances from the wall also revealed similarity with the spectra of the external turbulence which is associated with penetration of the external turbulence deep into the boundary layer (Thole and Bogard 1996; Sharp *et al.* 2009). In the case of wakes, the general effects of the external turbulence on the velocity field were an increased rate of decay of the centerline velocity defect (resulting in a reduction of the length of the wake), higher RMS velocities, and a wider wake than in a laminar external flow (Bagchi and Balachandar 2004; Legendre *et al.* 2006; Amoura *et al.* 2010; Eames *et al.* 2011). Bagchi and Kottam (2008) used direct numerical simulation (DNS) to investigate the heat transfer on the surface of a sphere in a turbulent stream. The results showed that the thermal wake was shortened and the half-width of the wake was increased due to the enhanced mixing produced by the external turbulence.

In the case of turbulent jets, external turbulence has generally been imposed by either a turbulent co-flowing stream or as background turbulence with zero mean flow. There are two principal hypotheses on the effect of background turbulence on turbulent jets. The standard assumption, assumed to be a conservative estimate for practical applications, was superposition of the dilution effects of the jet and of the turbulent surroundings. Wright (1994) proposed a model in which an additional term in the entrainment coefficient lead to increased rates of entrainment into the jet. Hunt (1994) argued that if the intensity of the external turbulence were high enough to disrupt the self-preserving structure of the jet, it would cause a reduction in the entrainment and thus in the rate of spreading of the jet.

There exists experimental work in support of both predictions. Wright (1994) observed increased dilution in co-flowing jets as the turbulence of the ambient flow was increased by changing the bottom roughness of a channel. This effect was observed to start near the jet outlet, indicating that the external turbulence could influence the jet mixing even when the jet velocity is dominant. The effect of grid-generated turbulence on plumes (Ching *et al.* 1995), momentum dominated jets (Guo *et al.* 1999, 2005; Law *et al.* 2001) and buoyant jets (Cuthbertson *et al.* 2006) has also been investigated. In these works the oscillating grid was oriented perpendicularly to the jet/plume axis. The results of the velocity field and flow visualizations showed an abrupt increase in the dispersion of the jet/plume at certain distance from the source. These observations were associated with increased rates of entrainment and the break-up location of the plume/jet. However, although the use of oscillating grids oriented perpendicular to the axis of the plume/jet creates a considerable increase in the dilution, the support of a superposition of effects can be challenged by the fact that the background turbulence is increasing in the direction of decreasing of the plume/jet turbulence (Gaskin *et al.* 2004). Lavertu (2006) included measurements of the effect of a turbulent background in his study of differential diffusion in turbulent jets employing laser-induced fluorescence (LIF). Although velocity measurements were not performed, it was hypothesized that the measured increases in differential diffusion could be attributed to an increase in the entrainment due to the ambient turbulence.

The first evidence in support of Hunt's prediction of a reduction in entrainment due to the presence of background turbulence is that of Gaskin *et al.* (2004), who studied the effect of background turbulence on the velocity and scalar fields of co-flowing plane jets. The results showed that the external turbulence increased the rate of decay of the velocity and reduced the dilution (or entrainment), with the effects being more marked and starting closer to the jet outlet with increasing ambient turbulence intensity. In addition, the entrainment changed from large scale engulfment to turbulent diffusion by the smaller scales of the background turbulence once the background turbulence disrupted the jet structure. The effect of nearly homogeneous, isotropic zero-mean-flow background turbulence on the velocity field of turbulent axisymmetric jets was studied by Khorsandi *et al.* (2013). In this work, the jet was oriented such that the level of background turbulence along the axis of the jet was constant (unlike previous studies). The results showed that in addition to increased decay rates of the mean axial velocities, jet widths, and RMS axial velocities in the presence of background turbulence, the mass flow rate of the jet decreased compared to the quiescent case. The latter is an especially interesting finding since it was associated with lower entrainment into the jet and confirms the results of Gaskin *et al.* (2004). The reduced mass flow rates of a jet emitted into a turbulent background may imply lower levels of scalar mixing. Additionally, based on the results of the velocity field, Khorsandi *et al.* (2013) hypothesized a change in the entrainment mechanism from a small-scale (nibbling) process in a quiescent background to one dominated by turbulent diffusion at the interface of the jet and ambient flow.

The present investigation builds on the work of Gaskin *et al.* (2004) and complements the work of Khorsandi *et al.* (2013). We examine the effect of an approximately homogeneous, isotropic, zero-mean-flow turbulent background on the scalar field of a turbulent jet complimenting the velocity field investigation of Khorsandi *et al.* (2013). To this end, we measured the concentrations of a high-Schmidt-number passive scalar within the jet by means of planar laser-induced fluorescence. Herein, we present the results pertaining to the scalar field of a jet emitted into a turbulent background to further our understanding of the effect of background turbulence on the mixing of a passive scalar within a jet, as well as any change in entrainment mechanism.

5.2 Experimental method

The purpose of this section is to describe the turbulent background, the jet setup, and the LIF apparatus. Both the background and jet conditions were identical to those of Khorsandi *et al.* (2013) and the reader is referred to Khorsandi (2011) for details beyond those provided herein.

5.2.1 Background conditions

The experiments investigated the effect of background turbulence on the scalar field of a turbulent jet by comparing the results of a jet issued into a quiescent background with those of a jet emitted into a turbulent background. They were carried out in a $1.5\times2.4\times0.9$ m^3 section of a glass tank ($1.5\times6\times0.9$ m^3) in the Environmental Hydraulics laboratory in the Department of Civil Engineering and Applied Mechanics at McGill University. The tank was filled with water and its top was open to the ambient air. When experiments in quiescent conditions were performed, the tank was slowly filled with water and sufficient time (around 1.5 hours) was given for the water to come to rest. When experiments in a turbulent background were performed, a random jet array (RJA) was used to produce an approximately homogeneous, isotropic, zero-mean turbulent flow in the 1.5×2.4×0.9 m^3 section of the tank. The jet array is based on that of Variano and Cowen (2008), but built to a larger scale. The RJA consists of an array of 6×10 bilge pumps (Rule 25D, 500 GPH) equally spaced in the horizontal and vertical directions (with a center-to-center distance (M) of 15 cm), attached to a 1 m by 1.5 m vertical sheet of high density polyethylene (Figure 5.1). A polyvinyl chloride (PVC) elbow joint (Spears 1407-010) was attached to the outlet of each pump to change the direction of the flow upon its exit from the pumps. Moreover, a male adapter (Spears 436-132) and a 15 cm long PVC extension (3.18 cm in diameter) were connected to each pump to expand the outlet diameter and straighten the flow. Thus, the pumps draw in water from their base (adjacent to the polyethylene sheet) and discharge it from the PVC extension at a distance of 24 cm from the plane of the polyethylene sheet. Since the suction and discharge occur simultaneously into the same fluid volume, there is a zero net mass flow rate in a control volume containing the pump and extension. This is an essential aspect of generating the zero-mean flow within the tank.

The distance of the center of the jets at the edges of the array to the glass side walls and free surface was chosen to be 0.5M, to obey symmetric boundary conditions to minimize possible secondary flows, in analogy with oscillating grid turbulence (Fernando and De Silva 1993).

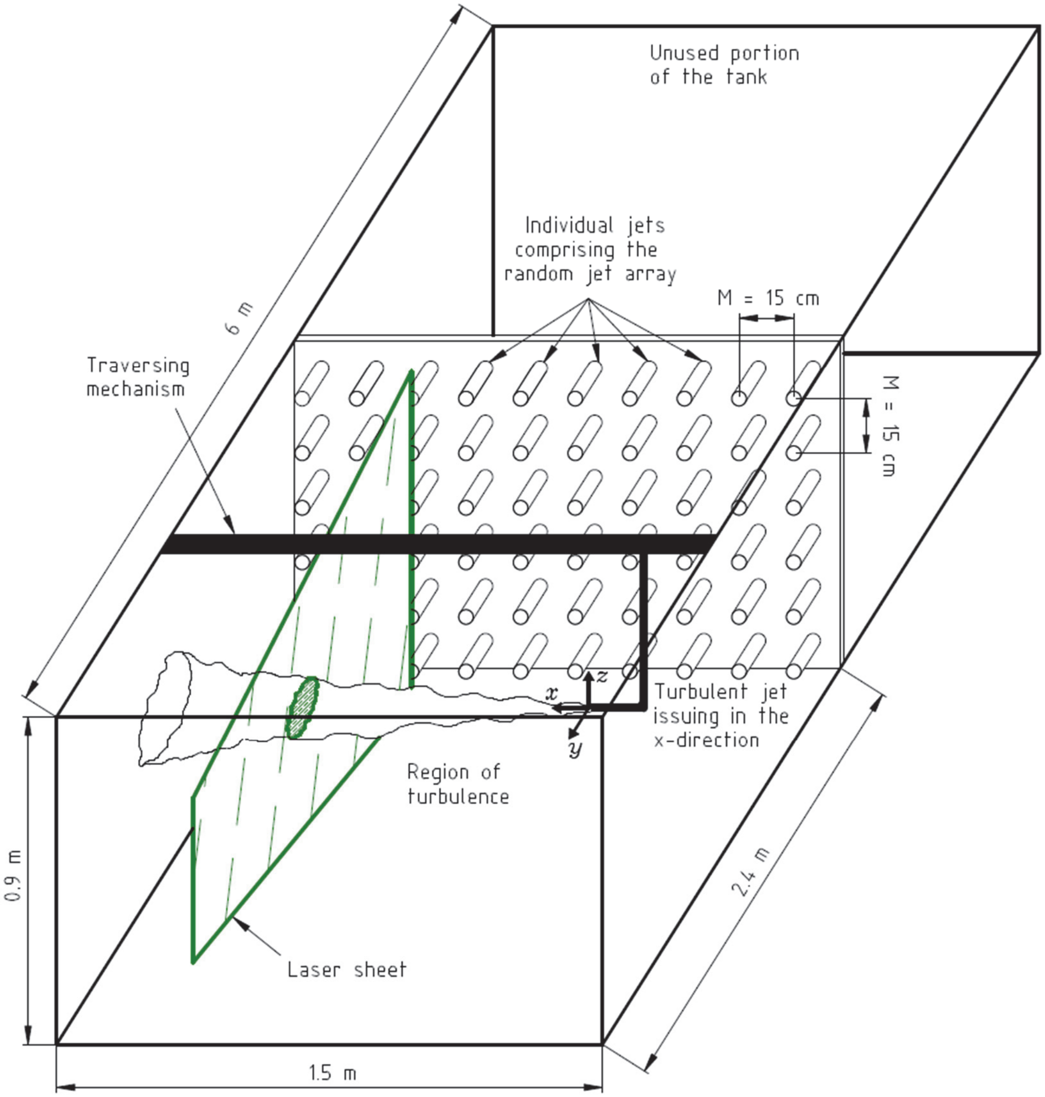

Figure 5.1 Schematic of the tank, RJA, jet and laser sheet (not to scale).

The random jet array was controlled using a custom algorithm programmed in LabVIEW, which independently turned the pumps on and off. The ability to independently operate and control each pump allowed the exploration of different driving algorithms to generate the closest approximation of a homogeneous, isotropic, zero-mean flow turbulent background. The “optimal” algorithm, called RANDOM, generated the flow with the lowest mean flow, high degrees of isotropy, and high RMS velocities. Details of the operation of the different algorithms tested and their generated flows can be found in Perez-Alvarado *et al.* (2016). The operation of the RANDOM algorithm is similar to the driving algorithm proposed by Variano and Cowen (2008) for their RJA, which they termed the “sunbathing” one. When the RANDOM algorithm is used, the state (i.e. “on” or “off”) of each pump is independently and randomly changed. The on and off times are random values determined from normal distributions with adjustable means (μ) and standard deviations (σ). In this situation, each pump is individually turned on for a randomly selected interval and then forced to turn off during a new randomly chosen amount of time, with the process being repeated indefinitely. Several variations of mean on times, mean off times, and standard deviations were investigated in the same experimental facility by Lavertu (2006), Khorsandi (2011), and Perez-Alvarado *et al.* (2016). The optimal values for the present RJA were found to be (μ_{on}, σ_{on}) = (12 ,4) seconds and (μ_{off}, σ_{off}) = (108, 36) seconds. These parameters maintain, on average, 10% of the pumps working at any given instant in time. Downstream of the jet array, the jets merge, generating a region of turbulence that slowly decays in the direction normal to the plane of the jet array. The inhomogeneity of the background turbulence across the turbulent jet in the y-direction is small. For example, for measurements made at x/D=50 in a jet emitted into a turbulent background, the turbulent kinetic energy decays by 6% over a distance equal to the jet half-width. Although the turbulence is slowly space decaying in the y-direction, the results of the scalar field are furthermore presented along transects in the vertical direction to ensure a constant intensity of the external turbulence. (The results indeed showed symmetry in the vertical direction.) Table 5.1 summarizes the statistics of the generated turbulence at the measurement section located at a distance of 110 cm (y/M = 7.3) from the PVC extensions of the RJA. At this plane the velocity measurements showed that the turbulence generated by the RJA was nearly homogeneous isotropic with zero-mean flow. Further details of the flow produced can be found in Khorsandi (2011) and Khorsandi *et al*. (2013).

u_α	$\langle U_\alpha \rangle$ [cm/s]	$u_{\alpha\text{-}RMS}$ [cm/s]	$\frac{\langle U_\alpha \rangle}{u_{\alpha\text{-}RMS}}$	Anisotropies			S	K	$\frac{1}{2}\langle u_i u_i \rangle$ [cm^2/s^2]	ℓ [cm]
				$\frac{u_{RMS}}{u_{\alpha\text{-}RMS}}$	$\frac{v_{RMS}}{u_{\alpha\text{-}RMS}}$	$\frac{w_{RMS}}{u_{\alpha\text{-}RMS}}$				
u	0.03±0.18	1.53±0.02	0.07±0.08	1	1.36	0.97	0.07±0.16	4.51±0.01	4.44±0.15	11.6
v	-0.30±0.17	2.08±0.14	-0.15±0.10	0.73	1	0.72	1.43±0.12	5.73±0.66		
w	0.10±0.10	1.49±0.05	0.07±0.07	1.03	1.40	1	-0.18±0.08	4.05±0.21		

Table 5.1 Statistics of the background turbulence at the measurement section located 110 cm from the RJA (y/M=7.3). The integral length scale, $\ell \equiv \int_0^\infty \rho_{uu} dx$, is calculated from the spatial autocorrelation of u (ρ_{uu}).

5.2.2 Turbulent jet setup

The jet was placed in the tank so as to discharge horizontally (in the x-direction) in a plane parallel to the RJA (Figure 5.1). The jet apparatus consisted of a supply reservoir, a pump, a constant head reservoir, traversing mechanism, and several jet components (Figure 5.2). The design of this setup allowed one to i) maintain a constant flowrate through the jet during the experiments, ii) easily vary the Reynolds number of the jet, and iii) place and align the turbulent jet in the tank.

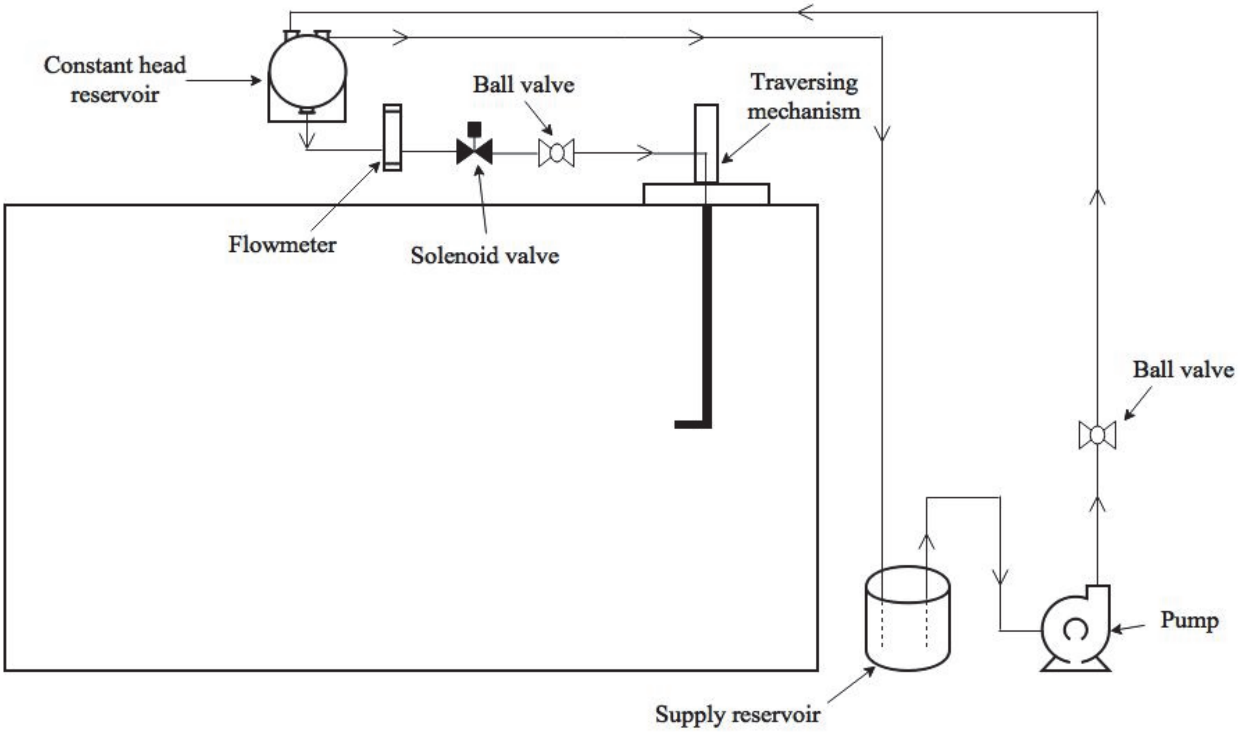

Figure 5.2 Schematic of the jet setup (not to scale).

The supply reservoir was a 35 liter glass cylindrical container placed outside of the tank. The supply reservoir was used to prepare the mixture of fluorescent dye and water before commencing the experiments. It also served as an overflow reservoir for the dyed water pumped to the constant head tank. A 1/3 hp pump was used to continuously pump dyed fluid during the experiments from the supply reservoir to the constant head tank through plastic tubing. A ball valve connected at the outlet of the pump controlled the flowrate towards the constant head tank. The constant head reservoir consisted of a 12 liter spherical glass container positioned approximated 2 m above the tank. It was used to maintain a constant pressure difference to drive the jet flow and hence maintain a constant jet Reynolds number during each experiment. The water from the constant head reservoir was directed to the jet through plastic tubing. Prior to reaching the jet, the dyed water passed through a flowmeter, a solenoid valve, and a ball valve. A flowmeter (Omega FL50002A) was used to read the actual flowrate through the jet. A solenoid valve (placed immediately after the flowmeter) was used to turn the jet on or off during the experiments. The solenoid valve controller was placed near the supply reservoir to allow remote control of the jet flow. Finally, a ball valve was used to adjust the flowrate towards the jet to achieve the desired Reynolds number. This ball valve along with the flowmeter were employed to set the flowrate for the experiments. The flowrates during the experiments were either 2.2 L/min or 4 L/min, corresponding to jet Reynolds numbers ($=UD/\nu$, where U is the velocity at the jet exit, D is the nozzle diameter, and ν is the kinematic viscosity of water) of 5,800 and 10,600 respectively (with $\nu = 1\text{x}10^{-6}$ m^2/s and D = 8 mm).

The jet consisted of a copper pipe of 8 mm inner diameter. The copper pipe extended vertically for 1.6 m and followed by a 90° bend that allowed the jet to discharge horizontally in the tank. After the 90° bend, the 8 mm pipe extended for 0.12 m, resulting in fully developed flow in the pipe at the jet exit. The jet's axis was located 45 cm below the free surface (*i.e.* at the half-depth of the water level). Since the turbulence generated by the RJA decays in the direction normal to the plane of the RJA, the turbulent jet issued horizontally (in the x-direction), in a plane parallel to the RJA to ensure a constant level of background turbulence along the axis of the jet. During the experiments the jet was located at a distance of 110 cm (y/M = 7.3) from the tip of the PVC extensions of the RJA.

5.2.3 Laser induced fluorescence (LIF) apparatus

Planar LIF was employed to obtain concentration measurements within radial cross-sections of the turbulent jet emitted into both quiescent and turbulent backgrounds. The LIF apparatus consisted of the laser sheet generation system and the signal detection system, which were aligned perpendicularly (facing different sides of the tank). The laser sheet generation system comprised a laser, some mirrors and the laser scanning device. The signal detection system consisted of an (optical) filter, an image intensifier and a camera. The schematic of the LIF system used in this investigation is shown in Figure 5.3.

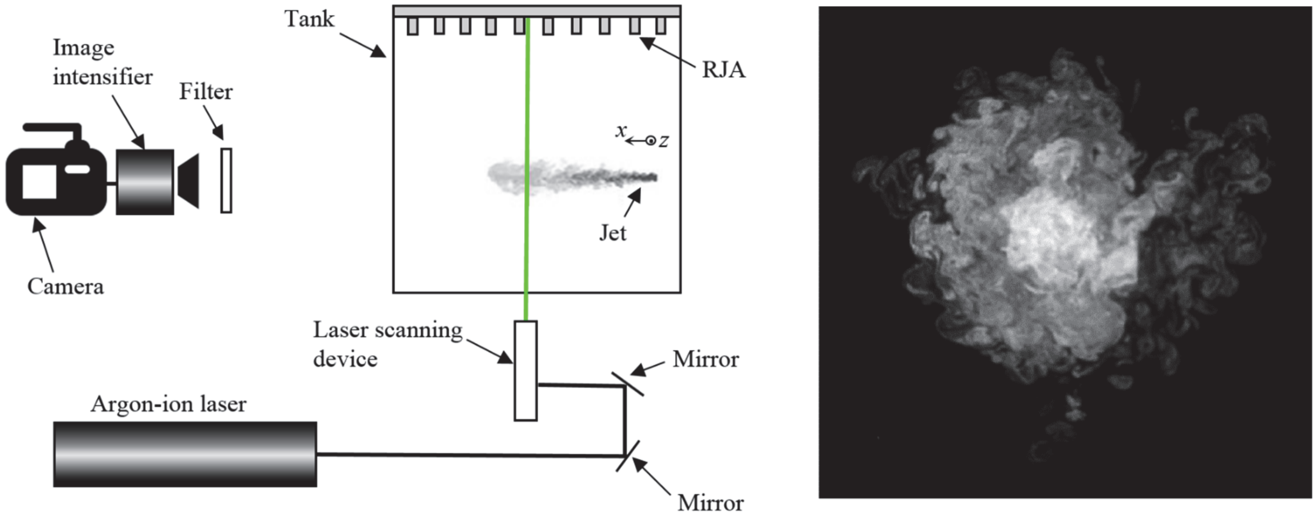

(a) (b)

Figure 5.3 (a) Schematic of the planar LIF system (top view). (Not to scale.) (b) An example of an LIF image.

A laser beam originating from an argon-ion laser (Coherent Innova 90) was used to excite the fluorescent dye at the measurement location, making it fluoresce. The laser was operated in the light regulated mode since this mode provided a stable output power (± 0.5% as estimated by the manufacturer). The aperture of the laser was set to 3.97 mm and the emanating beam was Gaussian in its cross-section. The laser was operated in single-line mode at a wavelength of 514.5 nm and an output power of 1 W. To ensure stability of its power in the long-term, the laser was warmed up for 60 minutes before commencing the experiments and its power output was monitored at the beginning and end of each test (the variation was less than 2% for all experiments). Upon exiting the laser, the beam was directed to the laser scanning device using two mirrors (Melles Griot 02MLQ003/009). A laser scanning device was used to focus the laser beam at the measurement location and produce the laser sheet for the planar measurements of concentration. The laser scanning device consisted of a mirror, a focusing lens and a rotating mirror, which were aligned and enclosed in an aluminum box. After entering the laser scanning device, the beam was reflected from a 12.7 mm dielectric mirror (Newport 5151) to reach the focusing lens. The focusing lens was a 1.5 m focal length plano-convex lens (PLCX-25.4-772.6-C). It focused the beam down to a waist diameter of 470 µm at the focal point and the Rayleigh range (defined as the distance at which the focused beam increases to $\sqrt{2}$ times the waist diameter) was 22.7 cm. After crossing the focusing lens, the beam reached the rotating mirror (Lincoln Laser Company DT-08-236-019). It consisted of an 8-sided polygonal mirror coupled to a motor. The motor was set to rotate at its maximum rate of 12000 rpm. The spinning of the mirror rapidly scanned the laser beam through the measurement area, effectively producing a laser sheet. The proper alignment of all the elements enable the generation of a laser sheet perpendicular to the axis of the turbulent jet (Figure 5.1).

The signal collection system was comprised of an optical filter, an image intensifier and a camera. These elements were aligned perpendicularly to the generated laser sheet. To ensure a correct alignment, they were secured along a 69 cm long optical rail. The fluorescence signal first reached a 25 mm diameter 550 nm longpass color filter (ThorLabs FGL550) attached to the camera lens (F-Micro-Nikkor 55mm f/2.8). The filter was attached to the front of the camera lens to block any scattered laser light, thus transmitting only fluorescence signal through the lens. Due to the characteristic low signal emitted by the fluorescent dye, an image intensifier (Video Scope VS4-1845) was employed to increase the sensitivity of the system. The image intensifier was coupled to the camera using a C-mount adapter so that the intensified signal was recorded by the camera. A 12-bit monochrome camera (pco.dimax) was used to record instantaneous images of a cross-section of the dye-containing jet. The camera has a 2016×2016 pixel resolution. Each data image obtained was a matrix whose elements contained the intensity of the light collected by each pixel and subsequently converted to concentrations. The coupling of the intensifier and camera reduced the size of the signal detection area to a central circular region of 800 pixels of radius. Additionally, the coupling caused the effective circular area to be more sensitive at the center (*i.e.* the central region reaching the saturation level of 4096 counts faster than the edges). However, a pixel by pixel calibration revealed that it did not affect the measurements of concentration and the only effect of the coupling was that only a portion of the whole dynamic range (0-4096 counts) was covered by the pixels away from the center of the image in the experiments.

The dye used in the experiments was disodium fluorescein, having a Schmidt number of 2000. Dilute dye concentrations (0.2 to 0.7 mg of disodium fluorescein mixed with 30 liters of water in the supply reservoir) were used to feed the jet. Dilute dye concentrations were desirable to ensure that the emitted fluorescence was within the linear range, prevent significant density differences with the ambient fluid, reduce the possibility of trapping (absorption of emitted fluorescence at another location), and minimize attenuation (decrease of the laser beam intensity along its path due to absorption of energy by the dyed fluid). Similar tests to those of Lavertu (2006) and Lavertu *et al.* (2008) were performed to confirm the negligible effect of the mentioned phenomena on the concentration measurements. The fluorescent dye is sensitive to external sources of light (with even the normal room lighting affecting its emitted fluorescence). Thus the lights of the laboratory were turned off before handling the dye and its mixing with water in the supply reservoir prior to the experiments, minimizing degradation of the dye. Additionally, the experimental apparatus was located in a darkroom, which ensured negligible background light, thus reducing any possible interference of external light with the measurements. Similarly, reflections of the emitted light from the fluorescent dye was minimized since the walls, floor and ceiling were painted black.

5.2.4 Data acquisition and post-processing

In the LIF setup, instantaneous images of cross sections of the dye-containing jet were recorded with a 12-bit monochromatic camera (pco.dimax). The camera was controlled by an external computer using a software package (Camware) provided by the camera supplier. During the experiments and calibrations, data was acquired at 30 frames per second with an exposure time of 30 ms and zero delay of the exposure. Each data image obtained was a 2016×2016 matrix whose elements contained the intensity of the light collected by each pixel. The image was focused such that each pixel covered an area of 250×250 μm^2 at the measurement plane. The acquired images were first stored in the internal memory of the camera, and then transferred to the hard disk of the external computer. The length of each experiment was limited by re-entrainment of dyed fluid into the jet (which would result in overestimated concentrations). Preliminary tests showed that 3 minutes were sufficient to acquire data before re-entrainment occurred. This time was also short enough to avoid filling the internal memory of the camera. Thus, the experiments lasted a maximum of 170 seconds allowing approximately 5000 images to be recorded in each test. The results showed that for a jet emitted into a quiescent background, data from one experiment was sufficient to ensure convergence of the mean and RMS concentrations at each axial location. On the other hand, 25000 to 35000 images were necessary for the jet emitted into a turbulent background. Hence 5 to 7 experiments were performed at each axial position in this latter situation. Images of cross sections of the jet were obtained at the following axial distances from the jet exit: x/D = 10, 20, 30, 40, 50, 60 and 70 (where D is the diameter of the nozzle). The size of each data file containing all the images of one experiment was around 44 GB. Due to the large size of each data file, the results were saved in external hard drives for post-processing. The post-processing was performed in an external computer using custom codes programmed in MATLAB to obtain the different results.

5.3 Validation of concentration measurements

In this section the experimental results pertaining to the concentration field within a turbulent jet emitted into a quiescent background are presented and compared with previous studies to validate the flow and measurement technique. The evolution of passive scalar fields in turbulent jets issued into quiescent backgrounds has been studied in air (e.g. Wilson and Danckerts 1964; Becker *et al*. 1967; Antonia *et al*. 1975; Birch *et al*. 1978; Lockwood and Moneib 1980; Dowling and Dimotakis 1990; Panchapakesan and Lumley 1993b; Tong and Warhaft 1995; Papadopoulus and Pitts 1998; Nobes and Nathan 2001; Darisse *et al.* 2015) and water (Dahm and Dimotakis 1987, 1990; Miller and Dimotakis 1991; Yoda *et al*. 1994; Buch and Dahm 1996; Catrakis and Dimotakis 1996; Law and Wang 2000; Su and Clemens 2003; Lavertu 2006). The statistics of the concentration field of the present study were compared with the works of Dahm and Dimotakis (1987, 1990), Law and Wang (2000) and Lavertu (2006). Those experimental works were performed in water jets and employed LIF for the concentration measurements, as in the present study. Dahm and Dimotakis (1987, 1990) reported concentration measurements (obtained using a linear photodiode array) at the centerline

(0<x/D<350) and radial profiles at x/D=300 for a jet at Re=5000. Law and Wang (2000) performed simultaneous velocity and concentration measurements combining digital particle image velocimetry (DPIV) and planar laser induced fluorescence (PLIF) in a jet at Re=12700. Axial and radial profiles of concentration were presented spanning the range 40<x/D<70. Lastly, Lavertu (2006) performed punctual LIF measurements and reported radial profiles of concentration at x/D=50 for a jet at Re=10600. In the following plots, results for a Re=10600 jet will be presented. This Reynolds number was chosen to be above the mixing transition (Dimotakis, 2000) and at a Reynolds number comparable to that of previous studies.

The downstream evolution of the centerline mean concentration ($\langle C_{CL} \rangle$) normalized by the concentration at the jet exit (C_o) is plotted in Figure 5.4 as function of x/D (where D is the diameter of the nozzle). The results of the present investigation are compared with data of Dahm and Dimotakis (1987, 1990) and Law and Wang (2000). Note that measurements of Lavertu (2006) were only recorded at x/D = 50 and thus, his results are not presented. It should be noted that the results of Law and Wang only span the range 40 ≤ x/D ≤ 70 in this and subsequent figures. The concentrations exhibit the expected x^{-1} decay rate, consistent with previous studies and theory (Pope, 2000), and thus serve as preliminary validation of the measurements and the flow at the centerline of the jet.

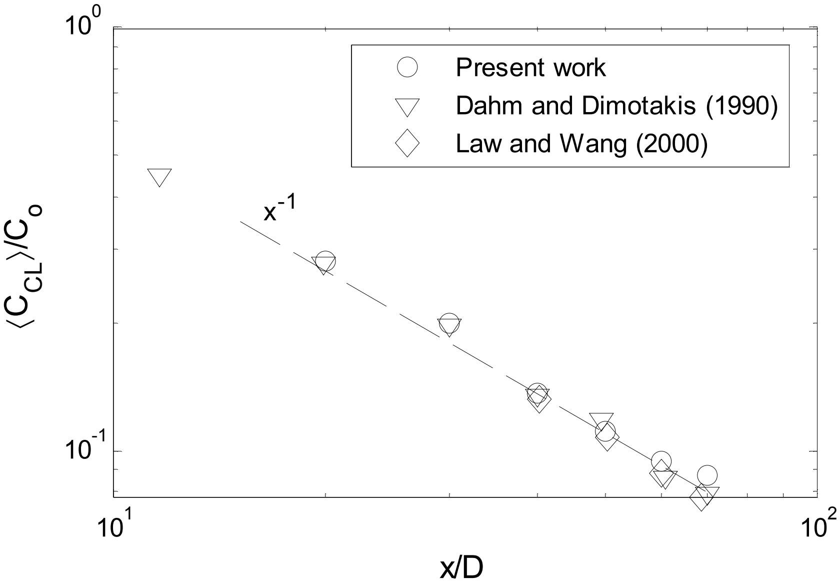

Figure 5.4 Downstream evolution of the normalized mean centerline concentration (○, present study, Re=10600; ▽, Dahm and Dimotakis (1990), Re=5000; ◇, Law and Wang (2000), Re=12700).

In the so-called self-similar region, the mean radial concentration profiles collapse onto a single (approximately Gaussian) curve when the mean concentrations are normalized by their respective centerline value (*i.e.* $\langle C(r)\rangle/\langle C_{CL}\rangle$) and the radial distance is normalized by the axial distance (*i.e.* r/x). Profiles at x/D = 50 and x/D =70 are presented in Figure 5.5 along with the results of other authors. Using the above normalization, the profiles (at x/D = 50 and 70) approximately collapse onto a single curve. Moreover, they are also consistent with those of previous authors. The data most closely agree with the results of Law and Wang (2000). This finding may be explained by the fact that Law and Wang (2000) also employed planar LIF for their concentration measurements at a comparable Re=12700 (versus Re=10600 for the present work).

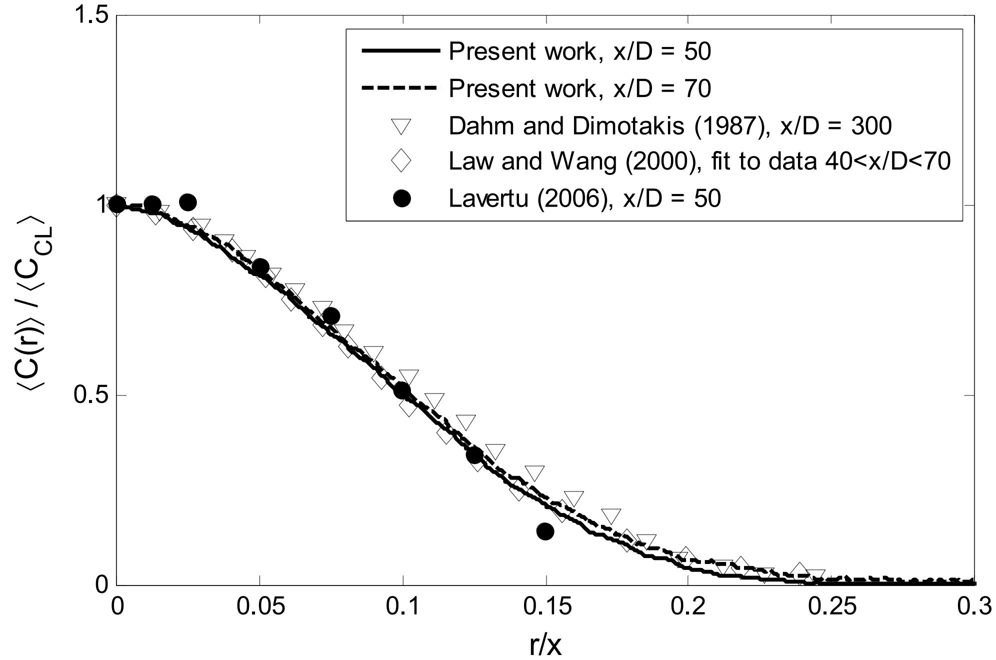

Figure 5.5 Radial profiles of mean concentration for a Re = 10600 turbulent jet at x/D = 50 and 70. Data of other author also included for comparison (— Present work, x/D = 50; ——Present work, x/D = 70; ▽, Dahm and Dimotakis (1987), x/D = 300; ◇, Law and Wang (2000), fit to data 40<x/D<70; ● Lavertu (2006), x/D = 50).

The downstream evolution of the centerline RMS concentration normalized by the mean concentration at centerline ($C_{rms}/\langle C_{CL}\rangle$) is presented in Figure 5.6. $C_{rms}/\langle C_{CL}\rangle$ is believed to asymptote to a constant value at certain distance from the jet exit in the same fashion as the equivalent velocity field statistic (Wygnanski and Fiedler 1969; Hussein *et al*. 1994; Lipari and Stansby 2011). However, very few studies have been able to determine a constant value of $C_{rms}/\langle C_{CL}\rangle$ and the values found in different studies range from 0.17 to 0.27 (Dowling and Dimotakis 1990). The profile for the present experiments is in agreement with the results of Dahm and Dimotakis (1990), although a constant value has not yet been reached in the range of the measurements studied herein. The effects of re-entrainment (due to the dye reaching the tank wall) limit the range of measurements thus precluding the determination of the asymptotic value (which appears to be around 0.18) with additional certainty. The higher values in the results of Law and Wang (2000) may be attributed to the fact that they added particles (with a nominal diameter of 50 μm) to the fluid to simultaneously measure the velocity field.

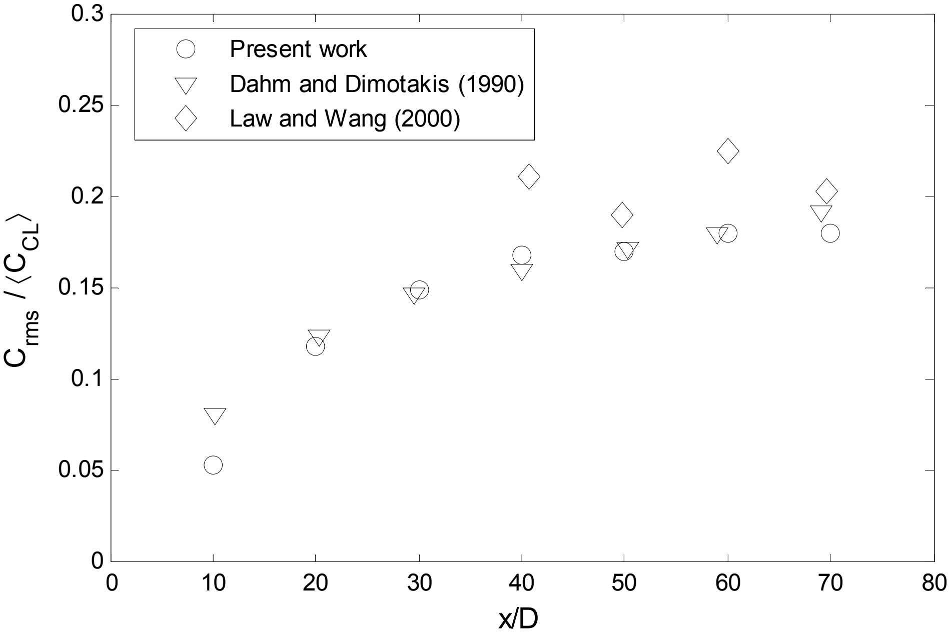

Figure 5.6 Downstream evolution of the RMS concentration normalized by the mean concentration at the centerline of the turbulent jet. Same symbols as Figure 5.4.

Similarly to the mean concentration, when the radial profiles of RMS concentration are normalized by their respective centerline value (*i.e.* $C_{rms}(r)/C_{rms\text{-}CL}$) and the radial distance is normalized by the axial distance (*i.e.* r/x), the radial profiles collapse in a single curve in the self-similar region. It has also been found that the radial profile exhibits an off-axis peak located around r/x = 0.1. Figure 5.7 depicts the radial profiles for the normalized RMS concentration. Note that radial profiles of $C_{rms}(r)/C_{rms\text{-}CL}$ were not presented in Law and Wang (2000).

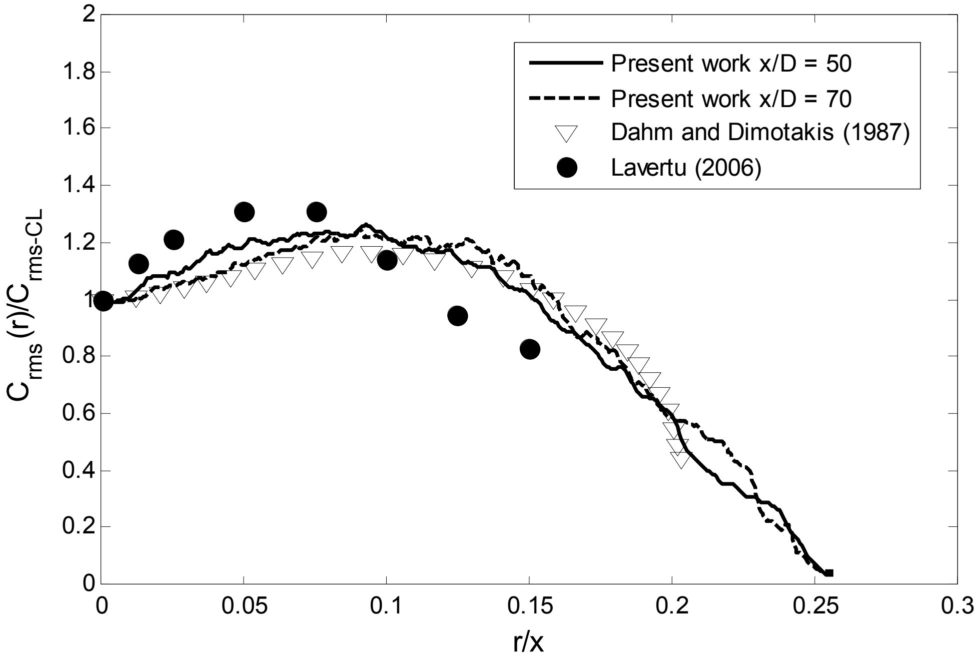

Figure 5.7 Radial profiles of RMS concentration for a Re = 10600 turbulent jet at x/D = 50 and 70. Data of other authors also included for comparison. (— Present work, x/D = 50; ——Present work, x/D = 70; ▽, Dahm and Dimotakis (1987), x/D = 300; ● Lavertu (2006), x/D = 50).

The applied normalization makes the profiles (at x/D = 50 and 70) approximately collapse onto a single curve. The results exhibit an off-axis peak (around r/x = 0.1), as found in previous investigations. There are some differences in the actual values of the present investigation with respect to the works of Dahm and Dimotakis (1987) and Lavertu (2006), but they may be attributed to the different axial locations, Reynolds numbers, and LIF techniques. Furthermore, differences in the radial profiles of RMS concentrations have also been observed for gas jets. Figure 5.8 shows the results for some gas jets along with the results of Figure 5.7. The results of the present investigation fall within the range of the reported data. The scatter in the measurements observed in Figure 5.8 has been attributed to differences in initial conditions, Reynolds numbers, techniques employed and, differences in spatial and temporal resolutions (Dowling and Dimotakis, 1990).

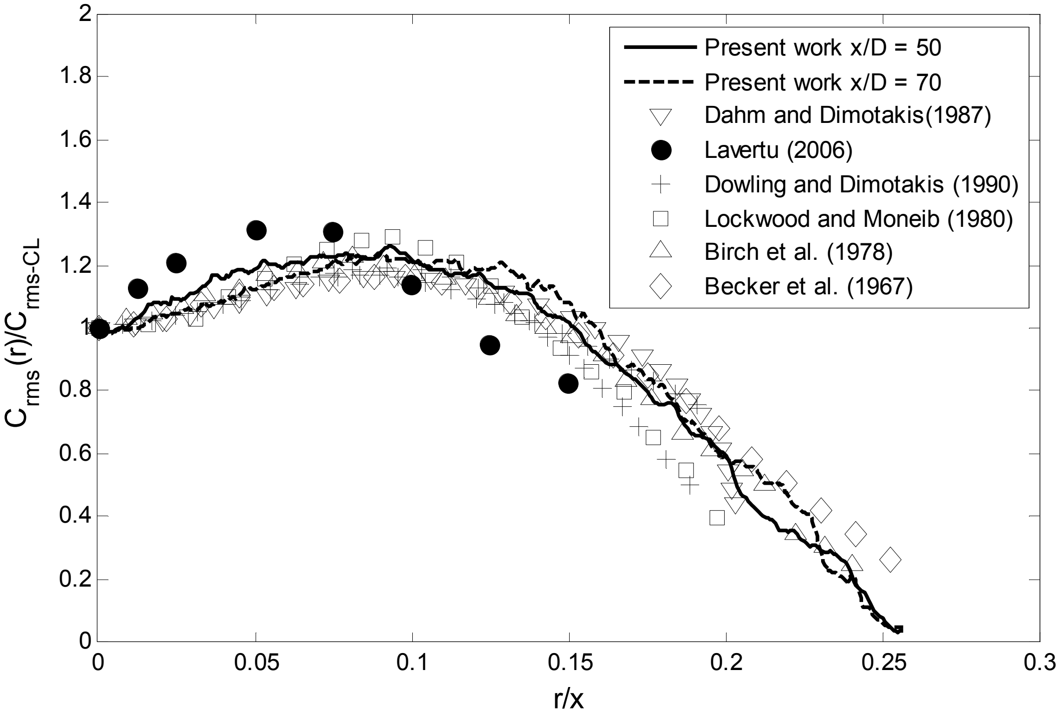

Figure 5.8 Radial profiles of normalized RMS concentration for different investigations.

The results presented in this section confirm the validity of the concentration measurement technique to determine the concentrations in the turbulent jet and, ultimately, the calculation of their mean and RMS concentrations. Although relatively few studies of concentration measurements in water jets at comparable Reynolds number and axial distances exist, the presented statistics of the concentration field were in general agreement with those of previous studies. The results followed the accepted behaviours for a passive scalar in a turbulent jet and hence serve to validate the technique employed in this study.

5.4 Results

In the present section, results pertaining to statistics of the scalar field generated by a jet emitted into quiescent and turbulent backgrounds will be presented. The results include the evolution of the mean and RMS centerline concentrations, radial profiles of mean and RMS concentrations, half-widths of the scalar field, probability density functions of concentration, downstream evolutions of the mean scalar flux, and comparisons with velocity field statistics from a previous study (Khorsandi, 2011) performed in the same experimental facility, under the same conditions.

The concentration measurements for a jet emitted into a turbulent background were performed with the jet discharging horizontally (x-direction), at mid-height in the facility (z/M = 0), and at a distance y/M = 7.3 from the RJA. The turbulent kinetic energy (TKE) at this position was 4.4 cm^2/s^2. The evolution of the scalar field was investigated for two jet Reynolds numbers: 5800 and 10600. The high Reynolds number (10600) was chosen to be above the mixing transition (Dimotakis, 2000). The low Reynolds number (5800) was selected to allow a clear observation of the effect of the turbulent background on the decay rates of the concentration, half-width of the scalar field, and breakup location within the range of measurements (10 ≤ x/D ≤ 70).

Moreover, the chosen jet Reynolds numbers also allowed for comparison with the velocity field data of Khorsandi (2011) and Khorsandi *et al.* (2013). Comparing the results of the scalar and velocity fields under the same conditions allows any differences in the evolution of the two fields to be identified.

Flow visualizations were also employed to interpret the changes in the statistics of the scalar fields of jets emitted into a turbulent background. The flow visualizations revealed significant changes in the flow dynamics and hence in the mixing process of jets emitted into a turbulent background. Typical flow visualizations of jets emitted into both quiescent and turbulent backgrounds are presented in Figure 5.9. The sequence of images shows a more complicated process of mixing in the presence of background turbulence. The jet emitted into a quiescent background maintains its position near the center of the image and a symmetric shape while the jet emitted into a turbulent background meanders about the centerline and is significantly distorted by the eddies of the background turbulence.

In the following subsections, the results for the jet emitted into both a quiescent and a turbulent background will be presented. Due to the similar nature of the profiles obtained for the jet at Re = 10600 and 5800 in a quiescent background, and for sake of clarity, only the results at Re=10600 will be presented in the plots as they are representative of a jet emitted into a quiescent background.

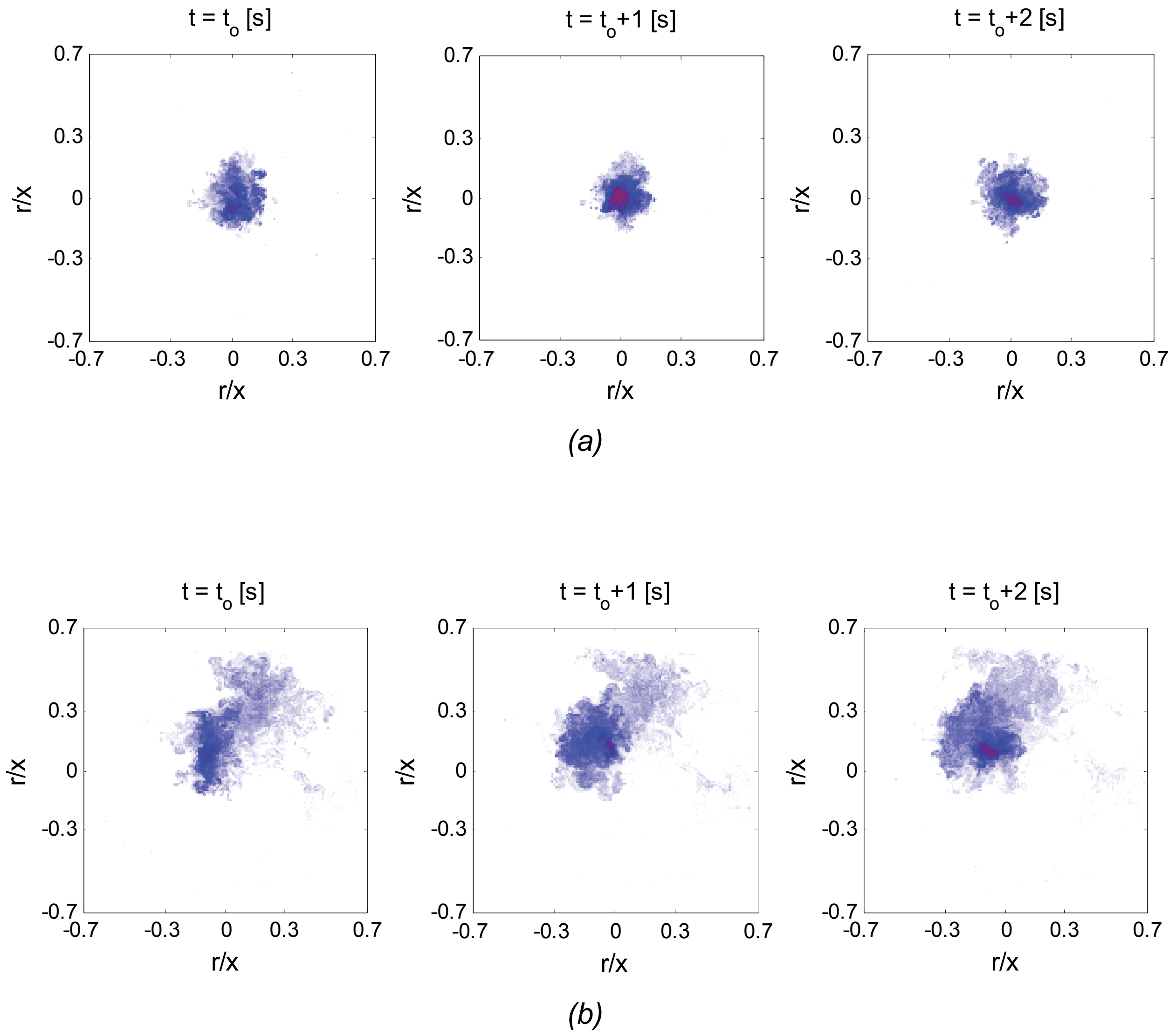

Figure 5.9 Flow visualizations of jets emitted into (a) a quiescent background, and (b) a turbulent background. Cross section at x/D = 40 for the jet at Re=10600.

5.4.1 Scalar field within a jet emitted into quiescent and turbulent backgrounds

The downstream evolution of the centerline mean concentration ($\langle C_{CL} \rangle$) normalized by the concentration at the nozzle exit (C_o) of a jet emitted into quiescent and turbulent backgrounds for the two Reynolds numbers (10600 and 5800) is plotted in Figure 5.10. The two jets at different Reynolds number were emitted into the same turbulent background (TKE = 4.4 cm^2/s^2) for comparison as it was hypothesized that the background turbulence would affect the lower Reynolds number jet more and/or closer to the jet exit based on previous results of Gaskin *et al.* (2004) and Khorsandi *et al.* (2013). The jet at a lower Re represents a “weaker” flow (with respect to the high Re jet) since there is less injection of momentum.

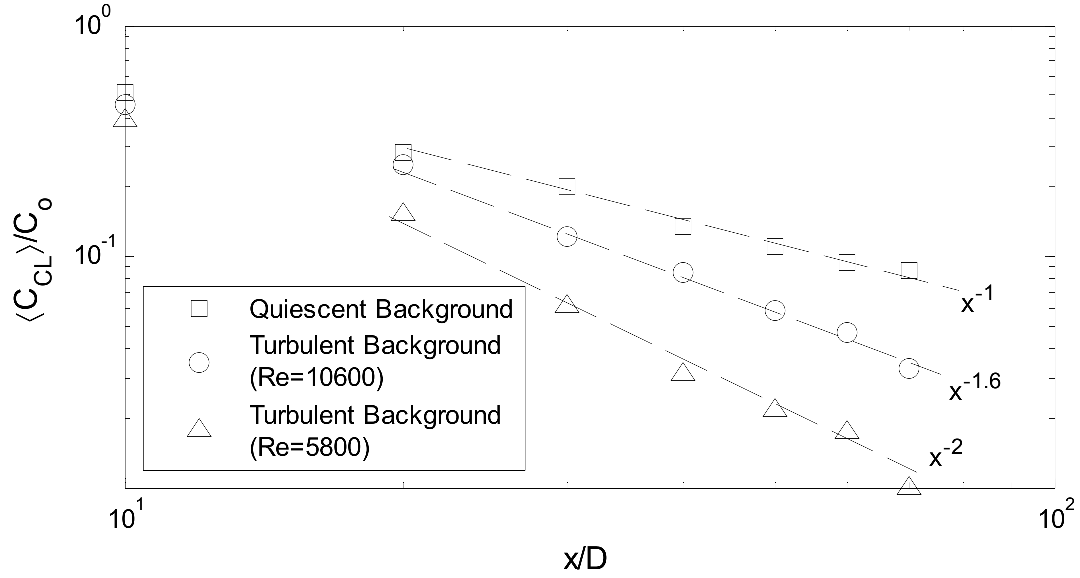

Figure 5.10 Downstream evolution of the centerline mean concentration normalized by the initial concentration ($\langle C_{CL} \rangle / C_o$). Log-log coordinates.

As observed in Figure 5.10, lower mean concentrations were measured in the two jets issuing into the turbulent background. The lowest concentrations were measured for the jet at Re= 5800, confirming that the jet is more affected by the action of the background turbulence at this lower Reynolds number, as the turbulent background more "easily" affects the evolution of the jet at Re=5800 with its lower injection of momentum. Furthermore, one concludes that the effects of the background turbulence on the jet are more noticeable farther downstream, given that the mean and RMS velocities in a jet decrease with downstream distance. Moreover, the rate of decay of the centerline concentration increases in the presence of the background turbulence. As expected $\langle C_{CL} \rangle / C_o$ decays at x^{-1} in a jet released into a quiescent background. However, the same quantity decays as $x^{-1.6}$ and x^{-2} for the jets at Re = 10600 and 5800 respectively in the presence of background turbulence.

Radial profiles of mean concentration were measured at different distances from the nozzle exit for the jets at the two Reynolds numbers issuing into quiescent and turbulent surroundings. Figure 5.11 depicts the radial profiles at x/D = 20, 30, 40, 50, 60, and 70. The results exhibit lower concentrations near the centerline for the jets emitted into a turbulent background. However, higher concentration were measured at the edges of the jet (beyond r/x = 0.15) for all the cases in which the jet issued into turbulent ambient. Also, one observes that the presence of the turbulent background serves to extend the scalar profile farther in the radial direction, albeit at very low concentrations. The larger radial extent of the jets issued into turbulent background can be explained by a radial turbulent transport by the external turbulence (which is non-existent in the quiescent background). Consistent with the evolution of the mean centerline concentrations, the effects of the background turbulence on the jet are more noticeable for the lower Reynolds number jet.

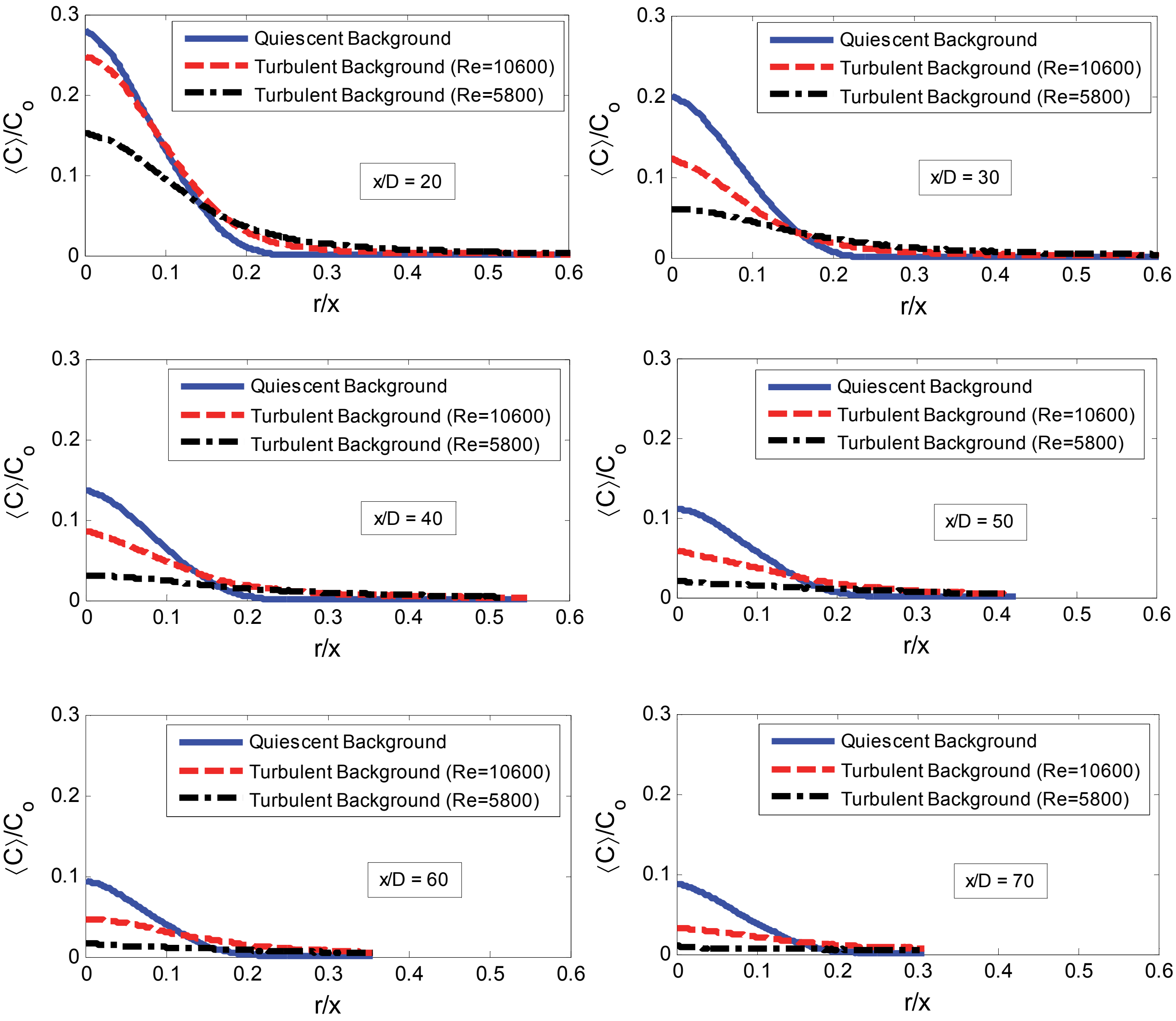

Figure 5.11 The effect of background turbulence on the radial profiles of mean concentration of an axisymmetric turbulent jet emitted into both quiescent and turbulent backgrounds. x/D = 20, 30, 40, 50, 60 and 70.

It can be observed in Figure 5.11 that the radial profiles of mean concentration are distorted by the presence of the background turbulence and they become flatter with increasing distance from the nozzle exit. The effect is more evident for the jet at Re = 5800, where the profile becomes flat at x/D = 70, indicating that the jet structure is being effectively destroyed by the background turbulence at this far downstream position. The range of measurement did not permit the observation of the profile for the jet at Re = 10600 to become totally flat, however its evolution is qualitatively similar to that of the jet at Re =5800, indicating that the jet would become flat at a farther downstream position (out of the range of the present measurements).

The half-width ($r_{1/2}$) of the scalar field is i) defined as the radial distance at which the concentration reaches half of its centerline value, ii) a measure of the width of the jet, and iii) plotted as function of downstream distance in Figure 5.12. As expected, due to self-similarity, the half-width of the jet in quiescent background grows linearly with downstream distance. In the presence of a turbulent background, the jets become wider and the half-width growth is no longer linear. The half-width of the jet at Re = 10600 issuing into the turbulent background exhibits a power-law growth proportional to $x^{1.3}$. In the presence of external turbulence, the half-width of the Re = 5800 jet grows as $\sim x^{1.4}$ for x/D ≤ 60. The half-width at x/D = 70 for the Re = 5800 jet emitted into the turbulent background falls above an extrapolation of the best fit power law for x/D ≤ 60, from which one can hypothesize that the jet structure has been destroyed at this position. This notion is validated by the fact that the radial profile of mean concentration at x/D = 70 is essentially flat (Figure 5.11).

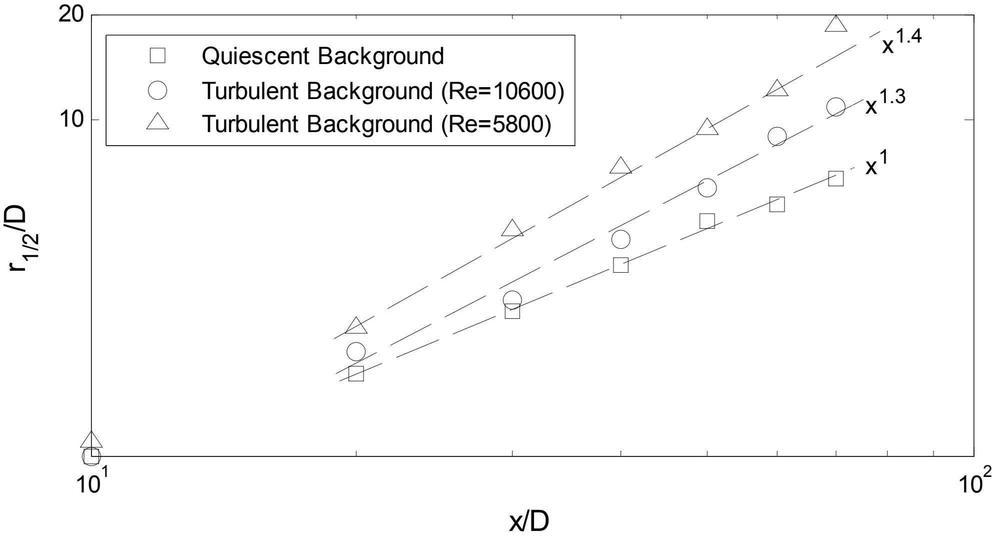

Figure 5.12 Downstream evolution of the half-width of the scalar field for jets emitted into quiescent and turbulent backgrounds.

Having examined the evolution of the mean concentration field, one can now consider the evolution of the normalized RMS concentration at the centerline (Figure 5.13). In the presence of the background turbulence, the RMS concentration is generally higher than that for jets emitted into quiescent backgrounds. For the jet at Re = 10600 issued into a turbulent background, the normalized centerline RMS concentration is always higher than that of the quiescent case (by a factor of approximately 2) and generally exhibits a similar behavior. On the other hand, the RMS concentration of the jet at Re = 5800 in the presence of the external turbulence is much higher close to the nozzle exit, then decreases fairly rapidly reaching similar values to those for the jet issued in quiescent background at x/D = 60.

One can hypothesize that when the jet structure is totally destroyed (at a certain position downstream from the nozzle exit), there is little large scale engulfment of ambient fluid and the turbulent background would serve to mix the remaining scalar, drastically reducing the RMS concentration, which would subsequently tend to zero (the scalar being effectively fully mixed by the turbulent background). This scenario appears to begin at x/D = 70 for the jet at Re = 5800 (for which the centerline RMS concentration is the lowest of all the cases at this position). At x/D = 70 the centerline RMS concentration of the jet at Re = 10600 is still higher than that of the free jet, however the difference decreases slowly with downstream distance and one can reasonably expect that it would exhibit the same trend as that of the jet at Re = 5800 at downstream distances beyond x/D = 70.

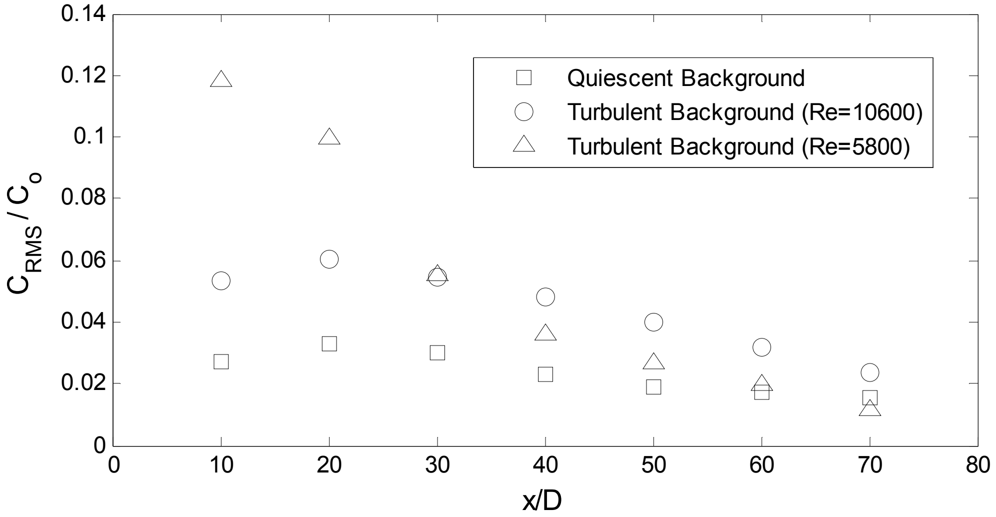

Figure 5.13 Downstream evolution of RMS concentration at the centerline for jets emitted into quiescent and turbulent backgrounds.

Figure 5.14 plots the radial profiles of RMS concentrations for the jets issued into quiescent and turbulent backgrounds at Re = 10600 and Re = 5800 at downstream distances of x/D = 20, 30, 40, 50, 60 and 70. The results indicate that the presence of the external turbulence serves to increase the RMS concentration at all radial and downstream positions for the jet at Re = 10600. Similarly, the RMS concentrations of the jet at Re = 5800 are increased for downstream distances x/D ≤ 60, however at x/D = 70 the profile becomes flat and lower RMS concentrations than those of the jet emitted into a quiescent background are measured (further indicating that the jet structure has been destroyed by the turbulent background). Also, for the cases emitted into a turbulent background, the RMS concentrations for the jet at Re = 5800 are larger than those of the jet at Re = 10600 for x/D < 30. Beyond x/D < 30, the RMS concentrations of the jet at Re = 5800 gradually decrease and become lower (starting at the centerline) than those of the jet at Re = 10600 (consistent with the behavior of the centerline RMS concentration in Figure 5.13). Additionally, the characteristic off-axis peak in the radial profile of the RMS concentration of a jet emitted into a quiescent background gradually disappears in the presence of the background turbulence. These observations of the changes in the relative magnitudes of the RMS concentration are consistent with the disruption of the jet structure (at lower x/D for Re=5800 and at higher x/D for Re=1600) and resulting asymptotic evolution to turbulent diffusion by the background turbulence with downstream distance.

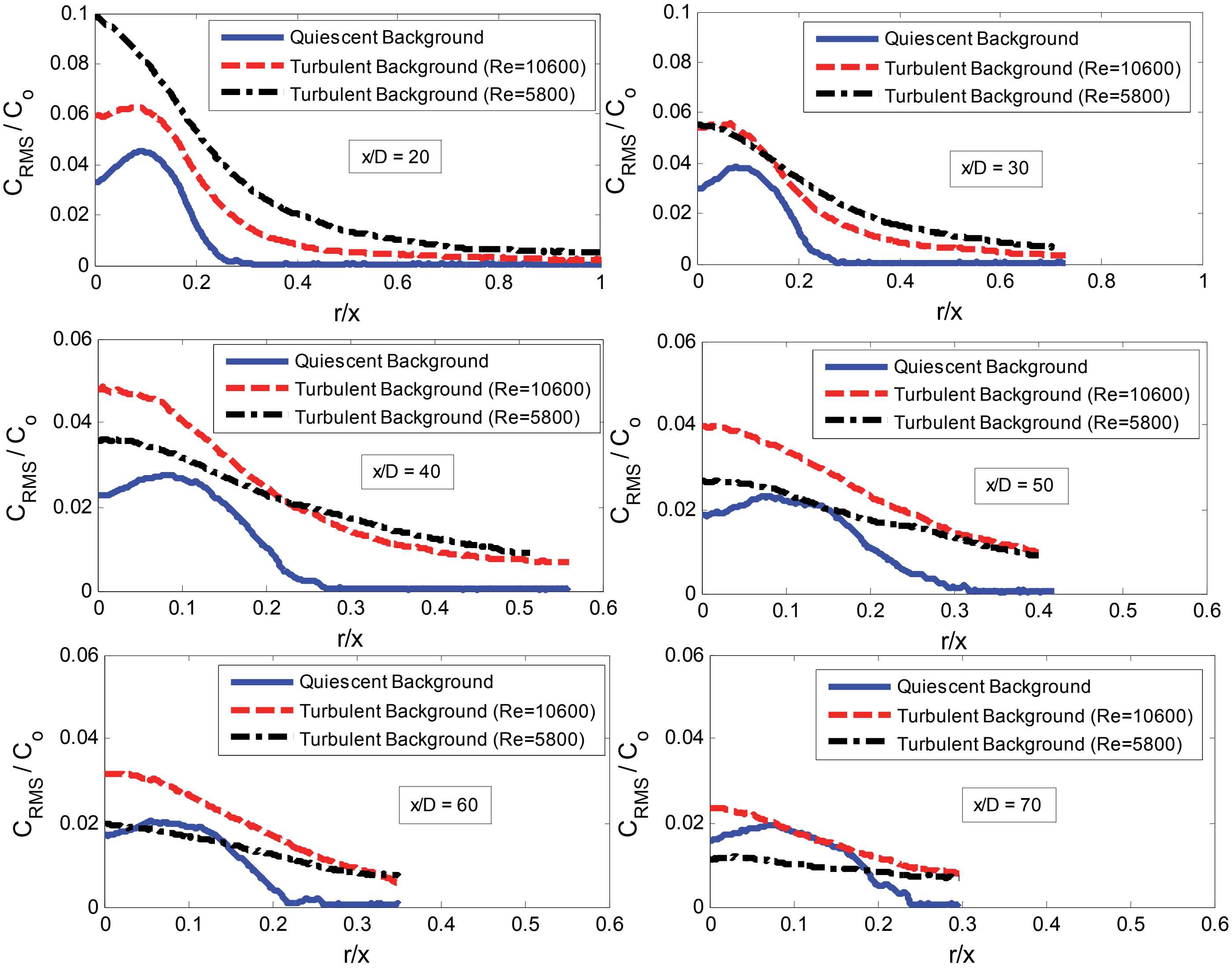

Figure 5.14 The effect of background turbulence on the radial profiles of the RMS concentration of an axisymmetric turbulent jet. x/D = 20, 30, 40, 50, 60 and 70.

The higher values of the RMS concentrations for the jets issued into turbulent background may imply that the flow becomes more intermittent. Given that the RMS is a measure of the deviation of the concentrations from their mean value, a larger range of concentrations may be expected for jets emitted into turbulent background. However, the RMS alone cannot conclusively determine whether higher concentrations are present for the jets emitted into turbulent background. To answer this question, probability density functions (PDFs) will be employed to compare the individual concentrations and observe changes due to the presence of the background turbulence.

The comparison of the probability density functions of the centerline concentration at different downstream distances for the jet at Re = 10600 is plotted in Figure 5.15. The results indeed confirm a larger range of concentrations for the jet emitted into a turbulent background. Recalling that the mean concentration profiles (Figure 5.11) imply overall lower mean concentrations for the jet emitted into a turbulent background, the increased intermittency of the scalar field (associated with its larger RMS concentrations) results in the largest concentrations being of similar value for the jet emitted into quiescent and turbulent backgrounds, but a significantly increased likelihood of low concentrations for the jet emitted into a turbulent background. Moreover, it is observed that while the PDF for the jet emitted into a quiescent background is unimodal and symmetric at all downstream distances, the PDF of the jet emitted into a turbulent background becomes bimodal with the peak at very low concentrations (at 10-15% of the peak concentration of the quiescent case) growing with downstream distance (and will ultimately be tending to an approximately exponential distribution, as opposed to the consistently Gaussian PDF for a jet emitted into a quiescent background). The measured low concentrations are associated with external fluid reaching the centerline of the jet being displaced from the centreline. Hence, despite the turbulent background resulting in more (clean) external fluid reaching the centerline of the jet (favoring the conditions for higher mixing if this is within the jet boundaries), high concentrations comparable to those measured in a quiescent background still exist. This behavior is in contrast with the notion of superposition of the jet and background turbulence for which lower concentrations would be expected.

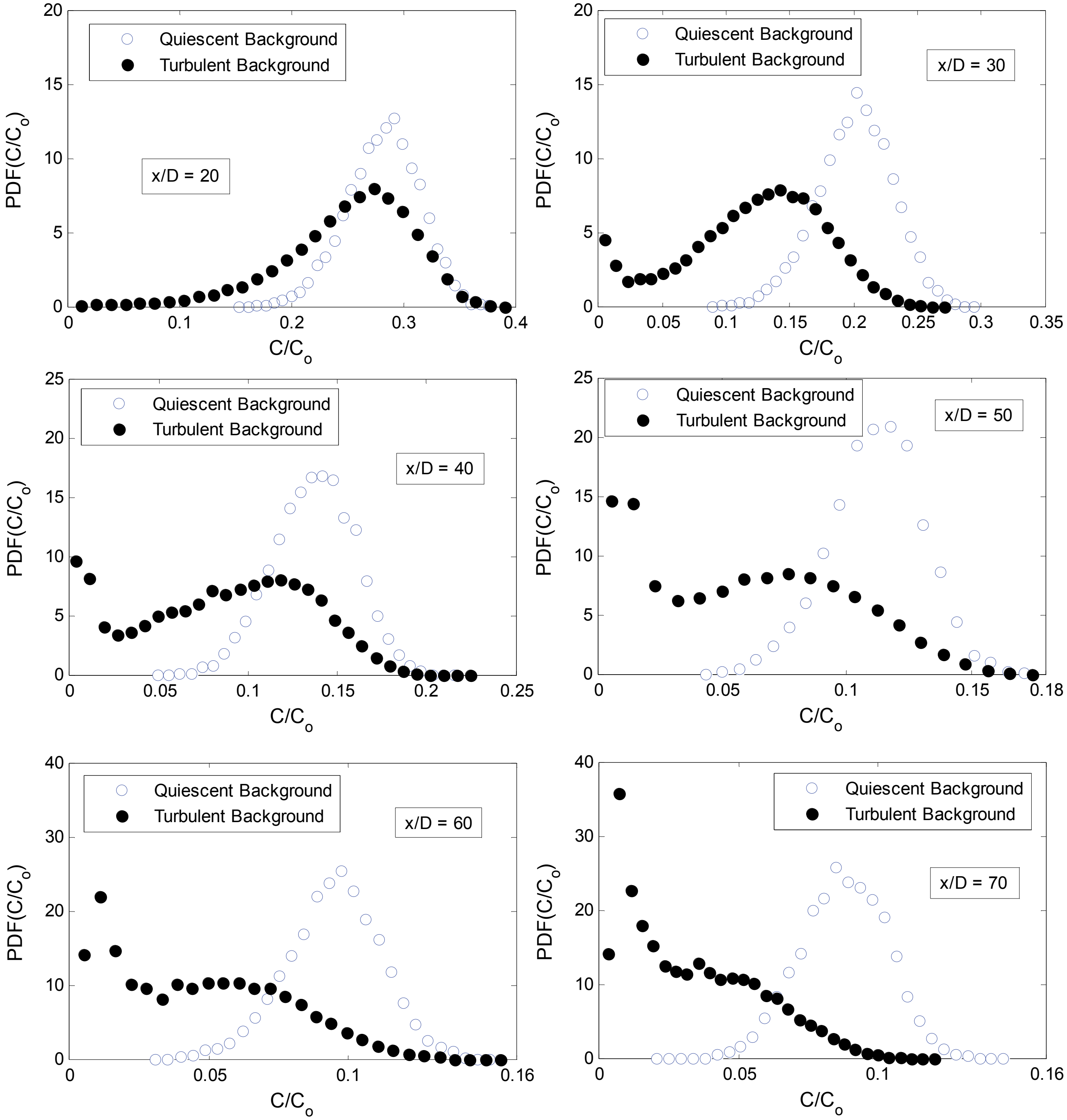

Figure 5.15 Effect of the background turbulence on the PDF of centerline concentration for Re = 10600.

The evolution of the PDF of concentration away from the jet axis is examined by measuring the PDF along r/x = 0.102 for the different downstream distances in Figure 5.16. (Such points coincide with the half-width of the jet emitted into a quiescent background, which correspond to the peak of the RMS profile for the jet in a quiescent background, and where the mean concentration is higher for the jet in quiescent background.) In the presence of the background turbulence the PDFs evolve gradually with downstream distance from being close to the unimodal shape exhibited by the jet in a quiescent background to an approximately exponential distribution by x/D = 70. This evolution passes through a bimodal stage with the peak at very low concentrations growing with increasing downstream distance from the jet exit, similar to the centerline case. However, at this radial position, the low-concentration peak is especially dominant (the PDF being clearly unimodal at x/D = 70 for the turbulent background case). At the centerline, the highest concentrations detected were similar for both cases, however a difference is clear when measured at r/x = 0.102 revealing higher concentrations for the jet emitted into a turbulent background from x/D = 20 to 60. The difference in the highest concentrations at x/D = 70 becomes smaller, presumably due to the start of the jet's loss of structure at this larger downstream distance.

Figure 5.17 compares the PDFs at different downstream distances along r/x = 0.183 (points coinciding with $\langle C \rangle / \langle C_{CL} \rangle = 0.1$ in the jet emitted into quiescent background, where the mean concentration of the jet in the quiescent background is lower than that in the turbulent background and the RMS concentration of the jet in the turbulent background is greater that than of the quiescent background for x/D <70). These points were selected since they are located near the edge of the jet emitted into quiescent background in which the scalar field is known to be intermittent. At these distant radial positions, the shape of the PDFs for the jet emitted into quiescent and turbulent backgrounds are similar with a peak at very low concentrations. However, in the presence of external turbulence, significantly higher concentrations were detected and less (clean) ambient fluid was detected with increasing distance from the jet exit, consistent with the finding that higher mean concentrations were measured in the presence of background turbulence at the jet edges.

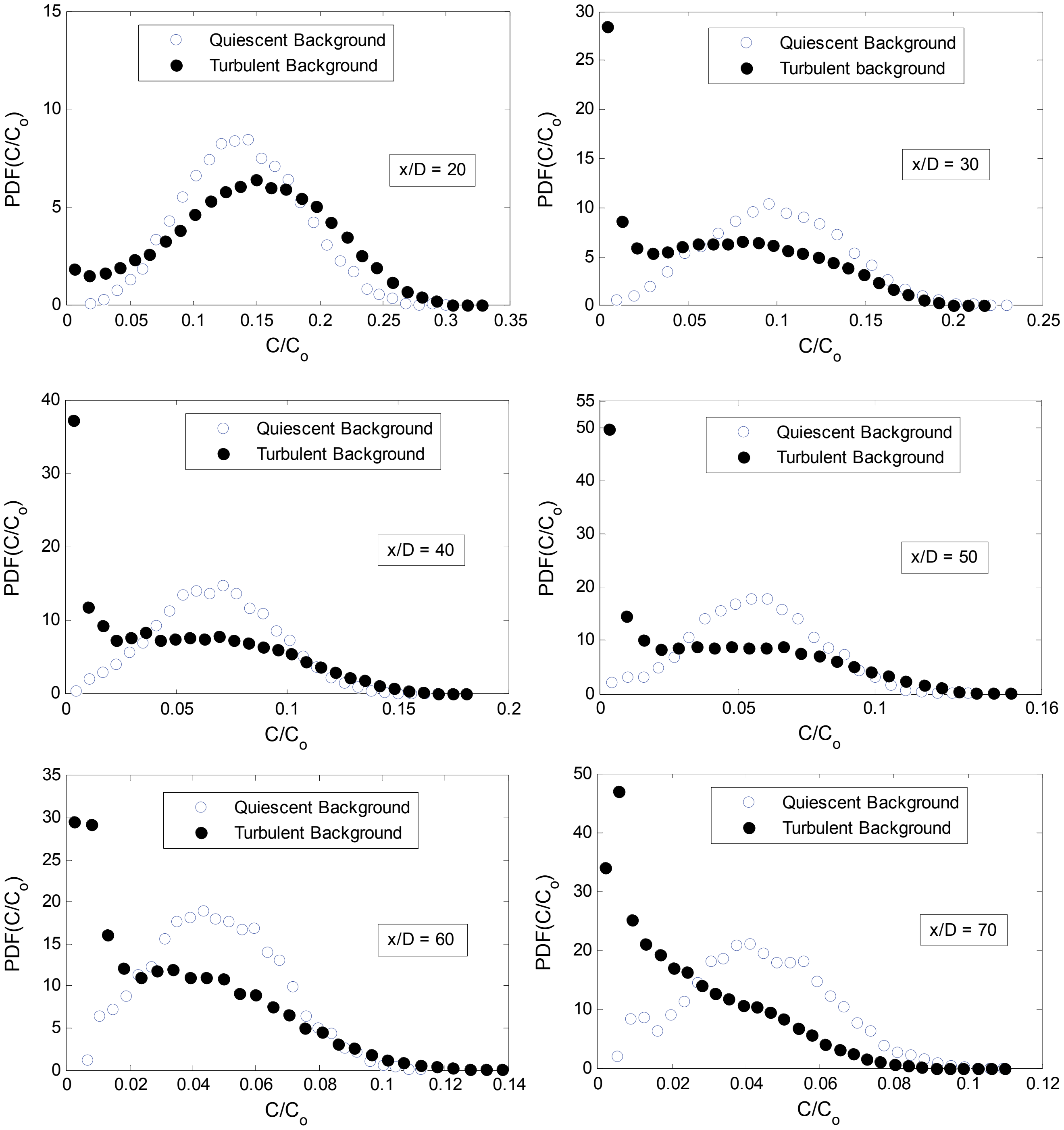

Figure 5.16 PDF of concentration at r/x = 0.102 in the jet emitted into quiescent and turbulent backgrounds. Re = 10600.

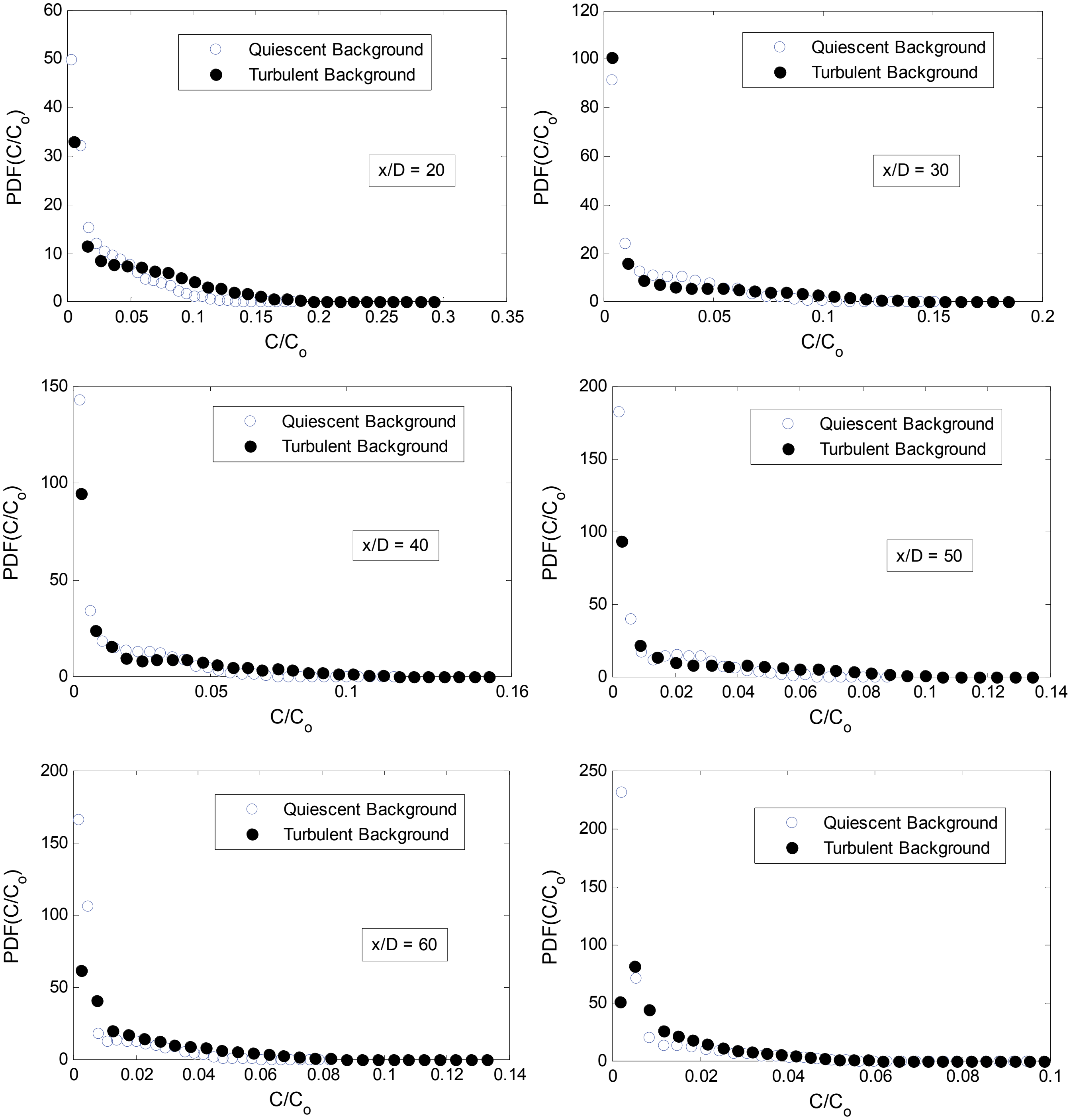

Figure 5.17 PDF of concentration at r/x = 0.183 in the jet emitted into quiescent and turbulent backgrounds. Re = 10600.

Figure 5.18, 5.19 and 5.20 show the downstream evolution of the PDFs of concentration at r/x = 0, 0.102 and 0.183 for the jet of Re = 5800, respectively. The effects of the turbulent background on the PDFs are similar to those described for the jet at Re = 10600, although the effects of the background turbulence are more intense and start closer to the jet exit. The shape of the PDF evolves more quickly with increasing the distance from the jet exit from being bimodal to a quasi-exponential distribution with a large single-peak at low concentrations. The peak at higher concentrations observed closer to the jet exit is likely associated with the jet, implying that its disappearance is indicative of the disruption of the jet structure. The shape of the PDF is similar irrespective of the radial position at x/D = 70, presumably due to the substantial destruction of the jet at this far position. In contrast, the jet's structure continued to prevail at x/D = 70 for the jet at Re = 10600 emitted into a turbulent background, since the shape of the PDF evolved with radial position (Figure 5.15, 5.16 and 5.17) from a bimodal distribution stage at the centerline to a unimodal distribution away from the jet's axis. Overall, the disruption of the jet's structure occurs gradually as the jet becomes "weaker" with downstream distance (due to the characteristic reduction in the mean and RMS velocities) while the turbulent background remains constant (nearly homogeneous isotropic turbulence). Moreover, at some downstream position, the background turbulence has disrupted the jet structure to the point that the jet structure is destroyed. The ultimate destruction of the jet causes the scalar to be mixed (only) by the action of the turbulent background, which results in the flat profiles of mean and RMS concentration, and shapes of the PDF of concentration being invariant with radial distance.

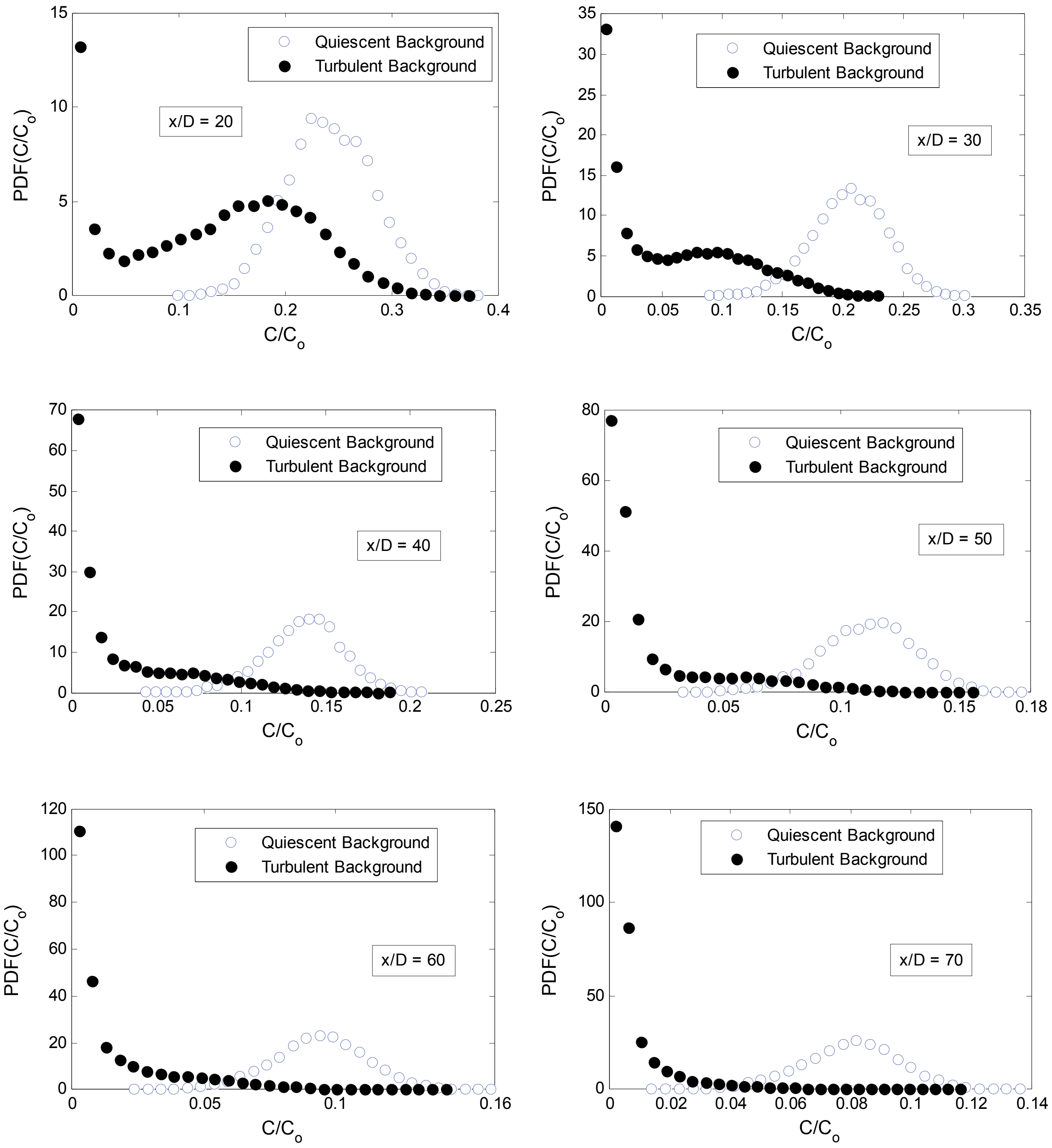

Figure 5.18 Effect of the background turbulence on the PDF of centerline concentration for the jet at Re = 5800

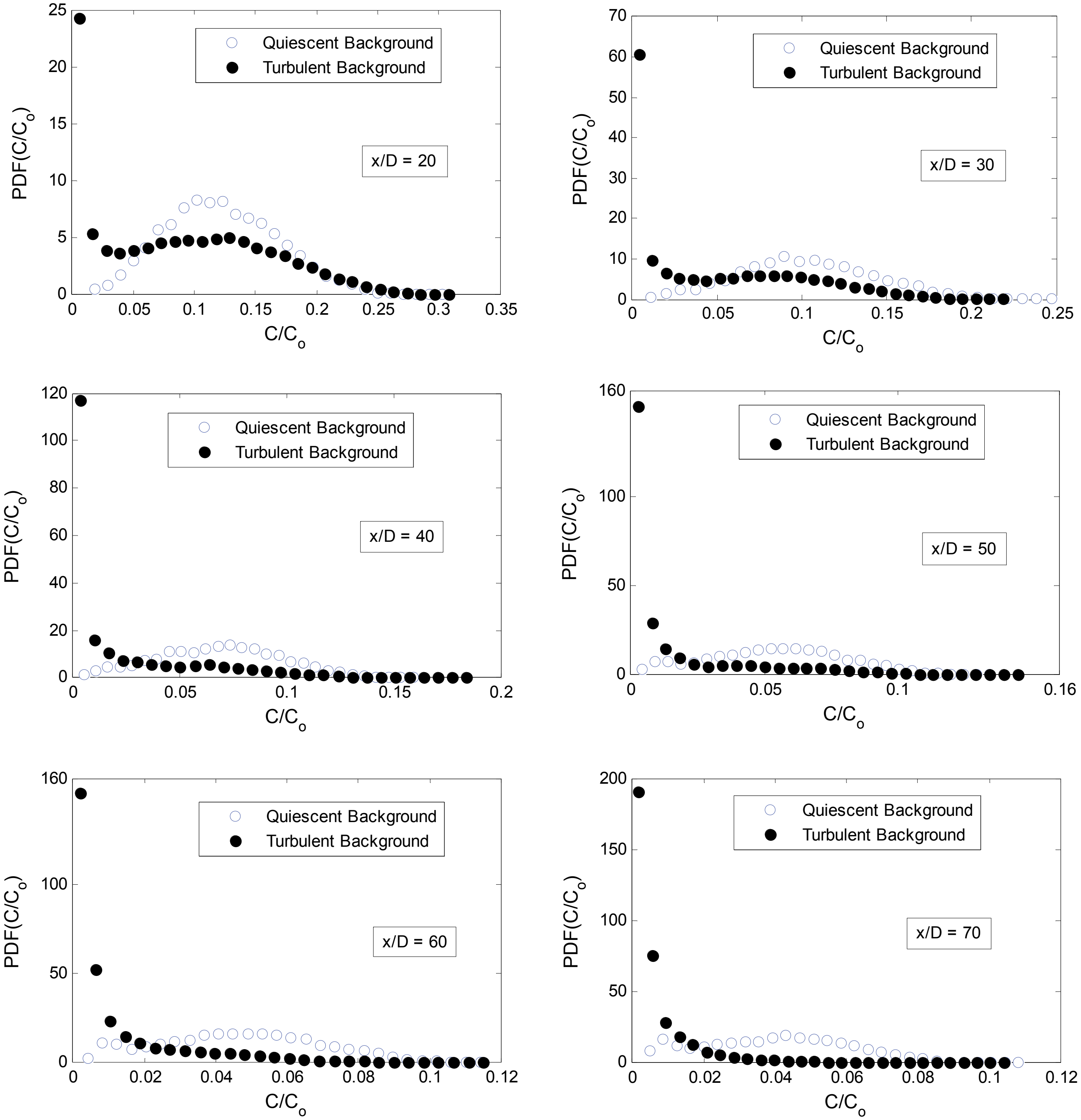

Figure 5.19 Effect of the background turbulence on the PDF of concentration at r/x = 0.102 (points coinciding with the half-width of the jet emitted into quiescent background). Re = 5800.

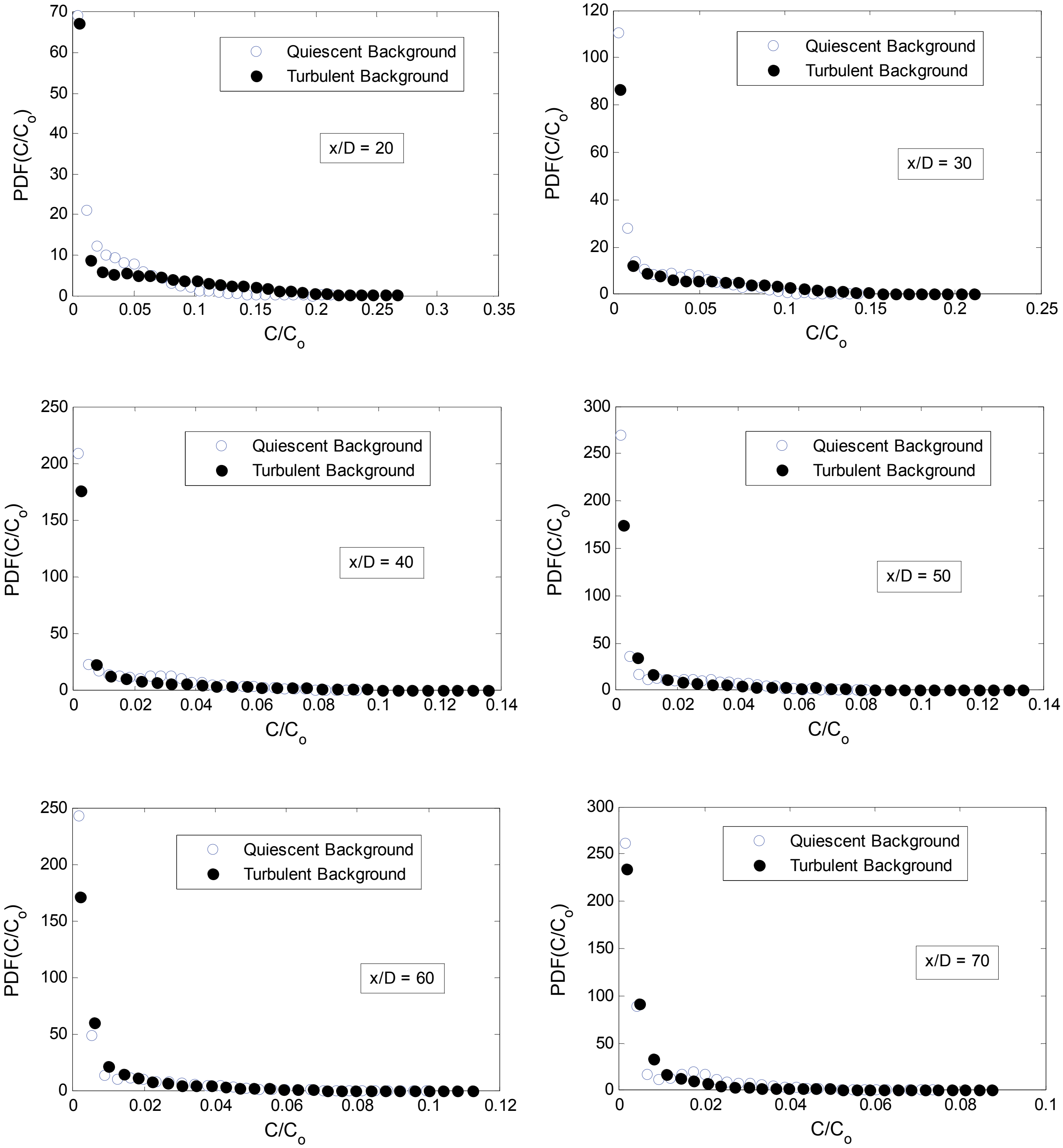

Figure 5.20 Effect of background turbulence on the PDF of concentration at r/x = 0.183 (points coincident with $\langle C\rangle/\langle C_{CL}\rangle = 0.1$ *in the jet emitted into quiescent background). Re = 5800.*

A pertinent result of the scalar field is the increased intermittency in the presence of the background turbulence resulting in significantly higher RMS concentrations (at all radial positions) and the highest concentrations detected at the centerline being comparable with those of a jet emitted into quiescent background. Furthermore, in the presence of external turbulence, higher concentrations were measured at the edges of the jet. Hence, the high intermittency of the scalar field caused the existence of both high and low concentrations, however the significantly higher probability of low concentrations resulted in the low mean concentrations (especially near the jet axis).

The highest concentrations within the jet are an important result because they i) characterize the mixing process, and ii) are relevant for practical applications in which instantaneous concentrations above a threshold may be undesirable. The highest concentrations detected for the jets emitted into both quiescent and turbulent backgrounds (quantified by the value of the bin containing the highest concentrations in the PDFs) are presented in Figure 5.21. The plots show the downstream evolution of the maximum concentrations along r/x=0 (data from Figure 5.15 and 5.18), r/x=0.102 (data from Figure 5.16 and 5.19) and r/x=0.183 (data from Figure 5.17 and 5.20). It can be observed that the maximum concentrations are similar for the jets in quiescent and turbulent backgrounds along the centerline (*i.e.* r/x=0). However, the maximum concentrations become higher for the jets emitted into a turbulent background away from the jet axis (e.g. r/x=0.183). The highest concentrations being comparable or higher than those in a jet emitted into a quiescent background is an interesting result since it i) contradicts the notion of superposition of the dilution effects of the jet and turbulent background, ii) reveals the inability of the background turbulence to increase the mixing homogenously, and iii) is important for applications such as the release of pollutants, which can be dangerous for the ecosystem at high concentrations.

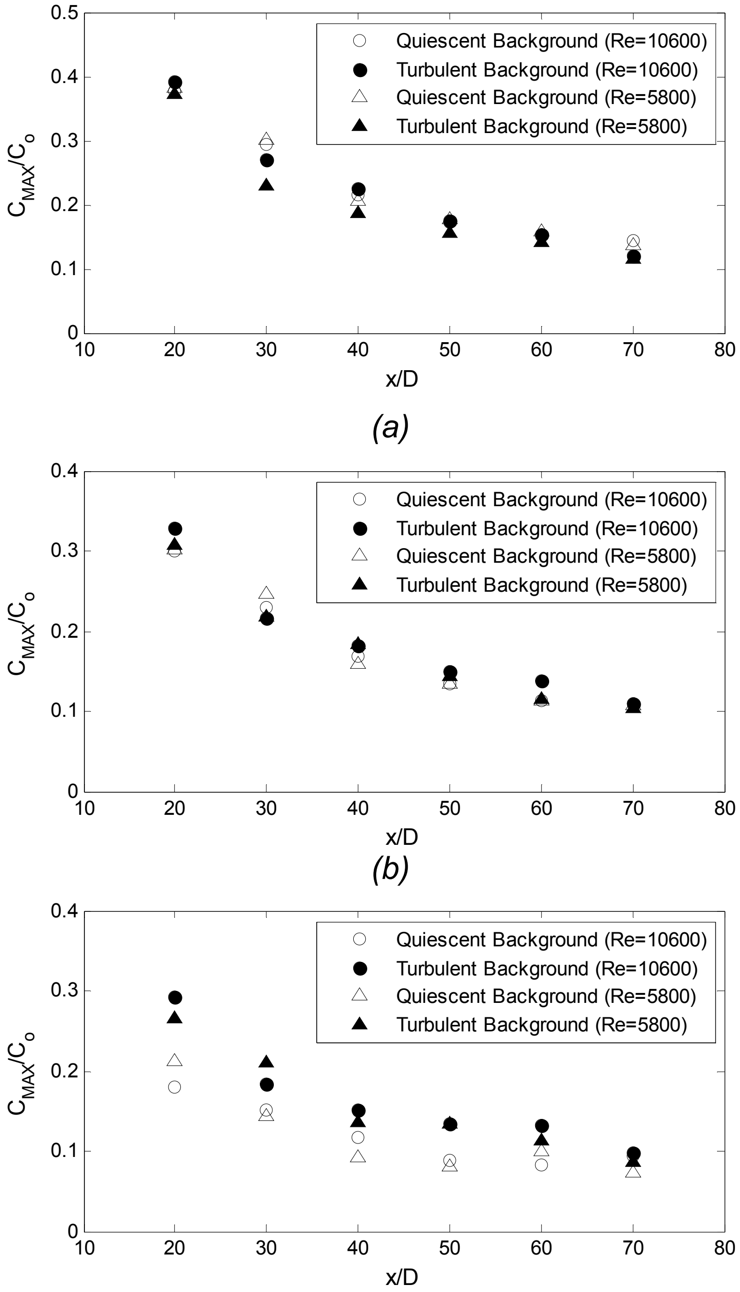

(a)

(b)

(c)

Figure 5.21 Downstream evolution of the maximum concentrations for the jets emitted into both quiescent and turbulent backgrounds. Results along a) r/x=0, b) r/x=0.102 and c) r/x=0.183.

Visualization of cross sections of the jet emitted into external turbulence showed that the jet meandered much more than one emitted into a quiescent environment. Figure 5.22 depicts one example of the characteristic movements of the jet in the presence of the background turbulence. (The RJA is located to the left of the images). The meandering of the jet was observed for all the axial positions (x/D) and was found to increase with downstream distance. Hence, the larger radial extent of the mean profiles (Figure 5.11) is due in part to the increased wandering of the jet causing it to be dispersed over a larger area (when averaged over time). Moreover, the high probability of low concentrations for a jet emitted into a turbulent background (in Figures 5.15, 5.16 and 5.17) is likely associated with the meandering of the jet, increasing the detection of clean ambient fluid that is not necessarily part of the jet. Similarly, the high concentrations detected at large radial distances can be attributed to the movement of the jet reaching those positions and transporting fluid with high concentrations of scalar. The visualizations helped identify the cause of the intermittency in the scalar field, as it results from the meandering of the jet, contrary to the notion (that may result from the mean profiles) of a quasi-stationary jet, with its width significantly increased and engulfing large volumes of ambient fluid.

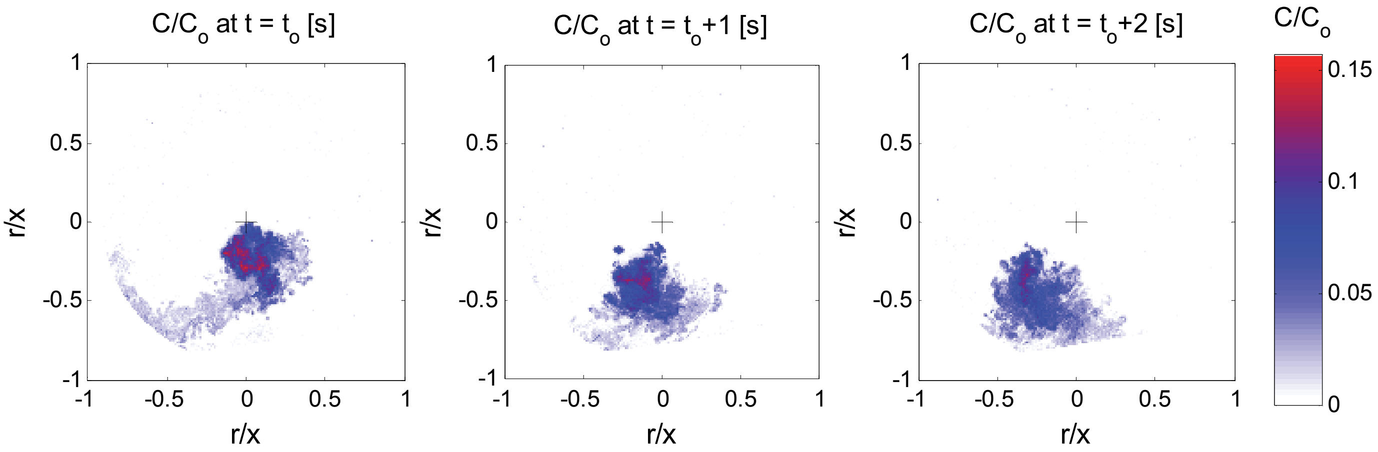

Figure 5.22 Example of the meandering of the jet emitted into the turbulent background as depicted by instantaneous planar concentration measurements. Cross section at x/D = 30 for the jet at Re=10600. The black cross represents the position of the center of the mean concentration profile.

The meandering of the jet was also observed for the jet at Re=5800 emitted into turbulent background (Figure 5.23). As expected, the advection of the jet fluid by the background turbulence is more evident in the jet at this lower Reynolds number. The effects on the mean concentration and PDFs can be explained in the same fashion as for the jet at Re=10600. Since there is less momentum in the jet at Re=5800, the turbulent background can more readily distort it, destroying its structure closer to the nozzle exit. Visualizations at x/D = 70 showed that although dyed fluid reached this axial position, a jet structure was hardly identifiable (Figure 5.24). The flow is characterized by low concentrations covering the whole measurements section with some locations being exposed to higher concentrations of dye reaching this far position. Ultimately, the scalar is mixed by the turbulent background in the absence of a clear jet structure, and results in the flat radial profiles of the mean and RMS concentrations.

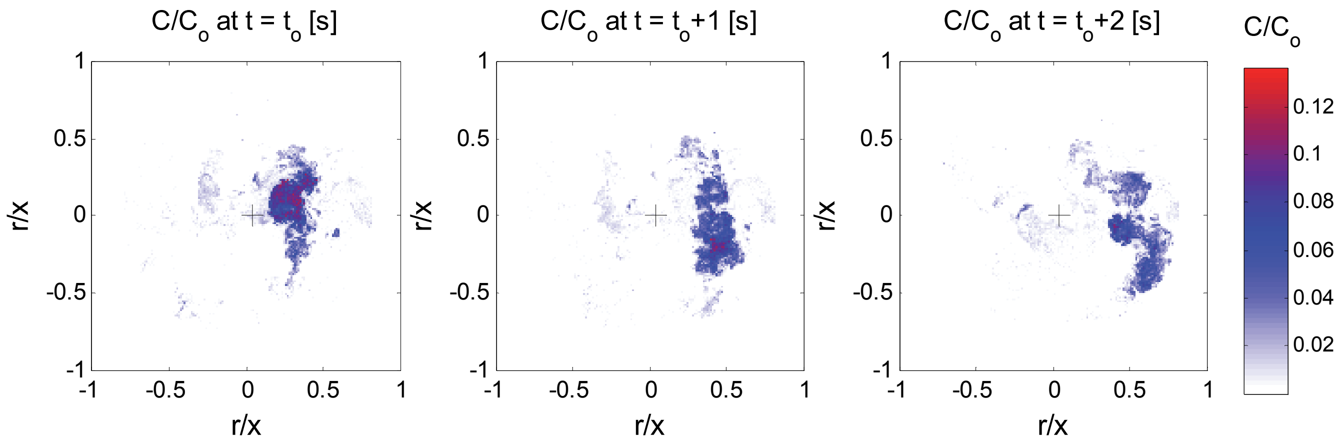

Figure 5.23 Meandering of the jet in the presence of the turbulent background. Cross section at x/D = 30 for the jet at Re=5800. The black cross represents the position of the center of the mean concentration profile.

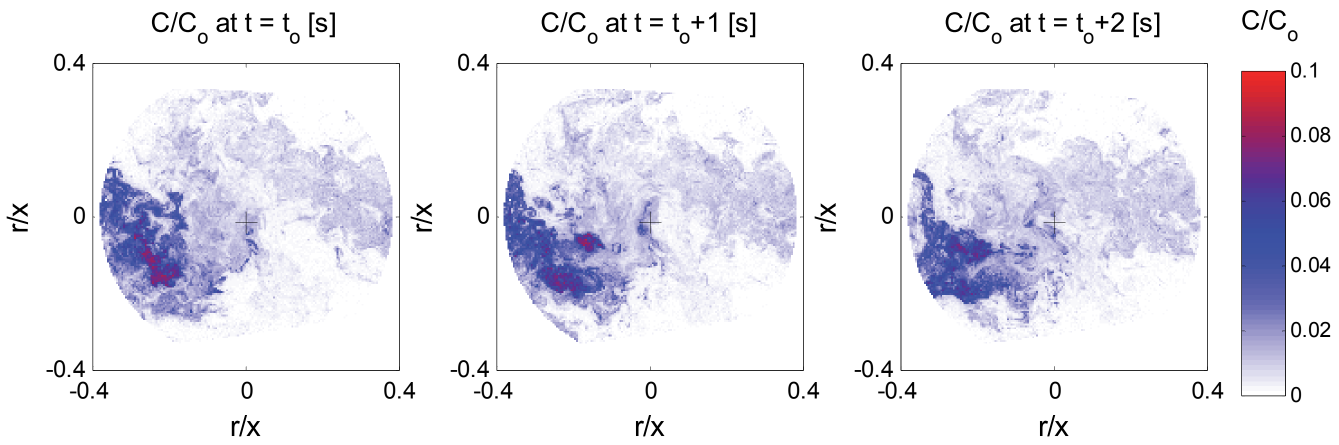

Figure 5.24 Cross section at x/D = 70 for the jet at Re=5800. Dyed fluid reaches this position but there is not a clear jet structure. The black cross represents the position of the center of the mean concentration profile. The circular (sides) and linear (top and bottom) boundaries in the images are the ends of the measurement section limited by the image intensifier and laser sheet, respectively.

5.4.2 Comparison of the scalar and velocity fields.

In the present sub-section, the results of the scalar field will be compared with those of Khorsandi *et al.* (2013) for the velocity field. Khorsandi *et al.* (2013) calculated the statistics of the velocity field from punctual measurements using flying hot-film anemometry and acoustic Doppler velocimetry (ADV) in the same experimental facility as that used herein. The present results pertain to jets emitted into a turbulent background of the same intensity (TKE = 4.4 cm^2/s^2). The results for jets emitted into quiescent background will be also presented for completeness. However, the differences with the results of jets emitted into a turbulent background will not be discussed in detail since they were presented in the previous section and in Khorsandi et al. (2013).

Figures 5.25 and 5.26 depict the evolution of the normalized mean centerline concentration and axial velocity in quiescent and background turbulence for Re=10600 and 5800 jets, respectively. The overall effect of the turbulent background is to reduce both the mean concentration and velocity (as discussed above and in Khorsandi *et al.* 2013). In the presence of background turbulence, the decay of the mean centerline quantities of the scalar and velocity fields for both jet Reynolds numbers investigated is similar although the mean axial velocity is slightly higher than the normalized mean concentration near the jet axis. However, farther downstream (x/D≥40) this trend reverses.

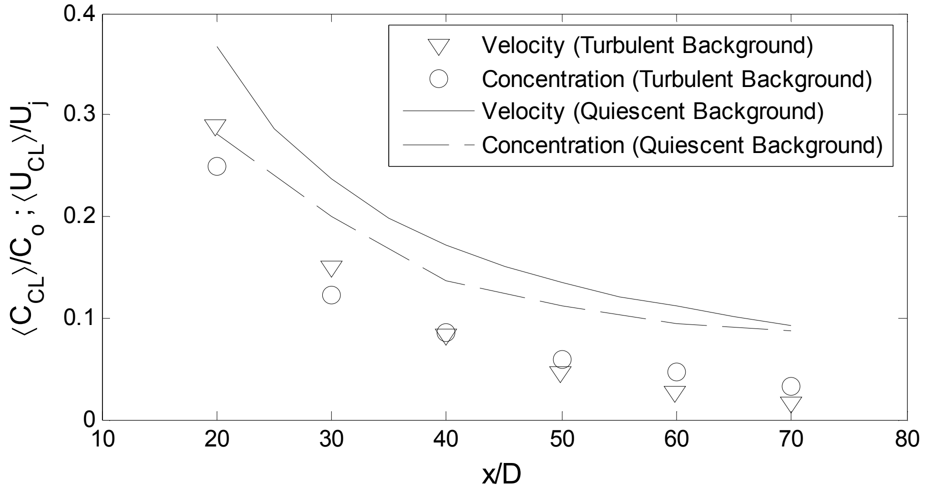

Figure 5.25 Comparison of the normalized mean centerline concentration and the normalized mean centerline axial velocity of Khorsandi et al. (2013). Re=10600. Jet emitted into quiescent and turbulent background (TKE=4.4 cm^2/s^2). The quantities are normalized by their value at the nozzle exit.

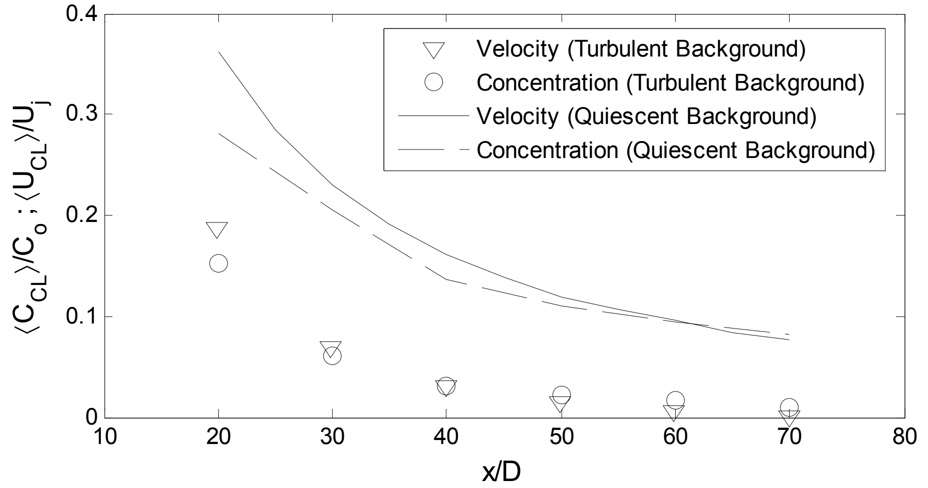

Figure 5.26 Comparison of the normalized mean centerline concentration and the normalized mean centerline axial velocity of Khorsandi et al. (2013). Re=5800. Jet emitted into quiescent and turbulent background (TKE=4.4 cm^2/s^2). The quantities are normalized by their value at the nozzle exit.

The evolution of the centerline RMS concentrations and velocities for both the quiescent and turbulent background is presented in Figures 5.27 and 5.28 for Re=10600 and 5800 jets, respectively. The effect of the turbulent background is to increase both the RMS concentration and velocity. In the presence of background turbulence, the decay of the RMS concentration and velocity at the centerline is similar for the two Reynolds numbers investigated. For the jet at Re=10600, the RMS axial velocity is higher than the RMS concentration (as for the mean quantities). For x/D > 50, the axial RMS velocity becomes only slightly higher than the RMS concentration at the centerline. For the Re = 5800 jet, the difference between the RMS axial velocity and the RMS concentration is less dependent on x/D, although the normalized RMS concentration is always lower than the normalized RMS axial velocity. For the jet of Re = 5800, the background turbulence has already disrupted the jet structure so that there is no double peaked profile of RMS velocities by x/D = 20, whereas the double peaked RMS profile in the jet of Re= 10600 remains until just short of x/D = 40 (refer to figure 5.14). The slightly higher values of RMS velocities compared to RMS concentrations are also consistent with previous observations of jets emitted into quiescent background or laminar co-flows (Law and Wang 2000; Antoine *et al.* 2001).

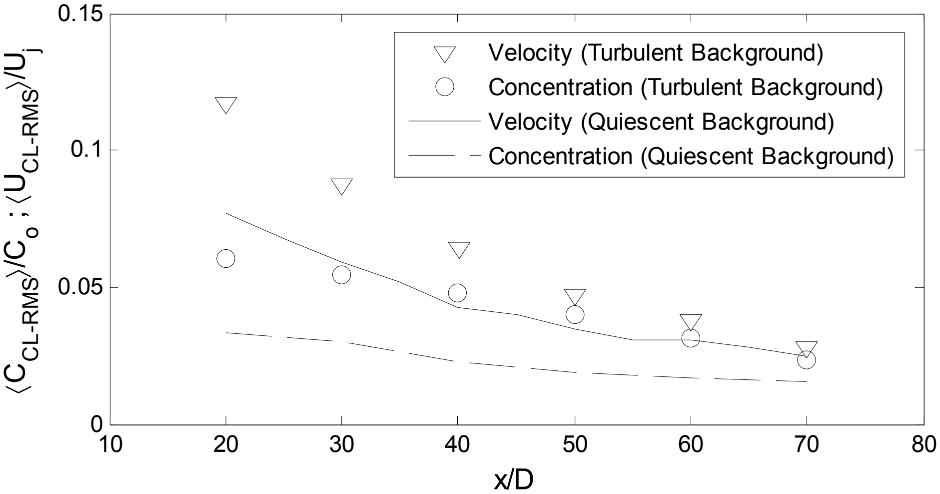

Figure 5.27 Comparison of the normalized centerline RMS concentration and normalized centerline RMS axial velocity of Khorsandi et al. (2013). Re=10600 jet emitted into quiescent and turbulent background (TKE=4.4 cm^2/s^2). The quantities are normalized by their value at the nozzle exit.

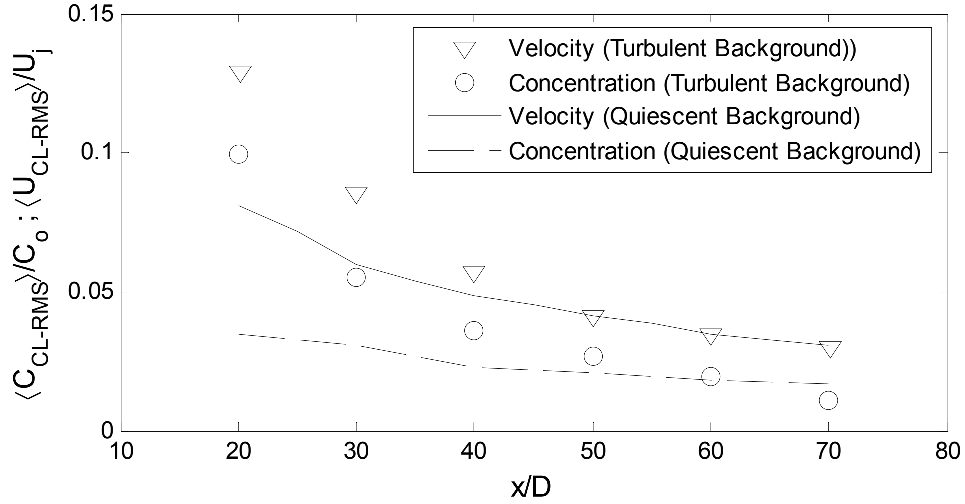

Figure 5.28 Comparison of the normalized centerline RMS concentration and normalized RMS axial velocity of Khorsandi et al. (2013) at centerline. Jet at Re=5800 emitted into quiescent and turbulent background (TKE=4.4 cm^2/s^2). The quantities are normalized by their value at the nozzle exit.

The radial profiles of mean concentration and velocity in both quiescent and turbulent backgrounds for jets at Re=10600 and 5800 are plotted in Figure 5.29 and 5.30, respectively. The turbulent background causes a reduction in the mean concentration and velocity with respect to the jet emitted into a quiescent background. In the presence of background turbulence, for the two Reynolds numbers investigated, the profiles of concentration and velocity exhibit clear jet structures near the jet exit and progressively lose their jet characteristics with increasing downstream distance (flatter profiles). The main difference is the larger extent (in the radial direction) of the scalar field, and lower values for the normalized mean concentration near the centerline at positions close to the jet exit. The difference near the jet exit may be attributable to different developing regions of the two fields, since the profiles of velocity and concentration become very similar farther downstream (x/D = 40 and 50).

The wider scalar-field profiles have also been observed in jets in quiescent backgrounds (Law and Wang 2000) and have been observed both in air jets using temperature as the passive scalar (Sc = 0.7) and in water jets using fluorescent dyes (Sc~2000) (Dowling and Dimotakis, 1990; Miller, 1990). Antoine *et al.* (2001) argued that the scalar profile may be wider due to the fact that the scalar is transported by the three components of the velocity.

The radial transport or relative effectiveness of mixing of a scalar compared to momentum is given by the turbulent Prandtl number (Pr_T). Pr_T can be defined as the ratio of the eddy viscosity, ν_T, to the eddy diffusivity, $\mathcal{D}_T$, or as the product of two ratios, the ratio of the radial turbulent flux of velocity to that of the scalar, f_{vu}/f_{vc}, and the ratio of the gradient of the mean scalar concentration to that of the axial velocity, f_c'/f_u' (van Reeuwijk *et al.* 2016).

$$Pr_T = \frac{\nu_T}{\mathcal{D}_T} = \frac{f_{vu} f_c'}{f_{vc} f_u'} \tag{5.1}$$

The spatially averaged turbulent Prandtl number can be inferred from the ratio of widths of the momentum and scalar fields (assuming Gaussian profiles) as the scalar and velocity fields obey the same similarity equation in which the radial mixing must balance the divergence in the axial flux. In jets emitted into quiescent backgrounds $Pr_T = 0.7$ (Chen & Rodi 1980), suggesting that turbulence mixes a scalar more efficiently than momentum (Chua *et al.* 1990). We hypothesize that the larger radial extent of the scalar field in the present work results from i) turbulent transport of scalar in the radial direction at the edge of the jet, and ii) from a comparison of scalar (concentration) and vector (one velocity component) quantities. Visualizations have shown that the edge of a jet emitted into a quiescent background mainly meanders in the radial direction (e.g. Westerweel *et al.* 2005) with nominally zero mean axial velocity. These fluctuations in the radial direction (meandering of the edge) may cause turbulent transport of the scalar field. Additionally, the axial velocity may take positive and negative values (especially at the edge of the jet) resulting in a zero mean axial velocity. However, the concentration of scalar tagging the fluid is a positive quantity and will not average to zero even if the velocity component does. Hence, comparing a scalar quantity with a component of the velocity vector (with nominal zero mean at the edge of the jet) may also contribute to the observed difference in the radial extents of the scalar fields.

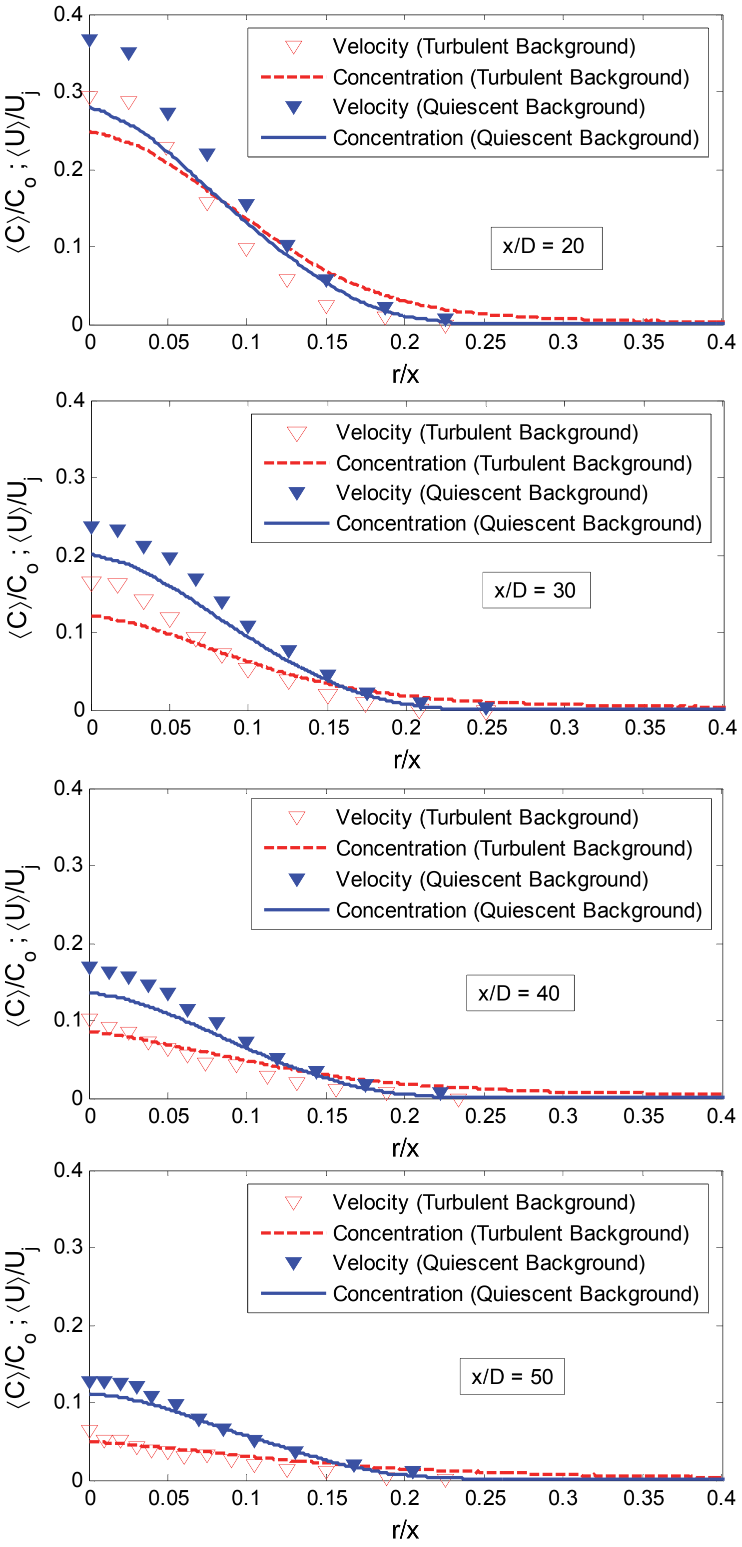

Figure 5.29 Radial profiles of mean concentration and mean axial velocity normalized by their value at the jet exit in quiescent and turbulent backgrounds (velocity results from Khorsandi et al. 2013). Jet at Re=10600.

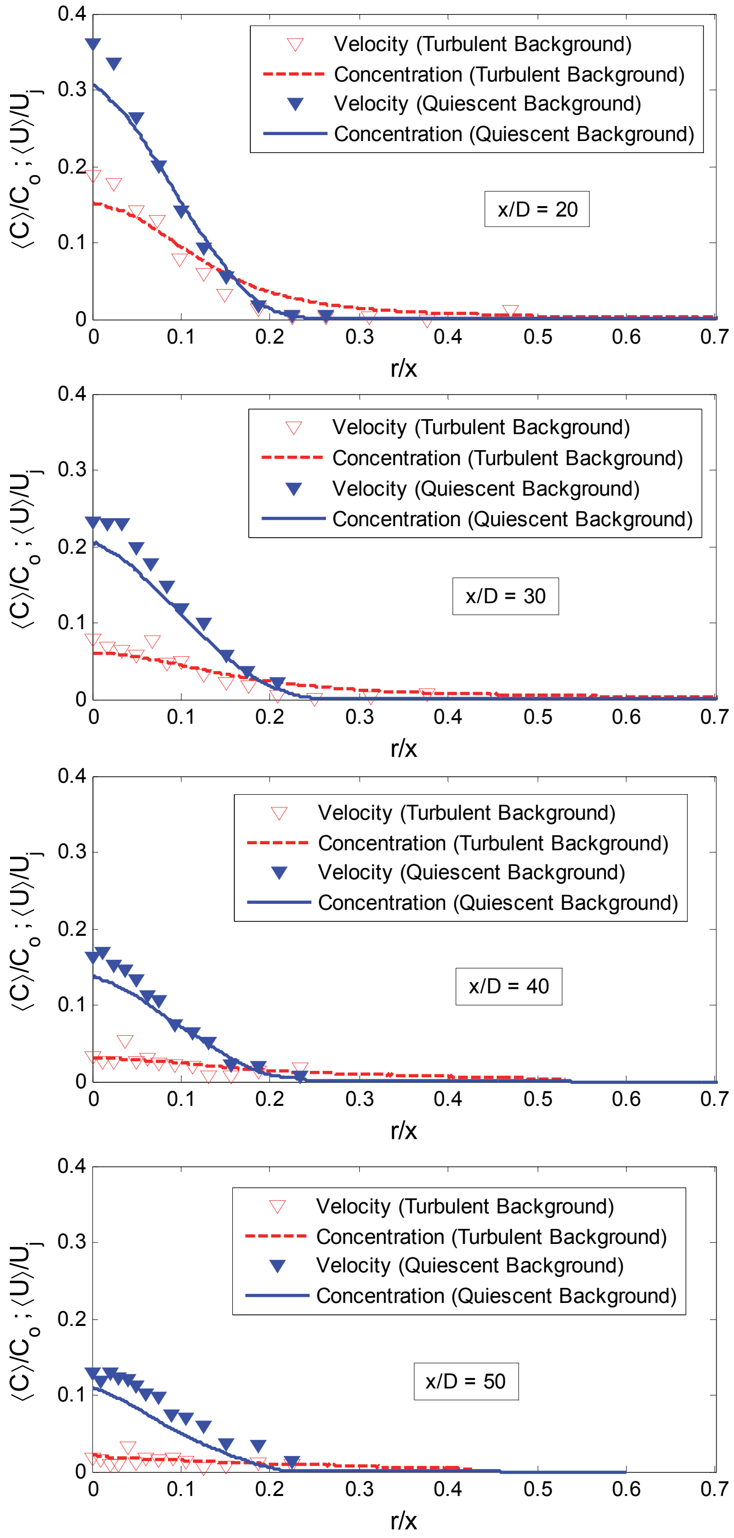

Figure 5.30 Radial profiles of mean concentration and mean axial velocity normalized by their value at jet exit in quiescent and turbulent backgrounds (velocity results from Khorsandi et al. *2013). Jet at Re=5800.*

Figure 5.31 plots the half-width of the scalar and velocity field for Re=10600 jets emitted into quiescent and turbulent backgrounds at different downstream positions. The evolution of the jet half-width for Re=5800 was not reported in Khorsandi *et al.* (2013), so a comparison cannot be made at this lower Reynolds number. The half-widths of the scalar field are slightly higher than that of the velocity field for the case of jets emitted into quiescent backgrounds. However, for jets emitted into turbulent background, the difference in the half-width of the scalar and velocity fields is notably larger than in the case of a quiescent background and increases with downstream distance. The larger difference is attributed to an increase in the radial transport of scalar resulting from the increased meandering of the jet in a turbulent background and turbulent diffusion enhanced by the turbulent background.

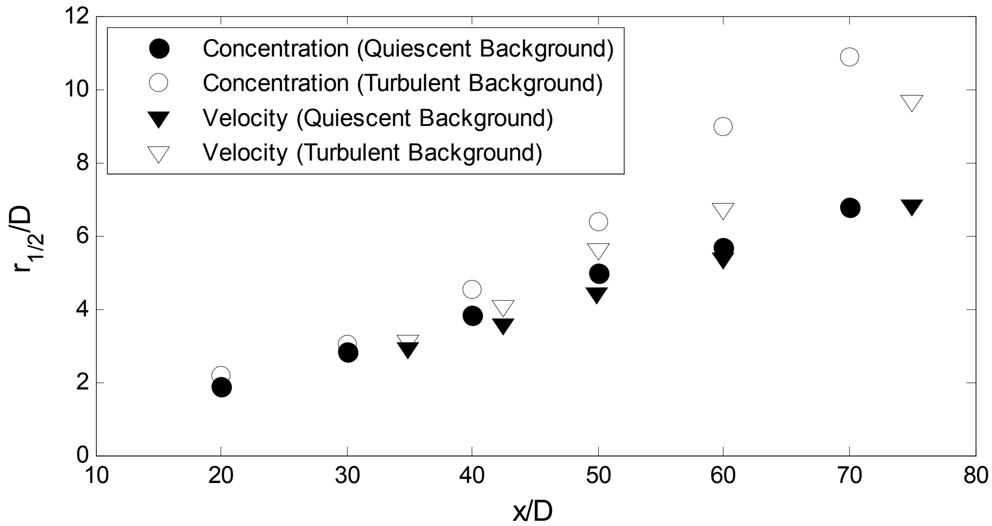

Figure 5.31 Downstream evolution of the half-width of the concentration and velocity fields for the jet at Re=10600 emitted into quiescent and turbulent backgrounds.

The radial profiles of normalized RMS concentrations and velocities for Re = 10600 and 5800 jets emitted into both quiescent and turbulent backgrounds are plotted in Figure 5.32 and 5.33, respectively. As discussed in the previous section and in Khorsandi *et al.* (2013), the turbulent background increases the RMS concentration and velocity (with respect to those of the jet emitted into a quiescent background). In the presence of background turbulence the velocity field exhibits overall higher values than the concentration field, especially near the jet centerline. This characteristic has also been observed in jets emitted into a quiescent background, where the normalized RMS velocity asymptotes to a value higher than that of the scalar field at the centerline ($U_{RMS}/\langle U_{CL}\rangle = 0.25$ and $C_{RMS}/\langle C_{CL}\rangle = 0.22$), although the turbulent background tends to magnify this difference. In the presence of a turbulent background, the characteristic off-axis peaks in the RMS profiles observed in jets emitted into quiescent background disappear as x/D increases. The radial extent of the scalar field is larger than that of the velocity field for the two Reynolds numbers studied as observed in the mean radial profiles. Similarly, the difference can be attributed to an increased scalar transport in the radial direction resulting from the meandering of the jets emitted into a turbulent background and turbulent diffusion enhanced by the turbulent background.

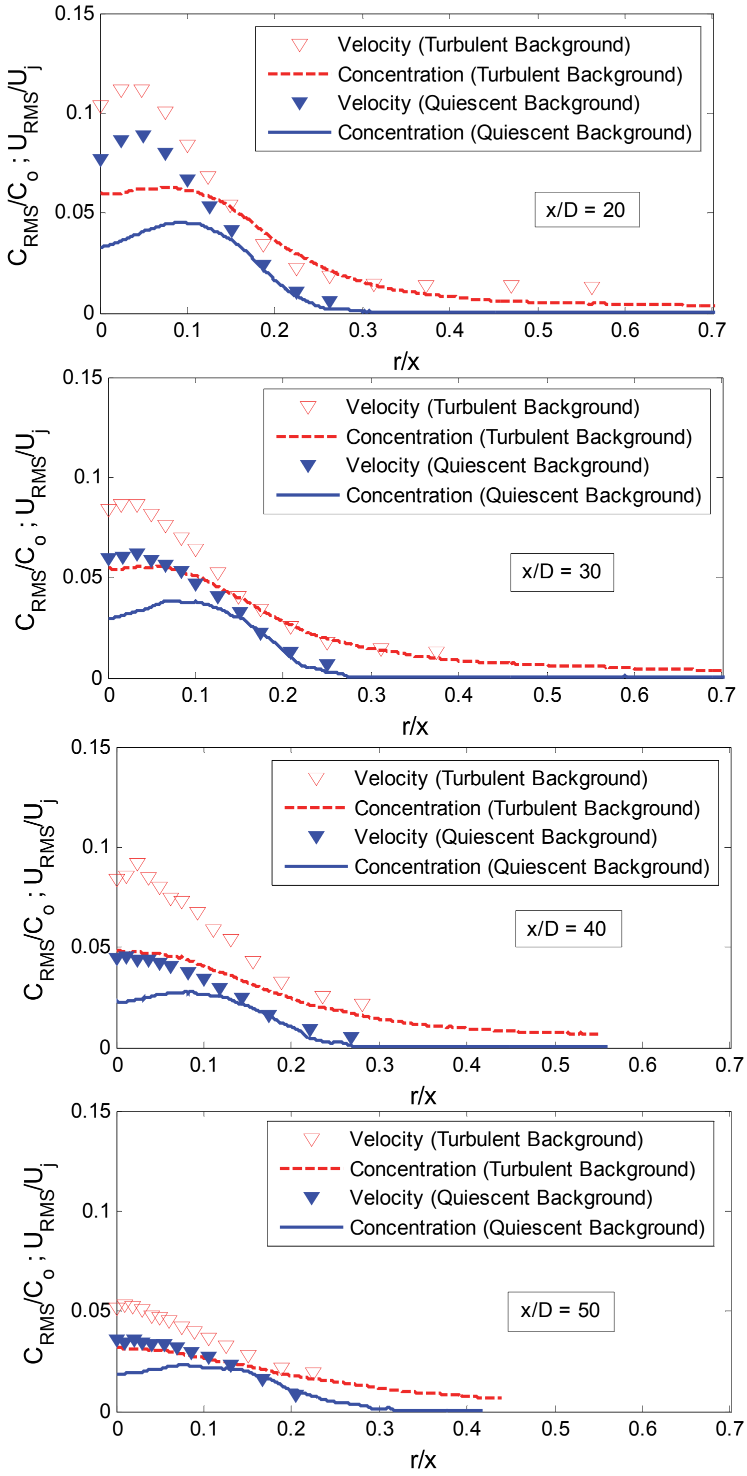

Figure 5.32 Comparison of the radial profiles of RMS concentration and RMS axial velocity of Khorsandi et al. (2013). Jet at Re=10600 emitted into quiescent and turbulent backgrounds (TKE=4.4 cm^2/s^2). The quantities are normalized by their value at the nozzle exit.

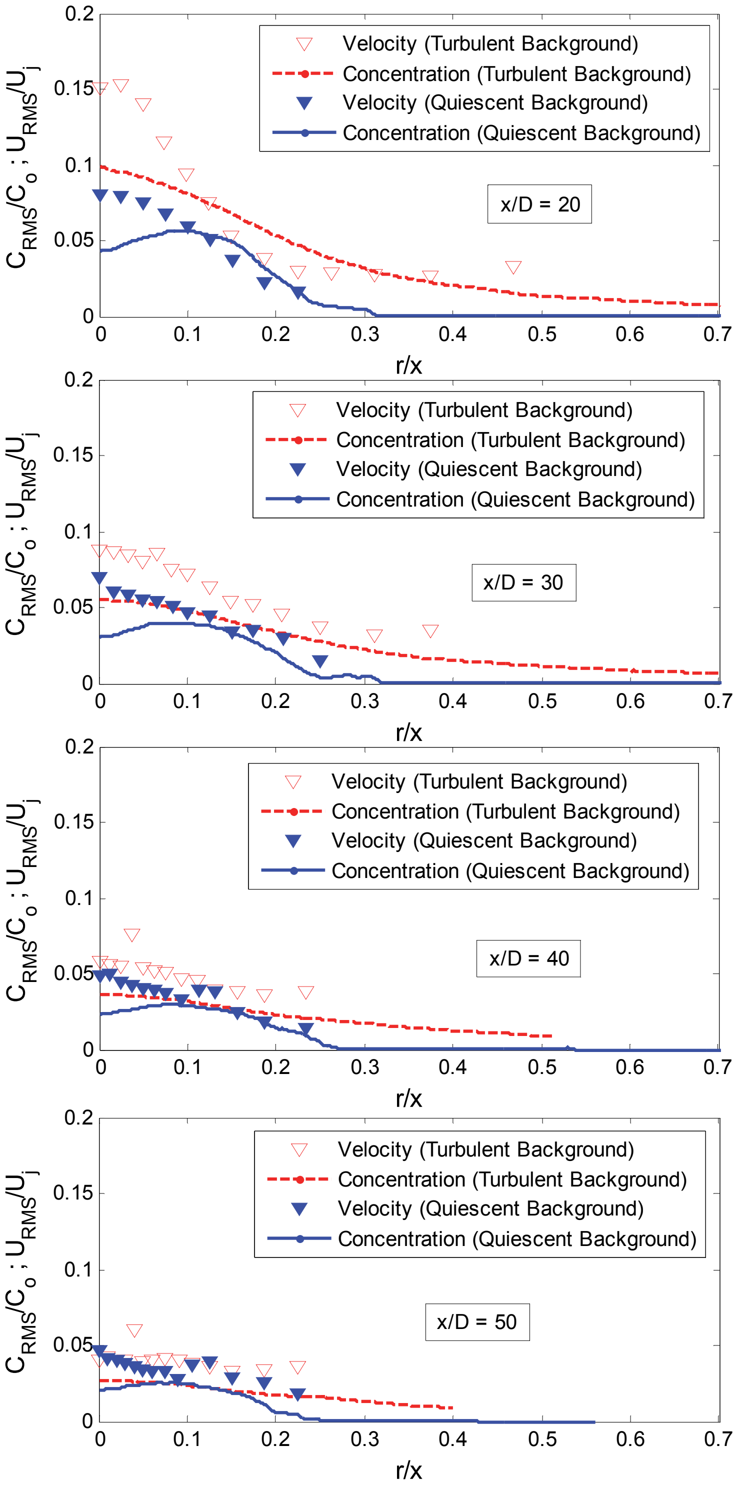

Figure 5.33 Comparison of the radial profiles of RMS concentration and RMS axial velocity of Khorsandi et al. (2013). Jet at Re=5800 emitted into quiescent and turbulent backgrounds (TKE=4.4 cm^2/s^2). The quantities are normalized by their value at the nozzle exit.

Furthermore, far away from the jet centerline, the radial profile of RMS velocity must asymptote to the RMS velocity of the background turbulence, whereas the RMS concentration must tend to zero — an inherent difference in the two quantities. The presence of the external turbulence thus renders it difficult to identify the velocity fluctuations from the jet (especially at large radial distances) and may hide/dissipate them at large radial distances. Given that the RMS concentration must asymptote to zero at large radial distances (the turbulent background ultimately fully mixes the scalar), the external turbulence cannot "hide" the presence of the scalar. The profiles of Figures 5.32 and 5.33 for the scalar field indeed decrease and seem to approach zero although the field of view is too small to observe this for the far downstream distances (e.g. x/D = 40 and 50).

The differences in the evolution of both the scalar (present work) and velocity fields (Khorsandi *et al.* 2013) for jets emitted into quiescent and turbulent backgrounds may be further understood by analyzing the governing equations. Specifically, studying the magnitude of the terms in the momentum equation and conservation of scalar flux may help to understand the effect of a turbulent background on turbulent jets. The evolution of the momentum in the x-direction neglecting the viscous term is governed by the following equation (Hussein *et al.*, 1994):

$$\int_0^\infty (\langle U\rangle^2 + \langle u^2\rangle - \langle v^2\rangle) r dr - \frac{M_o}{2\pi\rho} = \frac{1}{2}\frac{d}{dx}\int_0^\infty (\langle UV\rangle + \langle uv\rangle) r dr\bigg|_0^x + \frac{3}{2}\int_0^\infty \langle V\rangle^2 r dr \qquad (5.2)$$

where M_o is the momentum at the jet exit. In the case of a jet issuing into a quiescent background the terms on the right hand side of equation 5.2 are negligible compared to $M_o/2\pi\rho$. Moreover, the mean momentum flux in the x-direction ($M = 2\pi\rho \int_0^\infty \langle U\rangle^2 r dr$) accounts for at least 90% of M_o (Hussein *et al.* 1994; Law and Wang 2000). Analogously, one can verify the conservation of scalar flux in a jet emitted into a quiescent background by integrating the total flux in the x-direction ($F_T = 2\pi \int_0^\infty (\langle UC\rangle + \langle uc\rangle) r dr$) at different downstream distances. Similar to the case of the momentum flux, Law and Wang (2000) found that the mean scalar flux ($F = 2\pi \int_0^\infty \langle UC\rangle r dr$) was equal to 92% of the scalar flux at the jet exit (F_o).

It would be beneficial to investigate the evolution of the terms of the momentum equation and the scalar flux to further describe the effect of the turbulent background. However, given that only radial profiles of $\langle U\rangle$ and $\langle u^2\rangle^{1/2}$ were reported in Khorsandi *et al.* (2013), the magnitude of the terms involving $\langle v^2\rangle$ and $\langle uv\rangle$ in equation 5.2 cannot be calculated. Moreover, the reported radial profiles of $\langle V\rangle$ do not coincide with the downstream positions of the profiles of $\langle U\rangle$ and $\langle u^2\rangle^{1/2}$, preventing us from being able to calculate $\langle UV\rangle$. However, it is clear that although $\langle V\rangle$ increases in the presence of the external turbulence, it is an order of magnitude smaller than $\langle U\rangle$, and thus the last term in equation 5.2 is still negligible. Additionally, $\langle uc\rangle$ cannot be estimated from the present measurements (for the calculation of the scalar fluxes) since it requires simultaneous measurements of concentration and velocity.

Despite the lack of information to calculate all the terms one might ideally wish to study, one can still compare the mean momentum ($M = 2\pi\rho \int_0^\infty \langle U \rangle^2 r dr$) and mean scalar flux ($F = 2\pi \int_0^\infty \langle UC \rangle r dr$) in the x-direction which are the leading terms in the quiescent background. Figure 5.34 and 5.35 show the downstream evolution of M/M_o and F/F_o for the jet at Re = 10600 emitted into quiescent and turbulent backgrounds. The integrals for M were performed using the best fit curve to the velocity data points of Khorsandi *et al.* (2013). Although the results for the quiescent background in Figure 5.34 seem slightly overestimated (presumably from overestimated velocity measurements and amplified by computing $\langle U \rangle^2$), we are interested in their relative importance with respect to the results for the jet emitted into a turbulent background. In Figure 5.34 we can observe that the contribution of M to equation 5.2 is significantly decreased in the presence of external turbulence and it decreases with downstream distance. The decrease with downstream distance is expected since the jet structure is being destroyed. The fact that M decreases in the presence of background turbulence indicates that the remaining terms become important as opposed to the quiescent background, implying that the first term in the right hand side of equation 5.2 is no longer negligible (as noted above $\langle V \rangle$ is an order of magnitude smaller that $\langle U \rangle$, rendering the second term of the right hand side negligible). As the jet becomes weaker in the downstream distance, it is more easily affected by the turbulent background and results in larger gradients in the x-direction, ultimately increasing the magnitude of the first term in the right hand side. Additionally, the measurements show that $\langle u^2 \rangle^{1/2}$ is increased within the jet in the presence of external turbulence although $\langle v^2 \rangle^{1/2}$ may counteract it (not reported), but the term $\langle u^2 \rangle - \langle v^2 \rangle$ overall may be expected to be larger than in the case of the quiescent background. Thus, the increased RMS and derivatives in the x-direction in the presence of the turbulent background may decrease the relative magnitude of M. The evolution of F/F_o is most likely a consequence of the reduced magnitude of M, it can be observed that the evolution of F/F_o and M/M_o are quite similar. Since the results show that U_{RMS} and C_{RMS} increase in the presence of the external turbulence, it is expected that ⟨uc⟩ would increase as well. However, it is important to note that it may not make $F_T/F_o=1$ since the scalar present in the areas with ⟨U⟩=0 is the result of turbulent transport in the radial direction. The radial transport of scalar is mainly due to the meandering of the jet and is not taken into account in the classical scalar flux ($F_T = 2\pi\int_0^{\infty}(\langle UC\rangle + \langle uc\rangle)rdr$). To be able to confirm the conservation of scalar, simultaneous measurements of velocity and concentration are necessary, especially to account for the transport due to the meandering of the jet. The results were not computed for the jet at Re = 5800 due to the large scatter in the data points.

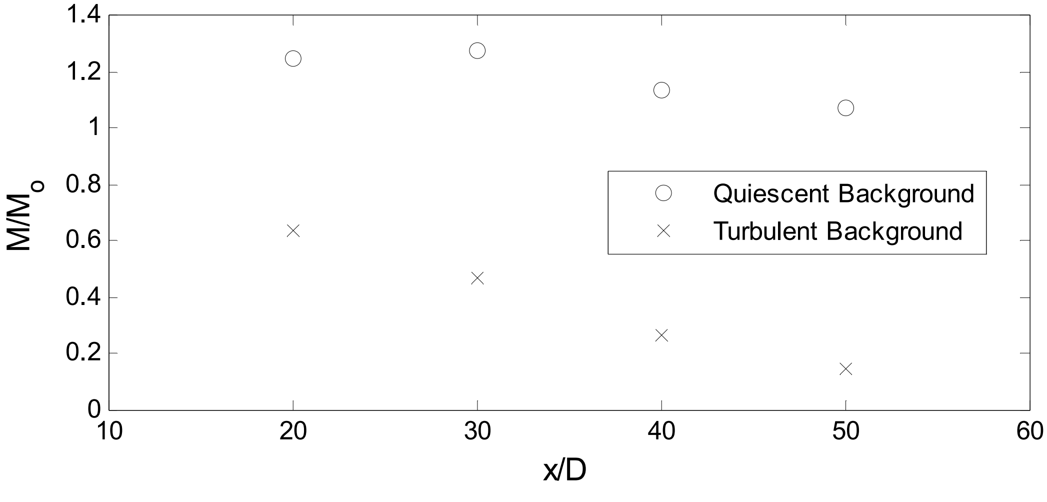

Figure 5.34 The downstream evolution of the mean momentum (M) in the x-direction. Jet at Re = 10600.

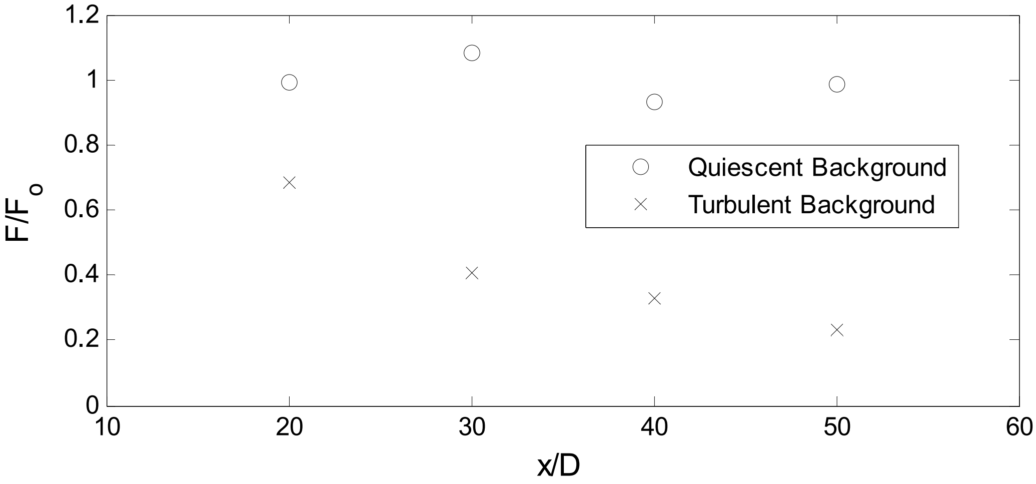

Figure 5.35 The downstream evolution of the mean scalar flux (F) in the x-direction. Jet at Re = 10600.

5.5 Discussion and relationship to previous studies

Given the results described in the previous section, it thus becomes sensible to discuss and interpret them in the context of previous studies, especially the work of Gaskin *et al.* 2004 who studied the planar jet in a shallow coflow with different turbulent intensities and Khorsandi *et al.* (2013), who analyzed the velocity field in the same facility under identical conditions. In particular, the questions of: i) self-similarity of the scalar field of the jet emitted into a turbulent background, ii) downstream evolution of the jet issued into a turbulent background, iii) mixing and entrainment in the presence of the background turbulence, and iv) the breakup location of the jet will be addressed.

5.5.1 The (lack of) self-similarity of a jet emitted into a turbulent background

The velocity and scalar fields of a turbulent jet emitted into a quiescent background become self-similar at sufficiently large downstream distances (e.g. Lockwood and Moneib 1980; Dowling and Dimotakis 1990; Hossein *et al.* 1994; Lipari *et al.* 2011; Darisse *et al.* 2015). However, the scalar (and velocity) fields were found to not exhibit self-similarity in the presence of background turbulence. More specifically, plots of $\langle C \rangle / \langle C_{CL} \rangle$ versus r/x (Figure 5.36) did not collapse onto a single curve for different downstream distances. Similarly, plots of $C_{RMS}/C_{RMS\text{-}CL}$ versus r/x did not exhibit self-similarity either (not shown). Given that the jet's velocity field was found to not be self-similar (Khorsandi *et al.* 2013), self-similarity of the scalar field would be somewhat unexpected. The lack of self-similarity for both fields can be presumably attributed to the multiplicity of velocity and length scales of a jet emitted into a turbulent background, as the background turbulence has velocity and length scales that are independent of those of the jet.

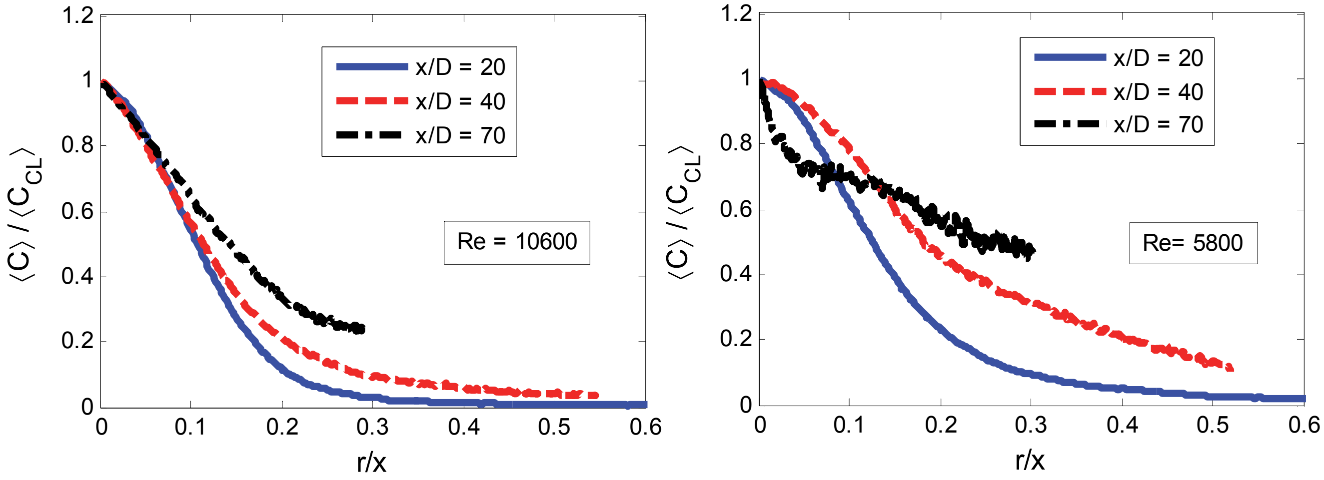

Figure 5.36 Radial profiles of mean concentration showing the lack of self-similarity for jets (Re = 10600 and 5800) emitted into a turbulent background.

5.5.2 Downstream evolution of the jet issued into a turbulent background

For the case of the jet emitted into a turbulent background, the downstream evolution of (radial and axial) profiles of mean concentration and half-widths of the scalar field have been identified by Gaskin *et al.* (2004) to occur in three regions. In the first region, near the nozzle exit, the background turbulence has a negligible effect on the jet and its evolution is similar to a jet emitted into a quiescent background. In the second region, the background turbulence begins to disrupt the structure of the jet resulting in mean momentum that is increasingly reduced with downstream distance. Finally in the third region the jet structure is destroyed by the turbulent background and scalar mixing is accomplished only by the fluctuations of the background turbulence. This general evolution of the jet behaviour is seen in the present study of the scalar mixing corresponding to the evolution of the jet velocities in Khorsandi *et al.* (2013). The evolution of the velocity and scalar statistics varies between the two different experiments due to the different geometry of the jet and ambient: a plane jet in a shallow coflow (Gaskin *et al.* 2004) and an axisymmetric jet in a quiescent ambient (Khorsandi *et al.* 2013 and current study).

As the background turbulence begins to disrupt the jet structure, the jet velocity in both jet configurations is reduced and the width of the velocity profile increases with increased turbulent intensity of the background. However, the evolution of the scalar statistics differs. In the jet in a shallow coflow, the increasing disruption of the jet structure results in a reduction of the strength and length scale of the two-dimensional eddies of the jet structure, due to the effect of the bottom friction in the shallow flow, resulting in an increase in the jet concentration and a reduction of its width. However, once the relative magnitude of the background turbulence is large enough and the jet structure is destroyed, the scalar concentration decreases and the scalar profile flattens and will then increase due to turbulent diffusion (Gaskin *et al.* 2004). In the case of the axisymmetric jet in the turbulent ambient produced by the RJA, the increasing disruption of the jet structure is accompanied by increased meandering of the jet path due to the eddies of the background turbulence, and the combination of these two effects results in a decrease in the scalar concentration of the jet and an increase in width of the scalar profile. Again once the relative magnitude of the background turbulence is large enough, the jet structure is destroyed (resulting in the flat profiles of mean and RMS concentrations).

The three regions were identifiable for the jet at Re = 5800 emitted into a turbulent background. Figure 5.37 shows the downstream evolution of the inverse of the centerline concentration and half-width of the scalar field with vertical lines indicating the approximate locations of the limits of the three regions. Near the jet exit, the values are identical to those of a jet emitted into a quiescent background. Subsequently, a difference is observed with respect to the statistics of the jet emitted into a quiescent background with this difference progressively increasing with downstream distance. Finally, the concentrations and widths no longer follow the trends, which implies the destruction of the jet structure (confirmed by the flat profiles of mean and RMS concentrations in Figures 5.11 and 5.14, respectively). The limited range for the measurements ($10 \leq x/D \leq 70$) prevented the clear observation of the three regions (especially the third one) for the jet at Re=10600. Similarly, the limited data reported in Khorsandi *et al.* (2013) for the velocity field prevent us from presenting the analogous regions for the velocity field. However, given the similar behavior of the two fields (presented in the previous section), it is reasonable to expect the existence of the three regions for the velocity field.

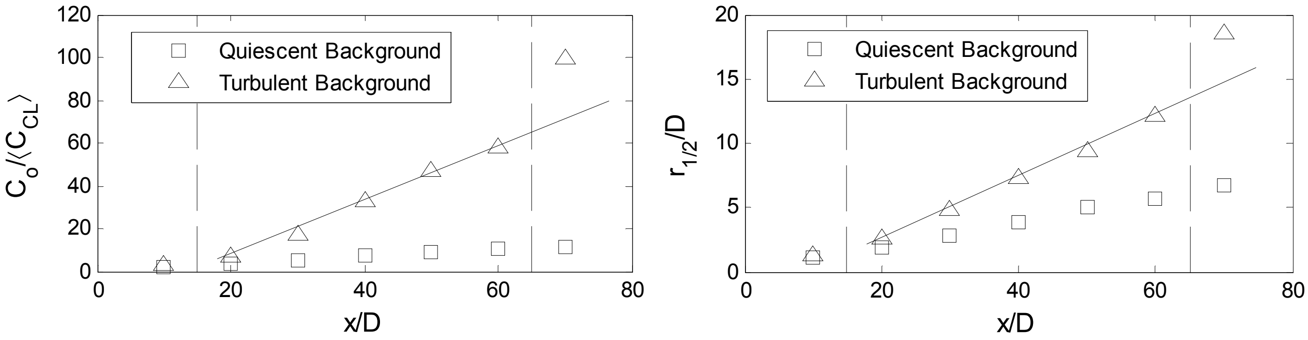

Figure 5.37 Downstream evolution of the inverse of the mean concentration and half-width of the scalar field for the jet at Re=5800. The dashed vertical lines indicate the approximate location of the limits of the three regions of the evolution of the jet emitted into a turbulent background.

5.5.3 Mixing and entrainment in the presence of background turbulence

Although the mean concentrations measured on the centerline of a jet emitted into a turbulent background exhibited lower values than a similar jet emitted into a quiescent one, which might imply an overall reduction in concentrations, inspection of the probability density functions of the concentration nevertheless revealed high concentrations on the order of those measured in a jet emitted into a quiescent background albeit with lower probability. The probability density functions also showed a significant increase in the probability of low concentrations for jets emitted into a turbulent background. The described changes in the probability density functions (resulting in significantly higher RMS concentrations) for jets emitted into background turbulence are the consequence of higher degrees of intermittency of the scalar field. The flow visualizations of a jet emitted into a turbulent background revealed a complex mixing process influenced by the jet meandering. The higher intermittency resulted presumably from the meandering of the jet. Similarly, the meandering of the jet caused higher mean and RMS concentrations at the edges of the jet emitted into a turbulent background as well as increased widths due to the enhanced (though intermittent) radial transport of scalar during the meandering of the jet. Hence, the increased intermittency in the scalar field (of a jet emitted into a turbulent background) resulted in high concentrations even at large radial distances (although the events occurred with a relatively lower probability). These findings have important practical implications since they show that i) mean quantities are not necessarily representative of the instantaneous concentrations in the presence of a turbulent background and ii) sufficient data must be collected to capture the high-concentration events. For example, certain contaminants measured in field studies may have toxic effects at sufficiently large instantaneous concentrations, even though their mean concentrations are deemed sufficiently small/safe. The increased intermittency in the scalar field and the meandering of jets emitted into turbulent backgrounds are consistent with the results and observations of previous related studies. Bagchi and Kottam (2008) studied the heat transfer from a sphere in a turbulent stream and found significantly higher fluctuations of the instantaneous Nusselt number in the presence of the background turbulence. The flow visualizations of Hubner (2004) showed the meandering of buoyant plumes emitted into grid-generated turbulence. These observations confirm the characteristic meandering of jets/plumes propagating into a turbulent background despite the different means of generation of the turbulence (grid-generated or from a RJA).

Historically (*i.e.* in the context of jets emitted into quiescent surroundings) the entrainment in a turbulent jet has been typically associated with an inward velocity at the edge of the jet. In such scenario, ambient fluid is continuously "absorbed" by the jet (at its edge, and directed towards the jet axis) and the mass flow rate associated with the mean velocity field ($\dot{m}(x) = \rho \int \langle U \rangle dA$) thus increases with downstream distance. The results of Khorsandi *et al.* (2013) demonstrated that the mass flow rate for a jet emitted into a turbulent background was lower than that of a jet emitted into a quiescent background. This lower entrainment may imply lower mixing within jets emitted into a turbulent background. The probability density functions of the concentrations showed that the maximum concentrations within a jet emitted into a turbulent background were on the order of those of a jet emitted into a quiescent background. The absence of significantly higher concentrations is attributed to the mixing and transport of scalar in the radial direction due to the meandering of the jet. Moreover, the meandering of the jet increases with downstream distance since the jet becomes "weaker" while the turbulent background is constant (at least in the present study) facilitating the displacements of the jet. Nevertheless, the decreased $\dot{m}(x)$ is consistent with the evolution of the momentum flux associated with the mean flow ($M = 2\pi\rho \int_0^\infty \langle U \rangle^2 r dr$) discussed in the last section. M decreases with downstream distance for a jet emitted into a turbulent background (Figure 5.34) and the rest of the terms must increase to conserve the momentum (equation 5.2). The fact that M ($= 2\pi\rho \int_0^\infty \langle U \rangle^2 r dr$) is not solely conserving the momentum and decreases with downstream distance implies automatically a decrease in the mass flow rate ($\dot{m}(x) = \rho \int \langle U \rangle dA$). Also, as presented above, the mean scalar flux ($F = 2\pi \int_0^\infty \langle UC \rangle r dr$) followed the same trend as the mean momentum (Figure 5.34 and 5.35). In this regard, the results of Hubner (2004) for a plume emitted into a turbulent background are relevant. In plumes emitted into a quiescent background, the mean buoyancy flux ($B = 2\pi \int_0^\infty \langle W \rangle \langle g' \rangle r dr$ where W is the axial velocity and g' is the local buoyancy) is constant along the plume axis, analogous to the mean scalar flux ($F = 2\pi \int_0^\infty \langle UC \rangle r dr$) in turbulent jets. Hubner (2004) observed a decrease in the mean buoyancy flux (B) in the presence of ambient turbulence with respect to a plume emitted into a quiescent background, confirming that the mean quantities are affected and the contribution of the different terms in the equations of conservation changes in the presence of background turbulence.

The lack of self-similarity, and the decrease in the mean momentum and scalar fluxes are directly related to changes of the jet structure in the presence of the background turbulence. Moreover, this may also imply a change in the entrainment mechanism. For a jet emitted into a quiescent background, recent investigations have shown that entrainment is principally effected by the small scales at the edge of the jet (Westerweel *et al.* 2005, 2009; Wolf *et al.* 2012). The transformation of ambient fluid into turbulent flow is accomplished by a small-scale process (termed “nibbling”), which occurs through a turbulent/nonturbulent interface (TNTI) separating the turbulent flow (jet) and ambient fluid. In the presence of background turbulence, Gaskin *et al.* (2004) proposed that, once the jet structure is disrupted, turbulent diffusion by the background turbulence dominates and Khorsandi *et al.* (2013) proposed that the entrainment mechanism may have changed from a small-scale (nibbling) process to a process dominated by turbulent diffusion at the interface of the jet and ambient flow. However, the effects of the meandering of the jet were not considered (in Khorsandi *et al.* 2013) and they described the entrainment in terms of the typical transport of ambient fluid in one direction (to the center of the jet) occurring in a wider jet. The flow visualizations of a jet emitted into a turbulent background in the present work revealed a more complicated mechanism of entrainment and mixing due to the jet meandering. In the presence of background turbulence the entrainment and mixing, with the destruction of the jet structure, changes from jet driven entrainment to become potentially dominated by i) increased lateral advection of the jet by large scales of the turbulent background during the meandering of the jet which is subsequently mixed by its smaller scales, and ii) turbulent diffusion significantly enhanced by the turbulent background. The second mechanism is observed as scalar moving radially and ultimately being mixed by the turbulent background (observed even when the jet is not meandering for a given period of time at a given position). Figure 5.38 shows a sequence of images of an example of this scenario. The jet axis (at Re=10600 and emitted into a turbulent background) stays essentially still and the background turbulence diffuses scalar in the radial direction (observed as scalar detected at large radial distances). The increased mixing due to large scales in the turbulent background is mainly observed when the jet is meandering (or just prior to commencing it). Figure 5.39 shows a sequence of images of the meandering of the jet and the resultant mixing of the fluid. The images correspond to a jet at Re=10600 emitted into a turbulent background. The large eddies of the turbulent background cause the jet to meander, in the movement the circular shape of the jet is distorted and ambient fluid is observed to mix with the jet fluid (lower concentrations are detected). Additionally, due to the meandering of the jet, the length of the path followed by the jet to reach the measurement section increases resulting in slightly lower concentrations within the jet (*i.e.* increase of the effective axial distance due to the deflection of the jet path). The movement of the jet, its deformation, and the enhanced mixing can also be observed in Figure 5.23 which is an example of this situation for a jet at Re=5800. The turbulent diffusion and increased mixing (during the jet meandering) occur simultaneously and randomly making the entrainment and mixing a complex process. Additionally, the observed enhanced transport of scalar in the radial direction by both turbulent diffusion and meandering of the jet explains the larger radial extents of the scalar field (compared to the velocity field) discussed in the results section. Lastly, a distinct surface separating the jet fluid and turbulent background (recognized by a discontinuity in velocity/concentration) that could be associated with nibbling was not observed (as in the case for a jet emitted into quiescent background). The absence of such a discontinuity may be attributed to the fact that quantities such as RMS velocity and (mean and fluctuating) vorticity asymptote to the values of the background turbulence instead of rapidly dropping to zero. As pointed out by Khorsandi *et al.* (2013), in terms of simple gradient transport arguments, the fluxes at the interface should decrease (compared with a jet emitted into a quiescent background) due to lower gradients at the interface and hence reducing the contribution of nibbling to the mixing process. In the case of the scalar field, the concentrations fluctuate in a larger range of magnitudes (at any radial position) than that for a jet emitted into a quiescent background. The increased intermittency further complicates the detection of an interface separating the flows since the concentrations no longer fluctuate within a narrow range of concentrations (as in the case of a jet emitted into a quiescent background) to be able to determine a threshold to distinguish the jet and ambient fluid. Moreover, the flow visualizations showed that the turbulent diffusion and meandering of the jet spread scalar all over the measurement section making discontinuities more difficult to both exist and detect in the scalar field. However, simultaneous measurements of velocity and concentration would be of further benefit to confirm these hypotheses and fully describe the mechanism of entrainment and mixing in the presence of background turbulence.

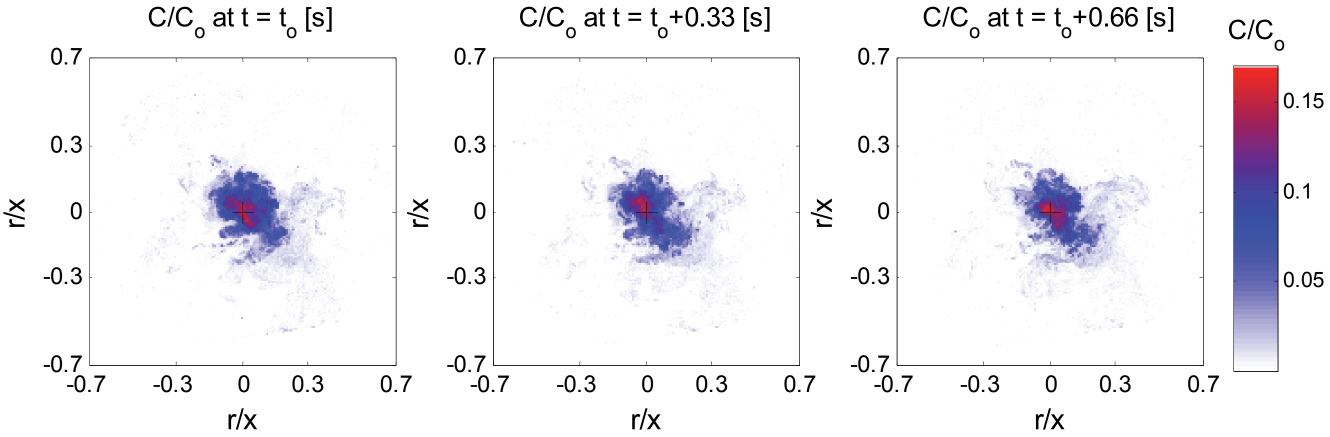

Figure 5.38 Sequence of images depicting turbulent diffusion by the background turbulence as evidenced by the scalar detected at large distances from the jet's axis. Cross section at x/D = 40, Re=10600. The black cross represents the position of the center of the mean concentration profile (i.e. the jet axis).

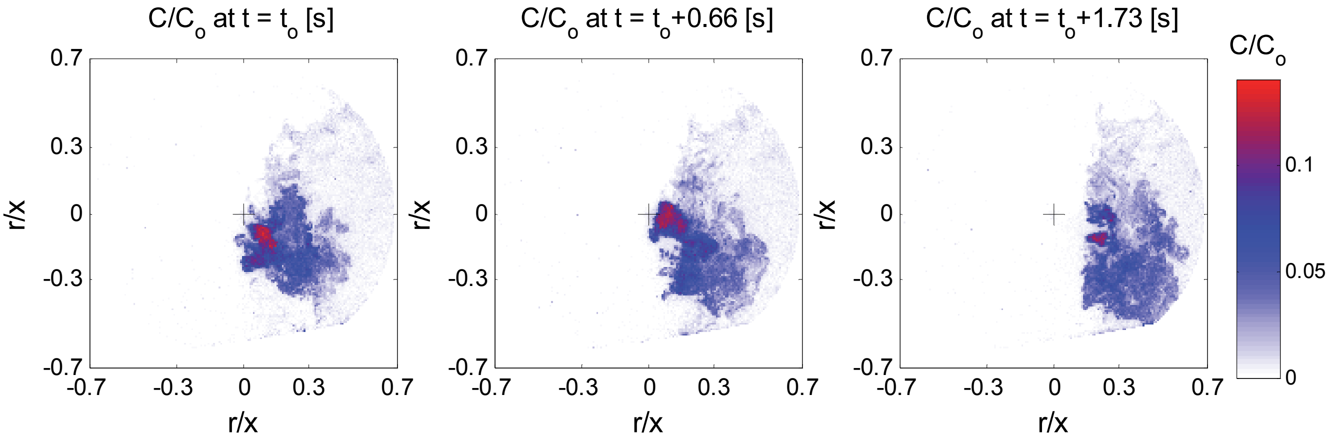

Figure 5.39 Sequence of images showing an example of the mixing associated with the meandering of the jet in a turbulent background. Cross section at x/D = 40, Re = 10600. The black cross represents the position of the center of the mean concentration profile (i.e. the jet axis).

5.5.4 Breakup location of the jet

For a turbulent jet emitted into a turbulent background, if the jet's (turbulent) Reynolds number is larger than that of the background turbulence, it is reasonable to expect that the jet would develop downstream (similarly to a jet emitted into a quiescent background) and then its structure would break up by the action of the external turbulence at some distance from the jet exit (due to the fact that the RMS and mean velocities within the jet decay with downstream distance) (Hunt 1994; Gaskin *et al.* 2004; Khorsandi *et al.* 2013). However, a conclusive and universal definition for the detection of the breakup location has not been found. The breakup location has been associated with a sudden increase in the spreading rate occurring when the external turbulence intensity reached a critical value in momentum jets (Guo *et al.* 1999; Law *et al.* 2001; Gou *et al.* 2005), buoyant jets (Cuthbertson *et al.* 2006) and plumes (Ching *et al.* 1999) in grid-generated turbulence. Nevertheless, in these studies the plume/jet was released perpendicularly to the grid resulting in: i) the background turbulence increasing in the direction of decrease of the plume/jet turbulence, and ii) the plume/jet being also blocked by the oscillation of the grid causing accumulation of mass (which explains the abrupt increase in spreading). Furthermore, the critical turbulence intensity (measured by the RMS velocity) was not identical for the different studies. Ching *et al.* (1999) detected the breakup at the point at which the RMS velocity of the background turbulence was around 0.625 the plume mean velocity, Guo *et al.* (1999) when it was approximately 0.125 of the jet mean centerline velocity, Law *et al.* (2001) when the jet was near the grid generating the background turbulence, Guo *et al.* (2005) at around 0.44 of the jet RMS velocity, and Cuthbertson *et al.* (2006) when it was of the order of the RMS velocity of the plume.

In the work of Khorsandi *et al.* (2013) on the study of a turbulent jet emitted into a turbulent background (such that the external turbulence intensity was constant along the axis of the jet), the breakup location was defined as the position where the mean axial velocity at centerline reached 1% of the exit velocity of the jet. In the present work, the breakup location of the scalar field was determined in the same fashion (i.e. the position at which the mean centerline concentration reached 1% of the initial concentration). Figure 5.40 shows the breakup locations for the scalar and velocity (Khorsandi *et al.* 2013) fields as a function of the ratio of the turbulent Reynolds number of the background turbulence to the jet Reynolds number defined as $Re_{T\text{-}RJA}/Re_{Jet} = u_{RMS\text{-}RJA}\,\ell_{RJA}/U_jD$, where $u_{RMS\text{-}RJA}$ is the RMS velocity of the background turbulence, ℓ_{RJA} is the integral length scale of the background turbulence, U_j is the velocity at the jet exit, and D is the diameter of the nozzle. With this definition, the breakup locations for the scalar field are observed to be slightly farther downstream than those for the velocity field. This may be attributed to the fact that although the turbulence can be dissipated, the scalar cannot be removed by the turbulent background as the mass remains, albeit at a much reduced concentration. This is furthermore consistent with the observation that the scalar field of a turbulent jet emitted into a quiescent background attains self-similarity at a downstream position slightly larger than that for the velocity field, so it may be reasonable to expect larger breakup locations for the scalar. Also, as observed in the figure, the breakup location is consistent with a decaying function of $Re_{T\text{-}RJA}/Re_{Jet}$ and extrapolation of the results predicts a breakup of the jet at the nozzle exit when $Re_{T\text{-}RJA}/Re_{Jet} \sim 0.4$ for both the scalar and velocity fields.

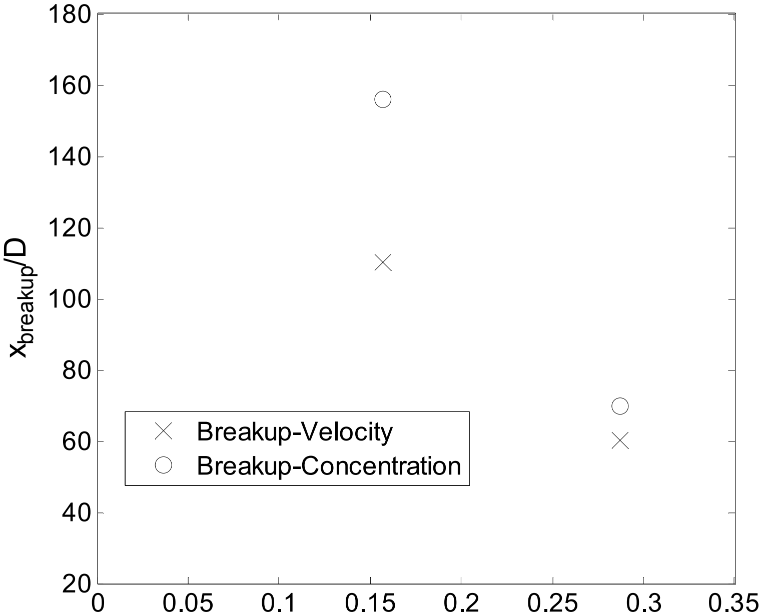

Figure 5.40 Breakup location of the mean velocity (×) and mean concentration (o) fields as a function of the ratio of the Reynolds number for the turbulent background to that of the jet.

Although the value (of 1% of the mean quantities at centerline) used herein to determine the breakup location is arbitrary and its validity may be questioned since the mean quantities also decay to these values in the absence of the turbulent background, one can compare the evolution of other statistics to confirm that the jet structure has been destroyed at those positions. For the jet at Re=5800 the breakup location of the scalar field was found to be located at x/D=70. This result can be validated by comparing the downstream evolutions of the statistics of the scalar field. The radial profiles of the mean (Figure 5.11) and RMS (Figure 5.14) concentrations became essentially flat at x/D = 70, with the inverse of the centerline concentration and half-width of the scalar field no longer following the trends measured upstream of this point (Figure 5.37). These observations support the notion that the jet's structure at this position has been decimated. Figure 5.41 summarizes the relevant results depicting the loss of the jet's structure at x/D = 70 for the jet at Re = 5800. In addition, the visualizations at x/D = 70 indicated a lack of jet structure at this location, where the scalar field was very well mixed by the background turbulence. Figure 5.42 shows a sequence of images of this situation, with Figure 5.24 being another example. Although the radial profiles of (mean and RMS) axial velocity up to x/D = 70 and the downstream evolution of the half-width of the velocity field (necessary to analyze in detail the loss of jet structure) were not reported in Khorsandi *et al.* (2013), the available data of the radial profiles at x/D=50 (the farthest downstream position reported) shows that the jet emitted into a turbulent background displays little jet structure at this position. The pertinent results of Khorsandi *et al.* (2013) are reproduced in Figure 5.43. The results are consistent with the jet being destroyed around this downstream position (x/D=50) given the approximate flat radial profiles, thus the $x_{breakup}/D = 60$ for the velocity field (determined from the 1% value at centerline in Khorsandi *et al.* 2013) seems adequate. The discussed results support the accuracy of the breakup location in this study and give a base for a more complete definition of the breakup location which includes the downstream evolution of the statistics of the fields. The $x_{breakup}/D = 156$ (from the 1% centerline value) of the scalar field for the jet at Re=10600 was estimated extrapolating a power law fitting to the available data (up to x/D=70). An analysis including the downstream evolution of the statistics cannot be conducted due to the lack of data at downstream positions farther than x/D=70 for the concentration field and x/D=50 for the velocity field. However, it is reasonable to expect that an analysis of the Re=10600 jet would show similar results to those for the Re=5800 jet since the higher injection of momentum may only cause the jet structure to prevail farther downstream.

Lastly, although the breakup location seems to coincide with the point at which the half-width of the jet becomes of the order of the integral length scale of the turbulent background for the jet at Re=5800 (see Figure 5.39), it is difficult to draw solid conclusions without further data. Experiments in a facility capable of varying the integral length scale of the background turbulence would be very beneficial to discuss the effects of the relative lengths scales of the jet and the turbulent background on the evolution and ultimate breakup of jets emitted into turbulent surroundings.

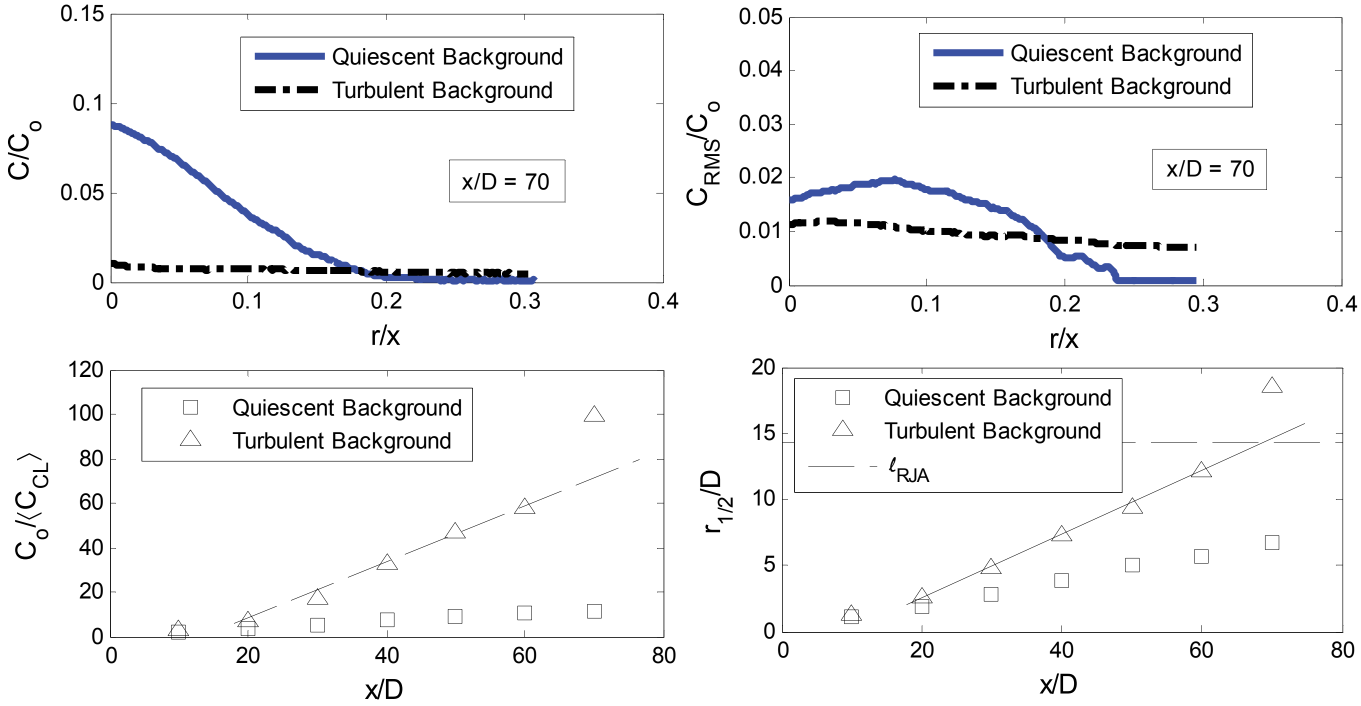

Figure 5.41 Relevant results in support of the distinct change in jet structure at x/D = 70 for the Re=5800 jet emitted into a turbulent background.

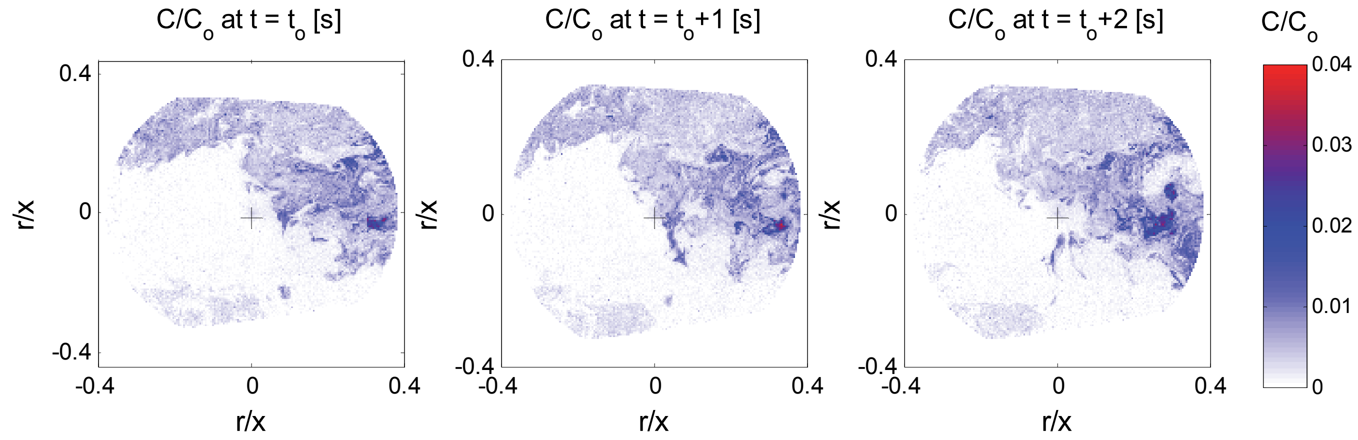

Figure 5.42 Sequence of images of a cross-section at x/D = 70 for the Re = 5800 jet emitted into a turbulent background. Observe the lack of a clear jet structure at this far downstream position.

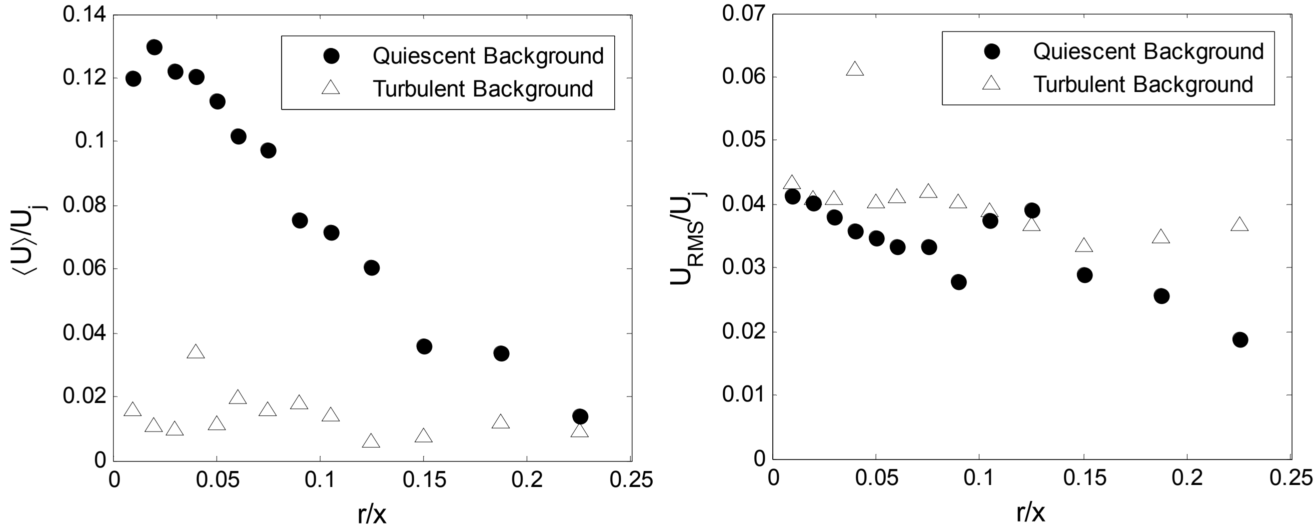

Figure 5.43 Radial profiles of the mean and RMS axial velocities for the Re=5800 jet at x/D=50. From Khorsandi et al. (2013).

5.6 Conclusions

The effect of background turbulence on the scalar field of a momentum-driven, axisymmetric turbulent jet at different Reynolds numbers was investigated. The present study builds on the work of Gaskin *et al.* (2004), who studied the concentration and velocity fields of a plane jet in a shallow coflow with different turbulence levels and complements the work of Khorsandi *et al.* (2013), who studied the velocity field of a turbulent jet emitted into a turbulent background. To the best of our knowledge, this represents the first study of the effect of quasi-homogeneous isotropic turbulence with negligible mean flow on the scalar mixing of a turbulent jet, the study of Gaskin *et al.*

(2004) includes mean flow and shallow flow effects. In the few previous studies of jets/plumes emitted into grid-generated turbulence, the prediction of scalar mixing were based on the velocity field or flow visualizations. Moreover, in those studies the jet/plume was released perpendicularly to the grid, experiencing an increasing turbulent background and subsequent blocking of the flow by the grid.

The results showed significant changes in the statistics of the scalar in the presence of background turbulence with respect to those of a jet emitted into quiescent background. The mean concentrations decreased near the centerline for jets emitted into a turbulent background. However, slightly larger mean concentrations were measured near the edge of the jet, which can be attributed to the observed increase in the width of jets issued into turbulent surroundings. The RMS concentrations were higher for the jets emitted into a turbulent background than those of the jet emitted into a quiescent one at all radial positions. Examination of the probability density functions of concentration revealed that the maximum concentrations were comparable for the quiescent and turbulent backgrounds. Nevertheless, the probability of lower concentrations was significantly increased for the jet emitted into a turbulent background. Flow visualizations revealed meandering of the jets that increases the intermittency of the scalar field and causes distinct changes in the probability density functions. The high degrees of intermittency of the scalar field for a jet emitted into a turbulent background allows the existence of high concentrations on the order of those of a jet emitted into a quiescent background, although with a lower probability. These findings are particularly important for practical applications such as the detection of instantaneous high concentrations of pollutants in flows whose mean concentrations have been considered safe.

The statistics of the scalar field within jets emitted into a turbulent background were compared to those of the velocity field of Khorsandi *et al.* (2013). The two fields exhibited overall a similar behavior on the mean and RMS quantities. However, a significant difference was observed in the half-widths of the fields. The half-widths of the scalar field were substantially larger than those of the velocity field. The observed difference in the widths is attributed to turbulent transport of scalar in the radial direction enhanced by i) the meandering of the jet, and ii) turbulent diffusion by the background turbulence, revealed by flow visualization. Also, the balance of terms in the equation of conservation of momentum were briefly discussed. The momentum associated with the mean flow (M) was observed to decrease with downstream distance which implies that the negligible terms for a jet emitted into a quiescent background increase in magnitude in the presence of background turbulence (although data confirming this has yet to be recorded).

Flow visualizations were employed to describe the entrainment and mixing in a jet emitted into a turbulent background. The visualizations revealed a complex mechanism of entrainment and mixing, especially complicated by the meandering of the jet, as opposed to a jet emitted into a quiescent background where nibbling is the principal mechanism of entrainment occurring at a well delimited interface (Westerweel *et al.* 2009). In the presence of background turbulence visualizations showed that the entrainment and mixing, which with the destruction of the jet structure, changes from jet driven entrainment to become potentially dominated by i) increased lateral advection of the jet by large scales of the turbulent background during the meandering of the jet which is subsequently mixed by its smaller scales, and ii) turbulent diffusion significantly enhanced by the turbulent background. (However, simultaneous measurements of velocity and concentration would be very beneficial to confirm this hypothesis.)

The changes in the downstream evolution of the statistics of the scalar field allowed the distinction of three regions in the jet issued into a turbulent background. In the first region, near the nozzle exit, the effect of the background turbulence is negligible. In the second region, the effects of the background turbulence on the statistics of the scalar field start to become noticeable and they increase with downstream distance. Finally, in the third region the jet structure is destroyed by the turbulent background and the scalar is mixed only by the turbulent background. In this regards, the breakup location of the jet based on the scalar field was determined as the location at which the mean centerline concentration decays to 1% of the nozzle exit value. The validity of the determination of the breakup location was confirmed by analysing the evolution of the statistics of the scalar field. This forms the base of a more complete definition of the breakup location.

Chapter 6

Conclusions

This chapter is divided into four sections. The first section presents the conclusions for the results of velocity field of the turbulence generated using different driving algorithms whereas the second presents the conclusions of the effect of background turbulence on the scalar field of a turbulent jet. In the third section, the original contributions of the present study are discussed, whereas the fourth section proposes some extensions of the present investigation.

6.1 Turbulence generated using different driving algorithms

All the algorithms tested generated flows with non-zero skewness of the velocity normal to the plane of the RJA. This is identified as an unavoidable feature of the RJA, presumably resulting from the unidirectional forcing in the tank and subsequent decay of the turbulence in one direction. Additionally, the kurtoses of the velocity fluctuations were also found to be slightly super-Gaussian in all directions, for all algorithms tested.

It was observed that the algorithms imposing a spatial configuration of jets working at any given time (identified as CHESSBOARD, EQUALCHESS, RANDOMCHESS) generated flows that were the most isotropic, although they suffered from large mean flows. Thus, those algorithms may be of potential use in investigations less concerned about the lack of a mean-flow, such as the study of advection and mixing of scalars in rivers or atmospheric/ocean circulation.

The results showed that the RMS velocities increase with the mean on-times of the pumps. This effect is attributed to longer periods of injection of momentum, facilitating its propagation in the downstream direction, and favoring the development of longer “instantaneous gradients of velocity,” allowing time for increased turbulent production.

The algorithm identified as RANDOM generated a flow with relatively high turbulent kinetic energy and the closest approximation of zero-mean-flow homogeneous isotropic turbulence. It generates turbulent flow with a relatively high Reynolds number (Re_T =

2360). One of the highest reported to date (when compared to grid–generated turbulence or the use of loudspeakers) and comparable to previous RJAs. The integral length scale (ℓ = 11.5 cm) in our flow is the largest reported, which may be beneficial for the study of large scales in turbulence. Moreover, along with Re, a large value of ℓ allows the existence of an inertial subrange covering a broad range of (readily measurable) scales.

The homogeneity of the flow (generated by RANDOM) in planes parallel to the RJA covers a large area of approximately 0.75×0.75 m^2 which cannot be achieved in other types of systems, such as those using propellers or loudspeakers. The capability of generating a relatively high-quality turbulent flow in a large facility proves the flexibility of RJAs to be scaled up to study turbulent flows at large scales.

6.2 Scalar mixing within a jet emitted into a turbulent background

The results showed significant changes in the statistics of the concentration field of jets emitted into turbulent surroundings compared to those of a jet emitted into a quiescent background. The radial profiles of mean concentration at different downstream positions showed lower mean concentrations near the centerline for the jets emitted into a turbulent background than those for a jet issued into a quiescent one. However, slightly higher mean concentrations were measured near the edges ($r/x > 0.15$) of the jet for the turbulent background cases, which is associated with the increased radial extents of the profiles.

The radial profiles become progressively flatter with increasing downstream distances – an observation attributed to the loss of jet structure (i.e. dominance of the turbulent background). The effects are more noticeable for the lower Reynolds number jet and the radial profile of mean concentration becomes essentially flat at x/D = 70, evidencing the destruction of the jet structure by the turbulent background.

The jet was observed to be wider in the presence of background turbulence. The downstream evolution of the half-width of the scalar field was also found to increase more rapidly than the linear growth of a jet emitted into a quiescent background. These findings are consistent with the observation of larger radial extents of the mean concentration profiles for jets emitted into a turbulent background and attributed to enhanced radial transport of scalar by the turbulent background.

In the presence of background turbulence, the radial profiles of RMS concentration showed increased values for the Re = 10600 jet at all radial positions and downstream distances as compared to the jet emitted into a quiescent background. For the Re=5800 jet, the profiles of RMS concentration in a turbulent background exhibited higher RMS concentrations than those of a jet released into quiescent surroundings near the jet exit. Farther downstream, however, the RMS concentrations became smaller and the radial profile became flat, consistent with the notion of loss of jet structure and subsequent mixing by the turbulent background.

Examination of the probability density functions (PDFs) of the concentration revealed substantial changes in the shape of the PDF. In the presence of background turbulence, the probability density functions evolved to become bimodal with the peak at low concentrations growing with downstream distance as opposed to the consistently Gaussian PDF for a jet emitted into a quiescent background. However, the maximum concentrations within the jets emitted into a turbulent background were on the order of those of a jet emitted into a turbulent background although with a lower probability. The increased intermittency of the scalar field of jets emitted into a turbulent background results in the highest concentrations being of similar value to those of the jet emitted into quiescent backgrounds, a behavior that is in contrast with the notion of superposition of the jet and background turbulence for which lower concentrations would be expected. These findings have important practical implications as they show that mean quantities are not necessarily representative of the instantaneous concentrations in the presence of a turbulent background. For example, certain contaminants measured in field studies may have toxic effects at sufficiently large instantaneous concentrations, even though their mean concentrations are deemed sufficiently small/safe.

Visualizations of cross sections of the jet emitted into a turbulent background showed significantly more meandering than that of a jet issued into quiescent surroundings. The increased meandering of the jet in the presence of background turbulence is a principal cause of the increased intermittency of the scalar field and the changes in its statistics. Specifically, the larger radial extents of the profiles (of mean and RMS concentrations) and higher concentrations near the edges of the jet are associated with transport of scalar at large radial positions during the meandering of the jet. Similarly, the peaks at low concentration in the PDFs of concentration of jets emitted into a turbulent background result from the movements of the jet (favoring the detection of ambient (clean) fluid for longer periods than for a jet issued into a quiescent background).

Examination of the flow visualizations of a jet emitted into a turbulent background revealed a complicated mechanism of entrainment and mixing due to the jet meandering. In the presence of background turbulence the entrainment and mixing changes from jet driven entrainment to become potentially dominated by i) increased lateral advection of the jet by large scales of the background turbulence during the meandering of the jet, and ii) turbulent diffusion significantly enhanced by the turbulent background. The increased mixing (during the jet meandering) and turbulent diffusion occur simultaneously and randomly making the entrainment and mixing a complex process.

The changes in the downstream evolution of the statistics of the scalar field allowed the distinction of three regions for a jet emitted into a turbulent background. In the first region, near the nozzle exit, the effect of the background turbulence is negligible and the jet development is similar to that of a jet emitted into a quiescent background. In the second region, the effects of the background turbulence on the statistics of the scalar field start to become noticeable and they increase with downstream distance. Finally, in the third region, the jet structure is destroyed by the turbulent background and the scalar is mixed only by the background turbulence. This third region is associated with the breakup location. The validity of the determination of the breakup location was supported by comparing the evolution of the various statistics of the scalar field to confirm that the jet structure has been destroyed at those positions. These measures formed the base of a more complete definition of the breakup location, which takes into account the changes in the statistics of the concentration/velocity field in the downstream direction.

The statistics of the scalar field within jets emitted into a turbulent background were compared to those of the velocity field of Khorsandi *et al.* (2013). The two fields exhibited overall a similar behavior with the main difference being a larger extent (in the radial direction) of the scalar field. The observed difference in the widths of the fields is attributed to turbulent transport of scalar in the radial direction enhanced by i) the meandering of the jet, ii) and turbulent diffusion by the background turbulence.

The momentum associated with the mean flow (M) in a jet emitted into a turbulent background was observed to decrease with downstream distance. Hence, the momentum is no longer conserved by only the mean flow (as in the case of a jet emitted into a turbulent background). Consequently, the contributions of other terms in the equation of conservation of momentum should increase to ensure an overall conservation of momentum. Specifically, the term $\frac{1}{2}\frac{d}{dx}\int_0^\infty(\langle UV\rangle + \langle uv\rangle)rdr\Big|_0^x$ is expected to increase due to the significant changes in the downstream evolution of the mean and RMS axial velocities in the presence of background turbulence (although the necessary data to calculate the integrals and derivatives is not currently available to confirm it). The downstream evolution of the mean scalar flux in the x-direction ($F = 2\pi\int_0^\infty\langle UC\rangle rdr$) was identical to the evolution of M. However, simultaneous measurements of velocity and concentration are necessary to be able to confirm the conservation of scalar, especially to account for the radial transport due to the meandering of the jet.

6.3 Contributions of the present study

Different driving algorithms for a large random jet array were tested in an attempt to further characterize their performance. This work explored the spatial configuration of jets operating at any given instant (an aspect that has not been documented in previous RJAs studies).

The limitations of mono-planar RJAs in generating turbulence were identified. They include the non-zero skewness of the velocity fluctuations normal to the plane of the RJA, slight anisotropy, and large kurtoses of the velocity fluctuations resulting from the asymmetric forcing.

The algorithm identified as RANDOM generated the flow that most closely approximated zero-mean-flow homogeneous isotropic turbulence in our large tank. The quality of the turbulence generated in the facility demonstrates the versatility of RJAs and their ability to be scaled-up to generate the largest quasi-homogeneous isotropic turbulent regions with zero mean flow. The availability of large experimental facilities is important in the study of natural and industrial phenomena such as injection of fuels in combustors or dilution of contaminants in the atmosphere/ocean which are dominated by scales much larger than the current laboratory setups.

The present tabulation and review of the 9 driving algorithms studied herein may be used by future researchers who require certain specific characteristics in a flow (e.g. large kurtosis/high levels of intermittency).

This thesis also presents a systematic study of the effect of homogeneous isotropic turbulence with negligible mean flow on the scalar field of a momentum-driven, axisymmetric turbulent jet at different Reynolds numbers. In this study, the background turbulence was constant along the jet axis to study the gradual effect of the external turbulence as opposed to previous studies in grid generated turbulence.

The results showed overall lower mean concentrations and larger widths of the jets emitted into a turbulent background. This overall higher scalar mixing is very interesting given the associated lower entrainment in jets emitted into turbulent backgrounds of Khorsandi *et al.* (2013). Hence, the present results imply enhanced mixing and radial transport of scalar by the background turbulence despite the lower entrainment into the jet.

In the presence of background turbulence, the maximum concentrations within the jet were comparable to those of a jet issued into a quiescent background. This result implies that although the external turbulence enhances the mixing, it is not homogeneous and high instantaneous concentrations still exist. These findings have important practical implications since, for example, certain contaminants measured in field studies may have toxic effects at sufficiently large instantaneous concentrations, even though their mean concentrations are deemed sufficiently small/safe. Similarly, turbulent combustion of fuels in combustors may be affected since the mixing with the turbulent surroundings provides the oxygen to sustain the combustion.

In the presence of background turbulence the entrainment and mixing changes from jet driven entrainment to become potentially dominated by i) increased advection of the jet by large scales of the background turbulence during the meandering of the jet, and ii) turbulent diffusion significantly enhanced by the turbulent background. The meandering and turbulent diffusion are associated with the high degrees of intermittency and the larger radial extents of the profiles of mean and RMS concentration since the two mechanism enhance the transport of scalar at large radial positions.

In the present investigation, a more complete definition of the breakup location was proposed. It includes the downstream evolution of the velocity/scalar fields to validate the breakup location.

Comparison of the statistics of the scalar and velocity fields of jets emitted into a turbulent background showed larger radial extents of the concentration profiles. The wider profiles of the scalar field is attributed to the enhanced transport of scalar in the radial direction by turbulent diffusion and meandering of the jet. These results imply a better transport of a scalar than momentum by the background turbulence. Consequently, care should be taken when hypothesizing about scalar transport solely from the velocity field.

The present investigation analyzed the equations of conservation of momentum and scalar to further understand the interaction of the jet and turbulent background. The leading terms were identified and their downstream evolution described, which was consistent with the results calculated with the data available. The study of the conservation equations complemented with the observations in the experiments is fundamental to the complete understanding of complex processes such as turbulent jets emitted into a turbulent background.

Lastly, the present results of the evolution of the statistics of the scalar field within turbulent jets emitted into a turbulent background may be used in future investigations to benchmark numerical simulations.

6.4 Recommendations for future work

The author recommends to study the effect of different levels of turbulent kinetic energy of the background turbulence on the scalar field of the jet. Higher turbulent kinetic energies of the turbulent background would be beneficial to further understand the effects on the scalar field while lower levels of external turbulent intensity would potentially eliminate the meandering of the jet and thus isolate the effects of the turbulent diffusion of scalar field.

Measurements with jets at different Reynolds numbers could also provide information on the three regions of the jet confirmed in the present study. The identification of the three regions on jets at different Reynolds number could allow the precise prediction of the limits of the regions based on parameters of the jet and turbulent background.

Simultaneous measurements of velocity and concentration will be very useful for a better description of the mechanism of entrainment and mixing in a jet emitted into a turbulent background. They will allow confirmation of the hypothesis of a process dominated by turbulent diffusion and increased mixing during the meandering of the jet. Additionally, the simultaneous measurements would permit quantification of the transport of scalar in the radial direction and confirm the conservation of scalar. Similarly, simultaneous measurements of concentration and velocity would allow calculation of the turbulent transport in the axial direction.

Measurements in a facility capable of varying the integral length scale of the background turbulence would be beneficial to study the effects of the relative lengths scales of the jet and the turbulent background on the evolution and ultimate breakup of jets emitted into turbulent surroundings.

Further measurements of the velocity field would be necessary to calculate all terms of the equation of conservation of momentum. Specifically, the complete statistics of the radial velocity (V), the Reynolds stresses and enough measurements to calculate the derivatives with confidence would be necessary for a complete discussion of the equation of conservation of momentum of jets emitted into a turbulent background.

References

Amoura, Z., Roig, V., Risso, F. and Billet A. M. 2010 Attenuation of the wake of a sphere in an intense incident turbulence with large length scales. *Phys. Fluids* 22, 055105.

Antoine, Y., Lemoine, F. and Lebouche, M. 2001. Turbulent transport of a passive scalar in a round jet discharging into a co-flowing stream. *Eur. J. Mech. B – Fluids* 20, pp. 275-301.

Antonia, R. A., Prabhu, A. and Stephenson, S. E. 1975. Conditionally sampled measurements in a heated turbulent jet. *J. Fluid Mech.* 72, pp. 455-480.

Aumaitre, S., Fauve, S. and Pinton, J. F. 2000. Large scale correlations for energy injection mechanisms in swirling turbulent flows. *Eur. Phys. J.* B 16, pp. 563-567.

Bagchi, P. and Balachandar, S. 2004. Response of the wake of an isolated particle to an isotropic turbulent flow. *J. Fluid Mech.* 518, pp. 95-123.

Bagchi, P. and Kottam, K. 2008. Effect of freestream isotropic turbulence on heat transfer from a sphere. *Phys. Fluids* 20, 073305.

Barrett T. K. and Van Atta C. W. 1991. Experiments on the inhibition of mixing in stably stratified decaying turbulence using laser Doppler anemometry and laser-induced fluorescence. *Phys. Fluids A Fluid Dyn.* 3, pp. 1321–1332.

Batchelor (1959). Small-scale variation of convected quantities like temperature in turbulent fluid Part 1. General discussion and the case of small conductivity. *J. Fluid Mech.* 5, pp. 113-133.

Becker, H. A., Hottel, H. C. and Williams, G. C. 1967. The nozzle-fluid concentration field of the round, turbulent, free jet. *J. Fluid Mech.* 30, pp. 285-303.

Belin, F., Maurer, J., Tabeling, P. and Willaime, H. 1997. Velocity gradient distributions in fully developed turbulence: An experimental study. *Phys. Fluids* 9, pp. 3843-3850.

Bellani, G. and Variano, E.A. 2014. Homogeneity and isotropy in a laboratory turbulent flow. *Exp. Fluids* (2014) 55, 1646.

Benson, D. M., Bryan, J., Plant, A. L., Gotto, A. M. and Smith, L. C. 1985. Digital imaging fluorescence microscopy: Spatial heterogeneity of photobleaching rate constants in individual cells. *J. Cell. Biol.* 100, pp. 1309-1323.

Berg, J., Luthi, B., Mann, J. and Ott, S. 2006. Backwards and forwards relative dispersion in turbulent flow: an experimental investigation. *Phys. Rev. E* 74, 016304.

Birch, A. D., Brown, D. R., Dodson, M. G. and Thomas, J. R. 1978. The turbulent concentration field of a methane jet. *J. Fluid Mech.* 88, pp. 431-449.

Birouk, M., Sarh, B., and Gokalp, I. 2003. An attempt to realize experimental isotropic turbulence at low Reynolds number. *Flow Turbul. Combust.* 70, pp. 325–348.

Bisset, D. K., Hunt, J. C. R. and Rogers, M. M. 2002. The turbulent/non-turbulent interface bounding a far wake. *J. Fluid Mech.* 451, pp. 383-410.

Blum, D. B., Kunwar, S. B., Johnson, J. and Voth, G. A. 2010. Effects of nonuniversal large scales on conditional structure functions in turbulence. *Phys. Fluids* 22, 015107.

Blum, D. B., Bewley, G. P., Bodenschatz, E., Gibert, M., Gylfason, A., Mydlarski, L., Voth, G. A., Xu, H., and Yeung, P. K. 2011 Signatures of non-universal large scales in conditional structure functions from various turbulent flows. *New J. Phys.* 13, 113020.

Bodenschatz, E., Bewley, G. P., Nobach, H., Sinhuber, M., and Xu, H. 2014. Variable density turbulence tunnel facility. *Rev. Sci. Instrum.* 85, 093908

Breidenthal, R. 1981. Structure in turbulent mixing layers and wakes using a chemical reaction. *J. Fluid Mech.* 109, pp. 1-24.

Brumley, B. H. and Jirka, G. H. 1987. Near-surface turbulence in a grid-stirred tank. *J. Fluid Mech.*183, pp. 235–263.

Buch, K. A. and Dahm, W. J. A. 1996. Experimental study of the fine scale structure of conserved scalar mixing in turbulent shear flows. Part 1. Sc>>1. *J. Fluid Mech.* 317, pp. 21-71.

Cadot, O., Douady, S. and Couder, Y. 1995. Characterization of the low-pressure filaments in a three-dimensional turbulent shear flow. *Phys. Fluids* 7, pp. 630-646.

Catrakis, H. J. and Dimotakis, P. E. 1996. Mixing in turbulent jets: scalar measures and isosurface geometry. *J. Fluid Mech.* 317, pp. 369-406.

Cetegen, B. M. and Mohamad, N. 1993. Experiments on liquid mixing and reaction in a vortex. *J. Fluid Mech.* 249, pp. 391-414.

Chang, K., Bewley, G. P. and Bodenschatz, E. 2012. Experimental study of the influence of anisotropy on the inertial scales of turbulence. *J. Fluid Mech.* 692, pp. 464–481.

Chauhan, K., Philip, J., de Silva, C. M., Hutchins, N. and Marusic, I. 2014. The turbulent/non-turbulent interface and entrainment in a boundary layer. *J. Fluid Mech.* 742, pp. 119-151.

Chen, C. J. and Rodi, W. 1980. *Vertical turbulent buoyant jets: a review of experimental data*. Pergamon Press.

Ching, C. Y., Fernando, H. J. S. and Robles, A. 1995. Break down of line plumes in turbulent environments. *J. Geophys. Res.* 100, pp. 4707-4713.

Chua, L. P. and Antonia, R. A. 1990. Turbulent Prandtl number in a circular jet. *Int. J. Heat Mass Trans.* 33, pp. 331-339.

Coppeta, J. and Rogers, C. 1998. Dual emission laser induced fluorescence for direct planar scalar behaviour measurements. *Exp. Fluids* 25, pp. 1-15.

Corrsin, S. 1951. On the spectrum of isotropic temperature fluctuations in an isotropic turbulence. *J. Appl. Phys.* 22, pp. 469-473.

Corrsin, S. and Kistler, A. L. 1955. Free-stream boundaries of turbulent flows. *NACA-TR-1244.*

Crimaldi, J. P. 1997. The effect of photobleaching and velocity fluctuations on single-point LIF measurements. *Exp. Fluids* 23, pp. 325-330.

Crimaldi, J. P. and Koseff, J. R. 2001. High-resolution measurements of the spatial and temporal scalar structure. *Exp. Fluids* 31, pp. 90-102.

Crimaldi, J. P. 2008. Planar laser induced fluorescence in aqueous flows. *Exp. Fluids* 44, pp. 851-863.

Cuthbertson, A. J. S., Malcangio, D., Davies, P. A. and Mossa, M. 2006. The influence of a localized region on turbulence on the structural development of a turbulent, round, buoyant jet. *Fluid Dyn. Res.* 38, pp. 683-698.

da Silva, C. B., Hunt, J. C. R., Eames, I. and Westerweel, J. 2014. Interfacial layers between regions of different turbulence intensity. *Annu. Rev. Fluid Mech.* 46, pp. 567-590.

Dahm, W. J. A. and Dimotakis, P. E. 1987. Measurements of entrainment and mixing in turbulent jets. *AIAA J.* 25, pp. 1216-1223.

Dahm, W. J. A. and Dimotakis, P. E. 1990. Mixing at large Schmidt number in the self-similar far field of turbulent jets. *J. Fluid Mech.* 217, pp. 299-330.

Darisse, A., Lemay, J. and Benaïssa, A. 2015. Budgets of turbulent kinetic energy, Reynolds stresses, variance of temperature fluctuations and turbulent heat fluxes in a round jet. *J. Fluid Mech.* 774, pp. 95-142.

de Jong, J., Cao, L., Woodward, S., Salazar, J., Collins, L., and Meng, H. 2008. Dissipation rate estimation from PIV in zero-mean isotropic turbulence. *Exp. Fluids,* 46, pp. 499–515

De Silva, I.P.D. and Fernando, H.J.S. 1994. Oscillating grids as a source of nearly isotropic turbulence. *Phys. Fluids* 6, pp. 2455-2465.

Delbos, S., Weitbrecht V., Bleninger T., Grand P. P., Chassaing E., Lincot D., Kerrec O., and Jirka G. H. 2009. Homogeneous turbulence at an electrodeposition surface induced by randomly firing jet arrays. *Exp. Fluids*, 46, 1105.

Deusch. S. and Dracos, T. 2001. Time resolved 3D passive scalar concentration-field imaging by laser induced fluorescence (LIF) in moving liquids. *Meas. Sci. Technol.* 12, pp. 188-200.

Dewey, C. F. 1976. Qualitative and quantitative flow field visualization utilizing laser-induced fluorescence. *AGARD Conf. Froc.* 193.

Dimotakis, P. E. 2000. The mixing transition in turbulent flows. *J. Fluid Mech.* 409, pp. 69-98.

Douady, S., Couder, Y., and Brachet, M. E. 1991. Direct observation of the intermittency of intense vorticity filaments in turbulence. *Phys. Rev. Lett.* 67, pp. 983-986.

Dowling, D.R. and Dimotakis, P.E. 1990. Similarity of the concentration field of gas-phase turbulent jets. *J. Fluid Mech.* 218, pp. 109-141.

Dyer, M. J. and Crosley, D. R. 1982. Two-dimensional imaging of OH laser-induced fluorescence in a flame. *Optics Letters* 7, pp. 382-384.

Fallon, T., and Rogers, C. B. (2002) Turbulence-induced preferential concentration of solid particles in microgravity conditions. *Exp. Fluids,* 33, pp. 233–241.

Fauve, S., Laroche, C. and Castaing, B. 1993. Pressure fluctuations in swirling turbulent flows*. J. Phys.* Paris II 3, pp. 271-278.

Fernando, H.J.S. and De Silva, I.P.D. 1993. Note on secondary flows in oscillating-grid, mixing-box experiments. *Phys. Fluids*, A5 (7), pp. 1849-1851.

Ferrier, A. J., Funk, D. R. and Roberts, P. J. W. 1993. Application of optical techniques to the study of plumes in stratified fluids. *Dynam. Atmos. Oceans* 20, pp. 155-183.

Gaskin, S. J., McKernan, M. and Xue, F. 2004. The effect of background turbulence on jet entrainment: an experimental study of a plane jet in a shallow coflow. *J. Hydraul. Res.* 42, pp. 531-540.

Goepfert, C., Marie´, J., Chareyron, D., and Lance, M. 2010. Characterization of a system generating a homogeneous isotropic turbulence field by free synthetic jets. *Exp. Fluids,* 48, pp. 809–822.

Good, G. H. and Warhaft, Z., 2011. On the probability distribution function of the velocity field and its derivative in multi-scale turbulence. *Phys. Fluids* 23, 095106.

Guilbault, G. G. 1973. *Practical fluorescence: Theory, methods, and techniques*. Marcel Dekker, INC.

Guillard, F., Fritzon, R, Revstedt, J., Tragardh, C., Alden, M. and Fuchs, L. 1998. Mixing in a confined turbulent impinging jet using planar laser-induced fluorescence. *Exp. Fluids* 25, pp. 143-150.

Guo, Y., Davies, P. A., Fernando, H. J. S. and Ching, C. Y. 1999. Influence of background turbulence on the evolution of turbulent jets. *Conference proceedings of the 28th IAHR congress*.

Guo, Y., Malcangio, D., Davies, P. A. and Fernando, H. J. S. 2005. A laboratory investigation into the influence of a localized region on turbulence on the evolution of a round turbulent jet. *Fluid Dyn. Res.* 36, pp. 78-89.

Hancock, P. E. and Bradshaw, P. 1983. The effect of free-stream turbulence on turbulent boundary layers. *ASME. J. Fluids Eng.* 105, pp. 284-289.

Hancock, P. E. and Bradshaw, P. 1989. Turbulence structure of a boundary layer beneath a turbulent free stream. *J. Fluid Mech.* 205, pp. 45-76.

Hannoun, I. A. and List, E. J. 1988. Turbulent mixing at a shear-free density interface. *J. Fluid Mech.* 189, pp. 211-234.

Hubner, J. Buoyant plumes in a turbulent environment. PhD Thesis. University of Cambridge.

Hunt, J. C. R. 1994. Atmospheric jets and plumes. In: Davies, P. A. and Valente Neves, M.I. (eds.). Recent Research Advances in the Fluid Mechanics of Turbulent Jets and Plumes, *NATO ASI Series E* 255, pp. 309-334.

Hussein, H. J., Capp, S. P. and George, W. K. 1994. Velocity measurements in a high-Reynolds-number, momentum-conserving, axisymmetric, turbulent jet. *J. Fluid Mech.* 258, pp. 31-75.

Hwang, W., and Eaton, J. K. 2004. Creating homogeneous and isotropic turbulence without a mean flow. *Exp. Fluids,* 36, pp. 444-454.

Iovieno, M., Di Savino, S., Gallana, L. and Tordella, D. 2014. Mixing of a passive scalar across a thin shearless layer: concentration of intermittency on the sides of the turbulent interface. *J. Turbul.* 15, pp. 311-334.

Khorsandi, B., 2011. PhD Thesis. Effect of background turbulence on an axisymmetric turbulent jet.

Khorsandi, B., Mydlarski, L. and Gaskin, S. J., 2012. Noise in turbulence measurements using acoustic Doppler velocimetry. *J. Hydraul. Eng.* vol. 138 No. 10, pp. 829-838.

Khorsandi, B., Gaskin, S. and Mydlarski, L., 2013. Effect of background turbulence on an axisymmetric turbulent jet. *J. Fluid Mech.* 736, pp. 250-286.

Kolmogorov, A. N. 1941a. The local structure of turbulence in incompressible viscous fluid for very large Reynolds numbers. *Dokl. Akad. Nauk. SSSR* 30, pp. 301-305.

Kolmogorov, A. N. 1941a. Dissipation of energy in the locally isotropic turbulence. *Dokl. Akad. Nauk. SSSR* 32, pp. 16-18.

Koochesfahani, M. 1984. Experiments on turbulent mixing and chemical reactions in a liquid mixing layer. PhD Thesis, Califomia Institute of Technology.

Koochesfahani, M. M. and Dimotakis, P. E. 1985. Laser-Induced Fluorescence Measurements of Mixed Fluid Concentration in a Liquid Plane Shear Layer. *AIAA J.* 23, pp. 1700-1707.

Kychakoff, G., Howe, R. D., Hanson, R. D. and McDaniel, J. C. 1982. Quantitative visualization of combustion species in a plane. *Applied Optics* 21, pp. 3225-3227.

Lavertu, T. M. 2006. Differential diffusion in a turbulent jet. PhD thesis, McGill University.

Lavertu, T. M., Mydlarski, L. and Gaskin, S. J. 2008. Differential diffusion of high-Schmidt-number passive scalars in a turbulent jet. *J. Fluid Mech.* 612, pp. 439-475.

Law, A. W. K. and Wang, H. 2000. Measurements of mixing processes using combined digital particle image velocimetry and planar laser induced fluorescence. *Expl. Thermal Fluid Sci.* 22, pp. 213-229.

Law, A. W. K., Cheng, N. S. and Davidson, M. J. 2001. Jet spreading in oscillating-grid turbulence. *Proceedings of the 3rd International Symposium on Environmental Hydraulics, IAHR*, pp. 1-6.

Legendre, D., Merle, A. and Magnaudet, J. 2006. Wake of a spherical bubble or a solid sphere set fixed in a turbulent environment. *Phys. Fluids* 18, 048102.

Liberzon, A., Guala, M., Lüthi, B., Kinzelbach, W., and Tsinober, A. 2005. Turbulence in dilute polymer solutions. *Phys. Fluids* 17, 031707.

Lipari, G. and Stansby, P. 2011. Review of experimental data on incompressible turbulent round jets. *Flow Turbul. Combust.* 87, pp. 79-114.

Liu, S., Katz, J., and Menevau, C. 1999. Evolution and modelling of subgrid scales during rapid straining of turbulence. *J. Fluid Mech.* 387, pp. 281–320

Lockwood, F. C. and Moneib, H. A. 1980. Fluctuating temperature measurements in a heated round free jet. *Combust. Sci. Tech.* 22, pp. 63-81.

Long, M. B. and Chu, B. T. 1981. Mixing mechanism and structure of an axisymmetric turbulent mixing layer. *AIAA J.* 19, pp. 1158-1163.

Lu, J., Fugal, J. P., Nordsiek, H., Saw, E. W., Shaw, R. A. and Yang, W. 2008. Lagrangian particle tracking in three dimensions via single-camera in-line digital holography. *New J. Phys.* 10,125013.

Machicoane, N., Zimmermann, R., Fiabane, F., Bourgoin, M., Pinton, J.-F. and Volk, R. 2014. Large sphere motion in a nonhomogeneous turbulent flow. *New J. Phys.* 16, 013053.

Makita, H. 1991. Realization of a large-scale turbulence field in a small wind tunnel. *Fluid Dyn. Res.* 8, pp. 53-64.

Mathew, J. and Basu, A. 2002. Some characteristics of entrainment at a cylindrical turbulence boundary. *Phys. Fluids* 14, pp. 2065-2072.

Maurer, J., Tabeling, P. and Zocchi, G. 1994. Statistics of turbulence between two counter-rotating disks in low-temperature helium gas. *Europhys. Lett.* 26, 31-36.

Maxey, M.R. 2007. The velocity skewness measured in grid turbulence. *Phys. Fluids* 30, pp. 935-938.

McDougall, T.J. 1979. Measurements of turbulence in a zero-mean shear mixed layer. *J. Fluid Mech.* 94, pp. 409–431.

McKenna, S.P. and McGillis, W.R. 2004. Observations of flow repeatability and secondary circulation in an oscillating grid-stirred tank. *Phys. Fluids* 16, pp. 3499-3502.

McLelland, S. J., and Nicholas, A. P. 2000. A new method for evaluating errors in a high-frequency ADV measurements. *Hydrol. Processes* 14, pp. 351-366.

Mi, J., Nobes, D. S. and Nathan G. J. 2001. Influence of jet exit conditions on the passive scalar field of an axisymmetric free jet. *J. Fluid Mech.* 432, pp. 91-125.

Miller, P. L. and Dimotakis, P. E. 1991a. Stochastic geometric properties of scalar interfaces in turbulent jets. *Phys. Fluids A* 3, pp. 168-177.

Miller, P. L. and Dimotakis, P. E. 1991b. Reynolds number dependence of scalar fluctuations in a high Schmidt number turbulent jet. *Phys. Fluids A* 3, pp. 1156-1163.

Miller, P. L. and Dimotakis, P. E. 1996. Measurements of scalar power spectra in high Schmidt number turbulent jets. *J. Fluid Mech.* 308, pp. 129-146.

Mordant, N., Metz, P., Michel, O. and Pinton, J. 2001. Measurement of Lagrangian velocity in fully developed turbulence. *Phys. Rev. Lett.* 87, 214501.

Morton, B.R., Taylor, G.I. and Turner, J.S. 1956. Turbulent gravitational convection from maintained and instantaneous sources. *Proc. Roy. Soc. Of London*, Series A 234, pp. 1-23.

Mydlarski, L. and Warhaft, Z. 1996. On the onset of high-Reynolds number grid-generated wind tunnel turbulence. *J. Fluid Mech.* 320, pp. 331-368.

Mydlarski, L. and Warhaft, Z. 1998. Passive scalar statistics in high-Péclet number grid turbulence. *J. Fluid Mech.* 358, pp. 135-175.

Oboukhov, A. M. 1949. Structure of the temperature field in turbulent flows. *Izv. Akad. Nauk. SSSR, Geogr. Geofiz.* 13, pp. 58-69.

Orszag, S. A. 1977. *Lectures on the statistical theory of turbulence*. In Fluid Dynamics (ed. R. Balian & J. L. Peube), p. 235. Gordon & Breach.

Ott, S. and Mann, J. 2000. An experimental investigation of the relative diffusion of particle pairs in three-dimensional turbulent flow. *J. Fluid Mech.* 422, pp. 207-223.

Owen, F. K. 1976. Simultaneous laser measurements of instantaneous velocity and concentration in turbulent mixing. *AGARD Conf. Proc.* 193.

Panchapakesan, N. R. and Lumley, J. L. 1993a. Turbulence measurements in axisymmetric jets of air and helium. Part 1. Air jet. *J. Fluid Mech*. 246, pp. 197-223.

Panchapakesan, N. R. and Lumley, J. L. 1993b. Turbulence measurements in axisymmetric jets of air and helium. Part 2. Helium jet. *J. Fluid Mech*. 246, pp. 225-247.

Papadopoulos, G. and Pitts, W. M. 1998. Scaling the near-field centerline mixing behavior of axisymmetric turbulent jets. *AIAA J.* 36, pp. 1635-1642.

Papantoniou, D. and List, E. J. 1989. Large-scale structure in the far field of buoyant jets. *J. Fluid Mech.* 209, pp. 151-190.

Perez-Alvarado, A., Mydlarski, L. and Gaskin, S. 2016. Effect of the driving algorithm on the turbulence generated by a random jet array. *Exp. Fluids* 57:20.

Philip, J., Meneveau, C., de Silva, C. M. and Marusic, I. 2014. Multiscale analysis of fluxes at the turbulent/non-turbulent interface in high Reynolds number boundary layers. *Phys. Fluids* 26, 015105.

Pope, S.B., 2000. *Turbulent Flow*. Cambridge Univ. Press.

Prasad, R. R. and Sreenivasan, K. R. 1990. Quantitative three-dimensional imaging and the structure of passive scalar fields in fully turbulent flows. *J. Fluid Mech.* 216, pp. 1-34.

Sahar, E. and Treves, D. 1977. Bleaching and diffusion of laser dyes in solution under high power UV Irradiation. *Optics Communications* 21, pp. 20-24.

Saylor, J. R. 1995. Photobleaching of disodium fluorescein in water. *Exp. Fluids* 18, pp. 445-447.

Saylor, J. R. and Sreenivasan, K. R. 1998. Differentiai diffusion in low Reynolds number water jets. *Phys. Fluids* 10, pp. 1135-1146.

Shan, J. W., Lang, D. B. and Dimotakis, P. E. 2014. Scalar concentration measurements in liquid-phase flows with pulsed lasers. *Exp. Fluids* 36, pp. 268-273.

Sharp, N. S., Neuscamman, S. and Warhaft, Z. 2009. Effects of large-scale free stream turbulence on a turbulent boundary layer. *Phys. Fluids* 21, 095105.

Shlien, D. J. 1987. Observations of dispersion of entrained fluid in the self-preserving region of a turbulent jet. *J. Fluid Mech*. 183, pp. 163-173.

Shy, S. S., Tang, C. Y., and Fann, S. Y. 1997. A nearly isotropic turbulence generated by a pair of vibrating grids. *Exp. Thermal Fluid Sci.* 14, pp. 251-262.

Srdic, A., Fernando, H.J.S., and Montenegro, L. 1996. Generation of nearly isotropic turbulence using two oscillating grids. *Exp. Fluids,* 20, pp. 395-397.

Stapountzis H., Westerweel J., Bessem J. M., Westendorp A. and Nieuwstadt F. T. M. 1992. Measurement of product concentration of 2 parallel reactive jets using digital image-processing. *Appl. Sci. Res.* 49, pp. 245-259.

Su, L. K. and Clemens, N. T. 2003. The structure of fine-scale scalar mixing in gas-phase planar turbulent jets. *J. Fluid Mech*. 488, pp. 1-29.

Taveira, R. R., Diogo, J. S., Lopes, D. C. and da Silva C. B. 2013. Lagrangian statistics across the turbulent-nonturbulent interface in a turbulent plane jet. *Phys. Rev. E* 88, 043001.

Taylor, J. R., 1997*. An Introduction to Error Analysis*. University Science Books.

Tennekes, H. and Lumley, J. L. 1972. *A First Course in Turbulence*. MIT Press.

Thole, K. A. and Bogard, D. G. High freestream turbulence effects on turbulent boundary layers. *ASME. J. Fluids Eng.* 118, pp. 276-284.

Thompson, S. and Turner, J. S. 1975. Mixing across an interface due to turbulence generated by an oscillating grid. *J. Fluid Mech.* 67, pp. 349-368.

Tian, X. D. and Roberts J. W. 2003. A 3D LIF system for turbulent buoyant jet flows. *Exp. Fluids* 35, pp. 636-647.

Tong, C. and Warhaft, Z. 1995. Passive scalar dispersion and mixing in a turbulent jet. *J. Fluid Mech*. 292, pp. 1-38.

Townsend, A. A. 1966. The mechanism of entrainment in free turbulent flows. *J. Fluid Mech.* 26, pp. 689-715.

Tsinober, A. 2004. *An informal introduction to turbulence*. Kluwer Academic Publisher.

Van Reeuwijk, M., Salizzoni, P., Hunt, G.R. and Craske, J. 2016. Turbulent transport and entrainment in jet and plumes: a DNS study. arXiv:1603.09078 [physics.flu-dyn].

Van Vliet, E., Van Bergen, S. M., Derksen, J. J., Portela, L. M. and Van den Akker, H. E. A. 2004. Time-resolved, 3D, laser-induced fluorescence measurements of fine-structure passive scalar mixing in a tubular reactor. *Exp. Fluids* 37, pp. 1-21.

Vanderweel, C. and Tavoularis, S. 2014. On the accuracy of PLIF measurements in slender plumes. *Exp. Fluids* 55, 1801.

Variano, E. A., Bodenschatz, E., and Cowen, E. A. 2004. A random synthetic jet array driven turbulence tank. *Exp. Fluids* 37, pp. 613-615

Variano, E. A., and Cowen E. A. 2008. A random-jet-stirred turbulence tank. *J. Fluid Mech.* 604, pp. 1-32

Vectrino Velocimeter User Guide, Nortek, 2004.

Villermaux, E., Sixou, B., and Gagne, Y. 1995. Intense Vortical Structures in Grid-Generated Turbulence. *Phys. Fluids* 7, pp. 2008-2013.

Voth G., Porta A. L., and Crawford A. 2002. Measurement of particle accelerations in fully developed turbulence. *J. Fluid Mech.* 469, pp. 121-160.

Voulgaris, G. and Trowbridge, J. H. 1998. Evaluation of the acoustic Doppler velocimeter (ADV) for turbulence measurements. *J. Atmos. Oceanic Tech.* 15, pp. 272-289.

Walker, D. A. 1987. A fluorescence technique for measurement of concentration in mixing liquids. *J. Phys. E: Sci. Instrum.* 20, pp. 217-224.

Wang, G. R. and Fiedler, H. E. 2000a. On high spatial resolution sca1ar measurement with LIF. Part 1: Photobleaching and thermal blooming. *Exp. Fluids* 29, pp. 257-264.

Wang, G. R. and Fiedler, H. E. 2000b. On high spatial resolution scalar measurement with LIF. Part 2: The noise characteristic. *Exp. Fluids* 29, pp. 265-274.

Warnaars, T. A., Hondzo, M. and Carper, M. A. 2006. A desktop apparatus for studying interactions between microorganisms and small-scale fluid motion. *Hydrobiologia,* 563, 431–443.

Watanabe, T., Sakai, Y., Nagata, K., Ito, Y. and Hayase, T. 2015. Turbulent mixing of passive scalar near turbulent and non-turbulent interface in mixing layers. *Phys. Fluids* 27, 085109.

Webster, D. R., Roberts, P. J. W., and Raad, L. 2001. Simultaneous DPTV/PLIF measurements of a turbulent jet. *Exp. Fluids* 30, pp. 65-72.

Webster, D. R., Brathwaite, A. and Yen, J. 2004. A novel laboratory apparatus for simulating isotropic oceanic turbulence at low Reynolds number*. Limnol. Oceanogr. Methods* 2, pp. 1–12.

Westerweel, J., Fukushima, C., Pedersen, J. M. and Hunt, J. C. R. 2005. Mechanics of the turbulent/nonturbulent interface of a jet. *Phys. Rev. Lett.* 95, 174501.

Westerweel, J., Fukushima, C., Pedersen, J. M. and Hunt, J. C. R. 2009. Momentum and scalar transport at the turbulent/non-turbulent interface of a jet. *J. Fluid Mech*. 631, pp. 199-230.

Wilson, R. A. M., and Danckwerts, P. V. 1964. Studies in turbulent mixing-II A hot-air jet. *Chem. Eng. Sci.* 19, pp. 885-895.

Wolf, M., Luthi, B., Holzner, M., Krug, D., Kinzelbach, W. and Tsinober, A. 2012 Investigations on the local entrainment velocity in a turbulent jet. *Phys. Fluids* 24, 105110

Wright, S.J. 1994. The effect of ambient turbulence on jet mixing. In: Davies, P. A. and Valente Neves, M.I. (eds.). Recent Research Advances in the Fluid Mechanics of Turbulent Jets and Plumes, *NATO ASI Series E* 255, pp. 13-27.

Wygnanski, I., and Fiedler, H. 1969. Some measurements in the self-preserving jet. *J. Fluid Mech*. 38, pp. 577-612.

Xu, G., and Antonia, R. A. 2002. Effect of different initial conditions on a turbulent round free jet. *Exp. Fluids* 33, pp. 677-683.

Yoda M., Hesselink, L. and Mungal, M. G. 1994. Instantaneous three-dimensional concentration measurements in the self-similar region of a round high-Schmidt-number jet. *J. Fluid Mech*. 279, pp. 313-350.

Yule, A. J. 1978. Large-scale structure in the mixing layer of a round jet. *J. Fluid Mech*. 89, pp. 413-432.

Zedel, L., Hay, A. E., Cabrera, R., and Lohrmann, A. 1996. Performance of a single-beam pulse-to-pulse coherent Doppler profiler. *IEEE Journal of Oceanic Engineering*, vol.21, no.3, pp. 290-297.

Zimmermann, R., Xu, H., Gasteuil, Y., Bourgoin, M., Volk, R., Pinton, J.F., and Bodenschatz, E. 2010. The Lagrangian exploration module: an apparatus for the study of statistically homogeneous and isotropic turbulence. *Rev. Sci. Instrum.* 81:055112.